

UDRI

UNIVERSITY
of DAYTON
RESEARCH
INSTITUTE

June 7, 2007

Dr. Paul Hoffman
Government Technical Program Manager
NAVAIR
NavairSysCom
48110 Shaw Road, Unit 5
Patuxent River, MD 20670-1906

Subject: Contract #F42620-00-D-0039, 0011

Dear Dr. Hoffman,

Please find enclosed two CDs which contain the final report entitled, "*Navy High Strength Steel Corrosion-Fatigue Modeling Program*", UDR-TR-2007-00039. This satisfies CDRL Data Item A241, Scientific Technical Reports. This delivery also satisfies the requirements of Data Item A102, Software User's Manual. StressCheck software and user's manual were delivered separately, however, examples which demonstrate the use of StressCheck on this program are included in the final report.

Sincerely,



Robert J. Andrews
Head, Structural Integrity Division

rja/as
Enclosure
File: 2944

UNIVERSITY
OF DAYTON
RESEARCH
INSTITUTE

Structural Integrity Division
300 College Park
Dayton, OH 45469-0120
(937) 229-4417
FAX (937) 229-3712

Report

NAVY HIGH-STRENGTH STEEL CORROSION-FATIGUE MODELING PROGRAM

.....

October 2006

Wally Hoppe, Ollie Scott,
Bill Braisted, Garry Abfalter,
Jennifer Pierce, Eric Burke,
Sarah Kuhlman, Brian Frock,
and Ray Ko

Report Documentation Page			Form Approved OMB No. 0704-0188		
Public reporting burden for the collection of information is estimated to average 1 hour per response, including the time for reviewing instructions, searching existing data sources, gathering and maintaining the data needed, and completing and reviewing the collection of information. Send comments regarding this burden estimate or any other aspect of this collection of information, including suggestions for reducing this burden, to Washington Headquarters Services, Directorate for Information Operations and Reports, 1215 Jefferson Davis Highway, Suite 1204, Arlington VA 22202-4302. Respondents should be aware that notwithstanding any other provision of law, no person shall be subject to a penalty for failing to comply with a collection of information if it does not display a currently valid OMB control number.					
1. REPORT DATE OCT 2006		2. REPORT TYPE Technical Report		3. DATES COVERED 30-06-2003 to 31-08-2006	
4. TITLE AND SUBTITLE Navy High-Strength Steel Corrosion-Fatigue Modeling Program			5a. CONTRACT NUMBER F42620-00-D-0039, 0011		
			5b. GRANT NUMBER		
			5c. PROGRAM ELEMENT NUMBER		
6. AUTHOR(S) Wally Hoppe; Ollie Scott; Bill Braisted; Gary Abfalter; Jennifer Pierce			5d. PROJECT NUMBER		
			5e. TASK NUMBER		
			5f. WORK UNIT NUMBER		
7. PERFORMING ORGANIZATION NAME(S) AND ADDRESS(ES) University of Dayton Research Institute, Structural Integrity Division, 300 College Park, Dayton, OH, 45469-0120			8. PERFORMING ORGANIZATION REPORT NUMBER UDR-TR-2007-00039		
9. SPONSORING/MONITORING AGENCY NAME(S) AND ADDRESS(ES) Office of Naval Research, One Liberty Center, 875 North Randolph Street Suite 1425, Arlington, VA, 22203-1995			10. SPONSOR/MONITOR'S ACRONYM(S) ONR		
			11. SPONSOR/MONITOR'S REPORT NUMBER(S)		
12. DISTRIBUTION/AVAILABILITY STATEMENT Approved for public release; distribution unlimited					
13. SUPPLEMENTARY NOTES					
14. ABSTRACT The High-Strength Steel Corrosion-Fatigue Assessment program was designed to ensure reliability and supportability of current and emerging Naval aircraft by providing requisite engineering support to evaluate issues relevant to corrosion-fatigue of aircraft components. In this multi-year, multi-contract program, tools have been developed to assist in the establishment of maintenance options for corroded components. Experimental and analytical tools have been developed to classify corrosion in a manner tied to a reduction in fatigue life, to assess corrosion classifications by corrosion metrics, to measure these metrics with nondestructive methods, and to model the effect of corrosion on fatigue life. This report describes the work accomplished during the first two years and first contract of the program.					
15. SUBJECT TERMS High-Strength Steel, AF1410, Corrosion, Fatigue, Inspection, Crack Initiation, Metrics, Corrosion methods					
16. SECURITY CLASSIFICATION OF:			17. LIMITATION OF ABSTRACT Same as Report (SAR)	18. NUMBER OF PAGES 294	19a. NAME OF RESPONSIBLE PERSON
a. REPORT unclassified	b. ABSTRACT unclassified	c. THIS PAGE unclassified			

**NAVY HIGH-STRENGTH STEEL
CORROSION-FATIGUE MODELING PROGRAM**

Contract No.: F42620-00-D-0039, 0011

October 2006

FINAL REPORT

Prepared for:

Dr. Paul Hoffman
Government Technical Program Manager
Naval Air Warfare Center – Aircraft Division
Code 4.3.3.1
48110 Shaw Rd., Unit 5
Patuxent River, MD 20670-1906

Prepared by:

Wally Hoppe, Ollie Scott, Bill Braisted, Garry Abfalter, Jennifer Pierce,
Eric Burke, Sarah Kuhlman, Brian Frock, and Ray Ko
UNIVERSITY OF DAYTON RESEARCH INSTITUTE
Structural Integrity Division
300 College Park
Dayton, OH 45469-0120

Table of Contents

<u>Section</u>	<u>Page</u>
1 Executive Summary	1
2 Introduction.....	4
2.0 Background.....	4
2.1 Purpose and Goals	4
2.2 Relationship to Other Contracts/Programs	5
2.3 Summary of Accomplishments.....	5
3 Information Gathering	12
3.0 Introduction.....	12
3.1 Review of Boeing Corrosion-Fatigue Test Program	12
3.2 Review of Air Force 300M Corrosion-Fatigue Test Report.....	15
3.3 NDE Literature Search.....	19
4 Effects of Corrosion Damage on Fatigue Life.....	22
4.0 Introduction.....	22
4.1 Baseline Mechanical Tests.....	24
4.1.1 Young's Modulus Tests	24
4.1.2 Poisson's Ratio Testing.....	28
4.1.3 Tensile Strength Testing from Lot A AF1410 Material	31
4.1.4 Tensile Strength Testing of Travelers from Lot B AF1410 Material	33
4.1.5 Fracture Toughness Tests (Heat-Treated Lot B Material).....	35
4.1.6 Fracture Toughness Tests of AF1410 (Heat-Treated and Overaged Lot B Material).....	36
4.1.7 Fatigue Crack Growth Rate Tests	37
4.2 Supportive Studies and Investigations	43
4.2.1 Corrosion Growth Methods and Time of Exposure Study	43
4.2.2 Corrosion Product Cleaning Methods Study	70
4.2.3 Materials Study: Effect of Corrosion Growth Method on Materials and Materials Properties	71
4.2.4 Corrosion Characterization Methods Study.....	84
4.2.5 Corrosion Metric Preliminary Study.....	89
4.2.6 Replication Method Study	94
4.2.7 Arrestment Shank Corrosion Characterization Study	98
4.2.8 Markerband Study.....	101
4.2.9 Quantitative Fractography Study	103
4.3 Corrosion-Fatigue Test – AF1410 Set A	106
4.3.1 Summary of Data Acquisition	106
4.3.2 Analysis and Results.....	112
4.4 Continuing and Future Corrosion-Fatigue Tests	116
4.5 NDE Investigation	116
4.5.1 Ultrasonic Technologies	117
4.5.2 Discussion.....	125

Table of Contents (cont'd.)

<u>Section</u>	<u>Page</u>
5 Modeling.....	126
5.0 Introduction.....	126
5.1 Analysis of the F-18 Arrestment Shank.....	126
5.2 Finite Element Modeling of Corrosion.....	126
5.2.1 Grain Size and Study of Continuum Assumption.....	127
5.2.2 k_{teff} Extraction Using Laser Profilometry Surface Mapping and Stress Check®	131
5.2.3 Corroded Surface Idealization with Consideration of k_t Sensitivity	132
5.2.4 Matrix of Simulated Corrosion Defects.....	132
5.2.5 Assessment of Various Corrosion Modeling Codes	134
5.2.6 Incorporation of Residual Stress Effects.....	136
5.2.7 Global-Local Modeling Technique.....	137
5.3 Development of a Pit Metric.....	139
5.4 Development of an Elasticity Solution and Limitations.....	140
6 Correlation	146
7 Conclusion	147
8 References.....	149
Appendix A ESRD Final Report	A-1
Appendix B Boeing Final Report.....	B-1
Appendix C Extensometer Calibration Data Sheets.....	C-1
Appendix D Residual Stress Profile Measurements Report.....	D-1
Appendix E Acronyms and Abbreviations	E-1

List of Figures

<u>Figure</u>	<u>Page</u>
3.1-1	Boxplot of Fatigue Life and the Test Type Correlating to the Number of Hours of Exposure to the Corrosive Agents14
3.1-2	Boxplot of the Fatigue Life and the Crack Initiation Location.....14
3.2-1	Axial Fatigue Test Specimen Geometry16
3.2-2	Fatigue-Life Curve for Pre-Corroded Axial Fatigue Specimens17
4.1.1-1	AF1410 Room Temperature Modulus Test on Specimen STL414-3, First Loading Sequence.....25
4.1.1-2	AF1410 Room Temperature Modulus Test on Specimen STL414-3, Second Loading Sequence25
4.1.1-3	AF1410 Room Temperature Modulus Test on Specimen STL414-3, Third Loading Sequence26
4.1.1-4	AF1410 Room Temperature Modulus Test on Specimen STL414-4, First Loading Sequence.....26
4.1.1-5	AF1410 Room Temperature Modulus Test on Specimen STL414-4, Second Loading Sequence27
4.1.1-6	AF1410 Room Temperature Modulus Test on Specimen STL414-4, Third Loading Sequence27
4.1.2-1	AF1410 Room Temperature Poisson's Ratio Test on Specimen STL414-5, First Loading Sequence.....29
4.1.2-2	AF1410 Room Temperature Poisson's Ratio Test on Specimen STL414-5, Second Loading Sequence29
4.1.2-3	AF1410 Room Temperature Poisson's Ratio Test on Specimen STL414-6, First Loading Sequence.....30
4.1.2-4	AF1410 Room Temperature Poisson's Ratio Test on Specimen STL414-6, Second Loading Sequence30
4.1.2-5	AF1410 Room Temperature Poisson's Ratio Test on Specimen STL414-6, Third Loading Sequence31
4.1.3-1	AF1410 Room Temperature Tensile Test on Specimen STL414-3.....32
4.1.3-2	AF1410 Room Temperature Tensile Test on Specimen STL414-4.....32
4.1.3-3	AF1410 Room Temperature Tensile Test on Specimen STL414-5.....33
4.1.3-4	AF1410 Room Temperature Tensile Test on Specimen STL414-6.....33
4.1.4-1	AF1410 Room Temperature Tensile Test on Specimen STL533-12 and STL533-3 ...34
4.1.7-1	C(T) Specimen37
4.1.7-2	M(T) Specimen38
4.1.7-3	Fatigue Crack Growth Rate Tests for AF1410 Steel in Ambient Laboratory Air with a Load Ratio of 0.1 Using C(T) Specimens.....40
4.1.7-4	Fatigue Crack Growth Rate Tests for AF1410 Steel in Ambient Laboratory Air with a Load Ratio of 0.1 Using C(T) and M(T) Specimens.....40
4.1.7-5	Fatigue Crack Growth Rate Tests for AF1410 Steel in Ambient Laboratory Air or in a High-Humidity and NaCl Environment with a Load Ratio of 0.1 Using C(T) Specimens.....41

List of Figures (cont'd.)

<u>Figure</u>	<u>Page</u>
4.1.7-6 Fatigue Crack Growth Rate Tests for AF1410 Steel in Ambient Laboratory Air Comparing Load Ratios of 0.1 and 0.5 Using C(T) Specimens.....	41
4.1.7-7 Fatigue Crack Growth Rate Tests for AF1410 Steel in Ambient Laboratory Air with a Load Ratio of 0.5 Using C(T) Specimens.....	42
4.1.7-8 Fatigue Crack Growth Rate Tests for AF1410 Steel in Ambient Laboratory Air or in a High-Humidity and NaCl Environment with a Load Ratio of 0.5 Using C(T) Specimens.....	42
4.1.7-9 Fatigue Crack Growth Rate Tests for AF1410 Steel in Ambient Laboratory Air Comparing Load Ratios of 0.1 and -1 Using C(T) and M(T) Specimens.....	43
4.2.1-1 Boeing Corrosion Fatigue Data, Stress vs. Cycles.....	46
4.2.1-2 Boeing Corrosion Fatigue Data, Cycles vs. Stress.....	46
4.2.1-3 Boeing Corrosion Fatigue Specimens: Examples of Fractures (a) outside the corroded region, (b) within the corroded region, and (c) at the corroded region edge.....	47
4.2.1-4 Profile of Boeing Fatigue Specimen 100-6 Scanned from the Non-Corroded Region into the Corroded Region Showing the “Trench” at the Interface	48
4.2.1-5 Cross-Section Image of Boeing Fatigue Specimen 100-9 Showing the “Trench” at the Interface Between the Non-Corroded Region and the Corroded Region.....	48
4.2.1-6 Specimen Provided by NAVAIR Exposed for 168 Hours of Neutral Salt Fog Exposure	49
4.2.1-7 Specimen Provided by NAVAIR Exposed for 312 Hours of Neutral Salt Fog Exposure	49
4.2.1-8 Example Line Scan in the Corroded Region of the Specimen Exposed for 168 Hours.....	50
4.2.1-9 Example Line Scan in the Corroded Region of the Specimen Exposed for 312 Hours.....	50
4.2.1-10 Example Line Scan from the Non-Corroded Region to Within the Corroded Region of the Specimen Exposed for 168 Hours.....	50
4.2.1-11 Example Line Scan from the Non-Corroded Region to Within the Corroded Region of the Specimen Exposed for 312 Hours.....	51
4.2.1-12 Alternate Immersion Specimen exposed for (a) 20 days, (b) 40 days, and (c) 60 days.....	52
4.2.1-13 Example Line Scan from the Non-Corroded Region to Within the Corroded Region of the Alternate Immersion Specimen Exposed for 20 Days	52
4.2.1-14 Wafer Masked Off with Beeswax and Exposed for 20 Days of Alternate Immersion.....	53
4.2.1-15 Example Line Scan Within the Corroded Region of Specimen Exposed to 20 Days of Alternate Immersion.....	53
4.2.1-16 Example Line Scan Within the Corroded Region of Specimen Exposed to 40 Days of Alternate Immersion.....	54

List of Figures

<u>Figure</u>	<u>Page</u>
4.2.1-17 Example Line Scan Within the Corroded Region of Specimen Exposed to 60 Days of Alternate Immersion	54
4.2.1-18 Samples Exposed with Filter Paper Soaked in 3.5% Salt Solution Using Different Methods	55
4.2.1-19 Profile Data Taken from Sample #5a Exposed to 40 Cycles of Filter Paper Replacement	55
4.2.1-20 Profile Data Taken from a Sample Exposed to 90 Cycles of Filter Paper Replacement	56
4.2.1-21 Schematic Diagram of the Test Setup for Accelerated Corrosion Testing with a Piece of Soaked Filter Paper	57
4.2.1-22 Data Taken on Samples Exposed to 2 mA/cm ² for a Total of 4 Hours	58
4.2.1-23 Test Wafer AF1410-3hr: (a) photograph of the corroded surface after 3-hour exposure, (b) height map of the corroded surface as measured using the white-light interferometer, and (c) line profile of the transition between the non-corroded and corroded surface taken at approximately the 7 o'clock position with a stylus.....	61
4.2.1-24 Cross-Section Images of Test Wafer AF1410-3 hr: (a) & (b) are micrographs of the transition region between the corroded and grit-blasted surfaces, (c) & (e) were taken in the corroded region, (d) & (f) were taken in the grit-blasted region	63
4.2.1-25 Test Wafer AF1410-6 hr: photograph of the corroded surface after the 6-hour exposure, (b) height map of the corroded surface as measured using the white-light interferometer, and (c) line profile of the transition between the non-corroded and corroded surface taken at approximately the 12 o'clock position with a stylus	64
4.2.1-26 Cross-Section Images of Test Wafer AF1410-6 hr: (a) & (b) are micrographs of the transition region between the corroded and grit-blasted surfaces, (c) & (e) were taken in the corroded region, (d) & (f) were taken in the grit-blasted region	66
4.2.1-27 Test Wafer AF1410-12 hr: (a) photograph of the corroded surface after the 12-hour exposure, (b) height map of the corroded surface as measured using the white-light interferometer, and (c) line profile of the transition between the non-corroded and corroded surface taken at approximately the 11 o'clock position with a stylus	67
4.2.1-28 Cross-Section Images of Test Wafer AF1410-12hr: (a) & (b) are micrographs of the transition region between the corroded and grit-blasted surfaces, (c) & (e) were taken in the corroded region, (d) & (f) were taken in the grit-blasted region	69
4.2.3-1 Micrograph of a Cross-Section of a Corroded AF1410 Wafer	73
4.2.3-2 X-Ray Energy Image for Iron with the Elemental Trace Along the Superimposed Yellow Line.....	73
4.2.3-3 X-Ray Energy Image for Chromium with the Elemental Trace Along the Superimposed Yellow Line.....	74
4.2.3-4 X-Ray Energy Image for Cobalt with the Elemental Trace Along the Superimposed Yellow Line.....	74
4.2.3-5 X-Ray Energy Image for Nickel with the Elemental Trace Along the Superimposed Yellow Line.....	75

List of Figures

<u>Figure</u>	<u>Page</u>
4.2.3-6 X-Ray Energy Image for Molybdenum with the Elemental Trace Along the Superimposed Yellow Line.....	75
4.2.3-7 X-Ray Energy Image for Manganese with the Elemental Trace Along the Superimposed Yellow Line.....	76
4.2.3-8 X-Ray Energy Image for Carbon with the Elemental Trace Along the Superimposed Yellow Line.....	76
4.2.3-9 Auger Electron Spectroscopy Results from a Non-Corroded, Polished AF1410 Sample.....	77
4.2.3-10 Auger Electron Spectroscopy of Corroded AF1410 Sample.....	78
4.2.3-11 Auger Electron Spectroscopy of a Non-Corroded, but Grit-Blasted AF1410 Wafer.....	80
4.2.3-12 A Comparison of the Amounts of the Different Constituents Normalized by the Amount of Iron for the Non-Corroded, Grit-Blasted, and Corroded Materials.....	81
4.2.3-13 OCP Curves AF1410 in Ambient or Deaerated 3.5% NaCl for 2 Hours.....	82
4.2.3-14 Potentiodynamic Scan of AF1410 in Ambient or Deaerated 3.5% NaCl.....	82
4.2.3-15 Cyclic Polarization Measurement of AF1410 in Deaerated 3.5% NaCl.....	83
4.2.4 -1 (a) Typical Laser Profilometry Measurement and (b) the Equivalent White-Light Profilometry Measurement.....	88
4.2.5-1 (a) Raw Profilometry Data from White-Light Interferometer and (b) after FFT Filtering.....	92
4.2.5-2 Post-Fracture Sample and NVL Local Analysis.....	93
4.2.6-1 White-Light Interference Microscope Images of President Lincoln's Head on a U.S. Penny: (a) the actual penny and (b) the replica.....	96
4.2.6-2 Profiles of Scratch on Penny Taken from White-Light Interference Microscopy Measurements on Actual Penny and a Replica.....	96
4.2.6-3 White-Light Interference Microscopic Images of Corrosion Feature Measured Directly from the AF1410 Wafer and the Replica.....	97
4.2.7-1 White-Light Interference Microscopic Image of Non-Corroded Arrestment Shank Replica.....	98
4.2.7-2 White-Light Interference Microscopic Image of Corroded Arrestment Shank Replica.....	99
4.2.8-1 Four Marker Band Pattern.....	102
4.2.8-2 Fracture Surface of Critical Crack on Specimen #19.....	103
4.2.9-1 QF Crack Depth Measurement Schematic.....	103
4.2.9-2 Crack Growth Curve for Specimen #19, 165 Ksi Max. Stress.....	104
4.2.9-3 Critical Crack Origin on Specimen #61.....	105
4.2.9-4 Critical Crack Origin on Specimen #29.....	106
4.3.1-1 Batch A Corrosion-Fatigue Test Plate Geometry.....	107
4.3.1-2 C-F Plate Warping Measurement.....	107
4.3.1-3 Specimen #3 Post Heat-Treat Residual Stress Profiles.....	110
4.3.1-4 Specimen #64 Post Heat-Treat Residual Stress Profiles.....	110
4.3.1-5 Specimen #3 Post Low-Temp. Stress Relief Residual Stress Profiles.....	111

List of Figures

<u>Figure</u>	<u>Page</u>
4.3.1-6 Specimen #64 Post Low-Temp. Stress Relief Residual Stress Profiles.....	112
4.3.2-1 Plot of Peak Stress vs. Cycles to Crack Initiation.....	113
4.5.1-1 Stylus Profilometer RMS Results vs. RMS Results from Ultrasonic Angle-Beam Backscattered Amplitude from Grit-Blasted Surfaces.....	118
4.5.1-2 Images of Specimen #23: (a) ultrasonic angle-beam backscattered amplitude and (b) white-light interference microscope topography.....	119
4.5.1-3 Images of Specimen #23: (a) ultrasonic normal-incidence reflected amplitude and (b) white-light interference microscope topography.....	120
4.5.1-4 Images of Specimen #23: (a) ultrasonic RMS and (b) white-light interference microscopy.....	122
4.5.1-5 Images of Specimen #23: (a) time-of-flight to peak and (b) white-light interference microscopy.....	123
4.5.1-6 Images of Specimen #23: (a) phase-slope, (b) white-light interference microscopy, and (c) time-of-flight to peak.....	124
5.2.1-1 Scanning Electron Micrograph of a Cross-Section of AF1410 Showing Martensitic Packets.....	128
5.2.1-2 Scanning Electron Micrograph of a Cross-Section of 300M Showing Martensitic Packets.....	129
5.2.1-3 AFM and UFM Images of a Sample of AF1410.....	131
5.2.1-4 AFM and UFM Images of Different Region of a Sample of AF1410.....	131
5.2.1-5 Increased Magnifications of AFM and UFM Images in Figure 5.2.1-4.....	131
5.2.4-1 Simulated Corrosion Defect Geometries.....	133
5.2.5-1 Analysis Results of Various Individual Spherical Pit Geometries (Case 5).....	135
5.2.5-2 Analysis Results of Various Adjacent Spherical Pit Geometries (Case 6, width $d=0.01''$, $D=0.125''$).....	135
5.2.5-3 Normalized Analysis Results of Individual Spherical Pit Geometries (Case 5).....	136
5.2.6-1 Experimental and Analytical Residual Stress Profile.....	137
5.2.7-1 Global-Local Model (Case 9) and Corresponding Stress Profile (Ksi).....	138
5.2.7-2 Global-Local Results at the Center of a Corroded Region (Case 9).....	139
5.3-1 Candidate Pit Metric for Stress Concentration Factor Estimation.....	139
5.4-1 Elasticity Approach for Corroded Surface Modeling.....	140
5.4-2 Elasticity Solution for Each Surface Profile Frequency Component.....	141
5.4-3 Elasticity Solution Two-Dimensional Single Frequency Validation Problem.....	141
5.4-4 Accuracy of Individual Frequency Component Elasticity Solutions.....	142
5.4-5 Combined Stress Concentration Factor Implications.....	143
5.4-6 Accuracy of Elasticity Solution Approach on a Complex Surface.....	143
5.4-7 Corrosion Surface and Surface Height Profiles in AF1410 Specimen #16.....	144
5.4-8 Zoomed Surface and Stress Concentration Profiles in AF1410 Specimen #16.....	145

List of Tables

<u>Table</u>	<u>Page</u>
3.1-1	Summary of Boeing Corrosion Fatigue Matrix and Crack Initiation Locations13
3.2-1	Fatigue-Life Cycles to Failure for Pre-Corroded Axial Fatigue Specimens.....17
4.1.1-1	Test Results from the Young’s Modulus Tests on Lot B AF1410 Specimen STL414-326
4.1.1-2	Test Results from the Young’s Modulus Tests on Lot B AF1410 Specimen STL414-427
4.1.2-1	Test Results from the Poisson’s Ratio Test AF1410 Specimen STL414-529
4.1.2-2	Test Results from the Young’s Modulus Tests on AF1410 Specimen STL414-631
4.1.4-1	Test Results from the Tensile Tests on Travelers from Lot B AF1410 Material35
4.1.5-1	Summary of Fracture Toughness Test Results36
4.1.6-1	Summary of Fracture Toughness Test Results with Overaging Heat Treatment37
4.1.7-1	Summary of Fatigue Crack Growth Rate Testing of AF1410 Steel39
4.2.1-1	Comparison of Profilometer Data Results45
4.2.1-2	Three-Hour Exposure Procedure59
4.2.1-3	Six-Hour Exposure Procedure59
4.2.1-4	Twelve-Hour Exposure Procedure.....59
4.2.1-5	Results of WLI Measurement on Specimen AF1410-3hr.....61
4.2.1-6	Results of WLI Measurement on Specimen AF1410-6hr.....64
4.2.1-7	Results of WLI Measurement on Specimen AF1410-12 hr.....68
4.2.2-1	Type III Process Detail71
4.2.4-1	Statistics for White-Light Interferometer vs. Laser Profilometry.....89
4.2.5-1	Standard Parameters vs. Time of Exposure (TOE).....90
4.2.5-2	Texture Parameters vs. Time of Exposure (TOE)90
4.2.5-3	Summary of Surface Metrics90
4.2.6-1	Comparison of Surface Metrics on Step Wedge.....95
4.2.7-1	Roughness Metrics for Comparing Corrosion-Fatigue Specimens to Arrestment Shanks.....99
4.2.8-1	Marker Band Schedule.....102
4.3.1-1	Chemical Composition of AF1410 0.375 in. Thick Steel Bars106
4.3.1-2	Surface Residual Stress Measurements on AF1410 C-F Plates.....109
4.3.2-1	Non-Corroded Corrosion-Fatigue Plate Test Results113
4.3.2-2	3-Hour Corrosion Exposure Plate Test Results114
4.3.2-3	6-Hour Corrosion Exposure Plate Test Results114
4.3.2-4	12-Hour Corrosion Exposure Plate Test Results115
4.5.1-1	Linear Correlation of Results from Ultrasonic Data with Results from White-Light Interference Microscope Data121
4.5.1-2	Linear Correlation of Results from Ultrasonic Time-to-Peak with Ultrasonic Phase-Slope Results125

<u>Table</u>	<u>Page</u>
5.2.1-1	Measurements of AF1410 Material Martensitic Packets.....128
5.2.1-2	Measurements of 300M Material Martensitic Packets129
5.2.4-1	Simulated Corrosion Defect Matrix.....134
5.4-1	Comparison of k_t on Each Crack on Specimen #16 to k_t in a Region Around the Crack145

Abstract

The High-Strength Steel Corrosion-Fatigue Assessment program was designed to ensure reliability and supportability of current and emerging Naval aircraft by providing requisite engineering support to evaluate issues relevant to corrosion-fatigue of aircraft components. In this multi-year, multi-contract program, tools have been developed to assist in the establishment of maintenance options for corroded components. Experimental and analytical tools have been developed to classify corrosion in a manner tied to a reduction in fatigue life, to assess corrosion classifications by corrosion metrics, to measure these metrics with nondestructive methods, and to model the effect of corrosion on fatigue life. This report describes the work accomplished during the first two years and first contract of the program.

Foreward

This report describes the technical work accomplished during the period from 30 June 2003 through 31 August 2006, for the Naval Air Warfare Center – Aircraft Division under Contract Number F4260-00-D-0039, 0011. The University of Dayton Research Institute (UDRI) was the prime contractor for the effort and Engineering Software Research and Development, Inc. (ESRD) and Boeing were the major subcontractors on the program. Mr. Paul Hoffman was the Contract Monitor.

Mr. Wally Hoppe of the UDRI Structural Integrity Division was the Principal Investigator for the contractual effort. Mr. Robert Andrews, Division Head of the Structural Integrity Division, served as the over all Program Manager. Ms. Ollie L. Scott and Ms. Gloria Hardy provided program management services. The following UDRI employees contributed to the major accomplishments on this contract: Dr. Bill Braisted, Mr. Garry Abfalter, Ms. Jennifer Pierce, Mr. Eric Burke, Ms. Sarah Kuhlman, Mr. Brian Frock, Mr. Norman Schehl, Mr. Bob Olding, and Dr. Ray Ko. Ms. Andrea Snell and Ms. Marla McCleskey provided administrative support. Additional contributors included: Mr. Dave Rusk of NAVAIR; Dr. Barna Szabo, Dr. Ricardo Actis and Mr. Brent Lancaster of ESRD; and, Dr. Krishnan K. Sankaran, Dr. Herb Smith, Jr., Mr. Bert Neal, and Mr. Dan Rich of Boeing.

Acknowledgements:

Mr. J. Douglas Wolf of the Microanalytical Laboratory at the University of Dayton Research Institute performed SEM and EDS analysis as well as Auger electron spectroscopy.

Dr. Douglas Hansen of the Materials Degradation & Electrochemical Engineering Group at the University of Dayton Research Institute performed the electrochemical analysis.

Section 1

Executive Summary

In June 2003, UDRI was placed on contract, as prime, to lead in the effort to study the effect that corrosion has on the fatigue life of high-strength steels on Navy applications. The Navy High-Strength Steel Corrosion-Fatigue Assessment Program was designed to ensure reliability and supportability of current and emerging Naval aircraft by providing requisite engineering support to evaluate issues relevant to corrosion-fatigue of airframe components. Its purpose was to develop tools that can be used to specify the maintenance options for corroded components and to provide a sound engineering basis for selecting the best fleet maintenance options. Essentially, the program was to provide quantifiably justified maintenance criteria for environmentally induced damage (i.e. corrosion) in high-strength steels.

The overall objectives of this program included the following outcomes:

- A corrosion severity classification scheme (i.e., cosmetic, mild, and severe) tied to component reliability or reduction in fatigue life,
- Corrosion metrics associated with these corrosion classifications,
- Nondestructive inspection (NDI) methods, requirements, and procedures for measuring corrosion severity via these corrosion metrics, and,
- Component disposition tools and procedures to make engineering disposition decisions based on detailed corrosion profiles and validated life prediction assessment models.

The plan to meet these overall objectives consisted of the following activities: determining the effect of corrosion on fatigue life of high-strength steels through corrosion-fatigue experiments supported by other baseline tests; developing corrosion metrics based on surface profiles, correlating metrics to life reduction and using these results to develop corrosion classification criteria; investigating and developing NDI methods and procedures that could determine corrosion severity via correlations of NDI to corrosion metrics; and, developing physics-based analysis methods to determine effective stress concentration factors for corrosion, correlating the analysis predictions to corrosion-fatigue tests and validating on component tests.

These research tasks are part of a multi-year, multi-contract program. The first contract was initially funded in June 2003 for one year, followed by a second year of funding and extensions to August 2006. The second contract was awarded in September 2005 for one year and has been extended to February 2007. The third and final contract is anticipated to be awarded in September 2006 and should run for one year. When completed, the entire effort will have lasted four years and two months. The University of Dayton Research Institute was prime on the first contract, with Engineering Software Research and Development (ESRD), Inc. and The Boeing Company as subcontractors.

This document reports activities under the first of these three contracts supporting the overall objectives of the program. Specific activities during this timeframe have focused primarily on development of tools and methods required for precise test and characterization of corrosion-fatigue experiments, as well as developing methods to model the effect that corrosion topography has on fatigue. Several relevant prior studies have been reviewed. Baseline materials property tests on AF1410 high-strength steel have been performed. A new accelerated method to grow corrosion on specimens has been developed and tested. A materials study was conducted to ensure that the corrosion growth method does not produce adverse affects on the material composition and the material properties. A method to remove the corrosion products without affecting the remaining substrate profile was chosen and tested. White-light interference microscopy was selected, based on tests on corroded wafers, for measurement of the corroded surface profile. A dental paste replication process was refined for use on corroded test specimens. Surface roughness metrics were tabulated and assessed for adequacy in characterizing corrosion severity. Metric values were ascertained for real corroded arrestment shanks to compare to the same metric values from corrosion-fatigue specimens. A marker band approach was optimized by NAVAIR for use in this study to determine the number of cycles to crack initiation in examinations of fracture surfaces. This step required the use of quantitative fractography methods, which have been developed by NAVAIR with the assistance of experts in Australia.

After these preliminary methods and processes were established, a complete corrosion-fatigue test was performed on a set of 60 AF1410 high-strength steel corrosion-fatigue specimens. Results of this test were not available until the end of this contract and are being used in the subsequent contracts on the program.

A nondestructive inspection investigation was also conducted in parallel with these activities, mostly directed at the use of ultrasonic inspection methods. Several approaches to measuring surface roughness and surface profiles were tested. Normal incidence, pulse-echo, amplitude, and time-of-flight methods seem to be the most promising.

An extensive modeling study was also conducted. This study found that fully three-dimensional, finite element analysis of corrosion might not be viable at this time due to the intensive computations required to capture the tremendous detail of the corrosion surface and the resulting errors introduced when simplifying these corrosion features. However, an elasticity solution was developed that makes use of the complete profile detail to construct an approximate stress concentration map. This approach produces good approximations in the limit of applicability of the corrosion levels seen in the test specimens. The elasticity approach stress concentration map has also been shown to identify stress risers associated with actual crack initiation sites.

The second program contract has significantly overlapped the timeframe of the first program contract. The second contract has focused on completion of the data acquisition and analysis of the first set of AF1410 corrosion-fatigue specimens; development of reliability models for life prediction; development of corrosion metrics and corrosion classification scheme; manufacture and testing of the second set of AF1410 corrosion-fatigue specimens (without residual stress) and associated analysis of the test results; preparation of 300M test specimens; and preparation of Aermet 100 test specimens. The final contract on this program will complete all testing and analysis, model development and validation, corrosion classification descriptions via accepted corrosion metrics, and the definition of NDI requirements for transition and implementation of the overall program objectives.

Section 2

Introduction

2.0 Background

Navy carrier-based aircrafts employ high-strength steel in many components, including landing gears and arrestment shanks. The service life of these components are generally defined by fatigue caused by load cycles. However, aircraft must operate in coastal environments that result in corrosion-assisted fatigue of airframe components. The effect of corrosion on component fatigue life has not been quantified. This problem is most acute for high-strength steel, such that it is important to determine how to quantify remaining life considering both cycle- and time-dependent damage mechanisms. A quantifiable metric must be established to estimate remaining life due to the presence of corrosion.

2.1 Purpose and Goals

The Navy High-Strength Steel Corrosion-Fatigue Assessment Program was designed to ensure reliability and supportability of current and emerging Naval aircraft by providing requisite engineering support to evaluate issues relevant to corrosion-fatigue of airframe components. Its purpose was to develop tools that can be used to specify the maintenance options for corroded components and to provide a sound engineering basis for selecting the best fleet maintenance options. Essentially, the program was to provide quantifiably justified maintenance criteria for environmentally induced damage (i.e., corrosion) in high-strength steels.

The overall objectives of this program included the following outcomes:

- A corrosion severity classification scheme (i.e., cosmetic, mild, and severe) tied to component reliability or reduction in fatigue life,
- Corrosion metrics associated with these corrosion classifications,
- Nondestructive inspection (NDI) methods, requirements, and procedures for measuring corrosion severity via these corrosion metrics, and
- Component disposition tools and procedures to make engineering disposition decisions based on detailed corrosion profiles and validated life prediction assessment models.

The plan to meet these overall objectives consisted of the following activities:

- Determining the effect of corrosion on fatigue life of high-strength steels through corrosion-fatigue experiments supported by other baseline tests,
- Developing corrosion metrics based on surface profiles, correlating metrics to life reduction and using these results to develop corrosion classification criteria,
- Investigating and developing NDI methods and procedures that could determine corrosion severity via correlations of NDI to corrosion metrics, and
- Developing physics-based analysis methods to determine effective stress concentration factors for corrosion, correlating the analysis predictions to corrosion-fatigue tests and validating on component tests.

2.2 Relationship to Other Contracts/Programs

These research tasks are part of a multi-year, multi-contract program. The first contract was initially funded in June 2003 for one year, followed by a second year of funding and extensions to August 2006. The second contract was awarded in September 2005 for one year and has been extended to February 2007. The third and final contract is anticipated to be awarded in September 2006 and should be for one year. When completed, the entire effort will have lasted four years and two months. The University of Dayton Research Institute was prime on the first contract, with Engineering Software Research and Development (ESRD), Inc. and The Boeing Company as subcontractors. The ESRD Final Report is included in this report in Appendix A and The Boeing Final Report is found in Appendix B. While both subcontractors have played central roles in this program, specific references to their final reports are not necessarily made in this report. Details of their activities are found in their respective final reports.

2.3 Summary of Accomplishments

This document reports activities under the first of these three contracts supporting the overall objectives of the program. Specific activities during this timeframe focused primarily on development of tools and methods required for precise test and characterization of corrosion-fatigue experiments, as well as developing methods to model the effect that corrosion topography has on fatigue.

Several investigations were conducted as part of the information-gathering task on the program. A review was conducted of a prior Boeing corrosion-fatigue program on AF1410 high-strength

steel. Another review was conducted of an Air Force corrosion prevention and control (CPC) test program in which 300M corroded high-strength steel specimens were tested in fatigue. As part of this test, the control group of specimens was not coated in CPC materials and was, therefore, relevant to the Navy corrosion-fatigue program. A literature search for NDI technologies pertinent to corrosion characterization was also completed. Subsequent program plans benefited from these reviews. These information-gathering activities are described in Section 3 of this report.

One of the primary tasks on the program was to experimentally study the effect that corrosion damage has on fatigue life of high-strength steels. Of particular interest to the Navy was the F-18 arrestment shank, made of AF1410 steel. Baseline tests of this material were conducted to establish modulus, Poisson's ratio, tensile strength, fracture toughness, and fatigue crack growth rates. Baseline tests are described in Section 4.1 of this report. In order to quantify the effect of corrosion on fatigue life, it was necessary to perform quantitative corrosion-fatigue tests on AF1410 steel specimens. Each specimen was carefully manufactured and exposed to accelerated corrosion-growth environments. After the corrosion products were chemically removed, the corroded surface profile was characterized and the specimens were tested in fatigue. Initially, the plan called for one test on AF1410 in a test matrix of 60 corrosion-fatigue specimens. After it was determined that specimen preparation produced unacceptable surface residual stresses due to grit blasting, it was decided to prepare and test a second set of 60 specimens that were not grit-blasted. Corrosion-fatigue tests were also planned for 300M, but considering the results of the Air Force study referenced above, it was decided that this test would use only nine specimens, attempting only to verify the Air Force study results. Extensive preliminary development efforts, described next, were required to support all of these corrosion-fatigue tests.

Various corrosion growth methods – discussed in Section 4.2.1 – were investigated, including a time-of-exposure study to plan for different levels of corrosion severity in the specimens. Examination of the extant specimens from the Boeing test, as well as NAVAIR and UDRI corrosion time-of-exposure test wafers, showed that masking produces crevice corrosion in the perimeter of the exposed area that can cause an unrealistic reduction in fatigue life. In addition, alternate immersion methods require extended periods of exposure totaling as long as several months. A newly developed electrochemical process that makes use of salt water-soaked filter paper sandwiched between electrodes was finally selected based on its potential to quickly apply varying levels of

corrosion in controlled locations without introducing any significant crevice corrosion or undercutting at the perimeter of the corrosion patch. In addition, methods to chemically remove corrosion products without adversely affecting the remaining corrosion profile were investigated and tested. See Section 4.2.2 for details. A Boeing corrosion removal specification using an alkaline solution, Turco[®], was selected for use on AF1410. In addition, a materials study was performed to rule out any possible change in material or material properties due to the use of the selected corrosion growth method. A discussion of this study and its results are found in Section 4.2.3.

Additional support activities included a comprehensive study of various surface profile characterization technologies that would be technically suitable in terms of spatial and depth resolutions that would be available and practical for this program. White-light interference microscopy was tested and, consequently, selected for use on this program. Details of this comparison and associated tests are found in Section 4.2.4. In addition, a survey was conducted of various surface roughness metrics. See Section 4.2.5 for a review of these metrics. Metric values were tabulated for the corrosion surfaces of the first set of AF1410 corrosion-fatigue specimens. In conjunction with the examination of different surface profile instruments, methods were researched for replicating corrosion surfaces; a dental paste technique was found to produce the best results. This investigation is described in Section 4.2.6. Dental paste replicas of real service-induced corrosion found in actual AF1410 arrestment shanks were characterized with the white-light interference microscope. Section 4.2.7 describes this task. Various features and surface roughness metrics determined from these arrestment shank profiles were compared to those from the corrosion-fatigue specimens. The arrestment shank corrosion was found to be somewhat different than that being created in the test specimens, probably due to the presence of the cadmium plating on the arrestment shank. This protective plating prevents corrosion except when the coating fails, which then results in localized corrosion and thickness loss. Additional corrosion-fatigue tests, as well as additional modeling, will be required to account for these observed differences.

To properly quantify the fatigue life to initiation of a 0.010-inch crack, the standard criteria used in the Navy, requires ascertaining the number of fatigue cycles to a crack of this size. This step was accomplished by introducing marker bands in the loading history of the corrosion-fatigue test. NAVAIR performed the necessary experiments to determine the appropriate parameters for such marker bands. See Section 4.2.8 for a summary of this study. In addition, a method was

required to measure the depth of these marker bands on the fracture surfaces of the specimens. NAVAIR, with council of experts in Australia, developed the capability at their facility to perform the necessary quantitative fractography on the corrosion-fatigue fracture surfaces. Other team members were subsequently trained on these methods. Section 4.2.9 contains a summary of these activities.

Once the necessary preliminary supporting studies were completed, it was possible to initiate fatigue tests of the first set of AF1410 corrosion-fatigue specimens. After fatigue failure, each fracture surface was microscopically examined to determine the number of cycles to a 0.010-inch crack. Plots of applied load versus cycles to crack initiation showed expected trends and evidence of the effect of corrosion on fatigue life. Analysis of these results was conducted on the second contract in this program. Section 4.3 summarizes these tests on the first set of AF1410 corrosion-fatigue test specimens.

An NDI study, described in Section 4.4, was performed in parallel to both the corrosion-fatigue tests discussed above and the modeling work discussed below. Ultrasonic inspection methods for characterizing the corrosion severity were investigated and tested based on the NDI literature search and the potential for acceptance of such a technique in the field (i.e., on-board an aircraft carrier and in the Navy depot). Angle beam and normal incidence pulse-echo techniques were tested. The study was directed towards determining surface roughness or generating maps of the surface profile. Angle beam backscattering amplitude allows for measurements of surface roughness, but has limitations. Normal incidence using reflected peak-to-peak amplitude did not produce adequate correlations to the white-light surface profile data or metrics. Normal incidence Fourier spectroscopy also did not provide adequate correlations to measured surface roughness. Normal incidence time-of-flight topography demonstrated quite good correlations to the white-light data. The normal incidence Fourier phase-slope technique provides the best correlation to the profiles and metrics determined from the white-light interference microscope. The NDI investigation continues as the program moves forward, with this research becoming more important in the final phases of the program. Additional ultrasonic and eddy current inspection data will be collected on all remaining corrosion-fatigue test specimens.

Preliminary modeling efforts focused on ways to input surface roughness profiles into StressCheck^{®1}, ESRD's finite element modeling software package. Two-dimensional analysis of corrosion surface profiles were attempted. In addition, methods to simplify the representation of the surface profiles for analysis purposes were investigated. This task turned out to be a great challenge since corrosion has sharp features at all length scales which require capture and inclusion of a tremendous amount of detail in the numerical models. It also turns out that analysis results are very sensitive to geometric details when the corroded surface is idealized in any way. The overall findings of the study were that fully three-dimensional finite element analysis of corrosion might not be viable at this time.

Other modeling tasks in support of this program included developing modeling and analysis techniques for the arrestment shank incorporating the loads that this component experiences, studying methods to incorporate residual stress in the modeling approach, and researching methods to predict the effect of grindouts on the component in the presence of residual stress. Later in the program, limits were established for a proposed corrosion analysis technique developed in this program and described below using finite element analysis on simple cases and comparing these results to the stress concentration calculated by this new elasticity approach.

Numerical modeling test cases based on simple features were analyzed to help understand interactions between closely spaced corrosion features (such as pits or sharp depressions). As the challenge of modeling corrosion became more pronounced, a global/local model for corrosion was attempted that had the potential to overcome the computational obstacles of including the vast amount of corrosion topography data available from the white-light measurements. In this attempted approach, the general shape of the corrosion would be incorporated into the global model, while details of the corrosion in a selected area would be incorporated into the local model. Appropriate boundary conditions would fit these solutions together into one integrated solution. However, the approach did not adequately account for the presence of corrosion and was abandoned.

¹ StressCheck is a trade mark of Engineering Software Research and Development, Inc.

Based on these unsuccessful attempts to model corrosion, a study was conducted to apply a pit metric proposed by UDRI earlier in the program to the broader question of a distributed corrosion profile. In this study, the corrosion surface is considered to be composed of a superposition of sinusoidal components. The magnitude and phase of each sinusoid is determined from a two-dimensional Fourier transform of the surface profile. The stress for each component is calculated based on an analytical elasticity solution for an applied load, an extension of the pit metric to a two-dimensional sinusoidal surface. The total stress, or stress concentration, is determined by performing an inverse Fourier transform on the ensemble of stress components. From this approach, a stress concentration map is produced over the entire corrosion patch. This technique allows all profile data to be incorporated into the solution and it allows production of the stress concentration map in a matter of minutes.

After this new elasticity approach was developed and proposed to the program team, a study was commenced to determine the limitations of the technique. One result of this study was that the approach, which is an approximation due to an assumption made in the derivation, breaks down when the wavelength-to-magnitude ratio of the sinusoidal components becomes small. Fortunately, reviews of component magnitudes over the frequency domain for the corrosion created on the AF1410 corrosion-fatigue specimens indicate that this wavelength-to-magnitude ratio is significantly larger than the limiting ratio. Furthermore, the new elasticity approach was applied to calculate effective stress concentration factors for selected corrosion fatigue specimens. Actual fatigue crack sites in these specimens were located using fluorescent penetrant microscopy. Each actual crack initiation site precisely matched high-stress sites within the stress concentration map generated by the elasticity approach. The elasticity model forms the basis of ongoing developments in predicting component reliability and remaining life. All of the modeling activities summarized above are discussed in detail in Section 5 of this report.

As it has turned out, the second program contract has significantly overlapped the timeframe of the first program contract. Activities on the second contract have focused on:

- completion of data acquisition and analysis of the first set of AF1410 corrosion-fatigue specimens,
- development of reliability models for life prediction,
- development of corrosion metrics and a corrosion classification scheme,

- manufacture and test of the second set of AF1410 corrosion-fatigue specimens (without residual stress) and associated analysis of the test results,
- preparation of 300M test specimens, and
- preparation of Aermet 100 test specimens.

The final contract on this program will complete all testing and analysis, model development and validation, corrosion classification descriptions via accepted corrosion metrics, and the definition of NDI requirements for transition and implementation of the overall program objectives.

Section 3

Information Gathering

3.0 Introduction

Several investigations were conducted as part of the information-gathering task on the program. A review was conducted of a prior Boeing corrosion-fatigue program on AF1410 high-strength steel. Another review was conducted of an Air Force corrosion prevention and control (CPC) test program in which 300M corroded high-strength steel specimens were tested in fatigue. As part of this test, the control group of specimens was not coated in CPC materials and was, therefore, relevant to the Navy corrosion-fatigue program. A literature search for NDI technologies pertinent to corrosion characterization was also completed. Subsequent program plans benefited from these reviews.

3.1 Review of Boeing Corrosion-Fatigue Test Program

Prior to the start of the UDRI effort to characterize corrosion on AF1410 Steel, researchers at Boeing conducted a program with similar goals. UDRI received a draft report [1] and the fractured specimens from Boeing's study on the corrosion and fatigue of AF1410. Researchers were interested in reviewing Boeing's test method and results so UDRI's tests would not be redundant and resources would be best used.

The Boeing results were statistically analyzed for trends in the crack initiation sites and the influence of the corrosion on the fatigue life. Flat dogbone specimens were used in the study. Non-corroded baseline specimens frequently saw cracks initiate outside of the gage section. Crack initiation on the baseline specimens invariably started at the corner of the specimen. Specimens corroded with NaCl fog also tended to initiate cracks at the corners, away from the corroded region. Very few of these NaCl specimens had cracks initiating in the region of corrosion. Specimens corroded with NaCl and SO₂ fog invariably initiated cracks at the interface between the corroded and non-corroded region. The test matrix can be seen in Table 3.1-1.

Table 3.1-1. Summary of Boeing Corrosion Fatigue Matrix and Crack Initiation Locations

Test Setup			Number of Specimens per Initiation Site		
Test Type Designation	Hours in Neutral NaCl Fog	Hours in SO ₂ Salt Fog	Corner	Corroded Side	Interface
0	0	0	14	0	0
2	50	0	8	4	0
4	100	0	2	2	5
24	25	0	11	1	0
100	0	100	0	0	9
104	4	106	0	0	3

The data showed no strong relationship between the fatigue life and the number of hours of exposure to neutral NaCl fog (Figure 3.1-1). There was little difference in the mean fatigue life whether the crack initiated at a corner or in the corroded gage area (Figure 3.1-2.). The only specimens that showed a significant reduction in life from corrosion exposure were those subjected to the SO₂ spray, and they primarily broke at the interface between the corroded and non-corroded material. It is believed that crevice corrosion caused the material to be undercut beneath the specimen's corrosion masking. This data was presented at the program review on March 16, 2004.

In their study, Boeing modeled surface damage with a pit parameter, cautioning that, "While the initiation of corrosion at localized sites in AF1410 results in localized pitting, corrosion proceeds further by continued rusting along the surface and not by true pitting as in alloys containing inclusions." This observation was further supported by later studies at UDRI. The review of the Boeing report resulted in a study performed by UDRI to determine how to corrode AF1410 without causing the features at the interface between the corroded and non-corroded metal, which would substantially lower fatigue life.

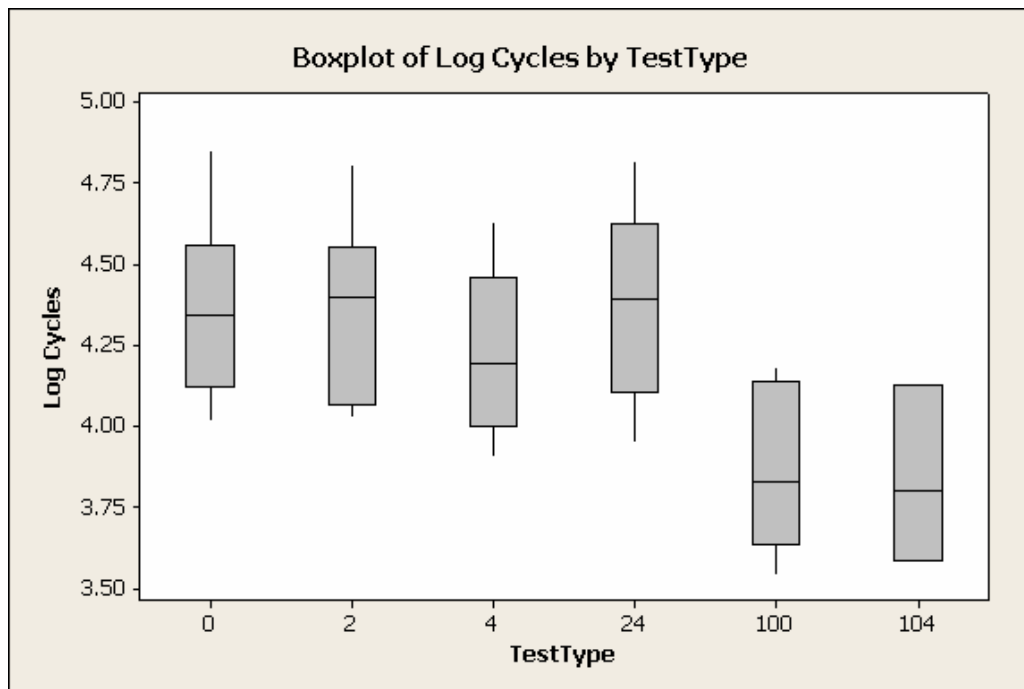


Figure 3.1-1. Boxplot of Fatigue Life and the Test Type Correlating to the Number of Hours of Exposure to the Corrosive Agents

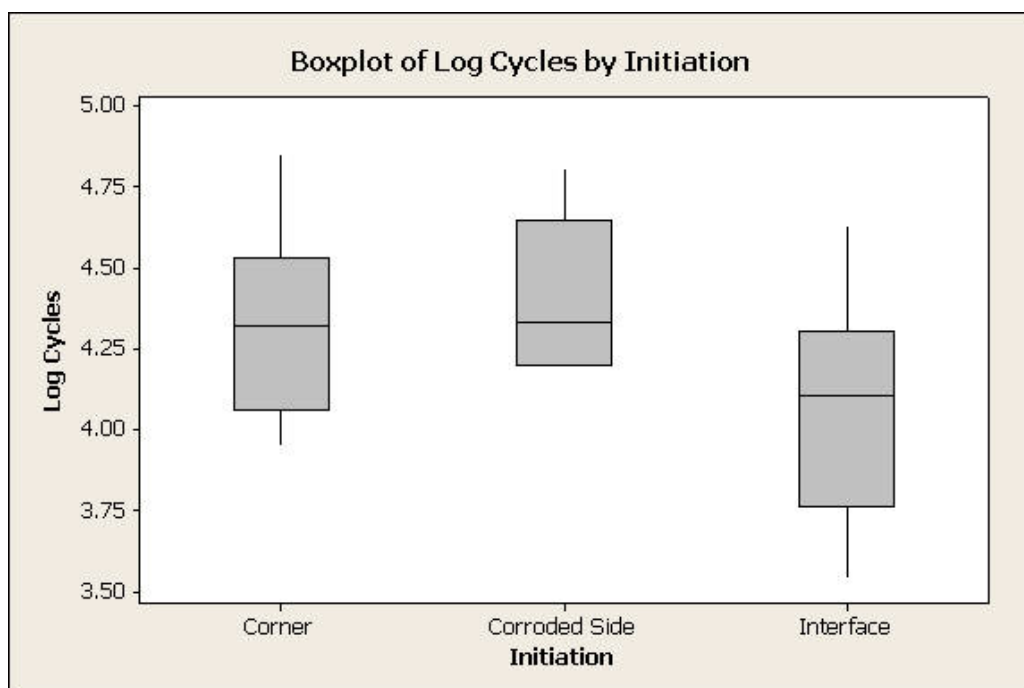


Figure 3.1-2. Boxplot of the Fatigue Life and the Crack Initiation Location

3.2 Review of U.S. Air Force 300M Corrosion-Fatigue Test Report

In 2003, UDRI published “Aging Aircraft Corrosion Preventive Compound Standardization Test Development Final Report 1 – 300M High Strength Steel” from work supporting the USAF (AFRL/MSLC) [2]. This report describes a study of the corrosion suppression capabilities of different corrosion-preventive compounds (CPCs) used on 300M, a high-strength steel. The goal of this research was to determine the ability of CPCs to extend the service life of an aging weapon system as related to fatigue crack initiation. To meet the objectives, it was proposed to use fatigue testing on both pristine specimens and specimens corroded prior to fatigue testing in order to quantify the corrosion suppression capabilities of a CPC. The method used for corroding the test material followed General Motors Engineering Standard GM9540P. The study was broken down into several main tasks:

Task 1 Quantify the corrosion imparted by standard GM9540P on flat panels in order to determine the appropriate number of exposure cycles to impart on fatigue specimens.

Task 2 Study the fatigue behavior of pristine material and specimens with varying numbers of corrosion exposure cycles as a baseline for the CPC study.

Task 3 Apply CPCs to corroded test specimens and compare the life to the baseline tests in order to determine the life extension or CPC suppression capability.

The most significant result from this work, as pertains to the Navy Corrosion-Fatigue study, is from Task 2 listed above – the baseline tests on the corroded substrates. Baseline tests were performed on a total of 34 axial fatigue specimens exposed to a varying number of GM9540P corrosion cycles (from 0 to 40). Three tests were performed at each condition except for the highest number of exposures. Axial fatigue specimens were prepared for this task in the geometry shown in Figure 3.2-1, which was taken directly from UDRI’s original report. The gage section was masked with tape on three sides, while the rest of the specimen was coated with MIL-PRE-23377 primer and MIL-PRF-85285 top coat to protect the grip and radius regions from the corrosion exposure(s).

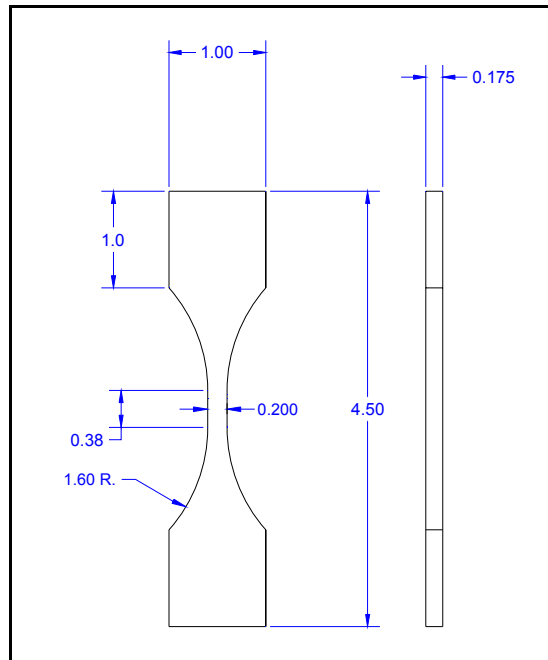


Figure 3.2-1. Axial Fatigue Test Specimen Geometry

The results of these tests, as taken directly from UDRI's original report, are shown in Table 3.2-1 and Figure 3.2-2. The data show that there is a significant debit in the fatigue life after the first cycle of exposure, with little additional debit between one and 16 cycles. Furthermore, the fatigue life is not noticeably different between 24 and 40 cycles of corrosion exposure. The significance of this result to the Air Force study showed that it is unlikely that adding CPCs after corroding would demonstrate measurable improvement on the steel specimens, since the fatigue lives between one and 16 cycles did not show a measurable difference without CPCs. Based on the test results, the test plan for Task 3 on the Air Force study, to apply CPCs to *corroded* test specimens and determine the CPC suppression capability by fatigue testing, was modified. Instead, CPCs were added to *pristine* test specimens, which were then corroded using 25 of the GM9540P cycles, and then fatigue tested for comparison to the baseline fatigue life. The final results included a relative ranking of the effectiveness of several commercial CPCs according to corrosion resistance and prevention of mechanical failure as related to fatigue lives.

Table 3.2-1. Fatigue-Life Cycle to Failure for Pre-Corroded Axial Fatigue Specimens

GM9540P Exposure Cycles	Fatigue Cycles to Failure	GM9540P Exposure Cycles	Fatigue Cycles to Failure
0	10000000*	10	39052
0	10000000*	10	39197
0	10000000*	10	56291
1	90970	12	31374
1	68172	12	34859
1	55739	12	38158
2	73444	14	34999
2	82328	14	37463
2	96716	14	45864
4	43390	16	35046
4	44416	16	33487
4	48774	16	28622
6	35724	24	19511
6	39912	32	19183
6	42076	40	12827
8	37852	40	11799
8	41497	120 ksi, $R = 0.1$, 30 Hz (*) denotes run-out at 10^7 cycles	
8	44232		

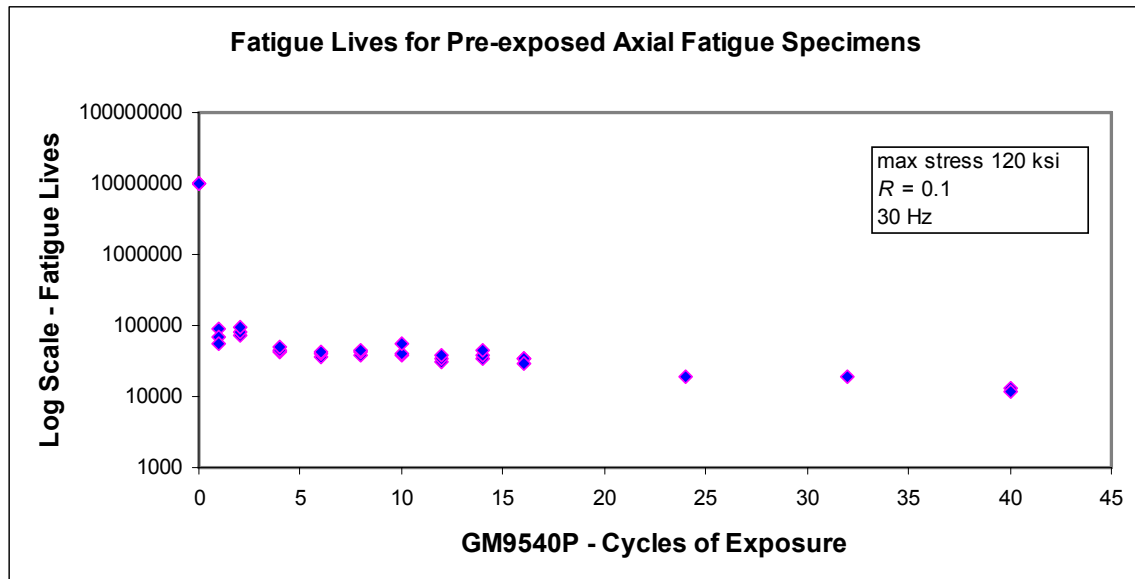


Figure 3.2-2. Fatigue-Life Curve for Pre-Corroded Axial Fatigue Specimens

The significance of their initial results to the Navy Corrosion-Fatigue study is that the mechanism for corrosion-fatigue interaction on 300M steel may be different from that seen on AF1410. A relatively small amount of corrosion (one GM9450P cycle) showed a significant debit in fatigue life and there appeared to be no significant or measurable relationship between the number of corrosion exposure cycles and the fatigue life. This behavior may be attributed to the inherent properties of the 300M high-strength steel, which has a high tensile strength and low fracture toughness as compared to AF1410. These properties make it susceptible to various forms of intergranular attack and/or stress-corrosion cracking (including hydrogen embrittlement) under the appropriate conditions, which can greatly reduce its fatigue life. The inherent low fracture toughness of the material may also mean that the smallest surface defect, such as a machining knick or corrosion feature, can greatly reduce the fatigue life. A study of the fracture surfaces from the Air Force study is currently being performed to help understand these issues so that a test plan can be developed for 300M and the Navy Corrosion-Fatigue study. The goal will be to design a test matrix that ultimately demonstrates the corrosion-fatigue relationship and/or demonstrates the lack thereof due to the corrosion mechanisms in the 300M material.

In order to learn more about why nearly all the debit in life occurred after 1 cycle, the fracture surfaces on several specimens that were fatigue tested in the Air Force study were examined. In particular, the specimens were studied for the presence of intergranular fracture, which may cause the trend in the fatigue life observed. It was observed that the fatigue cracks originated from pits and that those pits varied greatly in size. The fracture surfaces were fairly damaged around the initiation sites and contained a lot of corrosion damage that may have formed since they were tested. Even so, clear evidence of intergranular fracture and, therefore, intergranular corrosion attack was not observed. Further investigation into the corrosion-fatigue relationship on the dog-bone specimens and comparisons of cross-sections of the corrosion may provide additional insight for test matrix development.

In summary, UDRI's earlier study for the Air Force showed that 1 cycle of the GM5490P standard exposure caused nearly all the loss in fatigue life measured and showed that no relationship existed between the number of GM cycles and fatigue life. Comparisons of the corrosion produced using the GM method to that using UDRI's filter paper and applied current technique showed that a 3-hour exposure of UDRI's technique produced close to the same amount of

corrosion in terms of mass loss, and possibly in terms of topography characteristics, as 1 cycle of the GM exposure. This information provided a good starting point for development of a test matrix on the Navy Corrosion-Fatigue Program.

3.3 NDE Literature Search

A literature search and review effort was conducted at the beginning of this program to aid in determining what nondestructive inspection (NDI) techniques should be investigated for development of a corrosion metric, and in what order the chosen techniques should be investigated. Some of the criteria that were thought to be important for metric development included: surface topography, surface roughness, material thickness loss, high resolution in all three spatial dimensions, and possibly pit depth. In addition, the corrosion that must be assessed is on the inside diameter of the arrestment shank and the arrestment would most likely not be disassembled for the corrosion assessment. Therefore, the NDI technique(s) must be capable of assessing the corrosion from the outer surface of the arrestment shank. And, the NDI technique(s) must be applicable for use on aircraft carriers at sea. With those criteria in mind, literature was reviewed on the following techniques:

- Ultrasonics
- Eddy current
- Optical
- Magnetic flux leakage

Magnetic flux leakage techniques were eliminated because of poor spatial resolution.

Optical techniques were believed to best meet all of the criteria, with the exception of the need for inspecting through the thickness of the opaque arrestment shank. Therefore, optical techniques were removed from consideration for the first two years of the program.

Eddy current techniques have been used for many decades to detect and quantify material thickness loss due to corrosion. In addition, they may be capable of measuring topography as well, although the resolution that can be achieved has not been well documented. In addition, eddy current techniques can provide information through the thickness of suitable materials, although the resolution is diminished. However, ferromagnetic materials are difficult to inspect with eddy current, but some studies indicate that there may be methods for overcoming this problem.

Ultrasonic techniques appear to be quite promising for detecting and characterizing corrosion in terms of thickness loss, surface topography and surface roughness both on the inner and outer surface of components. Characterizations can be made on interior surfaces as well as exterior surfaces. Effective methodologies that have been reported in the literature include:

- Surface-roughness measurements by:
 - angle-beam back-scattered amplitude
 - normal-incidence reflected amplitude
 - Fourier spectroscopy – slope of the magnitude spectra of the transfer function (provides an estimate of “local” RMS roughness)
- Topographic (elevation) measurements by:
 - time-of-flight (TOF) to a peak in the reflected normal-incidence signal
 - location of the peak in the time-domain representation of the cross correlation of the normal-incidence reflected signal with a suitable reference signal
 - slope of the Fourier phase of the normal-incidence reflected signal
- Thickness-loss measurements by the same basic methods as used for surface-topography measurements.

Despite the capabilities that are listed above, there are some issues that exist relative to the use of ultrasonic techniques. These include:

- Frequency-sensitive scattering that degrades the signal-to-noise ratio as well as the lateral and depth resolutions – this can be due to roughness of the surface through which the ultrasound passes as it propagates to and from the surface of interest
- Frequency sensitive attenuation that degrades the signal-to-noise ratio as well as the lateral and depth resolutions – this is due to the properties of the material through which the ultrasound propagates
- Need for a medium (e.g., water) for coupling the ultrasound into the part
- Distortions due to the geometry of the part

After thoughtful consideration of the capabilities and limitations of the NDI techniques listed above, ultrasonic NDI was chosen as the primary candidate for investigation. A very small effort was undertaken to study the potential use of eddy current techniques for corrosion characterization.

The exact nature of the “corrosion metric” that will be required for successful implementation of all of the program objectives was not known at the time the program began. For that reason, a variety of ultrasonic techniques were explored. Also, because it was believed that some measure of roughness or topography would most likely contribute to the metric, all of the data from all of the ultrasonic techniques that appeared promising were compared to topography data that was generated from white-light interference microscope scans of the corroded regions of specimens.

Section 4

Effects of Corrosion Damage on Fatigue Life

4.0 Introduction

One of the primary tasks on the program was to experimentally study the effect that corrosion damage has on fatigue life of high-strength steels. Of particular interest to the Navy was the F-18 arrestment shank, made of AF1410 steel. Baseline tests of this material were conducted in support of these experiments. These tests are described in Section 4.1.

In order to quantify the effect of corrosion on fatigue life, it was necessary to perform quantitative corrosion-fatigue tests on AF1410 steel specimens. Each specimen was carefully manufactured and exposed to accelerated corrosion-growth environments. After the corrosion products were chemically removed, the corroded surface profile was characterized and the specimens were fatigued tested. Initially, the plan called for one test on AF1410 in a test matrix of 60 corrosion-fatigue specimens. After it was determined that specimen preparation produced unacceptable surface residual stresses due to grit blasting, it was decided to prepare and test a second set of 60 specimens that were not grit-blasted. Corrosion-fatigue tests were also planned for 300M, but considering the results of the Air Force study referenced in Section 3.2, it was decided that this test would use only nine specimens, attempting to only verify the Air Force study results. Extensive preliminary development efforts, described next, were required to support all of these corrosion-fatigue tests.

Various corrosion growth methods – discussed in Section 4.2.1 – were investigated, including a time-of-exposure study to plan for different levels of corrosion severity in the specimens. Examination of the extant specimens from the Boeing test, as well as NAVAIR and UDRI corrosion time-of-exposure test wafers, showed that masking produces crevice corrosion in the perimeter of the exposed area that can cause an unrealistic reduction in fatigue life. In addition, alternate immersion methods required extended periods of exposure totaling as long as several months. A newly developed enhanced electrochemical process that makes use of salt water-soaked filter paper sandwiched between electrodes was finally selected, based on its potential to quickly apply varying levels of corrosion in controlled locations without introducing any significant crevice corrosion or undercutting at the perimeter of the corrosion patch. In addition, methods to chemically remove

corrosion products without adversely affecting the remaining corrosion profile were investigated and tested. See Section 4.2.2 for details. A Boeing corrosion removal specification using an alk-line solution, Turco[®], was selected for use on AF1410. In addition, a materials study was performed to rule out any possible change in material or material properties due to the use of the selected corrosion growth method. A discussion of this study and its results are found in Section 4.2.3.

Additional support activities included a comprehensive study of various surface profile characterization technologies that would be technically suitable in terms of spatial and depth resolutions, and that would be available and practical for this program. White-light interference microscopy was tested and, consequently, selected for use on this program. Details of this comparison and associated tests are found in Section 4.2.4. In addition, a survey was conducted of various surface roughness metrics. See Section 4.2.5 for a review of these metrics. Metric values were tabulated for the corrosion surfaces of the first set of AF1410 corrosion-fatigue specimens. In conjunction with the examination of different surface profile instruments, methods were researched for replicating corrosion surfaces; a dental paste technique was found to produce the best results. This investigation is described in Section 4.2.6. Dental paste replicas of real service-induced corrosion found in actual AF1410 arrestment shanks were characterized with the white-light interference microscope. Section 4.2.7 describes this task. Various features and surface roughness metrics determined from these arrestment shank profiles were compared to those from the corrosion-fatigue specimens. The arrestment shank corrosion was found to be somewhat different from that being created in the test specimens, probably due to the presence of the cadmium plating on the arrestment shank. This protective plating prevents corrosion except when the coating fails, which then results in localized corrosion and thickness loss. Additional corrosion-fatigue tests, as well as additional modeling, will be required to account for these observed differences.

To properly quantify the fatigue life to initiation of a 0.010-inch crack, the standard criteria used in the Navy, requires ascertaining the number of fatigue cycles to a crack of this size. This step was accomplished by introducing marker bands in the loading history of the corrosion-fatigue test. NAVAIR performed the necessary experiments to determine the appropriate parameters for such marker bands. See Section 4.2.8 for a summary of this study. In addition, a method was required to measure the depth of these marker bands on the fracture surfaces of the specimens. NAVAIR, with council of experts in Australia, developed the capability at their facility to per-

form the necessary quantitative fractography on the corrosion-fatigue fracture surfaces. Other team members were subsequently trained on these methods. Section 4.2.9 contains a summary of these activities.

4.1 Baseline Mechanical Tests

Baseline tests were conducted to establish Young's modulus, Poisson's ratio, tensile strength, fracture toughness and fatigue crack growth rates of the specimens.

4.1.1 Young's Modulus Tests

Specimen

Two round dogbone tensile specimens were provided by NAVAIR. The gage section was nominally 0.25 inches in diameter and 1.0 inch long. The grip section was comprised of 3/8-16 threads.

Equipment

Specimens were tested in an MTS closed-loop, servo-hydraulic test machine equipped with an 11 kip actuator. Three Micro-Measurements strain gages of type CEA-06-031DE-350 were applied to the specimens equilaterally around the circumference at the midpoint of the gage length. An MTS 650.03 mechanical extensometer was calibrated to a Class A level. The results of the extensometer calibration can be found in Appendix C, along with calibration data for Poisson's ratio and ultimate tensile tests. Loads were measured with a 10 kip load cell, calibrated to a Class A level.

Procedure

Room temperature modulus tests were performed per ASTM E111 (Standard Test Method for Young's Modulus, Tangent Modulus, and Chord Modulus). Specimens were threaded into grips in the machine. The strain gages were zeroed and a shunt calibration was performed. The mechanical extensometer was fastened to the specimen using rubber bands. The load was raised by increments of 200 lbs using a hand control. The load and strain measurements were recorded at each increment. The load was increased until the maximum strain gage reading was 0.025 in/in strain. The load was then lowered back to zero. The loading and unloading process was repeated two more times. The specimen was rotated between loading sequences, and the mechanical extensometer was moved to help detect bending.

Results

Results from the three loading sequences for both specimens can be found in Figures 4.1.1-1 through 4.1.1-6 and Tables 4.1.1-1, 4.1.1-2, 4.1.2-1, and 4.1.2-2.

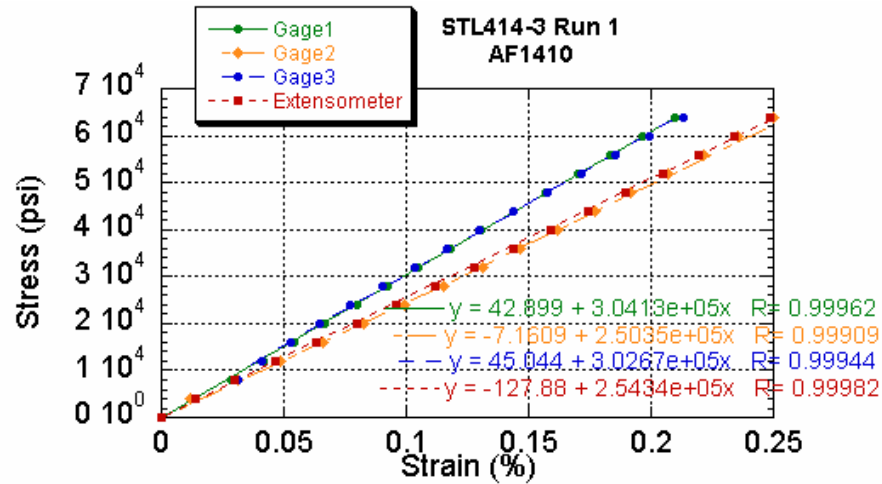


Figure 4.1.1-1. AF1410 Room Temperature Modulus Test on Specimen STL414-3, First Loading Sequence

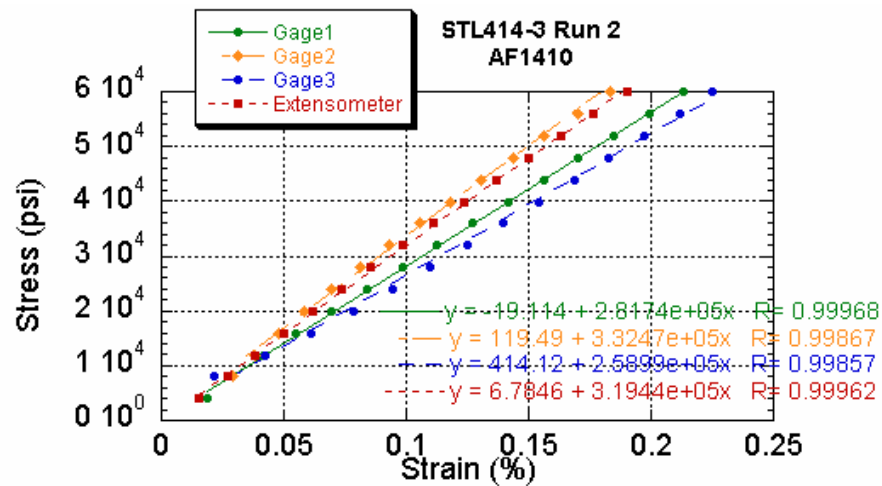


Figure 4.1.1-2. AF1410 Room Temperature Modulus Test on Specimen STL414-3, Second Loading Sequence

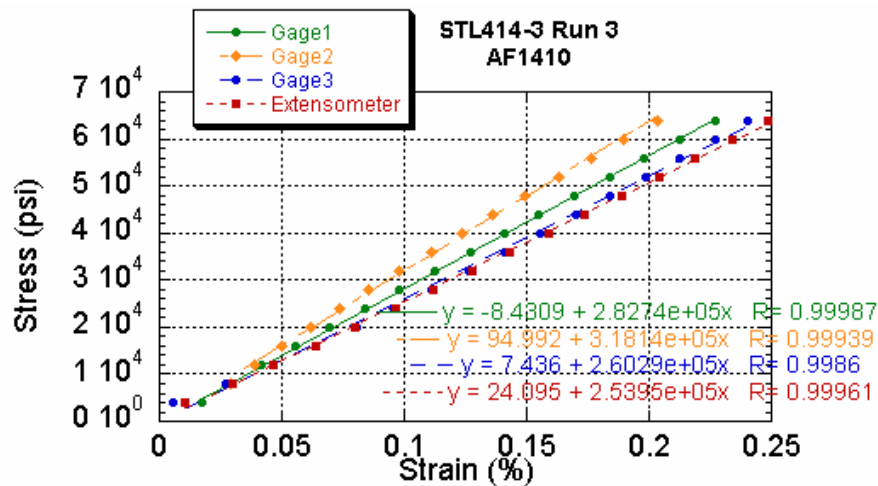


Figure 4.1.1-3. AF1410 Room Temperature Modulus Test on Specimen STL414-3, Third Loading Sequence

Table 4.1.1-1. Test Results from the Young's Modulus Tests on Lot B AF1410 Specimen STL414-3

AF1410 STL414-3	Run 1 Modulus (ksi)	Run 2 Modulus (ksi)	Run 3 Modulus (ksi)
Gage 1	30.41	28.17	28.27
Gage 2	25.04	33.25	31.81
Gage 3	30.27	25.90	26.03
Extensometer	25.43	31.94	25.40
Average	27.79	29.82	27.88
Overall Average Modulus	28.49		

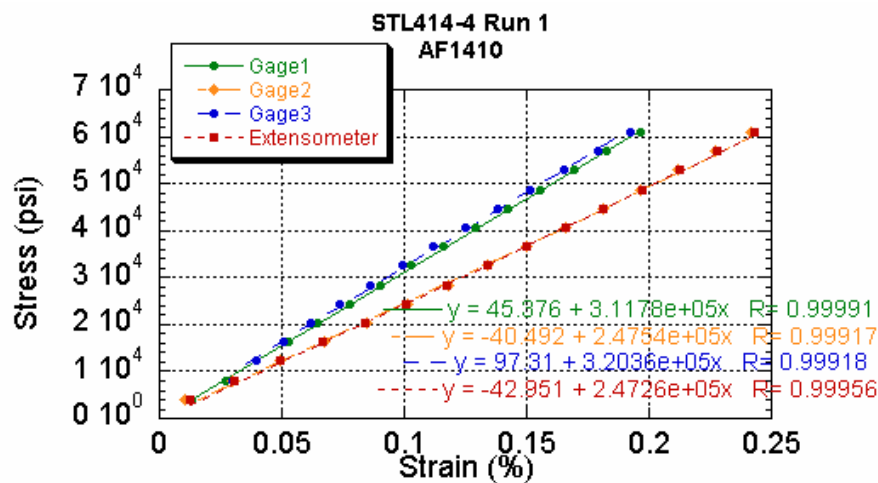


Figure 4.1.1-4. AF1410 Room Temperature Modulus Test on Specimen STL414-4, First Loading Sequence

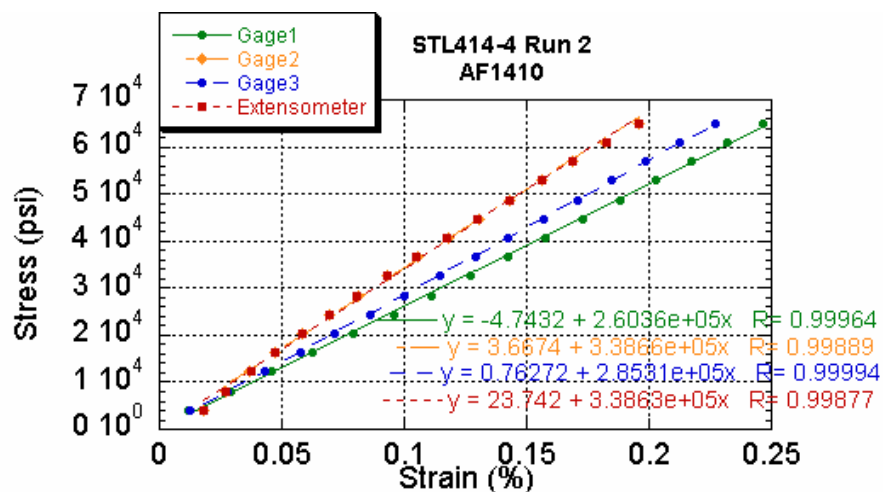


Figure 4.1.1-5. AF1410 Room Temperature Modulus Test on Specimen STL414-4, Second Loading Sequence

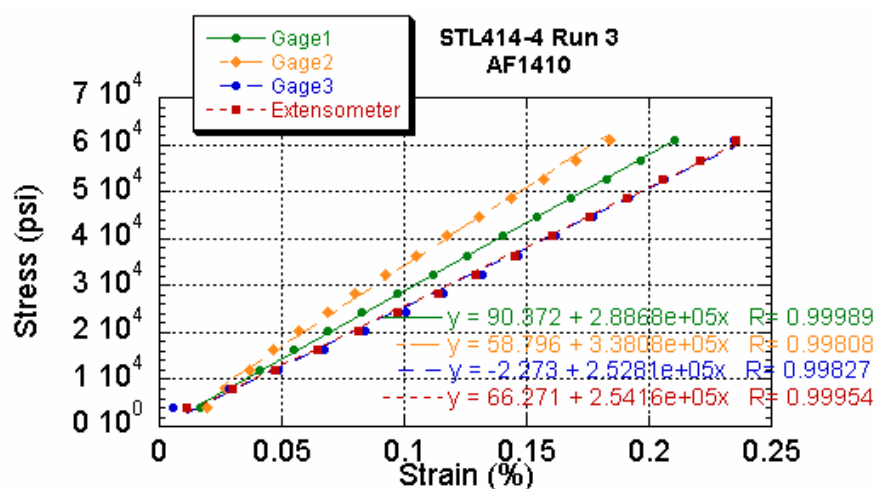


Figure 4.1.1-6. AF1410 Room Temperature Modulus Test on Specimen STL414-4, Third Loading Sequence

Table 4.1.1-2. Test Results from the Young's Modulus Tests on Lot B AF1410 Specimen STL414-4

AF1410 STL414-4	Run 1 Modulus (ksi)	Run 2 Modulus (ksi)	Run 3 Modulus (ksi)
Gage 1	31.18	26.04	28.87
Gage 2	24.75	33.87	31.81
Gage 3	32.04	28.53	25.28
Extensometer	24.73	33.86	25.42
Average	28.17	30.57	28.34
Overall Average Modulus	29.03		

4.1.2 Poisson's Ratio Testing

Specimen

Two round dogbone tensile specimens were provided by NAVAIR. The gage section was nominally 0.25 inches in diameter and 1.0 inch long. The grip section was comprised of 3/8-16 threads.

Equipment

Specimens were tested in an MTS closed-loop servo-hydraulic test machine equipped with an 11 kip actuator. Back-to-back Micro-Measurement strain gages of type CEA-06-062WT-350 were applied to the specimens. These gages were T-type, which means they could measure longitudinal and circumferential strain simultaneously. Loads were measured with a 10 kip load cell, calibrated to a Class A level.

Procedure

Poisson's Ratio Tests were performed in accordance with ASTM E132 (Standard Test Method for Poisson's Ratio at Room Temperature). Specimens were threaded into grips in the machine. The strain gages were zeroed and a shunt calibration was performed. The load was raised by increments of 200 lbs using a hand control. The load and strain measurements were recorded at each increment. The load was increased until the maximum strain gage reading was 0.025 in/in strain. The load was then lowered back to zero. The loading and unloading process was repeated one to two more times.

Results

Results from the three loading sequences for both specimens can be found in Figures 4.1.2-1 through 4.1.2-5

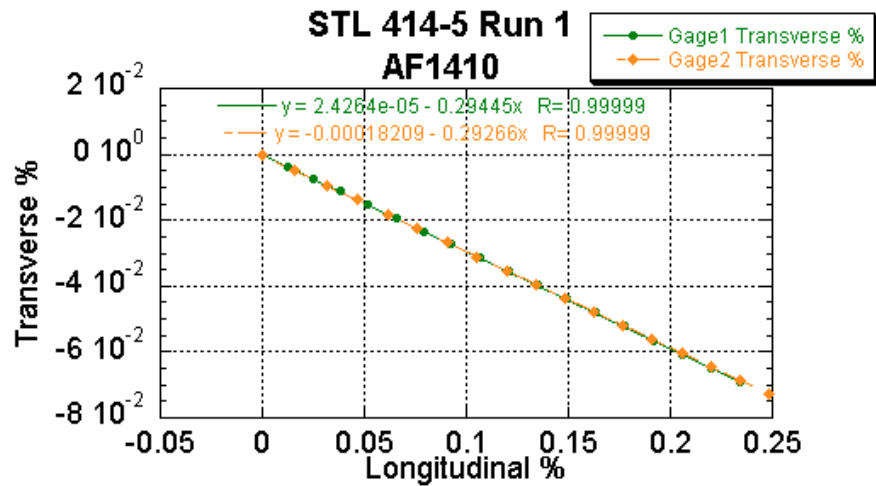


Figure 4.1.2-1. AF1410 Room Temperature Poisson's Ratio Test on Specimen STL414-5, First Loading Sequence

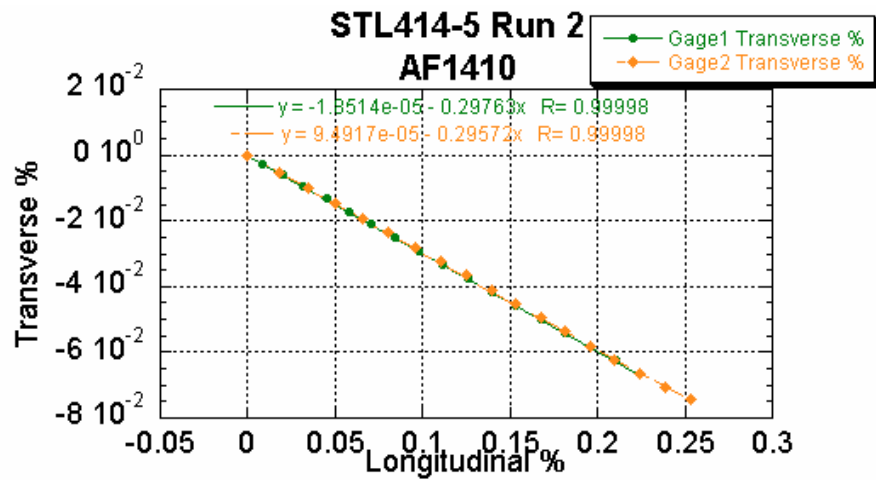


Figure 4.1.2-2. AF1410 Room Temperature Poisson's Ratio Test on Specimen STL414-5, Second Loading Sequence

Table 4.1.2-1. Test Results from the Poisson's Ratio Test AF1410 Specimen STL414-5

AF1410 STL414-5	Run 1 Modulus (ksi)	Run 2 Modulus (ksi)
Gage 1	0.294	0.298
Gage 2	0.293	0.296
Average	0.294	0.297
Overall Average Modulus		0.295

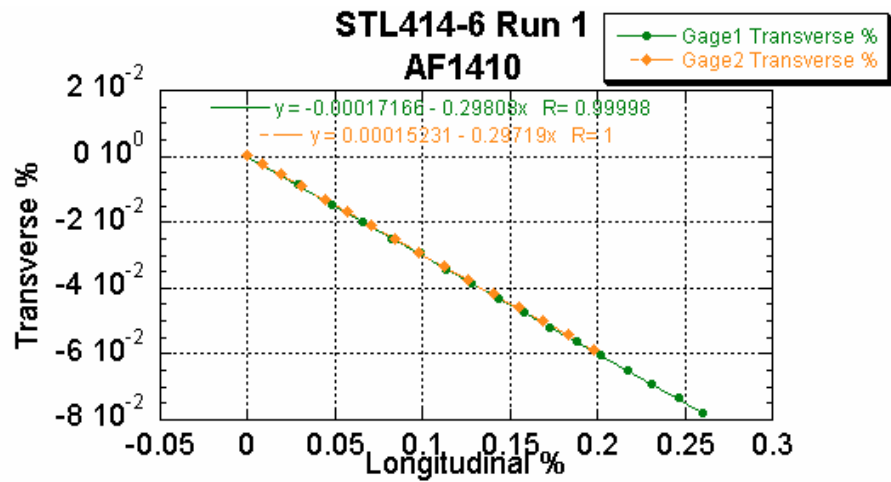


Figure 4.1.2-3. AF1410 Room Temperature Poisson's Ratio Test on Specimen STL414-6, First Loading Sequence

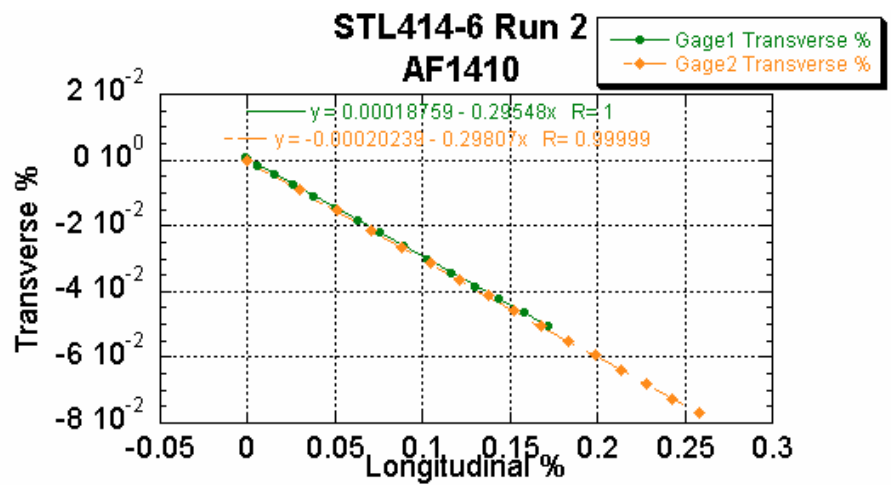


Figure 4.1.2-4. AF1410 Room Temperature Poisson's Ratio Test on Specimen STL414-6, Second Loading Sequence

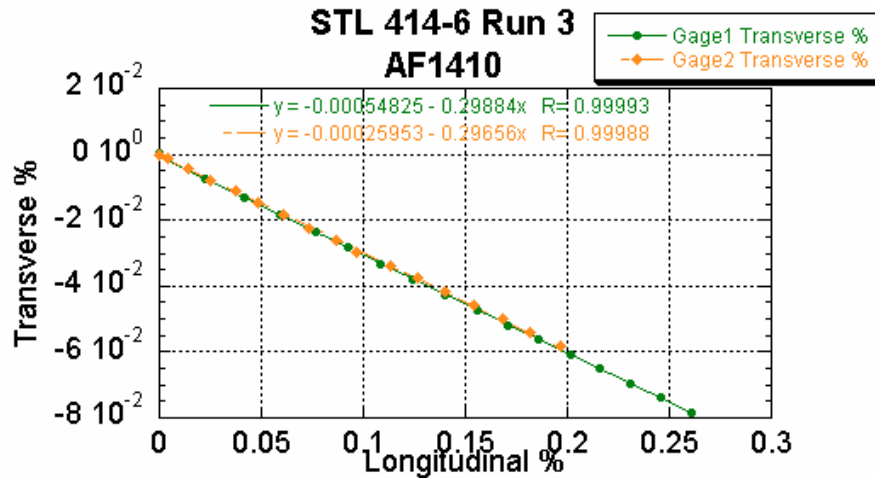


Figure 4.1.2-5. AF1410 Room Temperature Poisson’s Ratio Test on Specimen STL414-6, Third Loading Sequence

Table 4.1.2-2. Test Results from the Young’s Modulus Tests on AF1410 Specimen STL414-6

AF1410 STL414-6	Run 1 Modulus (ksi)	Run 2 Modulus (ksi)	Run 3 Modulus (ksi)
Gage 1	0.298	0.295	0.299
Gage 2	0.297	0.298	0.297
Average	0.298	0.297	0.298
Overall Average Modulus			0.297

4.1.3 Tensile Strength Testing from Lot A AF1410 Material

Specimen

Four round dogbone tensile specimens were provided by NAVAIR. The gage section was nominally 0.25 inches in diameter and 1.0 inch long. The grip section was comprised of 3/8-16 threads.

Equipment

Specimens were tested in an MTS closed-loop servo-hydraulic test. On specimens STL414-3 and STL414-4, three Micro-Measurement strain gages of type CEA-06-031DE-350 were applied to the specimens equilaterally around the circumference at the midpoint of the gage length. On specimens STL414-5 and STL414-6, back-to-back Micro-Measurement strain gages of type CEA-06-062WT-350 were applied. A mechanical extensometer was also used to measure elongation. Loads were measured with a load cell.

Procedure

Room temperature tensile tests were performed per ASTM E8 (Tension Testing of Metallic Materials). Specimens were threaded into grips in the machine. The mechanical extensometer was fastened to the specimen using rubber bands.

Results

Results from the tests can be found in Figures 4.1.3-1 through 4.1.3-4.

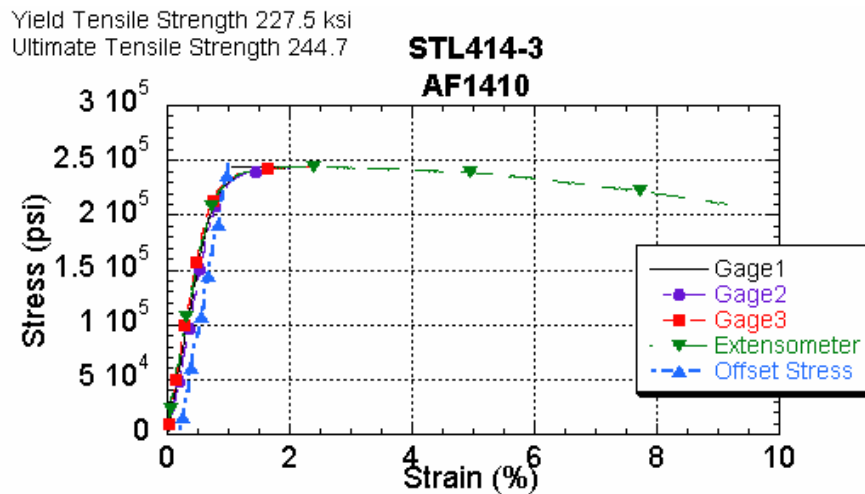


Figure 4.1.3-1. AF1410 Room Temperature Tensile Test on Specimen STL414-3

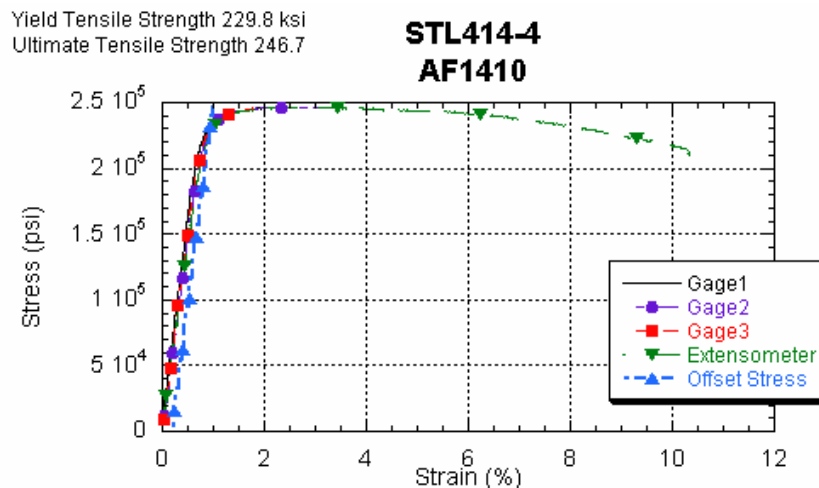


Figure 4.1.3-2. AF1410 Room Temperature Tensile Test on Specimen STL414-4

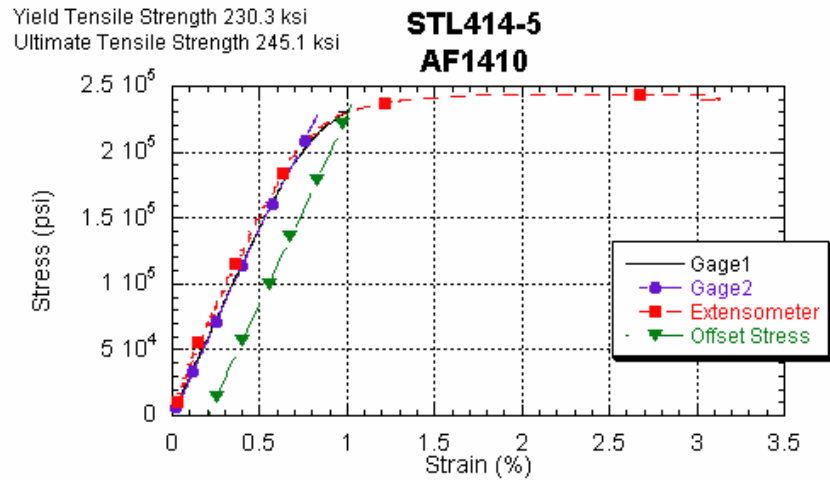


Figure 4.1.3-3. AF1410 Room Temperature Tensile Test on Specimen STL414-5

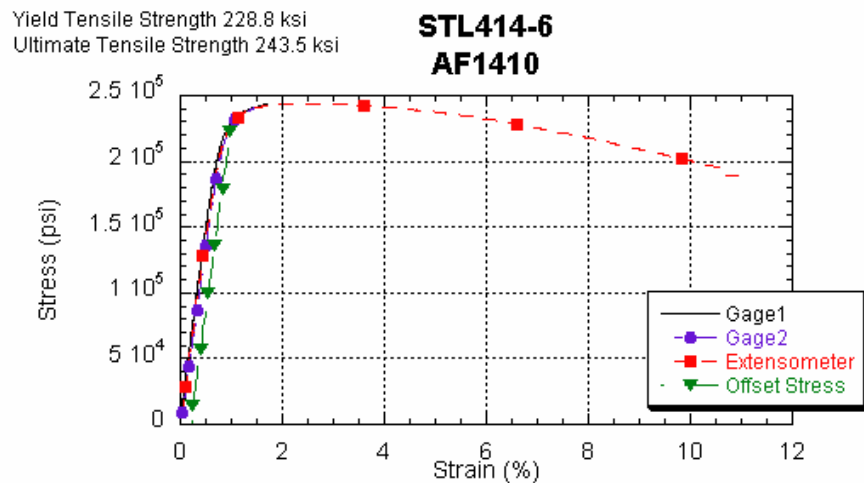


Figure 4.1.3-4. AF1410 Room Temperature Tensile Test on Specimen STL414-6

4.1.4 Tensile Strength Testing of Travelers from Lot B AF1410 Material

Specimen

Two round dogbone tensile specimens were provided by NAVAIR. The specimens had been used as travelers during the heat treatment of the Lot B AF1410 Corrosion Fatigue specimens. The gage section was nominally 0.25 inches in diameter and 1.0 inch long. The grip section was comprised of 3/8-16 threads.

Equipment

Specimens were tested in an MTS closed-loop servo-hydraulic test machine with a 22 kip actuator. A mechanical extensometer was also used to measure elongation. Loads were measured with a load cell.

Procedure

Room temperature tensile tests were performed per ASTM E8 (Tension Testing of Metallic Materials). Specimens were threaded into grips in the machine. The mechanical extensometer was fastened to the specimen using rubber bands.

Results

Specimen STL533-12 was initially loaded in an 11 kip machine, which did not have sufficient load to complete the test. The specimen experienced a stress of 200 ksi, which is below the 0.2% offset yield stress; however, this probably influenced later test results. One specimen from this heat treatment lot was also tested by Hercules Heat Treat. Results from the tests can be found in Figure 4.1.4-1 and Table 4.1.4-1.

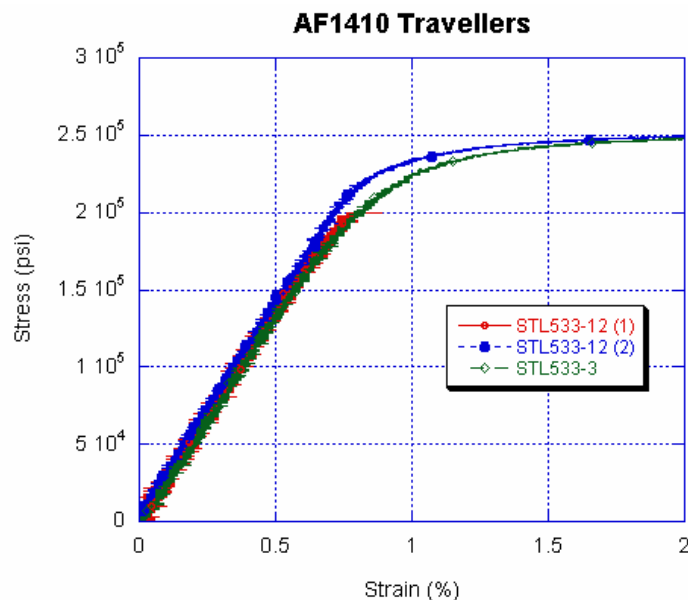


Figure 4.1.4-1. AF1410 Room Temperature Tensile Test on Specimen STL533-12 and STL533-3

Table 4.1.4-1. Test Results from the Tensile Tests on Travelers from Lot B AF1410 Material

Specimen	Ultimate Tensile Strength (ksi)	0.2% Offset Yield Strength (ksi)	Estimated Elastic Modulus (Msi)
STL533-12 (1)	NA	NA	26.7
STL533-12 (2)	250.8	236.8	27.4
STL533-3	249.8	228.6	27.0
Hercules Tested	254.0	223.3	

4.1.5 Fracture Toughness Tests (Heat-Treated Lot B Material)

Specimen

Compact tension, C(T), specimens were fabricated in the long-transverse, L-T, orientation from a forging of AF1410 obtained by NAVAIR. A section of forging was sent to UDRI for the making of the fracture toughness test specimens. Specimen blanks were austenitized, quenched, and aged at Hercules Heat Treat and then finish machined. Specimens had a width, W, of 2 inches and thickness, B, of 1 inch in accordance with ASTM E399 Standard Test Method for Plane-Strain Fracture Toughness of Metallic Materials.

Equipment

Tests were performed in a MTS closed-loop, servo-hydraulic test machine equipped with a 22 kip actuator. A strain gage displacement transducer was used to measure the crack-opening displacement (COD) during tests. Loads were measured using a load cell.

Procedure

Nine fracture toughness tests were performed in ambient laboratory air in accordance with ASTM E399. Specimens were first fatigue pre-cracked. Load and COD were sampled and digitally recorded during the test. Data were analyzed in accordance with ASTM E399 using Excel spreadsheets and plots.

Results

A summary of test results can be found in Table 4.1.5-1. All tests met the validity criteria listed by ASTM E399, however, the K_{IC} values determined were lower than expected for AF1410. The average fracture toughness found for this material was $120 \text{ ksi}\sqrt{\text{in}}$ and the expected minimum fracture toughness was $130 \text{ ksi}\sqrt{\text{in}}$.

Table 4.1.5-1. Summary of Fracture Toughness Test Results

Specimen ID	Fracture Toughness [130 ksi√(in)]
STL 461-8	114
STL 461-13	114
STL 461-25	118
STL 461-26	119
STL 461-28	124
STL 461-29	128
STL 461-30	121
STL 461-31	131
STL 461-32	112
Average	120

4.1.6 Fracture Toughness Tests of AF1410 (Heat-Treated and Overaged Lot B Material)

Specimen

Compact tension, C(T), specimens were fabricated in the long-transverse, L-T, orientation from the NAVAIR-supplied AF1410 forging used for the Lot B corrosion fatigue specimens. The forging was sent to UDRI for the making of the fracture toughness and corrosion fatigue test specimens. The material was given an additional over-aging heat treatment prior to fabrication of the specimens. Specimen blanks were austenitized, quenched, and aged at Hercules Heat Treat and then finish machined. Specimens had a width, W, of 2 inches and thickness, B, of 1 inch in accordance with ASTM E399 Standard Test Method for Plane-Strain Fracture Toughness of Metallic Materials.

Equipment

Tests were performed in an MTS closed-loop, servo-hydraulic test machine equipped with a 22 kip actuator. A strain gage displacement transducer was used to measure the crack-opening displacement (COD) during tests. Loads were measured using a load cell.

Procedure

Four fracture toughness tests were performed in ambient laboratory air in accordance with ASTM E399. Specimens were first fatigue pre-cracked. Load and COD were sampled and digitally recorded during the test. Data were analyzed in accordance with ASTM E399 using Excel spreadsheets and plots.

Results

A summary of test results can be found in Table 4.1.6-1. The test on specimen STL 532-1 was invalid due to the crack length at the start of the test being too long. The K_{IC} values determined were lower than expected for AF1410. The average fracture toughness found for this material was 105.7 ksi√(in) and the expected minimum fracture toughness was 130 ksi√(in).

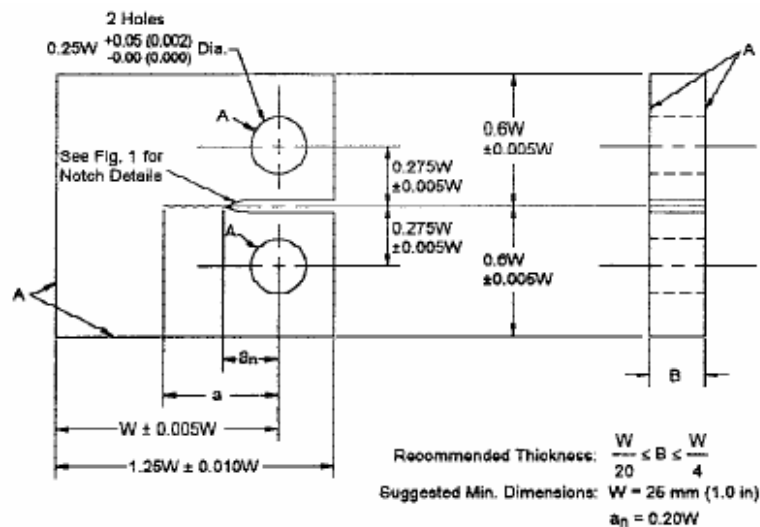
Table 4.1.6-1. Summary of Fracture Toughness Test Results with Overaging Heat Treatment

Specimen ID	Fracture Toughness [130 ksi√(in)]
STL 532-1	Invalid
STL 532-2	104
STL 563-1	106
STL 563-2	107
Average	105.7

4.1.7 Fatigue Crack Growth Rate Tests

Specimens

Compact-tension, C(T), specimens, as seen in Figure 4.1.7-1, had a nominal width of 2.50 inches and thickness of 0.30 inches. The C(T) specimens were used primarily for tests with positive load ratios. Center-cracked, M(T), specimens, as seen in Figure 4.1.7-2, had a nominal width of 3.00 inches and thickness of 0.30 inches. The M(T) specimens were primarily used for tests with a negative load ratio. Due to scarcity of material, some smaller M(T) specimens were manufactured from the fractured halves of previously-tested M(T) specimens. All specimens were fabricated from 0.38 inch thick plate material provided by the Navy. Specimens were austenitized, quenched, and aged at Hercules Heat Treat and then finish machined.



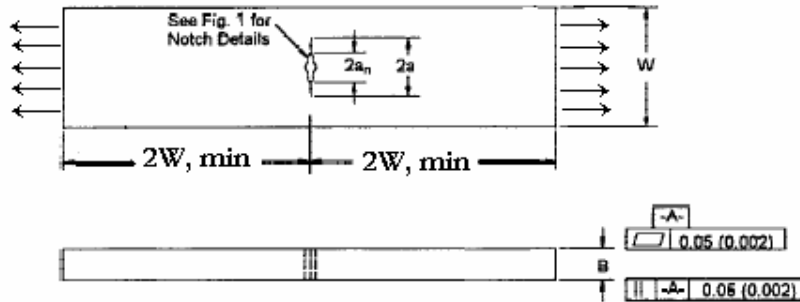
NOTE 1—Dimensions are in millimetres (inches).

NOTE 2—A-surfaces shall be perpendicular and parallel as applicable to within $\pm 0.002 W$, TIR.

NOTE 3—The intersection of the tips of the machined notch (a_n) with the specimen faces shall be equally distant from the top and bottom edges of the specimen to within $0.005 W$.

NOTE 4—Surface finish, including holes, shall be 0.8 (32) or better.

Figure 4.1.7-1. C(T) Specimen



- NOTE 1—Dimensions are in millimetres (inches).
- NOTE 2—The machined notch ($2a_n$) shall be centered to within ± 0.001 W.
- NOTE 3—For specimens with $W > 75$ mm (3 in.) a multiple pin gripping arrangement is recommended, similar to that described in Practice 561.
- NOTE 4—Surface finish, shall be 0.8 (32) or better.

Figure 4.1.7-2. M(T) Specimen

Equipment

All tests were conducted on MTS closed-loop, servo-hydraulic test stations. A PC-based computer system was used for test control and data acquisition. Loads were measured with a load cell and the crack length was measured using the crack opening displacement method outlined in ASTM E647. A strain gage displacement transducer was used to measure the crack-opening displacement (COD) during tests. Clevises and pins were used to load the C(T) specimens. Hydraulic grips were used to load the M(T) specimens.

Procedure

All tests were conducted in accordance with ASTM E647-00, Standard Test Method for Measurement of Fatigue Crack Growth Rates. Pre-cracking and most tests were done in a laboratory-air environment (72°F, 40 to 50% relative humidity). Three tests identified as being tested in a NaCl environment were conducted in a humidity chamber. These three specimens had NaCl dried onto the sides of the specimens. Pre-cracking and threshold tests were conducted using the decreasing K procedure method described in ASTM E647. Otherwise, tests were performed using the constant-force-amplitude procedure.

Data reduction was performed using either the secant method or the seven-point incremental polynomial method to calculate the crack growth rate. The slight differences in fatigue crack growth rates between duplicates are relatively insignificant and can be explained by specimen-to-specimen variability.

Results

A summary of the fatigue crack growth rate testing can be found in Table 4.1.7-1. Figures 4.1.7-3 through 4.1.7-9 show composites of the test results.

Table 4.1.7-1. Summary of Fatigue Crack Growth Rate Testing of AF1410 Steel

Load Ratio	Specimen Type	Test Type	Specimen ID	Comments
-1	M(T)	Constant Load Amplitude	STL419-32	All Valid
		Constant Load Amplitude	STL419-36	* Valid Through "a" = 0.633
		Constant Load Amplitude	STL419-36 Bottom	All Valid
		Constant Load Amplitude	STL419-36 Top	All Valid
		Constant Load Amplitude	STL419-37	* Test Invalid
		Constant Load Amplitude	STL419-37 Bottom	* Valid Through "a" = 0.552
		Constant Load Amplitude	STL419-37 Top	All Valid
0.1	M(T)	Constant Load Amplitude	STL419-34C	All Valid
		Constant Load Amplitude	STL419-35	* Test Invalid
0.1	C(T)	Constant Load Amplitude	STL414-1	** Test Valid Through "a" = 1.25
		Constant Load Amplitude	STL414-2	** Test Valid Through "a" = 1.625
		Constant Load Amplitude	STL419-1	Specimen fast fractured at end
		Constant Load Amplitude	STL419-2	All Valid
		Constant Load Amplitude	STL419-3	All Valid
		Constant Load Amplitude	STL419-4	All Valid
		Constant Load Amplitude	STL419-5	All Valid
		Constant Load Amplitude	STL419-13	All Valid
		Constant Load Amplitude	STL419-35A	All Valid
		Decreasing ΔK	STL419-21	All Valid
		Decreasing ΔK	STL419-22	All Valid
		Constant Load Amplitude in NaCl Environment	STL419-19	All Valid
		Constant Load Amplitude in NaCl Environment	STL419-20	All Valid
0.5	C(T)	Constant Load Amplitude	STL419-6	All Valid
		Constant Load Amplitude	STL419-7	All Valid
		Constant Load Amplitude	STL419-8	All Valid
		Constant Load Amplitude	STL419-9	All Valid
		Constant Load Amplitude	STL419-10	All Valid
		Constant Load Amplitude	STL419-11	All Valid
		Constant Load Amplitude	STL419-12	All Valid
		Constant Load Amplitude	STL419-17	All Valid
		Decreasing ΔK	STL419-14	All Valid
		Decreasing ΔK	STL419-16	All Valid
		Constant Load Amplitude in NaCl Environment	STL419-18	All Valid

* Beyond this point the crack length asymmetry from the centerline was too great per ASTM E647-00 A2.4.3

** Beyond this point the crack propagated by fast fracture shearing.

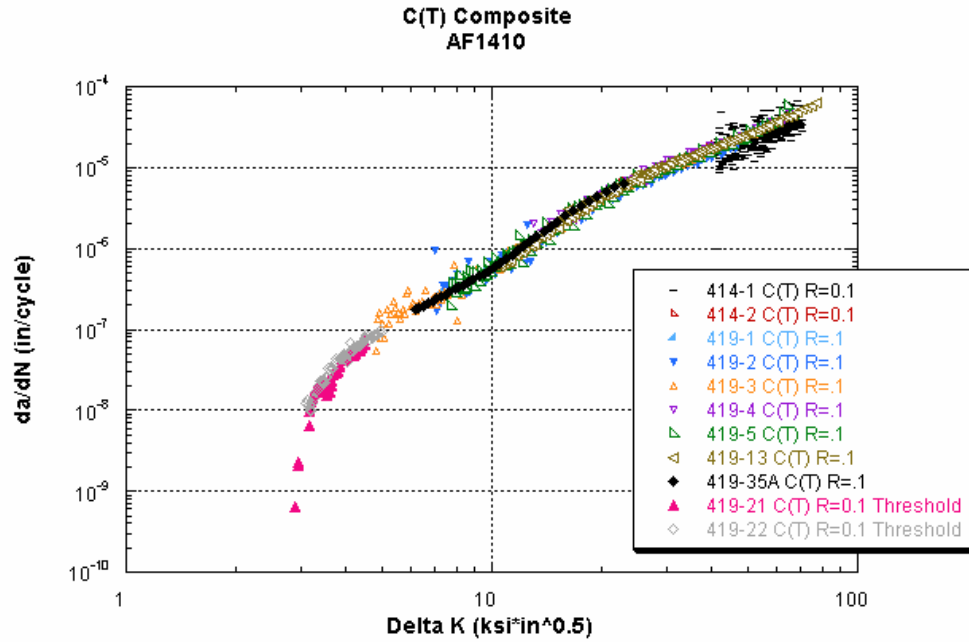


Figure 4.1.7-3. Fatigue Crack Growth Rate Tests for AF1410 Steel in Ambient Laboratory Air with a Load Ratio of 0.1 Using C(T) Specimens

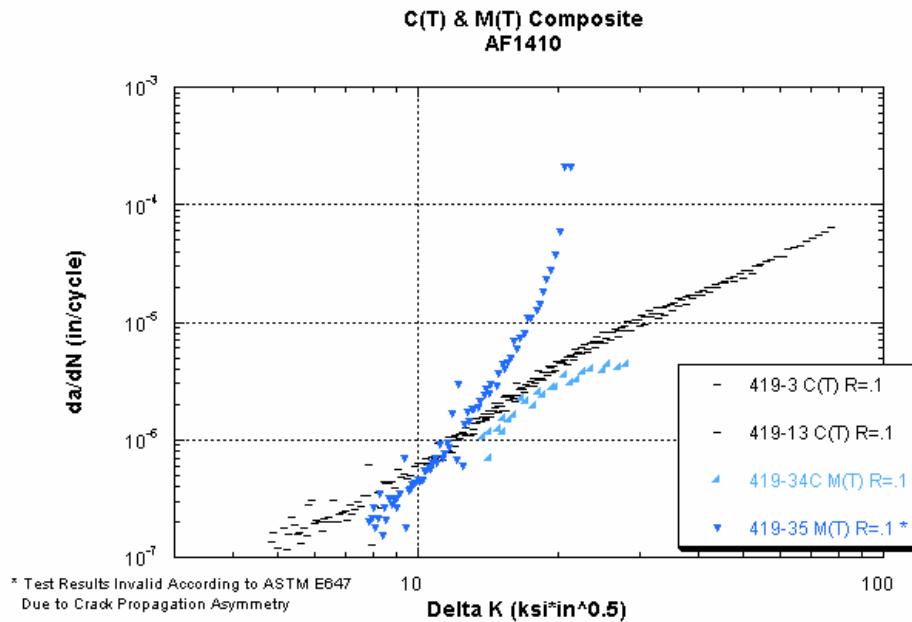


Figure 4.1.7-4. Fatigue Crack Growth Rate Tests for AF1410 Steel in Ambient Laboratory Air with a Load Ratio of 0.1 Using C(T) and M(T) Specimens

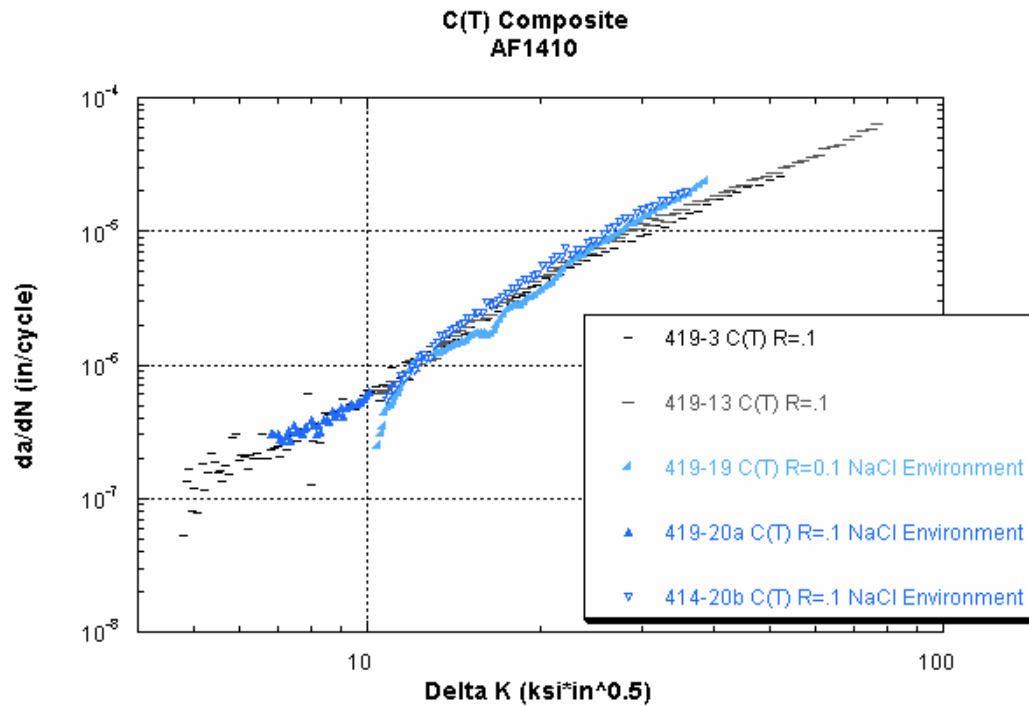


Figure 4.1.7-5. Fatigue Crack Growth Rate Tests for AF1410 Steel in Ambient Laboratory Air or in a High-Humidity and NaCl Environment with a Load Ratio of 0.1 Using C(T) Specimens

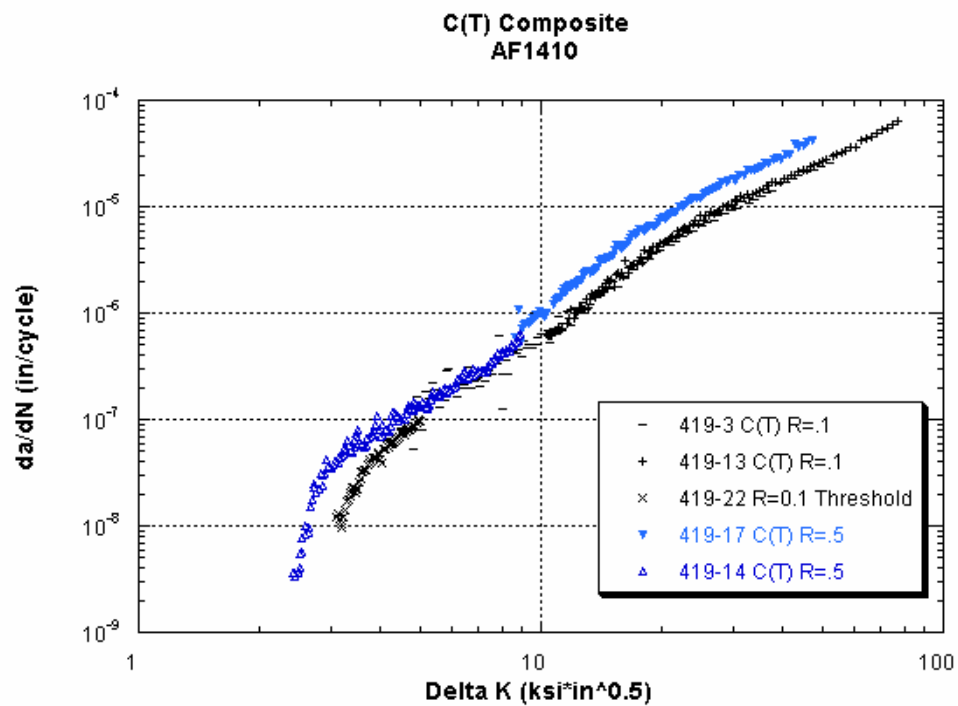


Figure 4.1.7-6. Fatigue Crack Growth Rate Tests for AF1410 Steel in Ambient Laboratory Air Comparing Load Ratios of 0.1 and 0.5 Using C(T) Specimens

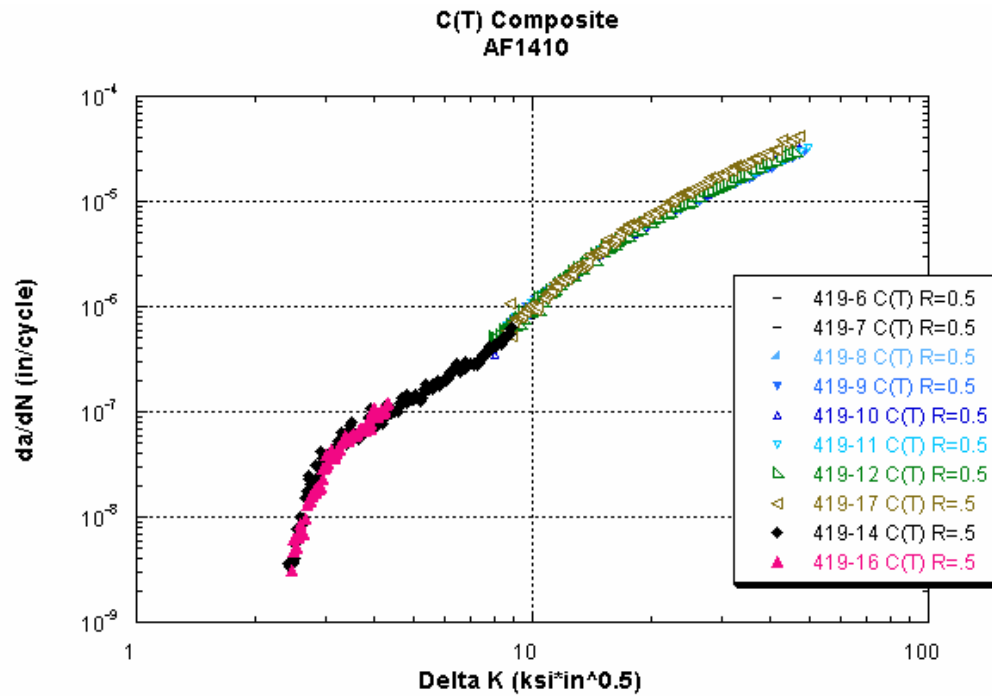


Figure 4.1.7-7. Fatigue Crack Growth Rate Tests for AF1410 Steel in Ambient Laboratory Air with a Load Ratio of 0.5 Using C(T) Specimens

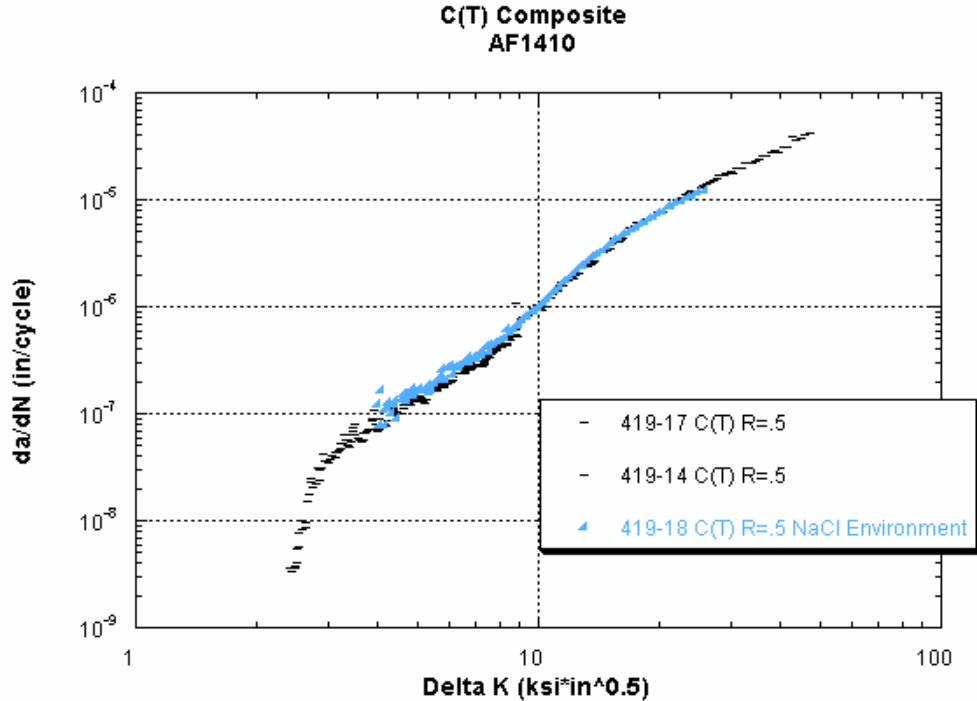


Figure 4.1.7-8. Fatigue Crack Growth Rate Tests for AF1410 Steel in Ambient Laboratory Air or in a High-Humidity and NaCl Environment with a Load Ratio of 0.5 Using C(T) Specimens

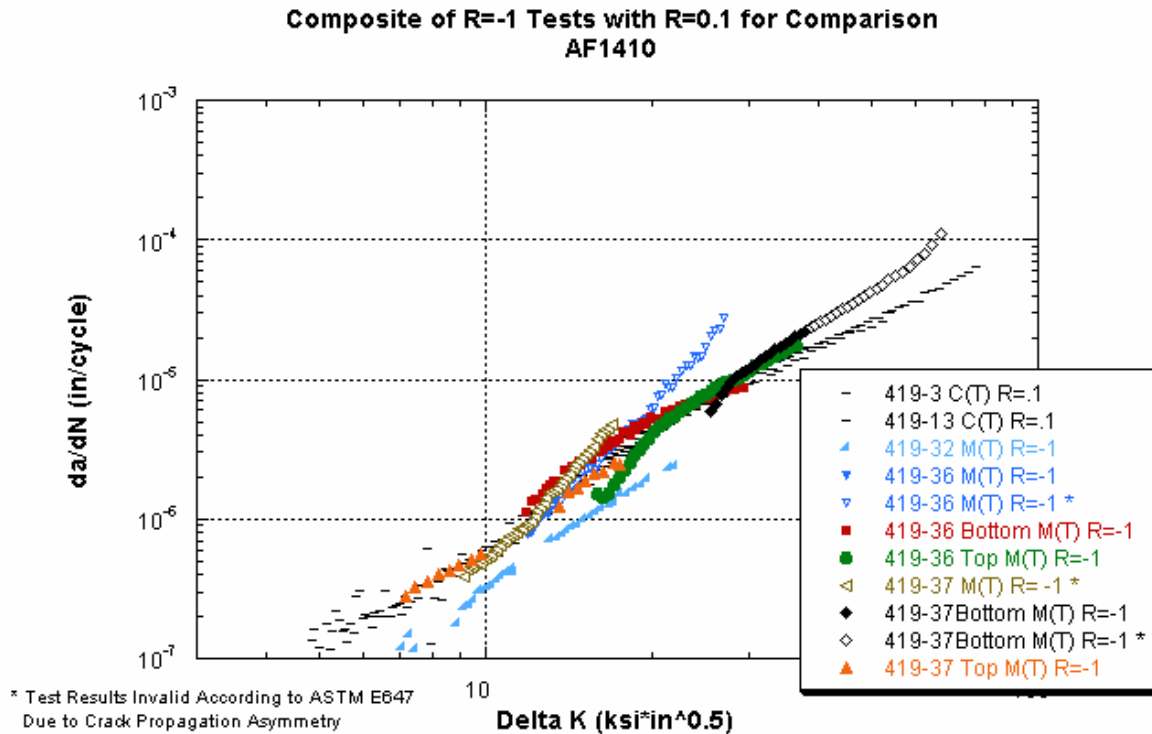


Figure 4.1.7-9. Fatigue Crack Growth Rate Tests for AF1410 Steel in Ambient Laboratory Air Comparing Load Ratios of 0.1 and -1 Using C(T) and M(T) Specimens

4.2 Supportive Studies and Investigations

Various studies were performed to support the corrosion-fatigue tests. These studies are described in following sections.

4.2.1 Corrosion Growth Methods and Time of Exposure Study

Several different exposure methods were explored for growing corrosion on fatigue test specimens that would meet test plan requirements. The ideal method would create corrosion damage that:

- 1) Can be controlled to various levels in terms of surface roughness (above the amount of roughness inherent to the fatigue specimen surface finish) in a consistent manner.
- 2) Has a similar roughness to the application of interest.
- 3) Is limited to a small defined area on one surface of the gage section of the fatigue test specimens.
- 4) Is created using accelerated means, so as to limit incubation times required to achieve desired amounts of corrosion.

During the test plan development, the requirement stated in (2) – that the corrosion should have a similar roughness to the application of interest – was considered carefully. Although it might be ideal to simulate the corrosion in the arrestment shank, it was beyond the scope of this effort. Simulating the corrosion found in the application field components would require their removal from service following different lengths of time in service. The logistics and practicality of performing that study, as well as the expected randomness of the results, would make it difficult to meet the program objectives. However, without extensive studies of fielded parts, it can be estimated that the mechanism and type of corrosion in the arrestment shank in the area of interest (the upper attachment point) is driven by multiple complicating factors including the plating on the surface of the material, wear damage, and physical crevices. Potentially, these issues would also complicate the ability to perform the basic research and meet the requirements stated in (1), (3), and (4) needed to develop the relationship between surface topography and fatigue behavior. Therefore, the means to grow corrosion of the kinds that were explored in this study were limited to standard or other controlled laboratory techniques². A limited number of fielded components were then to be used for comparison purposes to evaluate the roughness and severity of the corrosion grown using laboratory techniques.

The laboratory methods for growing corrosion explored included salt fog, alternate immersion, and several alternative techniques on bare material samples of the high-strength steels of interest.

Salt Fog

Boeing had previously studied corrosion-fatigue interaction on AF1410 using salt fog exposure where the time of exposure and salt solution pH were varied to create different levels of corrosion damage. It was decided that the corrosion studies on this program should springboard off the conclusions from Boeing's previous study. Collectively, the team (including NAVAIR, UDRI, Boeing, and ESRD) on this program revisited the procedures and results of the previous study and made some conclusions on several key issues regarding the technique used for accelerated corrosion.

² A small number of plated specimens that are subsequently corroded will be included in the second set of AF1410 fatigue tests in an attempt to verify that the model actually accounts for the types of corrosion found in real arrestment shanks.

In the Boeing study, specimens were exposed to neutral salt fog or salt fog plus SO₂ (with a lower pH) for different exposure times. The specimens were prepared such that a small rectangular area (with rounded corners) within the gage section of each fatigue test specimen was exposed, while the rest of the specimen was masked and remained pristine during the salt fog exposure. The corrosion damage that was created with a neutral salt solution for different lengths of time, namely 24 hours, 50 hours, and 100 hours, did not show measurable differences in the roughness measurements as taken using laser profilometry. UDRI made some limited measurements using a mechanical stylus profilometer that did show some differences in the surface roughness. However, the amount of roughness for the lower times are very similar to the roughness of the as-machined and grit-blasted surfaces of the specimens. See the profilometry data in Table 4.2.1-1.

Table 4.2.1-1. Comparison of Profilometer Data Results

Specimen #	Boeing Laser Profilometer Results						UDRI Profilometer Results	
	Ra			RMS			Ra range	RMS avg
	Area 1	Area 2	Area3	Area 1	Area 2	Area3		
24-3 (24hrs)	1.2008	1.2783	1.6163	1.7220	1.7783	2.2678	1.21 - 2.68	2.69
24-7 (24hrs)	1.4882	1.4714	1.3835	2.0869	2.0156	1.8573	1.42 - 2.75	2.72
2-1 (50hrs)	1.6498	1.5907	1.4960	2.2199	2.0725	1.9365	1.52 - 2.97	2.99
2-3 (50hrs)	1.3382	1.2234	1.2683	1.7692	1.6324	1.7154	1.27 - 3.59	3.61
4-8 (100hrs)	2.0312	1.6158	2.0399	2.7893	2.3358	2.7332	2.19 - 7.54	6.90
4-11 (100hrs)	1.2635	1.2371	1.2161	1.8730	1.8160	1.9097	—	—
100-6 (100hrs SO2)	0.9516	1.1187	1.0595	1.2614	1.5818	1.4370	1.04 - 3.86	2.85

It was also concluded from the neutral salt fog time-of-exposure tests, that there was no significant affect from the corrosion on the fatigue life of the AF1410 material outside the scatter of the baseline testing. There may have been an effect by the 100-hour neutral salt exposure, but it was also really within the baseline scatter. See Figures 4.2.1-1 and 4.2.1-2 for plots that show the fatigue life for the different exposures. In addition, a study of the failure locations of the specimens showed that only about 21% of the specimens exposed to neutral salt fog failed due to a crack that originated within the corroded region. Approximately 15% of the specimens tested failed due to an anomaly located at the corrosion region edge and 64% of the specimens exposed to neutral salt fog failed outside the corroded region. See Figure 4.2.1-3 for examples of the fractures in the three regions – outside the corroded region, within the corroded region, and at the corroded region edge. From this evidence, it was concluded that there was no measurable relationship between corrosion level and fatigue life as created by time-of-exposure with this salt fog method.

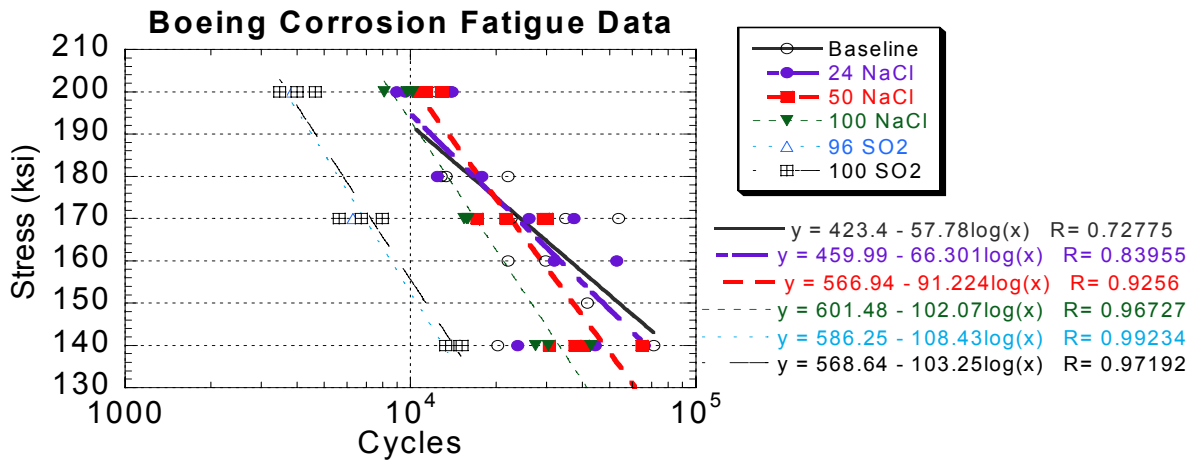


Figure 4.2.1-1. Boeing Corrosion Fatigue Data, Stress vs. Cycles

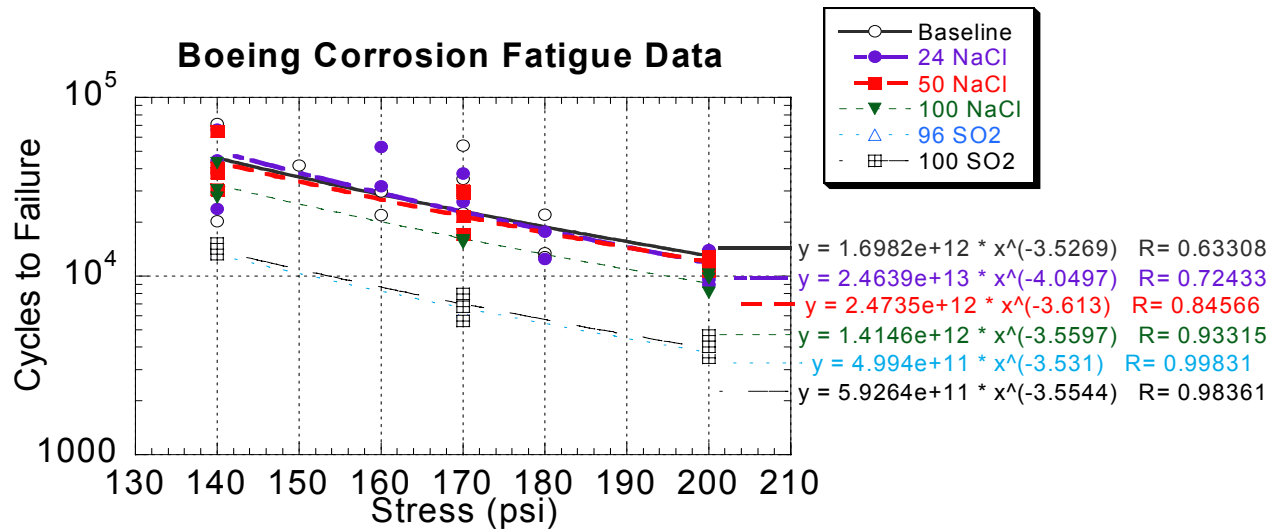


Figure 4.2.1-2. Boeing Corrosion Fatigue Data, Cycles vs. Stress

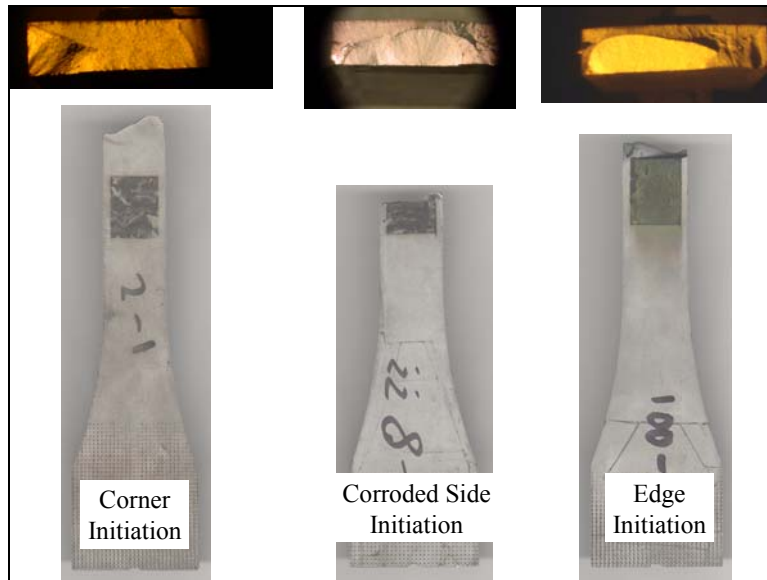


Figure 4.2.1-3. Boeing Corrosion Fatigue Specimens: Examples of Fractures (a) outside the corroded region, (b) within the corroded region, and (c) at the corroded region edge

Unlike the neutral salt fog exposure, the salt fog plus SO_2 (lower pH) exposure did seem to have an effect on the fatigue life. Refer to the plots in Figures 4.2.1-1 and 4.2.1-2. However, 100% of these specimens failed at the edges of the rectangular corroded areas. Thus, the stress concentration (k_t) at the corroded edge of these specimens was high enough to induce premature failure at those locations. Profile measurements and cross-section studies of the failures at the corrosion area edges showed that there was significant corrosion attack around the perimeter of the corroded area as compared to the interior of the corroded area. This accelerated attack made what will be referred to as a “trench” around the perimeter. See Figure 4.2.1-4 for an example of a profile measurement starting in the non-corroded region and scanning across into the corroded region of specimen 100-6 (100 hrs of salt fog + SO_2 exposure). The trench on this specimen is over 60 microns deep. Figure 4.2.1-5 shows an image taken of a cross-section made of specimen 100-9 (100 hrs of salt fog plus SO_2 exposure). The trench on this specimen is close to 100 microns deep.

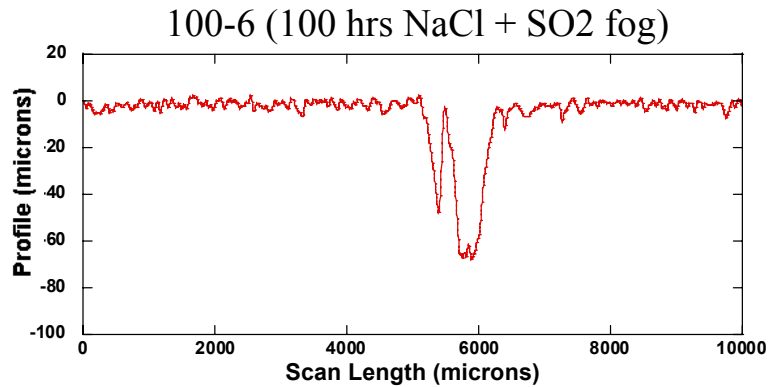


Figure 4.2.1-4. Profile of Boeing Fatigue Specimen 100-6 Scanned from the Non-Corroded Region into the Corroded Region Showing the “Trench” at the Interface

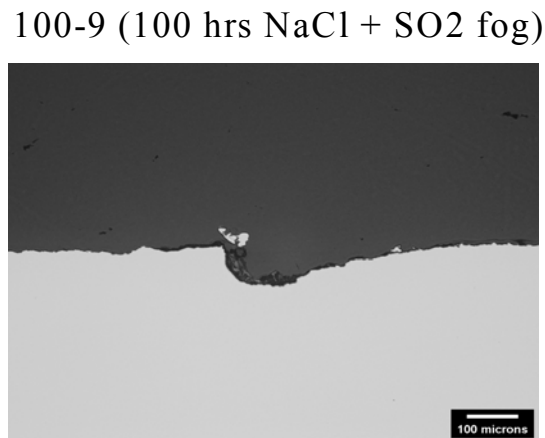


Figure 4.2.1-5. Cross-Section Image of Boeing Fatigue Specimen 100-9 Showing the “Trench” at the Interface Between the Non-Corroded Region and the Corroded Region

The use of the masking in conjunction with the accelerated method of attack was concluded to be the cause of the accelerated attack that formed the trench on the Boeing fatigue specimens. It is possibly a form of undercutting from a crevice or from a local anodic region set up by oxygen depletion. It should also be noted that the corrosion damage in the interior of the corroded region from the salt fog plus SO₂ was actually less rough than the neutral salt fog exposures. This observation is apparent in Table 4.2.1-1. Boeing measurements also revealed this fact concerning roughness.

On this program, NAVAIR initially exposed some small samples of AF1410 to neutral salt fog for longer exposure times than those in the Boeing study to determine the extent of corrosion formed.

The exposure times used were 168 hours and 312 hours. See Figures 4.2.1-6 and 4.2.1-7, respectively, for photographs of samples from this experiment. In this case, a masking was applied around the perimeter of the specimens in order to expose only a defined region on the surface, as Boeing did, and as would be required on a fatigue test specimen.

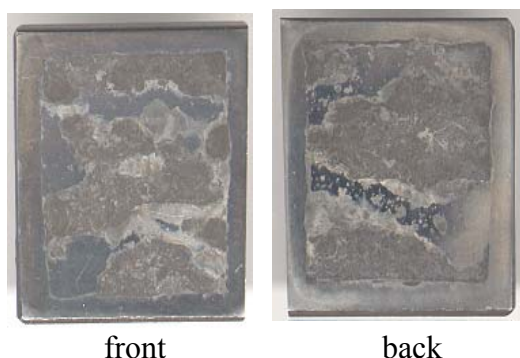


Figure 4.2.1-6. Specimen Provided by NAVAIR Exposed for 168 Hours of Neutral Salt Fog Exposure (approximate specimen dimensions: 1" □ 1.5")



Figure 4.2.1-7. Specimen Provided by NAVAIR Exposed for 312 Hours of Neutral Salt Fog Exposure (approximate specimen dimensions: 1" □ 1")

UDRI took a limited number of measurements from the corroded regions of these NAVAIR samples using a mechanical stylus profilometer. An example of one line of profile data from each specimen is shown in Figures 4.2.1-8 and 4.2.1-9, respectively. The statistics calculated from a total of 10 lines of profile data from each are also shown in the figures. It was concluded that, after 168 hours of salt fog exposure, the amount of surface roughness measured was similar to the typical roughness of the grit-blasted surface finish to be used for the corrosion-fatigue tests. The surface of the corrosion after 312 hours of exposure did have a greater average roughness than the expected fatigue specimen surface. Unfortunately, it was also determined that masking on the 312-hour exposure samples might have caused the same undercutting as seen on the salt fog plus SO₂-exposed specimens in the Boeing study. Profile data taken across the masked edge on the NAVAIR-exposed salt fog specimens are shown in Figures 4.2.1-10 and 4.2.1-11 for specimens exposed to 168 and 312 hours, respectively. These figures illustrate the large corrosion feature at the interface between the non-corroded and corroded areas of the specimen exposed for 312 hours. No such feature is evident for 168 hours of exposure.

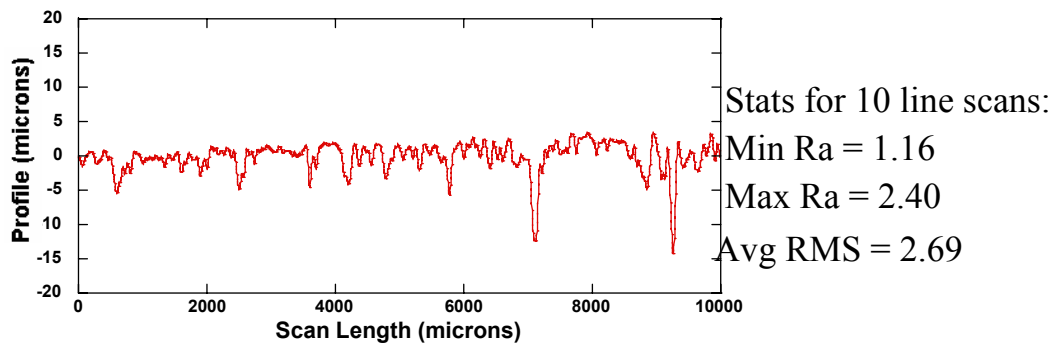


Figure 4.2.1-8. Example Line Scan in the Corroded Region of the Specimen Exposed for 168 Hours

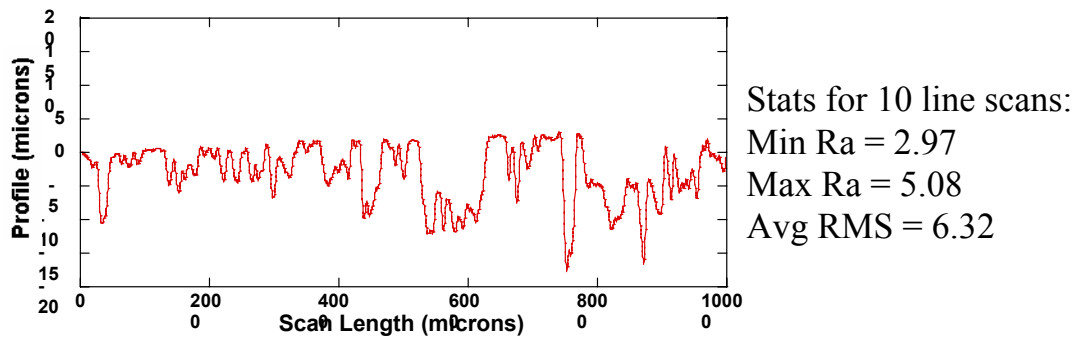


Figure 4.2.1-9. Example Line Scan in the Corroded Region of the Specimen Exposed for 312 Hours

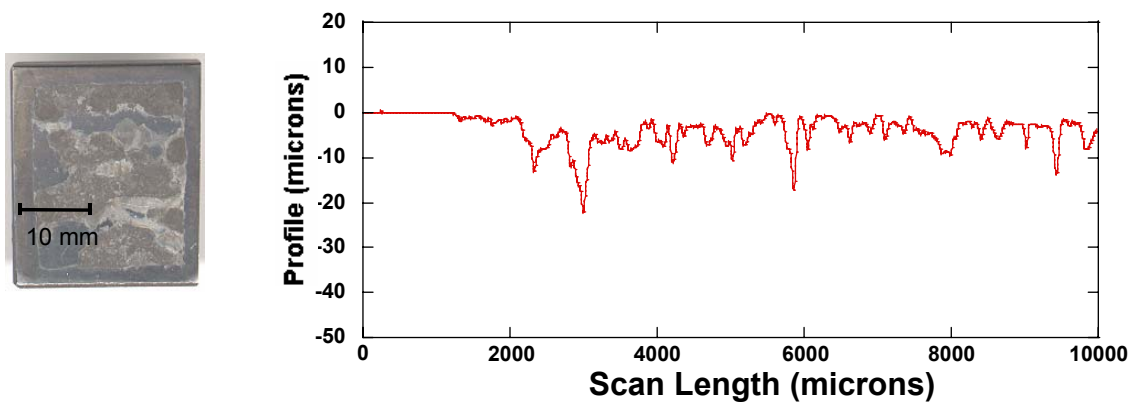


Figure 4.2.1-10. Example Line Scan from the Non-Corroded Region to Within the Corroded Region of the Specimen Exposed for 168 Hours

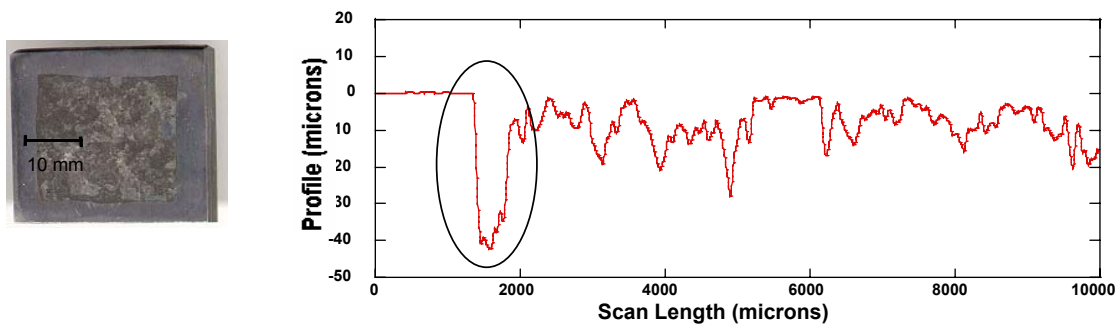


Figure 4.2.1-11. Example Line Scan from the Non-Corroded Region to Within the Corroded Region of the Specimen Exposed for 312 Hours

Alternate Immersion

In parallel to the NAVAIR salt fog studies, an alternate immersion technique was tested in order to determine if different amounts of roughness could be consistently produced based on time of exposure and if there were any effects of using masking. A number of test wafers of AF1410 were tested for 20 days, 40 days, and 60 days, respectively. Acrylic enamel (nail polish) was used to mask material so that only a rectangular area on the front and back surfaces was exposed. During one cycle of exposure, the specimens were immersed for 10 minutes in a 3.5% salt solution at ambient temperature and allowed to dry for 50 minutes of every hour. The exposure cycles continued 24 hours a day.

The alternate immersion test demonstrated that successfully masking an isolated area for alternate immersion exposure is more difficult than for salt fog exposure. The masking failed on each specimen tested by UDRI. Example photographs of specimens after 20, 40, and 60 days of exposure are shown in Figure 4.2.1-12. In the figures, each image on the left shows the respective specimen in the as-corroded condition, and each image on the right shows each respective corroded specimen after it had been cleaned of the oxides. The masking did leave an isolated area on the 20-day exposure sample, but not on the 40- and 60-day exposure samples.

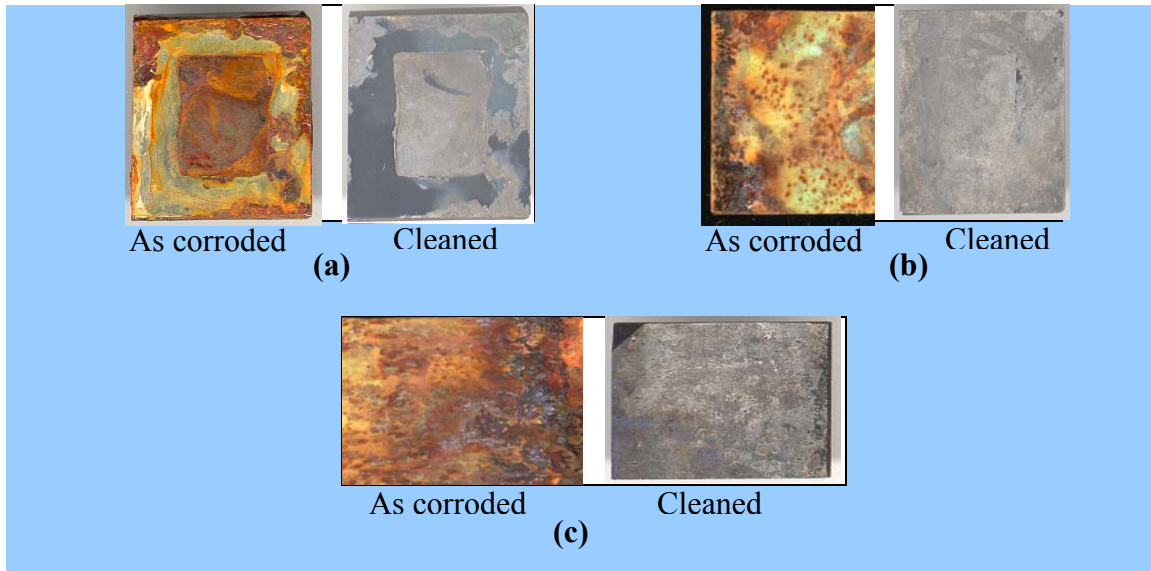


Figure 4.2.1-12. Alternate Immersion Specimen Exposed for: (a) 20 days, (b) 40 days, and (c) 60 days (approximate specimen dimensions: 1" □ 1.5")

Profile data were taken on the 20-day exposure wafer to see if the sample showed signs of undercutting at the masking when the masking was effective. Example data are shown in Figure 4.2.1-13. For the 20-day exposure, it did not appear that there was accelerated attack at the interface.

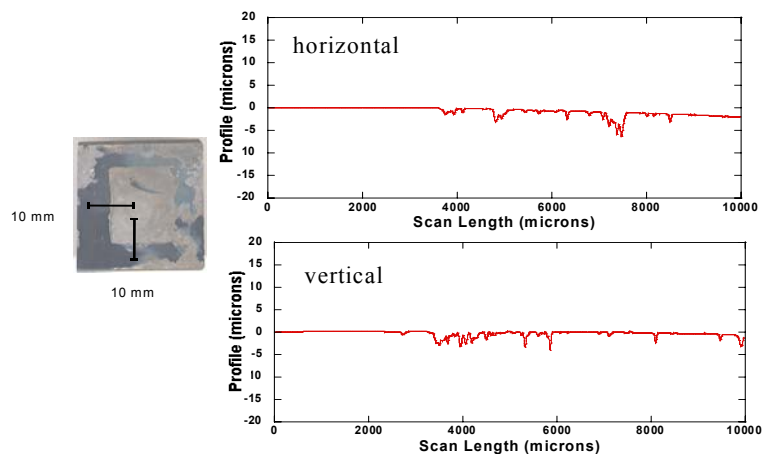


Figure 4.2.1-13. Example Line Scan from the Non-Corroded Region to Within the Corroded Region of the Alternate Immersion Specimen Exposed for 20 Days

Different types of masking were investigated in addition to the acrylic enamel, including water-proof tape and beeswax. The beeswax was the most successful during a 20-day exposure. A photo of the specimen masked with beeswax, exposed to alternate immersion for 20 days and cleaned of the corrosion by-products is shown Figure 4.2.1-14. The beeswax method of masking was not tested for longer times-of-exposure. Profile data taken on the beeswax sample was inconclusive as to whether it caused undercutting at the interface but cross sections did not show it to be problematic for the wafer tested.



Figure 4.2.1-14. Wafer Masked Off with Beeswax and Exposed for 20 Days of Alternate Immersion (approximate specimen dimensions: 1.5" □ 1")

Profile measurements from the corrosion on the 20-, 40- and 60-day exposure wafers showed that different amounts of surface roughness can be created fairly consistently based on time of exposure. Examples of data from each exposure are shown in Figures 4.2.1-15, 4.2.1-16, and 4.2.1-17. Several statistics that describe the surface roughness from a total of 20 line scans from each test wafer were calculated and shown in the respective figures. The results show that different amounts of roughness due to corrosion can be achieved but only the longer exposures provide surfaces more rough than the as-machined and grit-blasted surfaces expected on the fatigue test specimens.

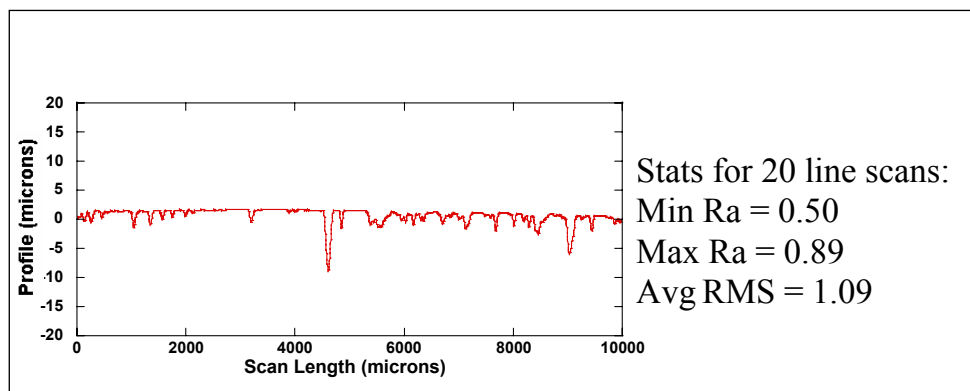


Figure 4.2.1-15. Example Line Scan Within the Corroded Region of Specimen Exposed to 20 Days of Alternate Immersion

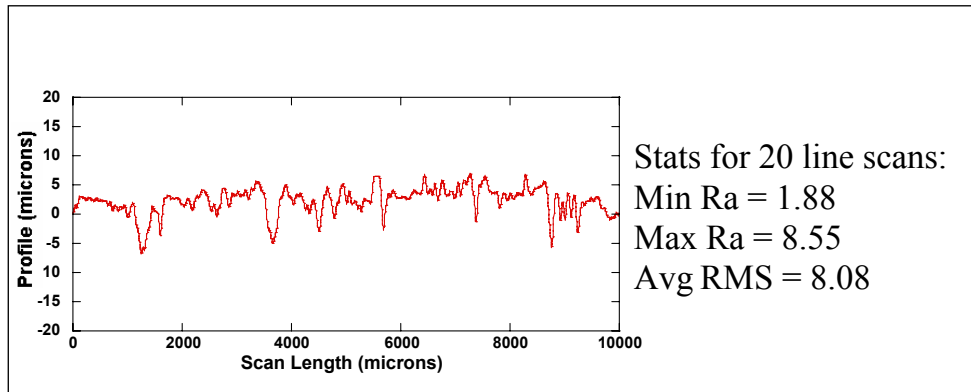


Figure 4.2.1-16. Example Line Scan Within the Corroded Region of Specimen Exposed to 40 Days of Alternate Immersion

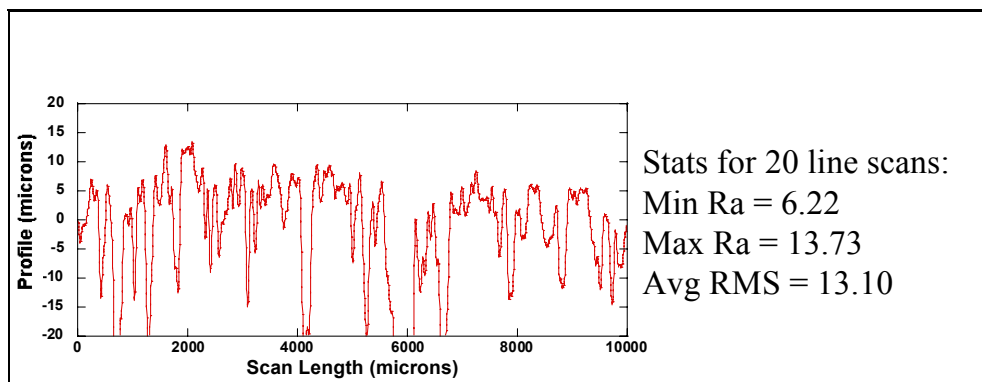


Figure 4.2.1-17. Example Line Scan Within the Corroded Region of Specimen Exposed to 60 Days of Alternate Immersion

Alternative Techniques

Due to the issues with masking and undercutting, low levels of corrosion, and long exposure times with the salt fog and alternate immersion techniques, several alternative methods were explored for creating corrosion that meets the requirements of the test plan. One alternative method was to use filter paper soaked in 3.5% salt solution to create a fairly controlled area of corrosion on a sample without the use of masking material. The key is to frequently remove the filter paper, dry the specimen and replace the filter paper with a newly soaked piece. This cycling replenishes the area to be corroded with new solution and air supply and should inherently change the placement of the paper slightly. This slight misplacement helps to keep the sharp edge or undercutting from forming. A number of trials examined how the filter paper could be used. Figure 4.2.1-18 shows a photograph of the different scenarios tested. The different trials are described to the right in the figure.

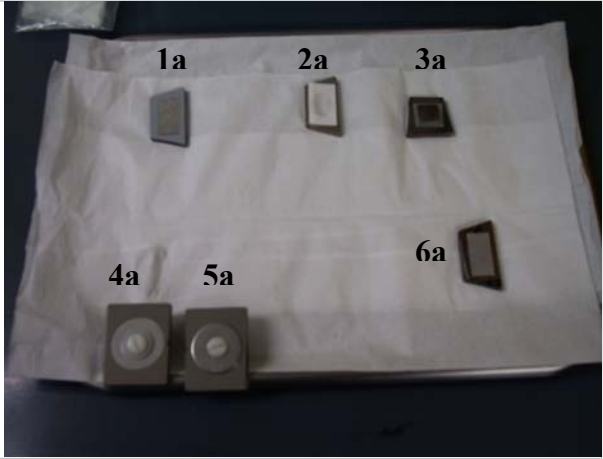
	1a – “Control Specimen” – This specimen is masked around the perimeter with paint and is to be used to compare to the masked corrosion wafers exposed to salt fog or alternate immersion.
	2a – A dry filter paper was placed on the specimen and salt solution dropped into the middle to test ability to force a corrosion pattern within the filter paper.
	3a – A wet filter paper was placed on a specimen and a piece of material, smaller than the filter paper, was centered on top. This was to limit the air exposure (crevice) in the center and to see if the block edges act like masking edges and cause the undercutting.
	4a – A wet disk-shaped filter paper was placed over a center-hole specimen, with a washer on top bolted onto the specimen. This setup was to test limited air exposure (crevice) – in this case the filter paper is partially outside of washer
	5a – A wet disk shaped filter paper was placed over a center-hole specimen, with a washer on top bolted onto the specimen. This set up was to test limited air exposure (crevice) – in this case the filter paper was completely covered by the washer.
	6a – This specimen had a wet filter paper placed on top – no masking or crevice.

Figure 4.2.1-18. Samples Exposed with Filter Paper Soaked in 3.5% Salt Solution Using the Different Methods Shown

The most successful scenario was #5a, where a crevice was created with a washer. The sample shown in #5a was tested for 8 hours per day for five business days. The filter paper was changed with new paper soaked in the salt solution every hour. The results showed no real evidence of an issue with undercutting at the filter paper interface, but there was also only a small amount of corrosion created. See Figure 4.2.1-19 for an example of the profile data taken from this specimen. This test also showed that a specimen with a center hole could be corroded without corrosion developing within the hole.

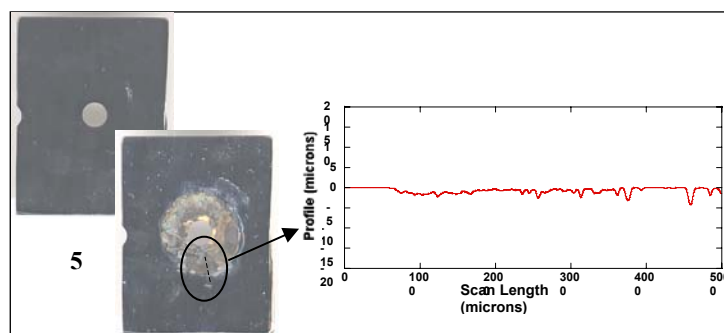


Figure 4.2.1-19. Profile Data Taken from Sample #5a Exposed to 40 Cycles of Filter Paper Replacement

A similar test was done for 90 cycles. In this test, two circular pieces of filter paper were placed at the 3 o'clock and 9 o'clock positions around the center hole. A washer secured with a bolt was used to create a crevice. A new piece of filter paper soaked in the salt solution was applied every hour for 8 hours a day. The exposure concluded after approximately 12 business days. The results showed that the corrosion measured using profilometry did become rougher with an increased number of cycles and still without an undercutting problem. An example of the profile data taken from this sample is shown in Figure 4.2.1-20.

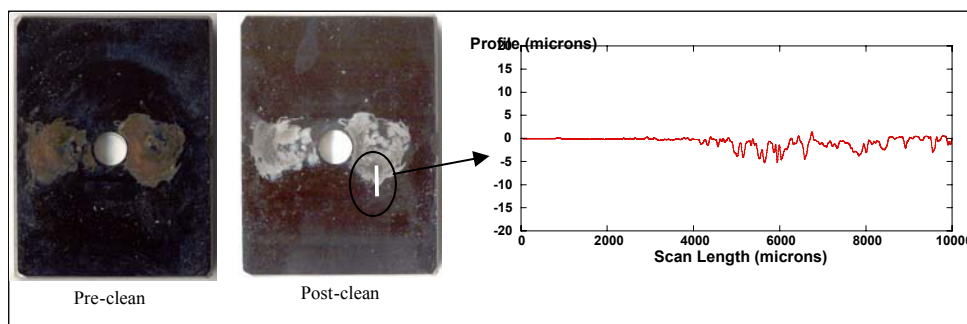


Figure 4.2.1-20. Profile Data Taken from a Sample Exposed to 90 Cycles of Filter Paper Replacement

The next method tested continued to use the filter paper technique, but with an applied voltage in order to accelerate the process. The goal was to consistently impart appropriate amounts of corrosion in a matter of hours, rather than days or weeks. The method employed to grow corrosion consists of soaking filter paper in a salt solution (3.5% NaCl), which is centered on the specimen to be corroded. A flat AF1410 wafer acts as an electrode, which is placed on top of the filter paper (the wafer is larger than the filter paper). A voltage source is connected to the electrode and to the specimen with the proper polarity to bias the direction of the reaction. The size of the filter paper and resistors in the circuitry are chosen to achieve the current desired for the voltages used. See Figure 4.2.1-21 for a diagram of the setup.

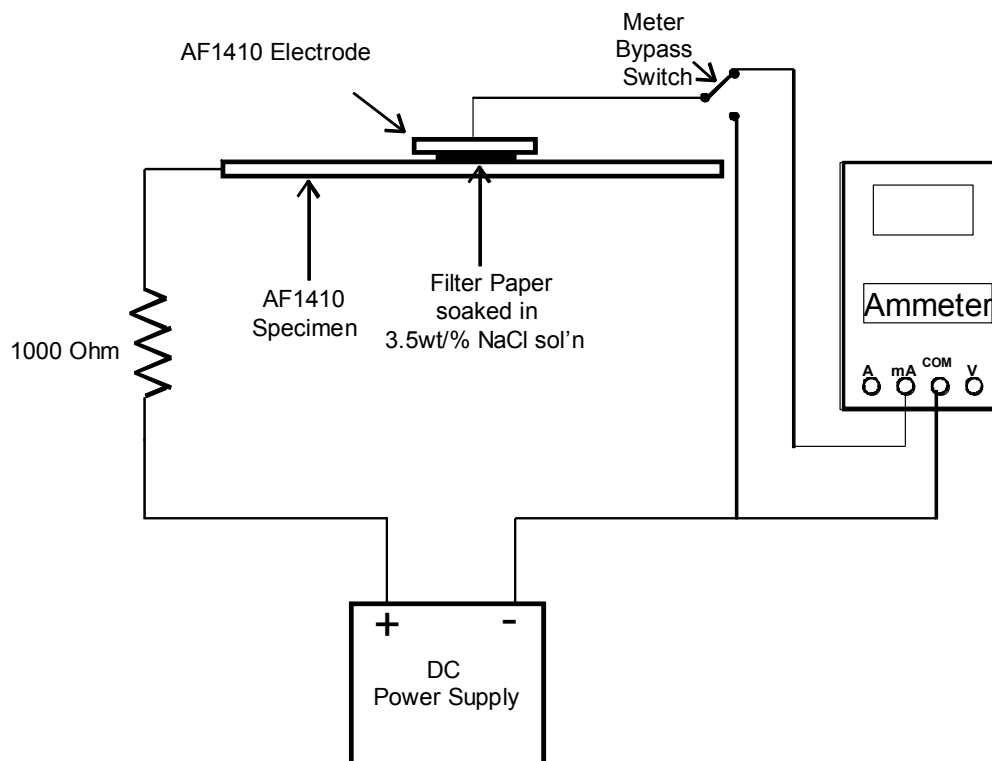


Figure 4.2.1-21. Schematic Diagram of the Test Setup for Accelerated Corrosion Testing with a Piece of Soaked Filter Paper

Results of testing showed that current density, wetness of the filter paper, and the number of interruptions incorporated into this process are key to the amount of roughness created and to preventing undercutting at the filter paper interface. The current density that was chosen for the finalized exposure setup was 2 mA/cm^2 . Examples of data taken on samples exposed to 2 mA/cm^2 for a total of 240 minutes (4 hours) are shown in Figure 4.2.1-22.

The plots on the left show profile data from a sample exposed without interruptions and the plots on the right show data from a sample whose exposure was interrupted and the filter paper replaced 5 times. The upper plots are from the edge of the corrosion patch and the lower plots are from the center. The exposure that was not interrupted created severe undercutting at the filter paper edge, observable thickness loss, but a fairly smooth corroded surface. The exposure that was interrupted did not show evidence of undercutting, but showed observable thickness loss and a rough surface.

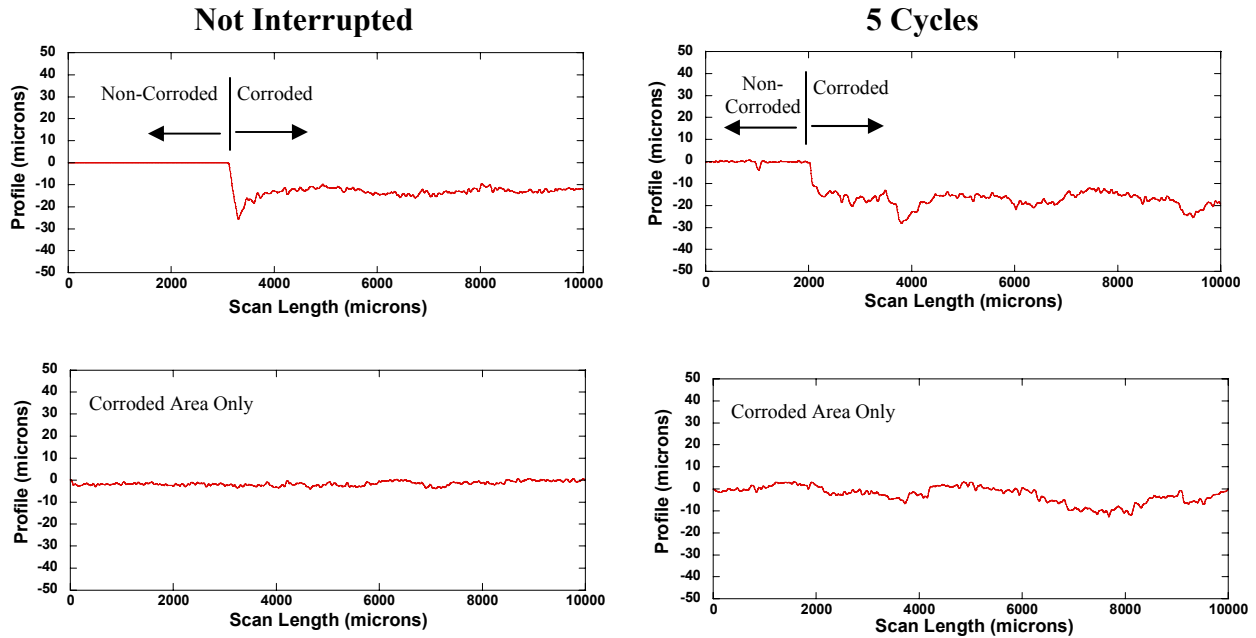


Figure 4.2.1-22. Data Taken on Samples Exposed to 2 mA/cm^2 for a Total of 4 Hours

The alternative method of growing corrosion using filter paper soaked in 3.5% salt solution with the bias voltage was found to be a viable technique to meet the requirements for corrosion grown on fatigue test specimens. This method was used in further tests to determine the appropriate exposure times to achieve measurably different amounts of corrosion for testing under fatigue.

Time-of-Exposure Study:

Tests were performed to determine the appropriate durations for exposure in order to produce corrosion with desirable amounts of surface roughness. The goal was to look at three levels of corrosion that may represent mild, moderate, and severe corrosion. The mild corrosion should be measurable above the surface roughness of the specimen's surface finish. The underlying assumption in the test plan is that the fatigue life should show a dependence on the level of corrosion. Time-of-exposure tests were conducted on test wafers and then a few initial sets of corrosion-fatigue specimens in order to determine if the amounts of surface roughness have effects on fatigue. Ultimately, it was determined that exposures performed for a total of 3, 6, and 12 hours provide appropriate amounts of surface roughness. The 3-, 6-, and 12-hour exposures were broken into cycles as shown in Tables 4.2.1-2, 4.2.1-3, and 4.2.1-4, respectively.

Table 4.2.1-2. Three-Hour Exposure Procedure

Cycle	Exp Time (min)	Total Time (min)	Filter Paper Diameter (in)	Voltage (V)	Current (mA)	Current Density (mA/in²)
1	1	1	0.875	7.66	7.66	~12.74
2	1	2	0.875	7.66	7.66	~12.74
3	8	10	0.875	7.66	7.66	~12.74
4	10	20	0.875	7.66	7.66	~12.74
5	40	60	0.9375	8.79	8.79	~12.74
6	60	120	1	10	10	~12.74
7	60	180	1.0625	11.29	11.29	~12.74

Table 4.2.1-3. Six-Hour Exposure Procedure

Cycle	Exp Time (min)	Total Time (min)	Filter Paper Diameter (in)	Voltage (V)	Current (mA)	Current Density (mA/in²)
1	1	1	0.875	7.66	7.66	~12.74
2	1	2	0.875	7.66	7.66	~12.74
3	8	10	0.875	7.66	7.66	~12.74
4	10	20	0.875	7.66	7.66	~12.74
5	40	60	0.875	7.66	7.66	~12.74
6	60	120	0.9375	8.79	8.79	~12.74
7	120	240	1	10	10	~12.74
8	120	360	1.0625	11.29	11.29	~12.74

Table 4.2.1-4. Twelve-Hour Exposure Procedure

Cycle	Exp Time (min)	Total Time (min)	Filter Paper Diameter (in)	Voltage (V)	Current (mA)	Current Density (mA/in²)
1	1	1	0.875	7.66	7.66	~12.74
2	1	2	0.875	7.66	7.66	~12.74
3	8	10	0.875	7.66	7.66	~12.74
4	10	20	0.875	7.66	7.66	~12.74
5	40	60	0.875	7.66	7.66	~12.74
6	60	120	0.875	7.66	7.66	~12.74
7	60	180	0.875	7.66	7.66	~12.74
8	60	240	0.9375	8.79	8.79	~12.74
9	120	360	0.9375	8.79	8.79	~12.74
10	120	480	1	10	10	~12.74
11	60	540	1	10	10	~12.74
12	60	600	1.0625	11.29	11.29	~12.74
13	120	720	1.0625	11.29	11.29	~12.74

Time of Exposure Results

Characterization of the corrosion formed from the time-of-exposure tests on the test wafers are presented in this section. Fatigue test results that correspond to the three different levels of corrosion are presented in section 4.3 of this report.

Test wafer AF1410-3hr was exposed using the cycle conditions outlined for the 3-hour exposure (listed in Table 4.2.1-2). This test wafer came from one of the radius sections of an AF1410 fatigue test specimen that was tested by, and provided by, Boeing. The wafer was grit-blasted, which was to have given it an approximate average roughness (Ra) between 1 and 1.5 microns. After being corroded, the wafer was cleaned using procedures recommended by Boeing. A digital image of the surface after a 3-hour exposure is shown in Figure 4.2.1-23(a). The corrosion patch is approximately 1.0625" in diameter.

The corroded surface of the specimen was then inspected using both a mechanical stylus and a white-light interferometer (WLI). Data from the stylus profilometer was utilized as a quick "spot check" of the surface in selected locations. The high-resolution depth measurements from the WLI microscope were used for analysis. The height map generated by the WLI microscope for test wafer AF1410-3hr is shown in Figure 4.2.1-23(b). An example line profile of the transition between the non-corroded and corroded surface was taken at approximately the 7 o'clock position with a stylus and is shown in Figure 4.2.1-23 (c). The statistical surface roughness metrics are shown in Table 4.2.1-5. The data show that the statistical metrics used to characterize corrosion that are based on average roughness or volume loss is measurable above the grit-blasted surface. Metrics are defined in Section 4.2.5.

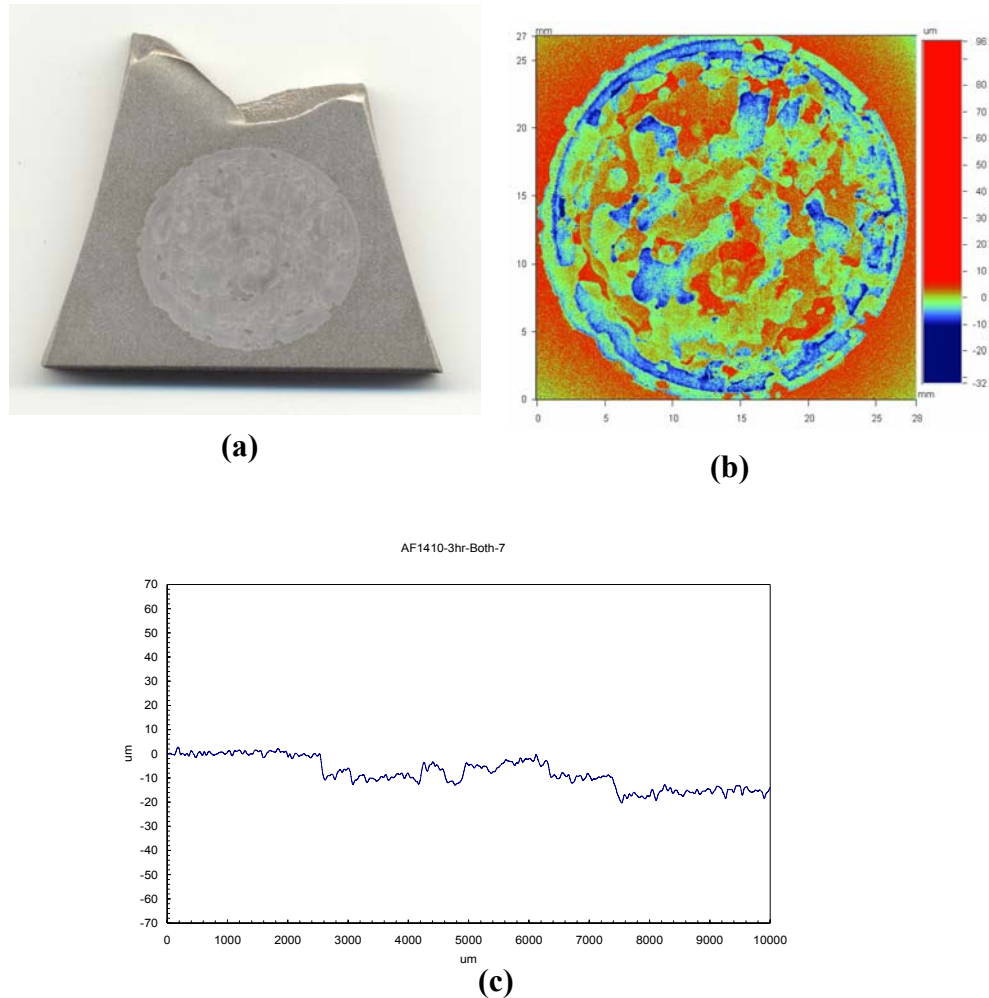


Figure 4.2.1-23. Test Wafer AF1410-3hr: (a) photograph of the corroded surface after 3-hour exposure (the diameter of the corrosion patch is approximately 1.0625"), (b) height map of the corroded surface as measured using the white-light interferometer, and (c) line profile of the transition between the non-corroded and corroded surface taken at approximately the 7 o'clock position with a stylus.

Table 4.2.1-5. Results of WLI Measurement on Specimen AF1410-3hr

Specimen AF1410-3hr	Exposure Time (Hrs.)	Ra	Rq	Rsk	Rku	Rv	Rp	Rt	NVL (cm ³ /m ²)	SD
Corroded surface	3	2.08	2.72	-0.28	6.13	-30.84	94.51	125.35	6.15	2.72
Grit blasted surface	0	1.11	1.55	-1.00	7.79	-24.04	16.03	40.08	4.25	1.55

A limited amount of metallography was performed on the AF1410-3hr wafer to provide a cross-sectional view of the actual corrosion profile. The goal of this study was to determine if the corrosion attack is limited to the topographical features measured by the WLI microscope, or if there

is significant sub-surface attack that might influence the fatigue life. Significant sub-surface effects would not lend itself to the goals of this program. Several micrographs of a cross-section from specimen AF1410-3hr are shown in Figure 4.2.1-24(a) through (f). The first two images, (a) and (b), show two different magnifications at the transition between the grit-blasted (non-corroded) surface and the corroded surface. At the location where this cross-section was taken, there appears to be a reasonable transition between the non-corroded and corroded surfaces, in that it is not steep and there is no undercutting or accelerated attack at the interface.

The next two images in Figure 4.2.1-24(c) and (d) are of the corroded region and of the grit-blasted region (non-corroded), respectively. It can be observed from these images that the size (depth and breadth) of the topographical features from the corrosion after a 3-hour exposure and from grit blasting are similar, which is consistent with the profilometry results; however, there are two important differences to note. The grit-blasted surface features are sharper, or more defined, in comparison. There is also damage from the grit blasting due to material rollover. This damage, coincidentally, has the appearance of corrosion attack – it has a crack-like appearance that tends to undercut the surface. In some cases, this damage is observed within the lighter-corroded areas, but is determined to be the material rollover due to grit blasting and not corrosion. It may be, however, that this damage has influenced the way the corrosion grew on the surface. It should be pointed out that these observations are made on the test wafer, which was grit-blasted in the lab. The material rollover problems are mostly due to changing the direction of the test piece under the blast. It is unknown if this type of damage exists on the Set A corrosion-fatigue specimens.

The last two images in Figure 4.2.1-24(e) and (f) are, again, of the corroded region and of the grit-blasted region (non-corroded region), respectively. In this case, the surfaces were etched with 2% Nital for several minutes in order to reveal the martensitic microstructure. Note that these images were not taken in the same locations as the images in Figures 4.2.1-24(c) and (d). It can be observed from these images that the corrosion does not seem to preferentially ingress along grain boundaries. Instead, it has a general corrosion appearance. During optical inspection, it was also observed that the corrosion attack at the surface does follow laths in the microstructure. The ingress observed is very shallow and is limited to a depth just below the surface. This phenomenon is not evident in these figures due to the quality of the sample preparation and of the images.

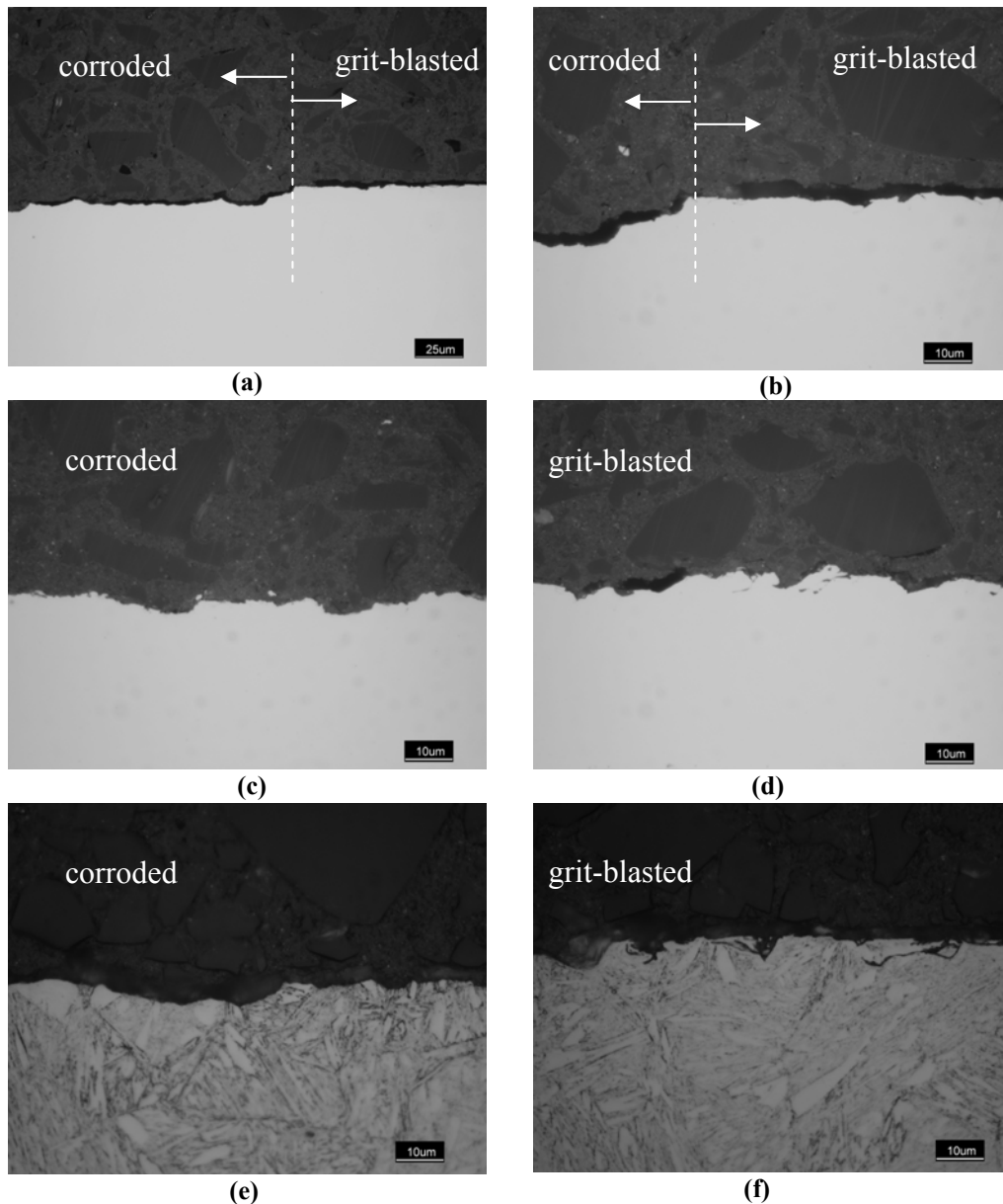


Figure 4.2.1-24. Cross-Section Images of Test Wafer AF1410-3hrs: (a) & (b) are micrographs of the transition region between the corroded and grit-blasted surfaces, (c) & (e) were taken in the corroded region, (d) & (f) were taken in the grit-blasted region. The images in (e) and (f) were taken after the cross-sections were etched in 2% Nital.

Test wafer AF1410-6hr was exposed using the cycles outlined for the 6-hour exposure (listed in Table 4.2.1-3). This test wafer also came from one of the radius sections of an AF1410 fatigue test specimen that was tested and provided by Boeing. The wafer was grit-blasted to give it an approximate average roughness (Ra) between 1 and 1.5 microns. After being corroded, the wafer was cleaned using the procedures Boeing recommended. A digital image of the surface after a 6-hour exposure is shown in Figure 4.2.1-25(a). The corrosion patch is approximately 1.0625" in diameter.

The corroded surface of the specimen was then inspected using both a mechanical stylus and a white-light interferometer. The height map generated by the WLI microscope for test wafer AF1410-6hr is shown in Figure 4.2.1-25(b). An example line profile of the transition between the non-corroded and corroded surface was taken at approximately the 12 o'clock position with a stylus and is shown in Figure 4.2.1-25(c). The statistical analysis for the data is shown in Table 4.2.1-6. The data show that there is an increased level of corrosion in terms of statistical metrics that are based on average roughness or volume loss with the increased time of exposure. It was found that this specimen's non-corroded, but grit-blasted surface is less rough than was targeted by the grit blasting. The Ra, which is less than 0.3, is well below the target range of 1 to 1.5.

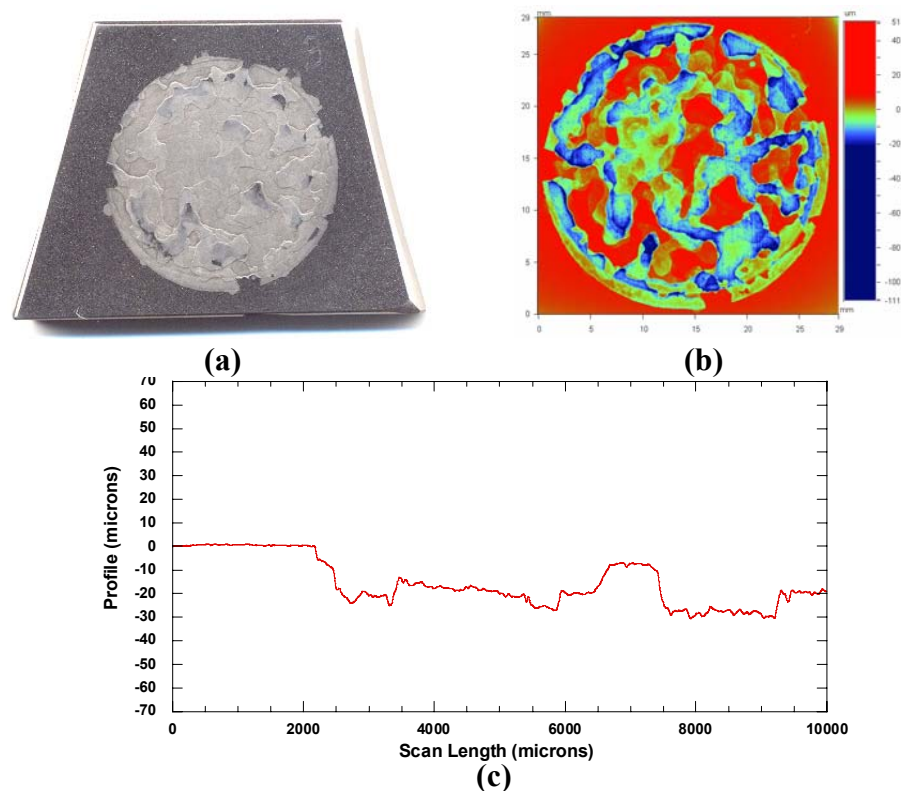


Figure 4.2.1-25. Test Wafer AF1410-6hr: (a) photograph of the corroded surface after the 6-hour exposure (the diameter of the corrosion patch is approximately 1.0625"), (b) height map of the corroded surface as measured using the white-light interferometer, and (c) line profile of the transition between the non-corroded and corroded surface taken at approximately the 12 o'clock position with a stylus.

Table 4.2.1-6. Results of WLI Measurement on Specimen AF1410-6hr

Specimen AF1410-6hr	Exposure Time (Hrs.)	Ra	Rq	Rsk	Rku	Rv	Rp	Rt	NVL (cm ³ /m ²)	SD
Corroded surface	6	3.33	4.64	-0.68	1.57	-102.28	48.45	150.73	9.07	4.64
Grit blasted surface	0	0.26	0.43	4.45	768.2	-39.67	28.98	68.65	2.65	0.40

A limited amount of metallography was performed on the AF1410-6hr wafer to provide a cross-sectional view of the actual corrosion profile. The goal was to determine if the corrosion attack was limited to the topographical features measured by the WLI microscope, or if there is significant sub-surface attack that might influence the fatigue life. Several micrographs of a cross-section from specimen AF1410-6hr are shown in Figure 4.2.1-26. The first two images, (a) and (b), show two different magnifications at the transition between the grit-blasted (non-corroded) surface and the corroded surface. At the location where this cross-section was taken, there appears to be a reasonable transition between the non-corroded and corroded surfaces; the transition is not steep and there is no undercutting or accelerated attack at the interface. As with the 3-hour exposed specimen, the thickness loss (or volume loss) due to corrosion is evident.

The next two images in Figure 4.2.1-26(c) and (d) are of the corroded region and of the grit-blasted region (non-corroded region), respectively. It can be observed from these images that the size of topographical features due to the grit blasting are much smaller than that of the corroded surface, which is consistent with the profilometry results. The damage due to material rollover is still an issue, the damage due to corrosion has a little different look than it did after the 3-hour exposure, and there seems to be less of the small-scale damage and more large-scale features. Small-scale damage might accumulate into larger features. There might also be effects due to the smaller amount of starting grit blast damage on the surface.

The last two images in Figure 4.2.1-26(e) and (f) are, again, of the corroded region and of the grit-blasted region (non-corroded region), respectively. In this case, the surfaces were etched with 2% Nital for several minutes in order to reveal the martensitic microstructure. Note that these images were not taken in the same locations as those in Figures 4.2.1-26(c) and (d). It can be observed from these images that the corrosion does not seem to preferentially ingress along grain boundaries. Instead, it has a general corrosion appearance. During optical inspection, it was also observed that the corrosion attack at the surface does follow laths in the microstructure. The ingress observed is very shallow and is limited to a depth just below the surface. This phenomenon is not evident in these figures due to the quality of the sample preparation and of the images.

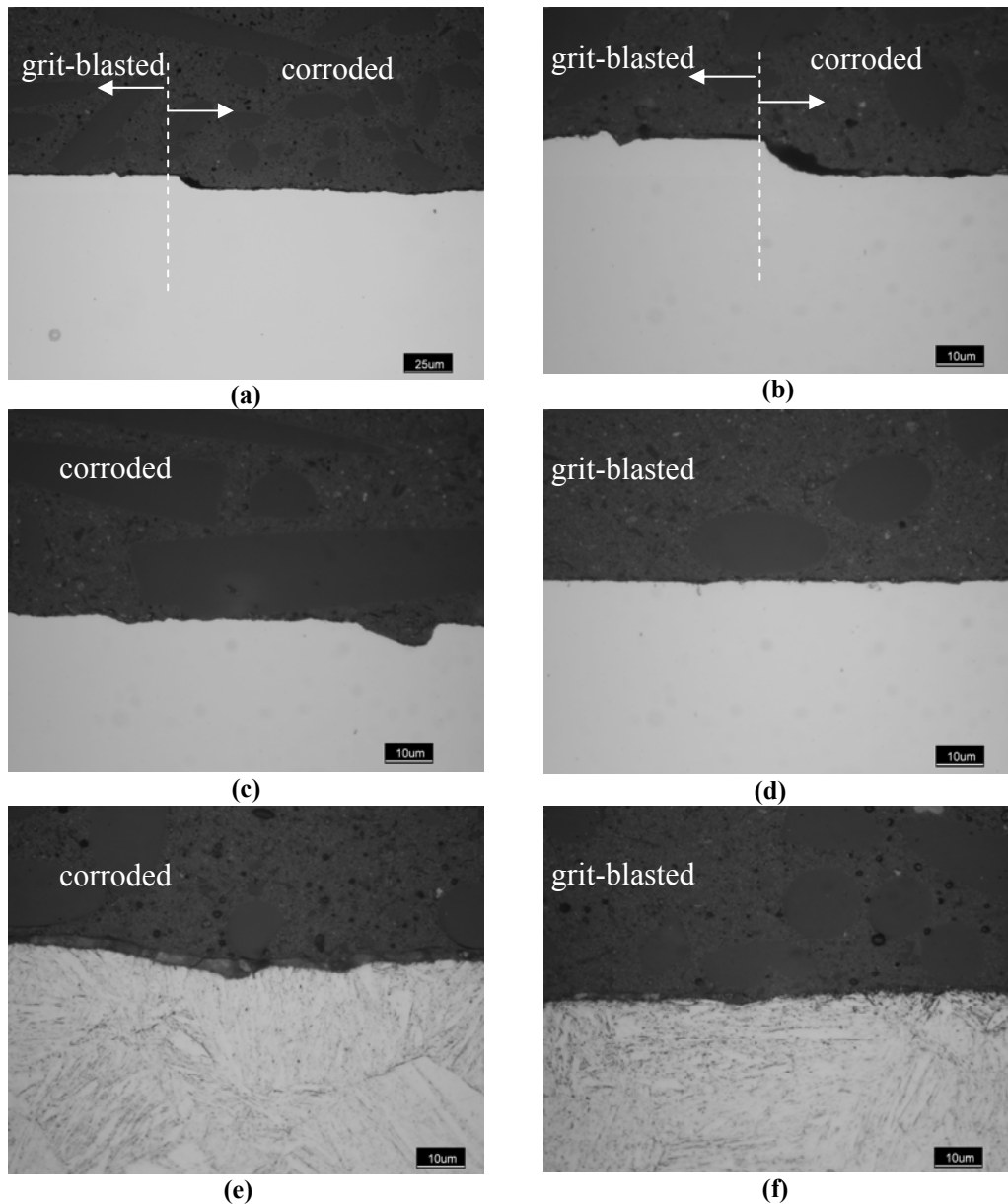


Figure 4.2.1-26. Cross-Section Images of Test Wafer AF1410-6hr: (a) & (b) are micrographs of the transition region between the corroded and grit-blasted surfaces, (c) & (e) were taken in the corroded region, (d) & (f) were taken in the grit-blasted region. The images in (e) and (f) were taken after the cross-sections were etched in 2% Nital.

Test wafer AF1410-12hr was exposed using the cycles outlined for the 12-hour exposure (listed in Table 4.2.1-4). This test wafer also came from one of the radius sections of an AF1410 fatigue test specimen that was tested and provided by Boeing. The wafer was grit-blasted to give it an approximate average roughness (Ra) between 1 and 1.5 microns. After being corroded, the wafer was cleaned using the procedures Boeing recommended. A digital image of the surface after a 12-hour exposure is shown in Figure 4.2.1-27(a). The corrosion patch is approximately 1.0625" in diameter.

The corroded surface of the specimen was then inspected using both a mechanical stylus and a white-light interferometer. The height map generated by the WLI microscope for test wafer AF1410-12hr is shown in Figure 4.2.1-27(b). An example line profile of the transition between the non-corroded and corroded surface was taken at approximately the 11 o'clock position with a stylus and is shown in Figure 4.2.1-27(c). The statistical analysis for the data is shown in Table 4.2.1-7. The data show that there is an increased level of corrosion in terms of statistical metrics that are based on average roughness or volume loss with the increased time of exposure. This specimen's non-corroded, but grit-blasted surface, had an average surface roughness that fell within the target range of 1 to 1.5 microns.

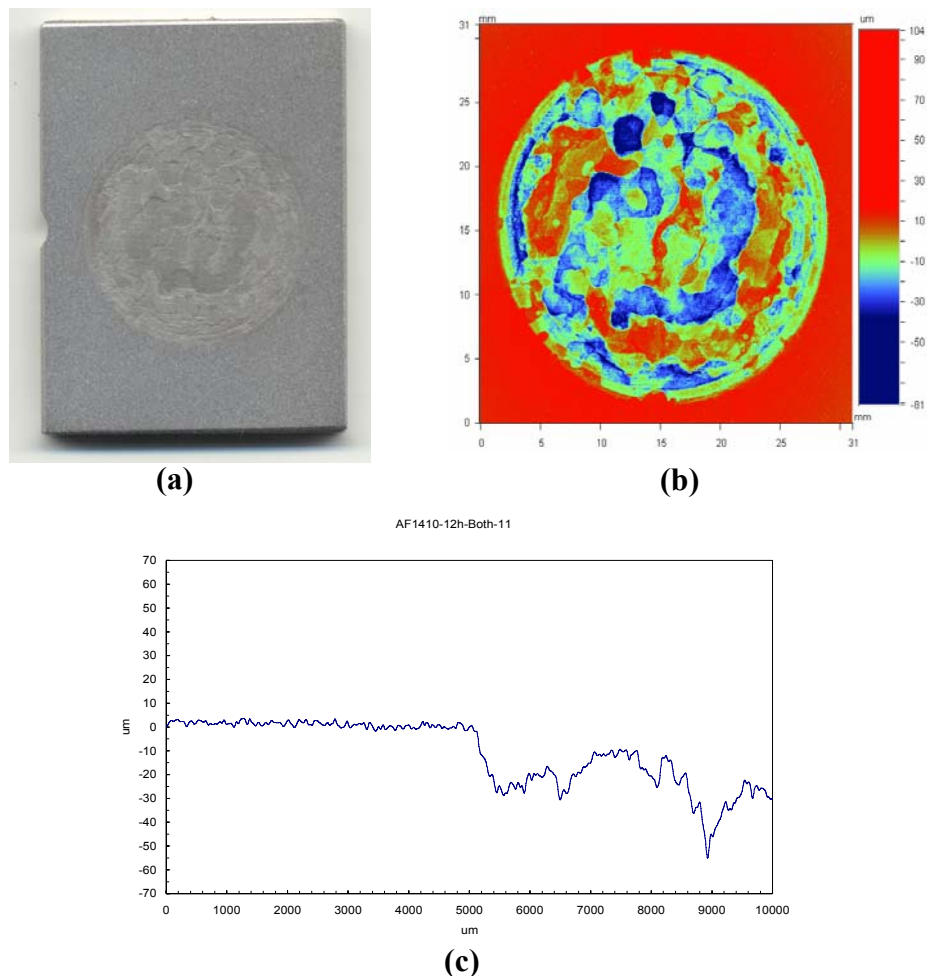


Figure 4.2.1-27. Test Wafer AF1410-12hr: (a) photograph of the corroded surface after the 12-hour exposure (the diameter of the corrosion patch is approximately 1.0625"), (b) height map of the corroded surface as measured using the white-light interferometer, and (c) line profile of the transition between the non-corroded and corroded surface taken at approximately the 11 o'clock position with a stylus.

Table 4.2.1-7. Results of WLI Measurement on Specimen AF1410-12hr

Specimen AF1410-12hr	Exposure Time (Hrs.)	Ra	Rq	Rsk	Rku	Rv	Rp	Rt	NVL (cm³/m²)	SD
Corroded surface	12	4.18	6.10	-0.75	2.77	-73.49	93.33	166.82	11.38	6.30
Non-corroded surface	0	1.12	1.68	2.97	160.72	-32.49	93.33	125.82	4.51	1.70

A limited amount of metallography was performed on the AF1410-12hr wafer to provide a cross-sectional view of the actual corrosion profile. The goal was to determine if the corrosion attack was limited to the topographical features measured by the WLI microscope, or if there was significant sub-surface attack that might influence the fatigue life. Several micrographs of a cross-section from specimen AF1410-12hr are shown in Figure 4.2.1-28. The first two images in Figure 4.2.1-28(a) and (b) are the transition region between the corroded region and the grit-blasted non-corroded region. The images in (c) and (d) show the corroded surface and the grit-blasted surface, respectively, at high magnification. The corrosion damage on this specimen has both the small-scale and large-scale damage, more like the 3-hour exposed specimens, with the same amount of grit blast damage. The depth of the thickness loss (volume loss) and the depth of the features are greater than that seen on the 3- and 6-hour exposures. The damage due to material rollover is definitely an issue on this specimen as well.

The last two images, Figure 4.2.1-28(e) and (f), are again of the corroded region and of the grit-blasted region (non-corroded region), respectively. In this case, the surfaces were etched with 2% Nital for several minutes in order to reveal the martensitic microstructure. Note that these images were not taken in the same locations as the images in Figures 4.2.1-28(c) and (d). It can be observed from these images that the corrosion does not seem to preferentially ingress along grain boundaries. Instead, it has a general corrosion appearance. During optical inspection, it was also observed that the corrosion attack at the surface does follow laths in the microstructure. The ingress observed is very shallow and is limited to a depth just below the surface. This phenomenon is not evident in these figures due to the quality of the sample preparation and of the images.

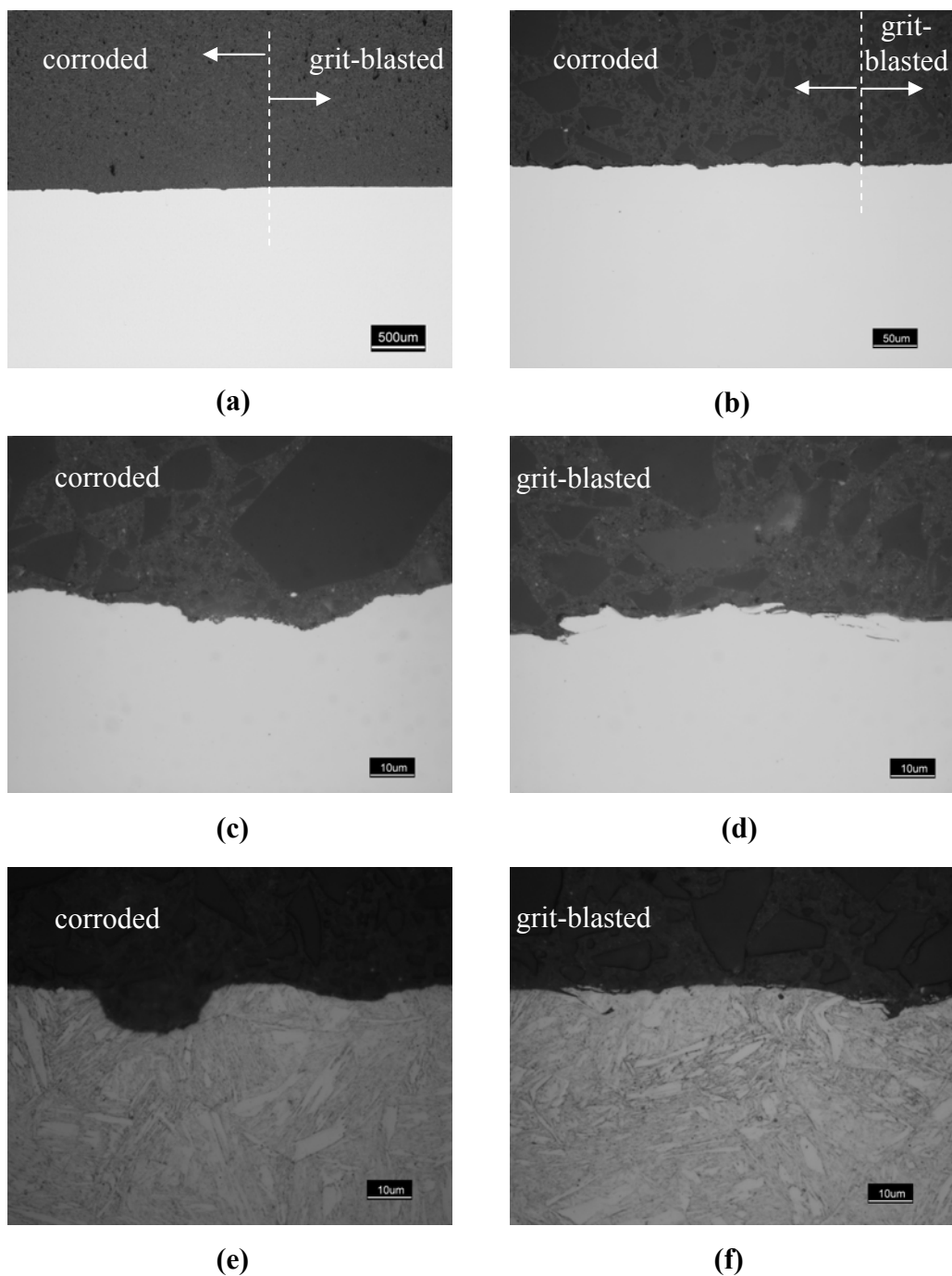


Figure 4.2.1-28. Cross-Section Images of Test Wafer AF1410-12hr: (a) & (b) are micrographs of the transition region between the corroded and grit-blasted surfaces, (c) & (e) were taken in the corroded region, (d) & (f) were taken in the grit-blasted region. The images in (e) and (f) were taken after the cross-sections were etched in 2% Nital.

4.2.2 Corrosion Product Cleaning Methods Study

In order to study the corrosion surface of the corrosion-fatigue test specimens, it was necessary to remove oxides from the corroded area without causing further damage that could potentially affect the fatigue results. A method for cleaning ferrous alloys that is based on a Boeing Process Specification (P.S.) for Alkaline Cleaning has been successful at removing corrosion by-products on the AF1410 steel without significant observable affects to the material. Members of the Boeing team on this program have successfully used this cleaning process for similar purposes on other programs and recommended its use. The Boeing P.S. is broken down into three types according to the category of the material to be cleaned. The Type I processes are for alkaline cleaning of aluminum alloys. The Type II processes are for alkaline cleaning of magnesium, ferrous, and copper alloys. The Type III processes are for alkaline cleaning of ferrous, nickel, cobalt, titanium, and molybdenum alloys, and stainless steels. The process recommended by Boeing is the Type III. The chemical, concentration, and temperature requirements in the P.S. for Type III is shown in Table 4.2.2-1 below.

The first chemical listed in the Type III process, the Turco Alkaline Rust Remover – MAC, is the chemical recommended by Boeing. It is to be used at the highest concentration and lowest temperature found in the specification. The Turco MAC chemical is no longer manufactured, so the Turco T4181L was the product chosen for this program.

UDRI adapted the process from the specification by submerging the corroded samples in a 70% concentrated solution of the Turco 4181L at approximately 190°F for up to 10 minutes at a time with subsequent rinsing and light mechanical rubbing of the surface. The samples were left in the bath for up to 10 minutes at a time, depending on the amount of corrosion byproducts. If the specimen was not cleaned after one cleaning cycle, the process was repeated.

It should be noted that, although the Boeing Process Specification indicates that Type III cleaners usually discolor or oxidize alloy surfaces, it was not a problem with the AF1410 material. Slight discolorations may have occurred on the surrounding bare material of test specimens of AF1410, but did not appear to affect fatigue test results, especially in the case of the more-

severely corroded test specimens. Those discolorations may be formation of oxide that the P.S. mentions can easily occur once cleaned using the Type III process. No specific tests were performed to investigate the effects of the cleaning process itself on the baseline material behavior of the AF1410. Such tests might be included in future testing on the program.

Table 4.2.2-1. Type III Process Detail

(Taken from Boeing Process Specification for Alkaline Cleaning – 12030)

Chemical <u>1/</u> <u>2/</u>	Concentration	Temp.
Either – Turco Alkaline Rust Remover-MAC (Turco Products, Inc. Cornwells Heights, PA)	16 to 48 wt.oz/gal or 1.0 to 3.0 lb/gal	190 to 200° F
Tap Water	Remainder	
Or – Turco Alkaline Rust Remover-T4181 (Turco Products, Inc. Cornwells Heights, PA)	15 to 44 wt.oz/gal or 0.9 to 2.75 lb/gal	190 to 200°F
Tap Water	Remainder	
Or – Turco Alkaline Rust Remover Liquid - T4181L (Turco Products, Inc. Cornwells Heights, PA)	32 to 95 fl.oz/gal or 25 to 74% by volume	190 to 200°F
Tap Water	Remainder	
<u>NOTES:</u> 1/ Different proprietary cleaners shall not be mixed together in the same tank. 2/ Use alkaline cleaning solutions specified in P.S. 12037 to clean titanium detail parts for adhesive bonding.		

4.2.3 Materials Study: Effect of Corrosion Growth Method on Materials and Materials Properties

UDRI used two different surface analysis techniques, including energy dispersive and Auger electron spectroscopy, to determine if the electrochemical process selected to grow corrosion on this program has significant effects on the composition of the surface layers of the material. Energy dispersive spectroscopy (EDS) is used to determine the constituents present in a material using a material cross-section within a scanning electron microscope. Each element emits its own unique fluorescent x-ray energy spectrum. In this case, the goal was to measure the quantity of each element present as a function of depth below the surface. To do so, the EDS measurements were conducted on a polished cross-section of a sample that was corroded for 12 hours with UDRI's electrochemical method.

Results from the EDS analysis are shown in Figures 4.2.3-1 through 4.2.3-8. The micrograph in Figure 4.2.3-1 is from the corroded material cross-section using a scanning electron microscope. The white band at the top of the image is an imaging artifact at the corroded surface. The vertical yellow line indicates the approximate location of the analysis in the images that follow. Note that the micrograph in Figure 4.2.3-2 and the images that follow in Figures 4.2.3-3 through 4.2.3-8 are at the same scale and aligned vertically and horizontally. Also notice that the surface of the sample is not at the exact top of the image, but is located a short distance below the edge of the frame, as is apparent in the micrograph and as identified in the images that follow. The size of the cross-section, or depth below the surface, included in the micrograph and the image analysis is, therefore, less than 49.3 microns, which is the height of the image.

Figures 4.2.3-3 through 4.2.3-8 are the results from the EDS measurements in the form of images calibrated to x-ray energy. The figures show the x-ray images for iron, chromium, cobalt, nickel, molybdenum, manganese, and carbon, respectively. The images have enhanced contrast to show any material variations that might be present. The image analysis result for the respective constituent along the vertical yellow line is superimposed on each figure. The analysis shows that some return signal was detected outside of the material above the corroded surface. This anomaly might be due to beam spread, surface roughness, edge roughness or exposure of corroded surface below the top surface of the cross section (grazing incidence parallel to the instrument interrogation direction).

The results show that there is no apparent material variation as a function of depth below the top surface of the sample, except possibly within the first micron of material. For all of the constituents except for carbon, there might be a slight “ramping up” or increase in the traces just below the surface. Using the micron bar, it is estimated that the increase occurs over a depth within 1 micron of the surface. Carbon shows the opposite trend. Figure 4.2.3-8 shows that there is an increased amount of carbon present at the surface that quickly decreases within a depth of about 1 micron below the surface. It is not possible to be more definitive than this with the resolution of this technique and this specimen.

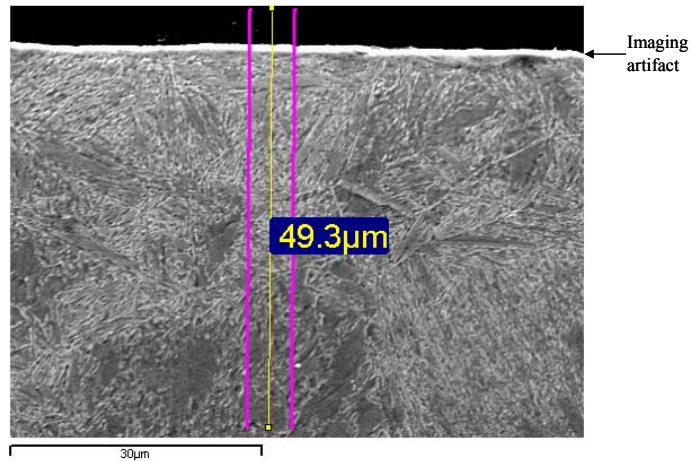


Figure 4.2.3-1. Micrograph of a Cross-Section of a Corroded AF1410 Wafer. The white band at the top of the image is an imaging artifact at the corroded surface. The vertical yellow line indicates the approximate location of the image analysis in the following figures.

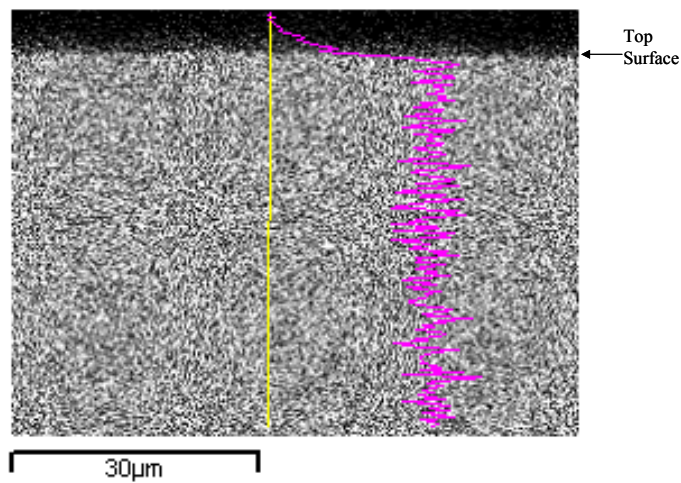


Figure 4.2.3-2. X-Ray Energy Image for Iron with the Elemental Trace Along the Superimposed Yellow Line

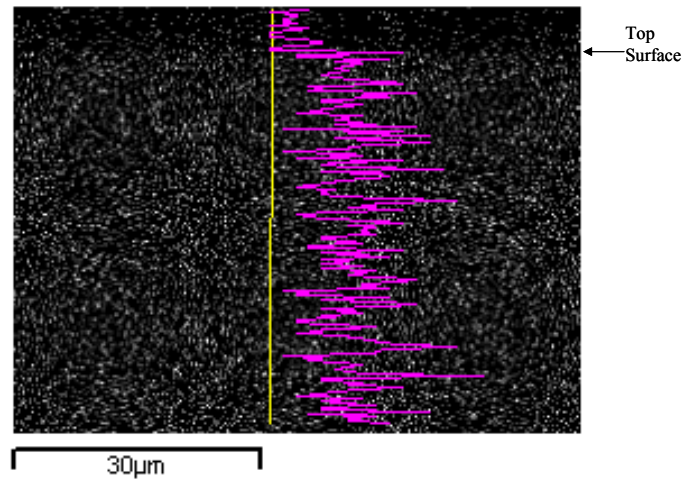


Figure 4.2.3-3. X-Ray Energy Image for Chromium with the Elemental Trace Along the Superimposed Yellow Line

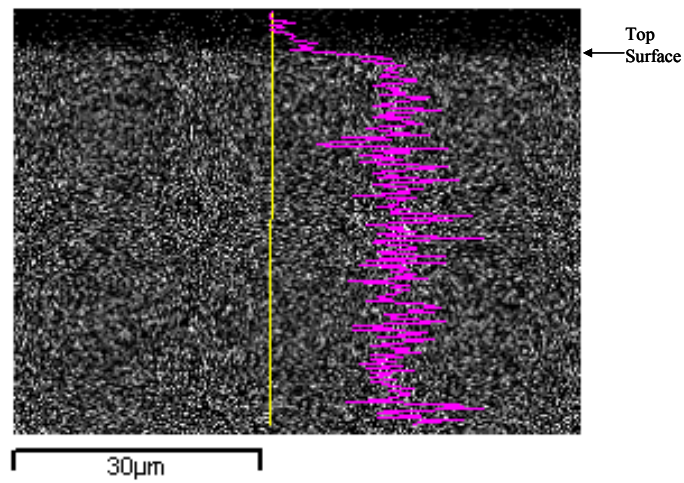


Figure 4.2.3-4. X-Ray Energy Image for Cobalt with the Elemental Trace Along the Superimposed Yellow Line

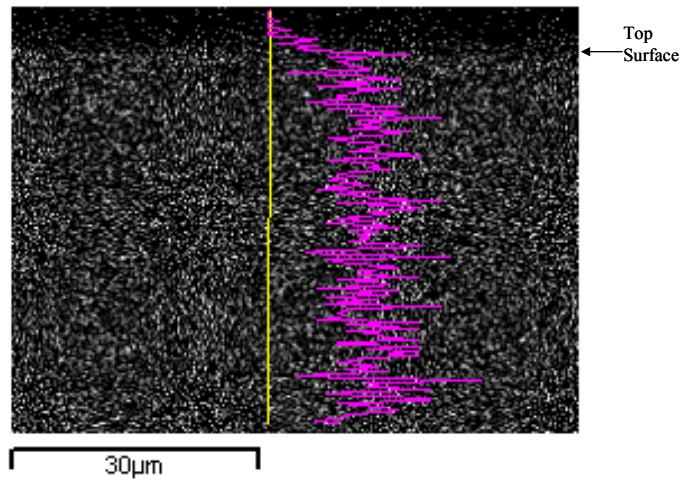


Figure 4.2.3-5. X-Ray Energy Image for Nickel with the Elemental Trace Along the Superimposed Yellow Line

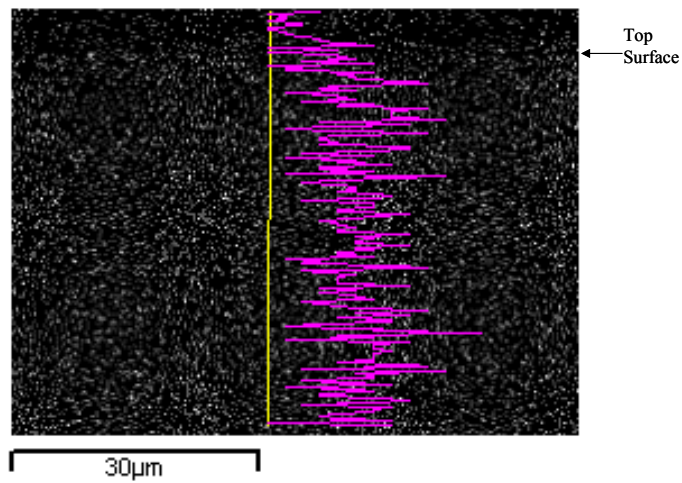


Figure 4.2.3-6. X-Ray Energy Image for Molybdenum with the Elemental Trace Along the Superimposed Yellow Line

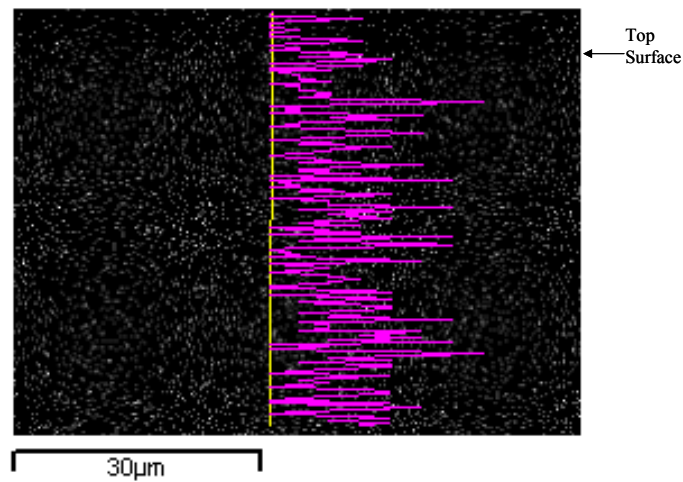


Figure 4.2.3-7. X-Ray Energy Image for Manganese with the Elemental Trace Along the Superimposed Yellow Line

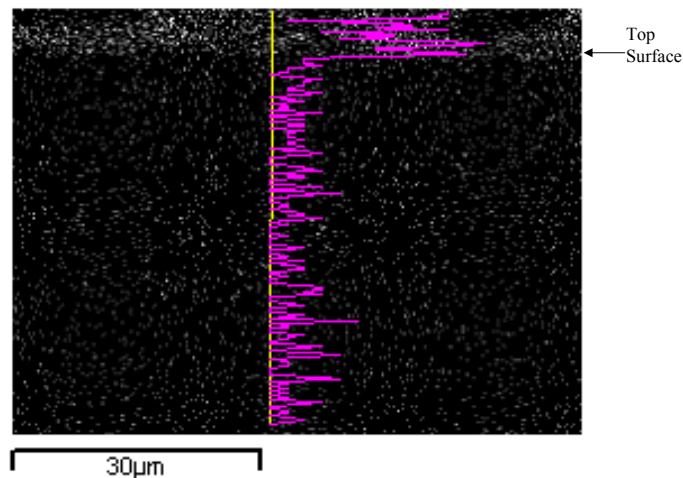


Figure 4.2.3-8. X-Ray Energy Image for Carbon with the Elemental Trace Along the Superimposed Yellow Line

In order to verify observations made using EDS and image analysis techniques, Auger electron spectroscopy (AES) was performed on corroded and non-corroded samples to quantitatively examine the near-surface chemical makeup of the material to depths within 1 micron below the surface. AES is based upon the measurement of the kinetic energies of emitted electrons. In this case, an Auger depth profiling technique was used, which is a destructive process whereby layers of

material are removed to expose new material that can then be assessed. For the measurements performed, each minute of sputter time corresponds to approximately 2.5 nm of material removal. Limitations of Auger electron spectroscopy in this material include its sensitivity to surface roughness and absorbed carbon. Many other variables (such as specimen cleanliness, vacuum quality, specimen-to-specimen composition variability and measurement location, for example), can also significantly affect the results of these highly sensitive measurements. In light of the inherent variability, typically a number of measurements are made in different locations and on different samples to gather statistically significant information. For this study, a single sample and single measurement were taken for each condition.

AES measurements were first taken on a non-corroded specimen as a baseline. Figure 4.2.3-9 shows the results from the Auger measurements for a non-un corroded specimen that had a polished (mirror-finish) surface. The plot is the atomic percent of the constituents detected (where the total number of atoms equals 100%) versus the sputter time. With a sputter rate of approximately 2.5 nm of material removed per minute, the plot shows data up to approximately 40 nm below the sample surface.

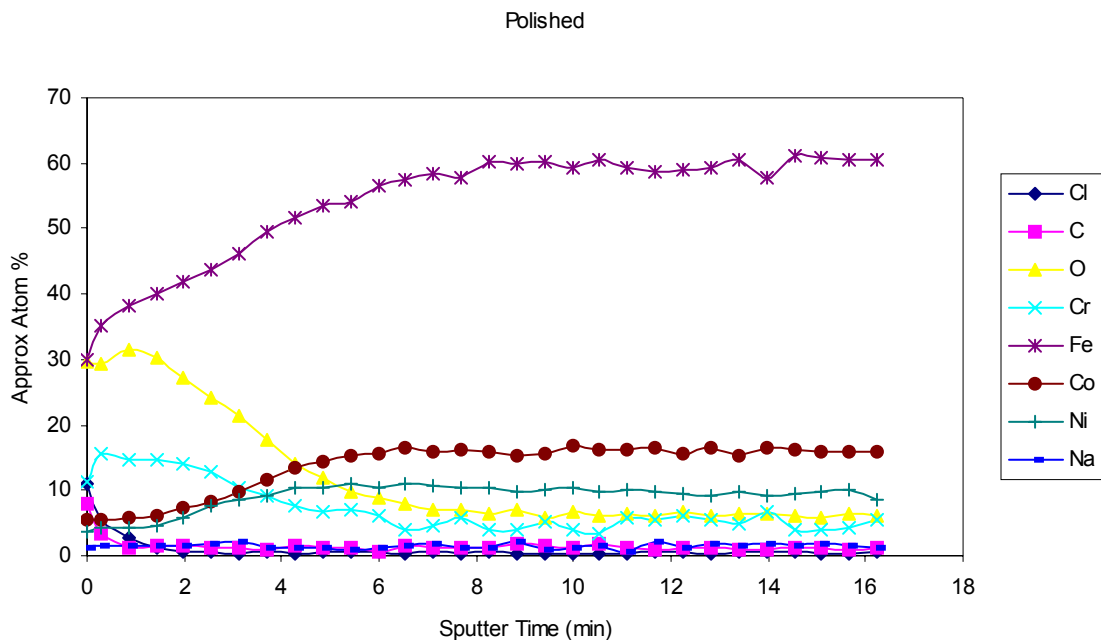


Figure 4.2.3-9. Auger Electron Spectroscopy Results from a Non-Corroded, Polished AF1410 Sample

The major constituents in AF1410 are iron, cobalt, nickel, and chromium, which are also shown as the major constituents detected by the AES. Many of the trace elements that make-up this steel are not detected. The exception is carbon. There is a slightly increased amount of carbon evident at the surface, which decreases with depth. The carbon at the surface is potentially due to absorbed hydrocarbons. A relatively large amount of oxygen detected may be from absorbed oxygen at the surface or, perhaps, suggests the presence of oxides on the surface. There are also small, but detectable, amounts of chlorine and sodium evident, which are probably also contaminants.

AES was also performed on a piece of corroded material that came from the same specimen as the non-corroded material. This sample was corroded using UDRI's electrochemical technique with a current density of 2 mA/cm², for a 12-hour exposure. Figure 4.2.3-10 shows Auger electron spectroscopy measurements results for the corroded sample. Each minute of sputter time represents approximately 2.5 nm of material removed and the plot shows data up to approximately 40 nm below the sample surface. The results are similar to the polished material. Again, in addition to the major constituents, the measurements show the presence of oxygen with small levels of sodium and chlorine. In this case, the amount of carbon detected at the surface and overall is much larger. In general, the AES data show similar trends in the composition just below the corroded surface, as was observed in the EDS data, but are shown to occur over a very small depth below the surface.

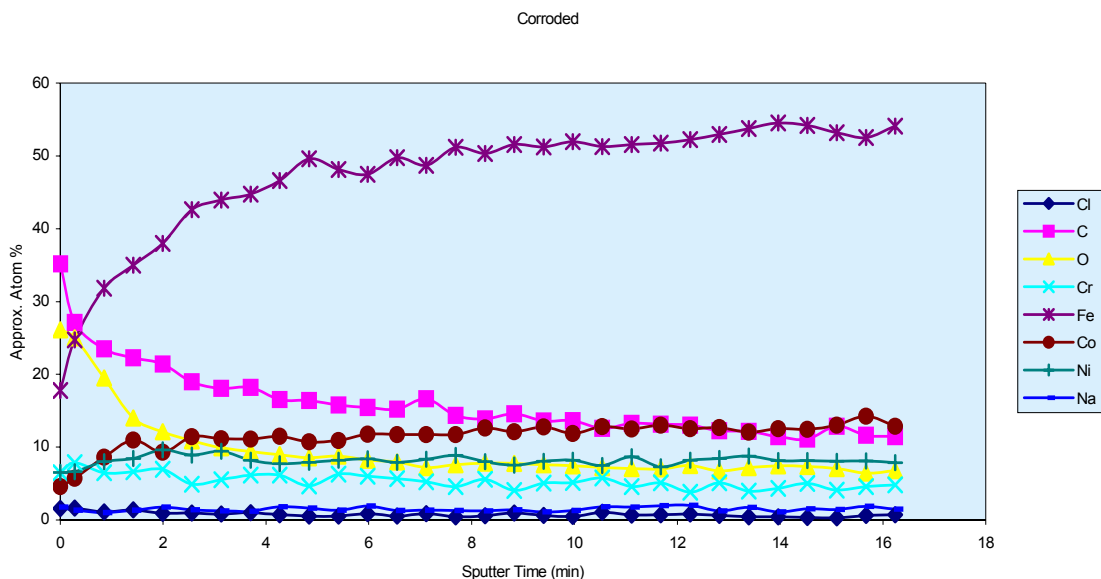


Figure 4.2.3-10. Auger Electron Spectroscopy of Corroded AF1410 Sample

What appears to be a relatively significant amount of carbon absorbed at the surface is speculated to be a combined effect of the surface roughness and the measurement technique. There is no doubt that the small carbon atoms are readily absorbed at the surface of the steel and that a rough and/or relatively torturous surface would contain a larger amount of carbon due to the larger amount of surface area, as compared to the polished surface. However, it is speculated that the amount of carbon detected by the highly sensitive Auger technique is not real, but amplified, due to the surface roughness and the depth profiling technique. Since the surface has peaks and valleys, carbon is continuously being exposed and detected as the sputtering progresses, thus, making it appear that a relatively large amount of carbon is present at depths below the surface to a larger extent. In turn, it affects the atomic percents calculated for the other constituents as well.

To test the effects of surface roughness on the amount of absorbed carbon, a third piece of metal from the same specimen was prepared by polishing and then grit blasting the surface to create a lesser amount of surface roughness than the corroded specimen. This specimen was then analyzed using AES. The results for the grit-blasted material, shown in Figure 4.2.3-11, are very similar to both the non-corroded material with the highly polished surface and to the corroded material. Again, each minute of sputter time represents approximately 2.5 nm of material removed and the plot shows data up to approximately 40 nm below the sample surface. The major difference is the amount of carbon, which is larger in the case of the grit-blasted surface compared to the polished surface, and smaller compared to the corroded surface. This indicates a possible relationship between the absorbed carbon detected with the amount of surface roughness and/or surface area using this measurement technique.

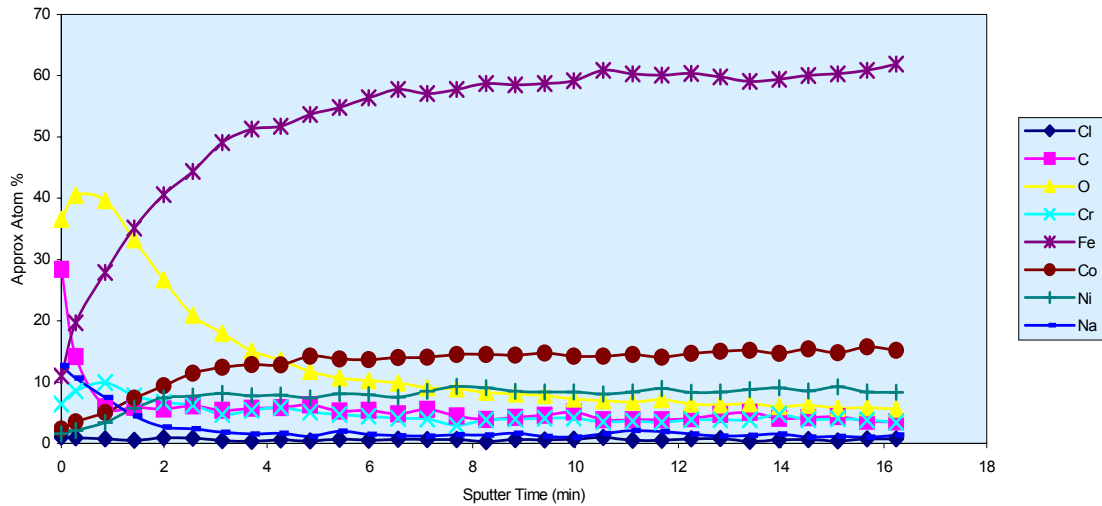


Figure 4.2.3-11. Auger Electron Spectroscopy of a Non-Corroded, but Grit-Blasted AF1410 Wafer

To further examine the data from the near-surface layer of the corroded sample, relative amounts of the major constituents for the non-corroded, grit-blasted and corroded samples are compared. Relative amounts of the different atoms detected are the most appropriate comparison due to the inherent variability in the depth profiling AES measurements and effects of surface roughness. Since the amounts of all of the constituents at the surface change within the first 15 to 20 nm or so, a comparison of the relative amounts of the major constituents is best performed starting after 10 minutes of sputter time, or at a depth under the surface layer of approximately 25 nm. Therefore, the last 6 minutes of data from each sample (Figures 4.2.3-9, 10, and 11) were averaged for the major constituents of the material, oxygen, and carbon. The ratio of the average amount of each constituent to the average amount of iron detected in each case was determined and the results are plotted in Figure 4.2.3-12. A comparison of the non-corroded, grit-blasted and corroded samples show that there are no significant differences in the relative amounts of any of the *major* constituents or oxygen to the amount of iron detected. As a result, it does not appear that the corrosion process has affected the material chemistry very near the surface layer. The plot does show that there is a significant difference in the relative amounts of carbon, presumed to be absorbed carbon, between the three samples. The trend implies that the relative amount of absorbed carbon near the surface may be dependent on the amount of surface roughness and/or surface area using this measurement technique.

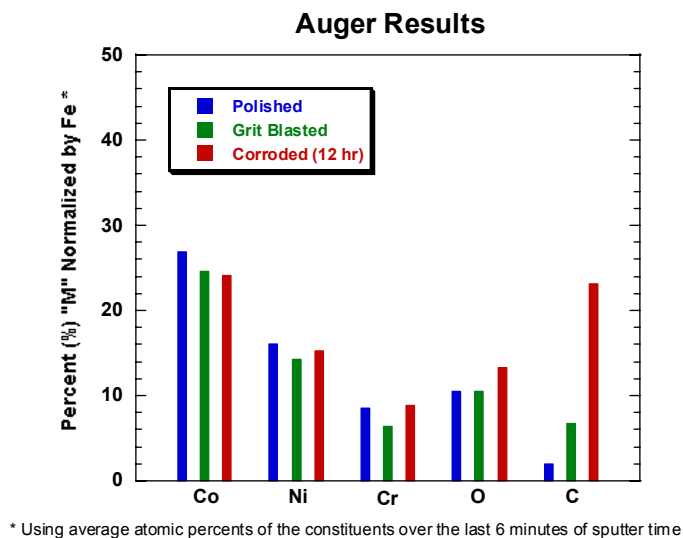


Figure 4.2.3-12. A Comparison of the Amounts of the Different Constituents Normalized by the Amount of Iron for the Non-Corroded, Grit-Blasted, and Corroded Materials

Given the Auger electron spectroscopy data and an understanding of the limitations of the measurement process, it can be deduced that there is no evidence of material effects due to the corrosion process.

Electrochemical Analysis

In order to better understand the corrosion mechanisms of the AF1410 material and the observations made while testing UDRI's corrosion growth process, a series of electrochemical measurements were made. First, measurements were taken using a standard electrochemical cell to determine the equilibrium potential, or Open Circuit Potential (OCP), of the AF1410 alloy sample in ambient and deaerated 3.5% NaCl. Next, corrosion rate information on the steel alloy in 3.5% NaCl was gathered using a potentiostat.

A sample of AF1410 was obtained that had already undergone stress testing and exhibited failure, which yielded 2 identical halves for testing. One of the halves was tested in 3.5% NaCl solution and the other in deaerated 3.5% NaCl. The first sample was cleaned with methanol, air-dried, and exposed to 3.5% NaCl using a commercially available corrosion flat cell. The exposure area was 1 cm² using a knife-edge Teflon gasket that had been polished perpendicular to the exposed crack edge. The OCP was measured for 2 hours versus a saturated calomel reference electrode (SCE) using a Princeton Applied Research Model 273 potentiostat (Figure 4.2.3-13). Next, the sample was polarized from the OCP to +1.8 volts (vs. OCP) at a dynamic rate of 10

mV/minute and the current recorded (Figure 4.2.3-14). The method was repeated on the other half of the sample using deaerated 3.5% NaCl. A second sample was polarized from 50 mV below the OCP up to +1.8 V (vs. SCE).

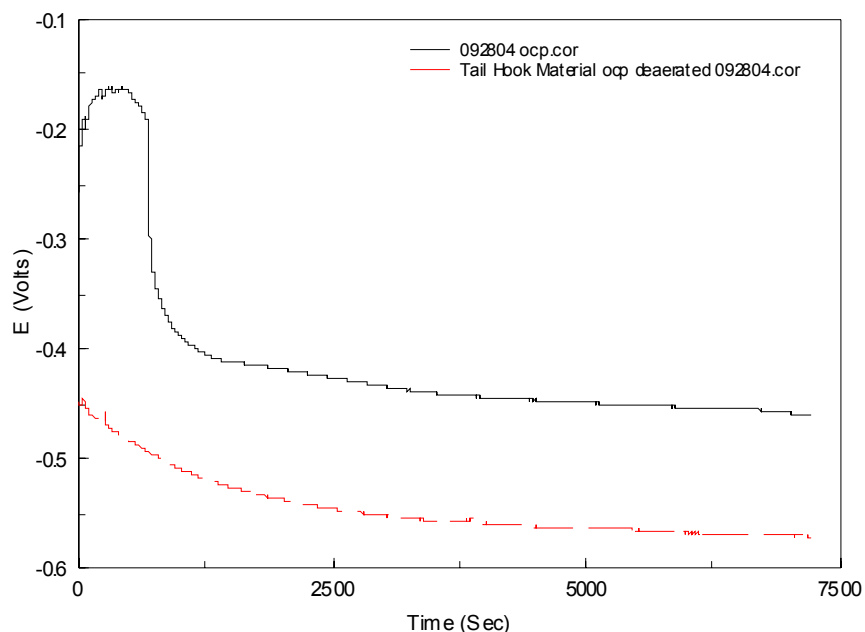


Figure 4.2.3-13. OCP Curves AF1410 in Ambient (Black) or Deaerated (Red) 3.5% NaCl for 2 Hours

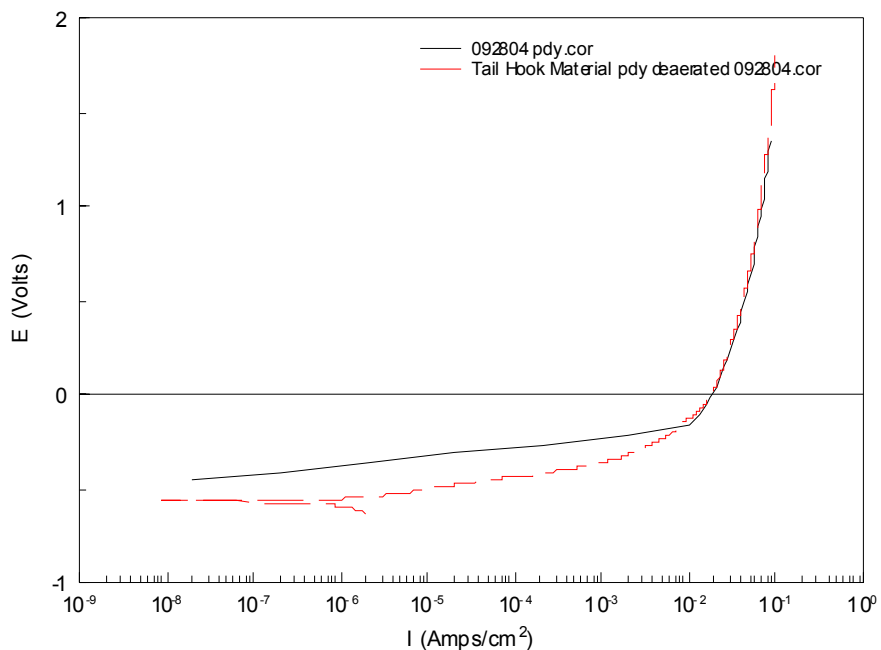


Figure 4.2.3-14. Potentiodynamic Scan of AF1410 in Ambient (Black) or Deaerated (Red) 3.5% NaCl

A third sample (the reverse side of the second sample) was exposed to deaerated 3.5% NaCl and used to make a cyclic polarization measurement. The OCP was measured for 2 hours on this sample prior to making a cyclic polarization measurement (not shown). The sample was polarized anodically from -50 mV below the OCP to 1.8 V (vs. SCE) and back down again to -50 mV below the OCP (Figure 4.2.3-15).

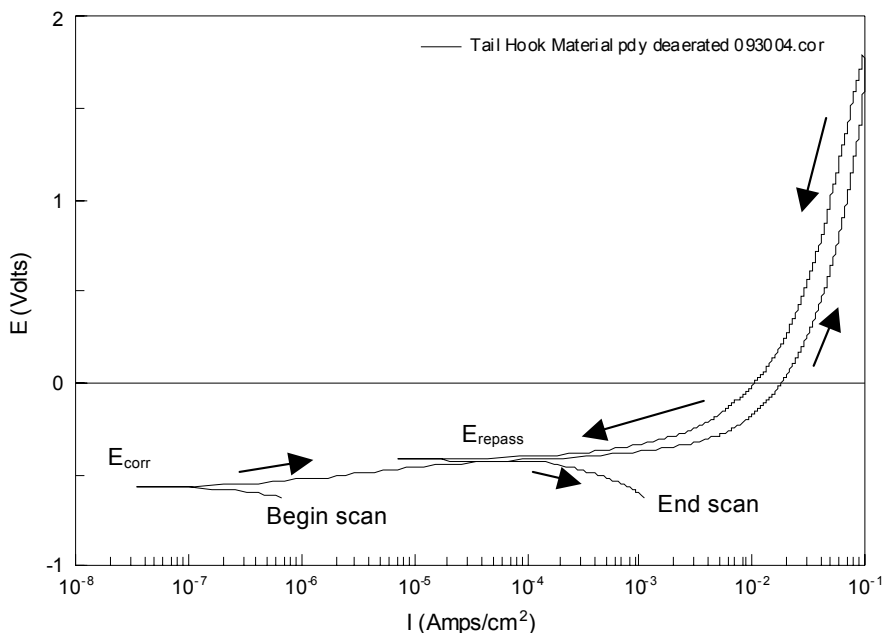


Figure 4.2.3-15. Cyclic Polarization Measurement of AF1410 in Deaerated 3.5% NaCl. Arrows indicate direction of potential scan; E_{corr} is the OCP or corrosion potential; E_{repass} is the repassivation potential.

The results show that exposure to deaerated solution over 2 hours results in a more cathodic OCP (Figure 4.2.3-13), suggesting that the OCP is under cathodic control (i.e., cathodic reactions at the metal-solution interface) and, possibly, a lower corrosion rate. This indicates that, prior to polarization, the sample immersed in the deaerated solution has not undergone as much corrosion (formation of a passivating oxide). However, in both exposure conditions, the anodic polarization of AF1410 alloy exhibits reproducible uniform corrosion with no localized pitting. At a potential of approximately -82 mV (vs. SCE) and a current density of 13 mA/cm^2 , both samples exhibit identical passivation behavior, indicating that the corrosion of the alloy is under anodic control and the passivation potential has been attained (Figure 4.2.3-14). Therefore, at potentials above -82 mV (vs. SCE) or a current density of 13 mA/cm^2 , the sample will undergo uniform corrosion in 3.5% NaCl.

Finally, cyclic polarization of the sample in deaerated 3.5% NaCl shows that, when the potential scan direction is reversed at +1.8V, the sample exhibits a negative hysteresis curve (Figure 4.2.3-15). This indicates that the sample will not undergo localized corrosion (pitting) and will passivate and corrode uniformly. Furthermore, since the repassivation potential (E_{repass}) is more positive than the OCP or corrosion potential (E_{corr}), this indicates that this material is susceptible to crevice corrosion.

Conclusion

Results of the surface analysis measurements (the energy dispersive and Auger electron spectroscopy) show no significant changes in the material chemistry very near the surface layer due to the electrochemical method for creating corrosion on AF1410. However, it may not be possible to rule out a material effect, particularly for the minor alloying constituents, within approximately the first micron below the surface. Results of the electrochemical analysis show that UDRI's corrosion growth method (with 2 mA/cm² applied current) is well below the point at which passivation occurs (at 13 mA/cm² applied current). This observation indicates that the material will corrode uniformly using UDRI's method. The electrochemical results also support the observation that this material does not pit and is susceptible to crevice corrosion, as is evident when masking a specimen corroded with salt fog or alternate immersion techniques. In conclusion, there is no evidence that UDRI's corrosion growth method is leaching out constituents in a non-uniform manner (i.e., by localized corrosion) or that there is a significant layer in which the relative amounts of the major alloying constituents are changed compared to the base metal. Therefore, no effects on the mechanical behavior are expected due to material changes very near the surface layer of material.

4.2.4 Corrosion Characterization Methods Study

Through the research performed early in the program, it became obvious that small localized topographic measurements may not properly reflect the severity of the corrosion over an entire region affected by corrosion. This led to the development of corrosion mapping methods for larger areas of topography that encompass the entire area affected by the corrosion. There are some errors inherent in generating profilometry maps on this size. Post-processing filtering becomes necessary to filter the data in order to make it more closely resemble the actual surface that is being modeled.

The ultimate goal of this program was to find correlations between surface topography and loss of fatigue life in various materials. Surface characterization methods must capture the detail necessary to establish these correlations.

Samples

Corrosion was induced in samples using the electrochemical method with salt-water soaked filter paper placed between electrode and specimen, which is described in Section 4.2.1. Exposure times were 3, 6, and 12 hours. All corrosion products were cleaned from the samples using the solution described in Section 4.2.2.

Data Acquisition

There are three main methods of obtaining profilometry commonly used in metallurgy: contact stylus, laser interference, and white-light interference microscopy. Only the latter two are capable of easily producing a three-dimensional map of surface height points. Of those two methods, the white-light interference method has both the fastest data acquisition and the highest theoretical accuracy. White-light interferometry also tends to be the more expensive of the two methods to pursue, which provides some reason as to its general lack of use.

A laser profilometer uses the difference in the interference patterns of coherent laser light to obtain height information. The accuracy of the system depends on a system of highly accurate stepper motors that are used to move the measurement head. Some of the physical limitations that occur in this type of measurement are the spot size of the laser, the accuracy of the stepper motors, and the wavelength of the laser light that is used. Typical wavelengths tend to be in the 680 nm range.

White-light interferometers are not as limited in these respects. One advantage of using a white-light interferometer compared with a laser interferometer is that it has no need for spot size adjustment. Also white-light interferometers are capable of better lateral and vertical resolution by using shorter wavelengths of the visible spectrum of light. In addition to higher resolution, white-light interferometers are capable of taking a group of points all in one measurement, thus speeding measurement time.

Measurements were made at the University of Dayton Center for Materials Diagnostics using a WYKO NT-8000 white-light interferometer capable of a lateral resolution of $0.2\text{ }\mu\text{m}$ and a vertical resolution of 3 nm (1 nm if multiple images are averaged together). For a typical corrosion measurement, the lateral resolution is set to $6.3\text{ }\mu\text{m}$ and the vertical resolution tends toward $0.1\text{ }\mu\text{m}$. The main reason for using these resolution settings is to keep measurement times reasonable.

Due to the high roughness of the surface being measured, it is necessary to use vertical scanning interferometry. This method creates changes in the interference patterns by precisely moving the focus of the objective using a highly calibrated piezoelectric transducer (PZT) in a closed-loop feedback system. At the point of optimal focus, the strongest intensity interference patterns are observed and profilometry data points are taken. These signals are recorded using a CCD camera located at the top of the microscope. Individual topographic images are 736×480 pixels in size. Using a high-accuracy motorized stage, a series of these images are taken in a linear manner and automatically stitched into a single image using the WYKO software. One stitched measurement is $11\times 11\text{ mm}$ and consists of 1,283,168 pixels. The process takes approximately three hours per image, but varies exponentially as the surface features become deeper. This process is then repeated at 10 mm intervals to provide 1 mm of overlap for each image. In the final measurement, these $11\times 11\text{ mm}$ images are stitched together using the recorded stage position of the measurement. The final stitched image consists of approximately 35,882,620 pixels and takes about forty-eight hours to complete the $41\times 41\text{ mm}$ measurement. Not only does this method provide high spatial resolution, it is also the fastest measurement technique for a map of this size. The equivalent measurement would take approximately fifty-two days to complete with a laser profilometer and is practically impossible with a contact profilometer.

There are some inherent problems with creating a measurement of this type. Most of the errors that occur are due to the stitching process. The only current way to stitch the $11\times 11\text{ mm}$ data sets is by using the recorded stage position, which does a very good job as far as the lateral spacing is concerned. Nevertheless, each measurement has an average tip and tilt that is purposely introduced into the measurement process for removal by linear regression in the post-processing portion of the measurement process. When stitching the images becomes necessary, the tip and tilt of each image add to a cumulative error that creates a surface that is not representative of the actual surface. With measurements exceeding tens of millions of pixels, removing this error

becomes exceedingly difficult. Errors such as this are not uncommon in the profilometry field and methods to remove them are readily available.

The error that is introduced in the measurement through the stitching procedure is often referred to as the “waviness” of the image. The waviness consists of the low-frequency components of the data. In order to remove the unwanted waviness from the topographical data, it becomes necessary to perform a high-pass filter to flatten the image. One very robust method for the removal of this waviness is to use a Gaussian blur to form a waviness image and then subtract that image from the initial dataset. This solution works very well, but begins to run into problems when the data sets get very large. In the case of the corrosion samples of interest on this program, all attempts to directly filter the data in this manner have led to computer memory failures.

Another method of performing a Gaussian-type filtering process is to use a Fast Fourier Transform (FFT) method of filtering. This has many advantages that have been well documented [3]. For filtering large topographical data sets, FFT filtering has appeal for two reasons. First, the FFT of a Gaussian filter is again a Gaussian, which greatly simplifies implementation. The second, and main, advantage of using an FFT filtering process in this application is that the amount of mathematical operations required to complete the filtering operation is greatly reduced, saving both time and memory. Using the FFT filtering method, the waviness can be removed in a few minutes. This FFT filtering process used on the Navy Corrosion-Fatigue program removes all frequency components with a spatial wavelength greater than 8 mm. This is a very effective method for removing the waviness from the data leaving a surface that is not exactly the same as the measured surface, but is highly representative of it.

White-Light vs. Laser Profilometer

In order to verify the topographical maps generated by the white-light interferometer, it was necessary to compare them to maps created by another profilometry method. In this case, laser profilometry was used as a standard for comparison. As mentioned above, white-light interferometry is not as limited in its resolution capabilities as the laser profilometer. Due to the white-light interferometers higher resolution, the images generated appear to be sharper than those generated by the laser profilometer. Figure 4.2.4-1 is a comparison of two profilometry readings taken at the same location on a typical test sample. In Figure 4.2.4-1(a), the topographical data was

taken with a laser profilometer and has a pixel density of 10,000 pixels/mm². Figure 4.2.4-1(b) is the equivalent measurement taken with the white-light interferometer that contains a pixel density of 21,480 pixels/mm². It is clear that the image on the right is sharper than the laser profilometry reading on the left. Other than the image sharpness, these two methods show excellent agreement.

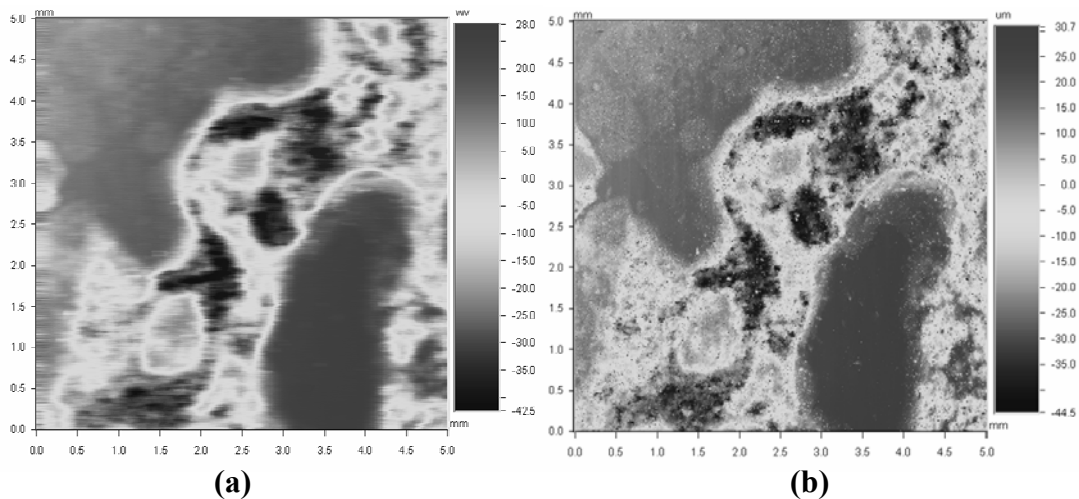


Figure 4.2.4-1. (a) Typical Laser Profilometry Measurement and (b) the Equivalent White-Light Profilometry Measurement

Using white-light interferometry to perform high-resolution corrosion topography can be very time consuming, but offers the best lateral and vertical resolution of any available measurement technique that can be applied on this scale. Although there are some differences between the laser and white-light profilometer metric values (see Table 4.2.4-1), the average statistics between the laser and white-light measurements are very comparable. Parameters that utilize the outliers of the data, such as R_t and R_p (see definitions in Section 4.2.5), demonstrate the most variability. Also, the 300M metrics demonstrated a greater difference than the AF1410 metrics. As mentioned before, laser profilometers have some limitation on how accurately they can perform measurements. The 300M data sets were particularly blurry when compared with the other data sets; this blurriness is most likely caused by a larger spot size used in the measurement. This helps to illustrate one of the advantages of using a white-light interferometer; white-light interferometry does not require a spot-size adjustment. In repeated measurements, the white-light interferometer has performed, on average, to better than 1% error on the average surface

statistics. Since one errant pixel can influence the entire metric, extremum statistics (e.g., maximum or minimum) are not a very good judge of repeatability. Much of the outliers affecting the extremum statistics can be handled by using low pass filters to reduce data noise. And since the white-light images have more than double the pixel density of the laser interferometer, they are more susceptible to these isolated peaks and valleys. The white-light instrument is more likely to pick up the actual extremes due to the higher spatial resolution.

A variety of samples were made of AF1410 and 300M high-strength steels. These samples were corroded and characterized using both white-light interferometry and laser profilometry. A summary of those statistics are listed in Table 4.2.4-1.

Based on the results of this study, a decision was made to use the white-light interference microscope for all corrosion profiles on this program.

Table 4.2.4-1. Statistics for White-Light Interferometer vs. Laser Profilometry

AF1410	Ra	Rq	Rp	Rv	Rt	Rz
Laser Profilometer	1.47	2.21	17.21	18.49	35.67	28.42
White-Light Interferometer	1.97	2.84	17.26	23.66	40.91	41.20
300M						
Laser Profilometer	1.50	2.02	8.63	11.01	42.14	17.12
White-Light Interferometer	2.46	3.39	15.28	26.07	41.36	37.90

4.2.5 Corrosion Metric Preliminary Study

Statistics and Time of Exposure

In order to determine which surface metrics would be useful in the determination of the severity of corrosion, standard roughness metrics and many texture analysis metrics have been tracked for various times of exposure. The texture metrics help to quantify certain aspects of a profilometry, such as the spikiness [6,7]. All of these metrics have been well documented as to their applications. A summary of the standard roughness parameters at given times of exposure (TOE) can be found in Table 4.2.5-1. Table 4.2.5-2 lists some of the texture parameters versus time of exposure. A short description of these parameters is given in Table 4.2.5-3.

Table 4.2.5-1. Standard Parameters vs. Time of Exposure (TOE)

TOE (Hr)	Ra	Rq	Rp	Rv	Rt	Rz
AF1410						
240.5	1.52	2.22	15.42	17.14	32.56	27.06
507	1.78	2.64	20.62	19.78	40.34	31.37
300M						
24	0.80	1.07	4.35	6.79	11.13	9.48
72	1.67	2.25	10.56	13.15	23.71	20.05
192	2.74	3.71	15.26	17.33	122.59	29.46

Table 4.2.5-2. Texture Parameters vs. Time of Exposure (TOE)

TOE (Hr)	S Index	NVL (cm ³ /m ²)	Skewness (μm)	Kurtosis (μm)	Rpk (μm)	Rvk (μm)	Htp (μm)
AF1410							
240.5	1.01	9.15	-0.85	5.74	3.80	6.47	45.55
507	1.01	11.11	-1.00	6.53	5.22	10.10	46.46
300M							
24	1.11	4.77	-1.40	6.84	1.97	6.58	28.81
72	1.31	9.73	-1.04	4.17	3.88	13.23	49.86
192	1.26	19.88	-0.29	2.51	6.32	12.65	58.69

Table 4.2.5-3. Summary of Surface Metrics

- Ra – Average Surface Roughness
- Rq – Root Mean Square Surface Roughness
- Rp – Maximum Surface Height Peak
- Rv – Maximum Surface Height Valley
- Rt – Maximum difference from the highest peak to the lowest valley
- Rz – Average maximum height of the profile
- S Index (Surface Area Index) – The ratio of the surface area of the profile to the surface area of an ideal plane.
- NVL (Normalized Volume Loss) – The ratio of the volume missing to the lateral area
- Rsk (Skewness) – A measure of the symmetry of the profile about the mean line
- Rku (Kurtosis) – A measure of the sharpness of the profile about the mean line
- Rpk (Reduced Peak Height) – The top portion of the surface that will be worn away during the run-in period
- Rvk (Reduced Valley Depth) – The lowest portion of the surface that will retain lubricant
- Htp – Defined by setting the tp1 (peak threshold bearing ratio value) and tp2 (the valley threshold bearing ratio value) to be separated by 40%

Many of these surface metrics rise as time of exposure increases. Information about the current state of the corrosion can also be extracted by comparing the metrics to each other; however, the main focus of this study was to identify a parameter that would increase with time of exposure, which is expected to be somewhat correlated to corrosion severity.

In the corrosion process, material is removed from the sample in its oxide form. This suggests the use of a metric that uses the volume of material missing as an indicator of the level of corrosion. With this in mind, normalized volume loss (NVL) becomes a promising candidate. As seen from the data in Table 4.2.5-2, this metric increased substantially with time of exposure in both materials.

In the initial study of metrics vs. time of exposure, almost all of the metrics studied showed some pattern that seemed to agree with expectations that corrosion could possibly make the surface rougher than the as-machined surface. Tracking texture parameters has provided insight into the various stages through which corrosion goes. While volume loss seems to constantly increase in both materials, this is not the case for skewness. In 300M, the skewness starts at a value that indicates a topography that is predominantly valleys. This value decreases dramatically approaching an almost even distribution of hills and valleys. Kurtosis in AF1410 does not follow this pattern; in AF1410, kurtosis slightly decreases with exposure time. Since volume is constantly being lost, a skewness value that moves from high to low indicates that, initially, most of the volume was lost in the formation of sharp valleys but, at some point, the upper parts of the surface began to provide the majority of the volume loss, leveling the surface. This is backed by the kurtosis value, which also decreases moving to a more even and less spiky surface. In contrast, the kurtosis in 300M increases indicating a volume loss that may be uniform at first and then more localized. But volume loss seems to be constantly increasing and may not be affected by how the corrosion grows.

Corrosion Maps

When creating a topographical map of the entire surface affected by corrosion, large data maps often have large amounts of waviness. This waviness is introduced due to the stitching process. It can clearly be seen in Figure 4.2.5-1(a) that the cumulative tip and tilt of the unfiltered data completely dominates the measurement. The ratio of the tip and tilt to the height of the actual

topography is more than ten to one, which absolutely requires that the waviness be removed. Figure 4.2.5-1(b) is the same data after an 8 mm band pass FFT filter has been applied. Not only is the waviness removed, but also the topography of the corrosion dominates the surface. Although this surface may not be the exact shape of the topography, it is very close. These large data sets can often be very difficult and time consuming to generate, but due to the unpredictable nature of corrosion, UDRI felt that it was necessary to measure the entire corroded region in order to ensure that the regions of large stress concentration would be found. Note that the images below have been cropped differently, but are of the same magnification.

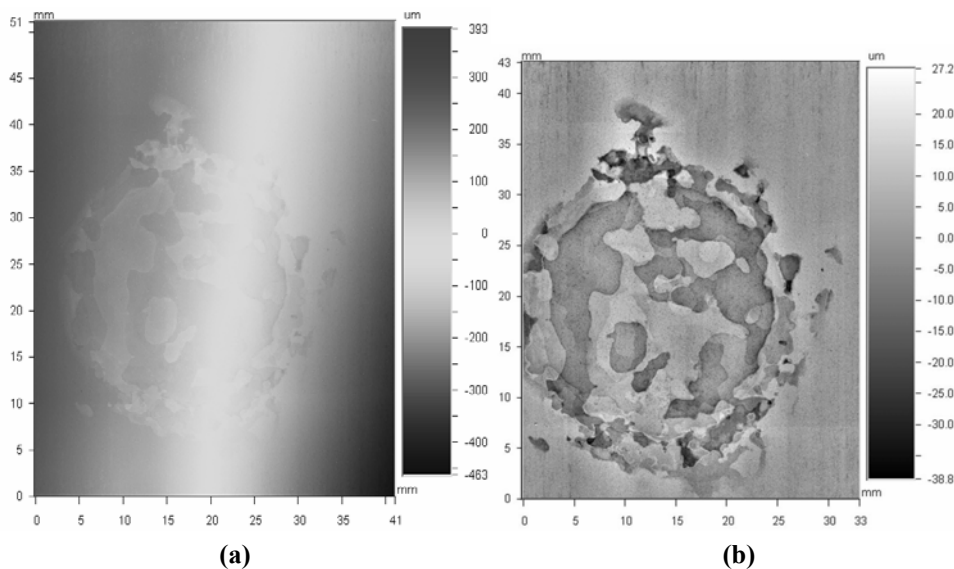


Figure 4.2.5-1. (a) Raw Profilometry Data from White-Light Interferometer and (b) after FFT Filtering

Mapping corrosion using the image stitching techniques can be very difficult, but the use of the stage position to stitch the images has skirted the problem of image registration. The use of Fast Fourier Transform to remove the waviness from the image was the only successful method of removing the waviness from an image of that size. Once the waviness is removed, the surface that is left is very close to the shape of the actual corroded surface. Very little low-pass filtering has been implemented up to this point in the research, but such filters may be used in the future to help remove noise.

Metric Mapping

Once a corrosion map has been created, it becomes necessary to analyze that map to find areas of the corrosion surface that will cause areas of high stress concentration. It is logical that these areas of higher stress concentration would be likely candidates for the initiation of cracks. There have been many ideas on how to analyze this topographical data. One method of analyzing this data is to perform metric analysis on the local level and plot those values to create a map of the distribution of the chosen metric over the surface of the corrosion. This method has been used with metrics that grew with exposure time. These metrics were analyzed and a map of these values was made.

For example, on the left in Figure 4.2.5-2(a) is a photograph that shows the locations of various cracks numbered 1-8 that formed during fatigue testing of AF1410 set A specimen #16. The final fracture occurred as indicated by the black line through the image. On the right in Figure 4.2.5-2(b) is a map of the local analysis of the Normalized Volume Loss metric. Many of the regions that indicated high volume loss are also regions where cracks initiated in the sample picture on the left.

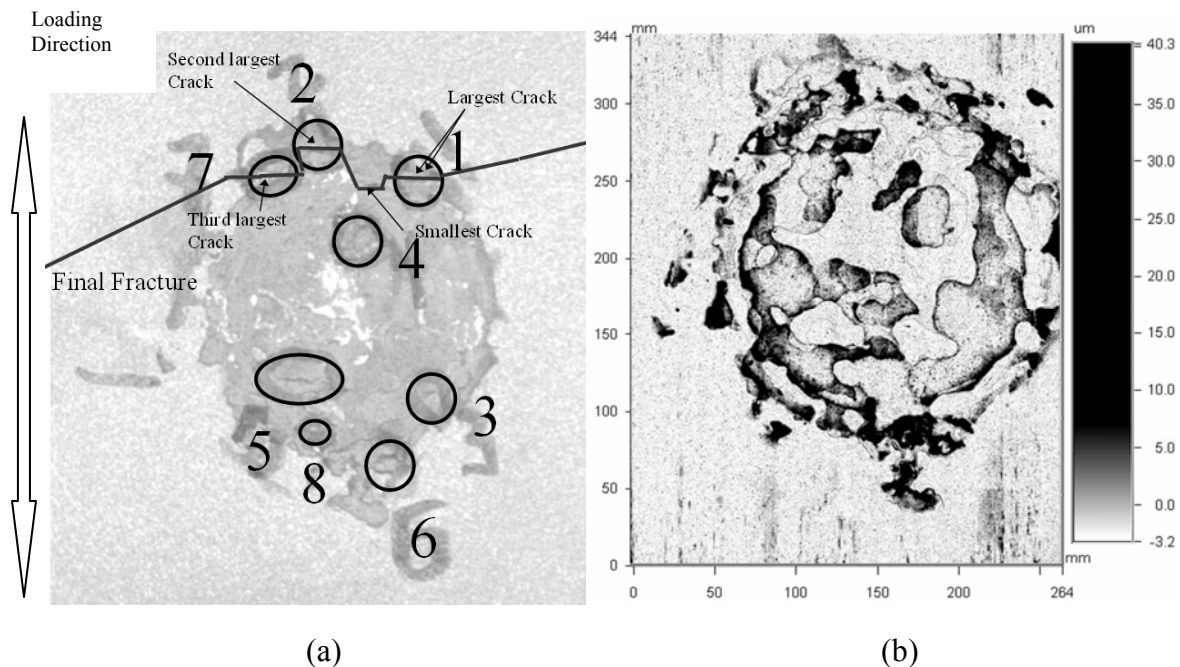


Figure 4.2.5-2. Post-Fracture Sample and NVL Local Analysis

To make use of this research, it is necessary to have a process for finding regions of interest in the corrosion patch. Analyzing the metrics on the local level promised to show zones of high stress concentration that are predisposed to nucleate cracks. The hope was that the surface topography would point to the region of high stress concentration. In this initial work, fatigue test results indicated that the final fracture surface might not form as the result of a single highest stress concentration point. Interactions between the high stress regions and corrosion feature orientation might play roles in the formation and growth of cracks.

Conclusion

When compared to alternate methods of acquiring topographic data such as laser interferometry, white-light interferometry has superior performance due to its ability to acquire very high-resolution data. Using topographic data, statistical parameters were generated to characterize the surface. Trends in these parameters were found as a function of time of exposure and a few metrics were found to give good indications of the characteristics of corrosion occurring on the sample surface. Normalized volume loss increases with increased time of exposure for all of the samples tested, indicating the overall level of corrosion the sample had experienced. Topographic maps were created for analysis using these surface characterization parameters. Analysis of the final fractographic images of the corrosion-fatigue specimens has indicated that examination of these parameters on the local level will highlight regions that are likely to crack.

4.2.6 Replication Method Study

In conjunction with the examination of different surface profile instruments, methods were researched for replicating corrosion surfaces. Replication is important when the corroded surface is not readily accessible to the instrument being used to map surface profiles. Such is the case of the interior of the arrestment shanks of interest on this program. Replication can also provide a permanent record of the corroded surface of corrosion-fatigue test specimens. When a specimen fractures in fatigue, it will produce “necking” of the surface and, thereby, distort the corrosion profile. In the event it is necessary to reexamine a corrosion surface, a replication of the surface is essential. Any replication technique that is employed should accurately reproduce the surface being replicated. Given these concerns, a study was performed of various replication methods that are available and have been used in the industry.

Veeco, the manufacturer of the white-light instrument, has conducted research on replication methods and has identified several candidate techniques [5]. One technique uses pressure-sensitive film. A second technique makes use of a two-part polymer. A third technique employs dental paste typically used to make molds of teeth. In the Veeco study, the latter two materials performed better than the pressure-sensitive tape on a variety of test standards, which included surface roughness, steps, and lateral spacing specimens. Under the Navy Corrosion-Fatigue program, additional tests were performed on the suitability of the dental paste material for use in accurately reproducing corroded surface profiles. These tests included comparisons of white-light interference microscopy measurements on test samples and corresponding replicas, including a step wedge, President Lincoln's head on a US penny, as well as a scratch found on the penny, and corrosion induced on a corrosion wafer.

Measurements on a 10.05-micron step wedge, seen in Table 4.2.6-1, show an excellent agreement between measurements on the actual step wedge and those of the replica.

Table 4.2.6-1. Comparison of Surface Metrics on Step Wedge

Surface Metrics	Step Wedge (μ)	Replica of Step Wedge (μ)
Ra	4.91	4.97
Rq	4.80	4.92
Rt	10.23	10.13

Measurements performed on President Lincoln's head on a US penny also confirm the accuracy of the dental paste material in reproducing microscopic details. Figure 4.2.6-1 compares white-light interference microscopy images of (a) the actual penny and (b) of the replica.

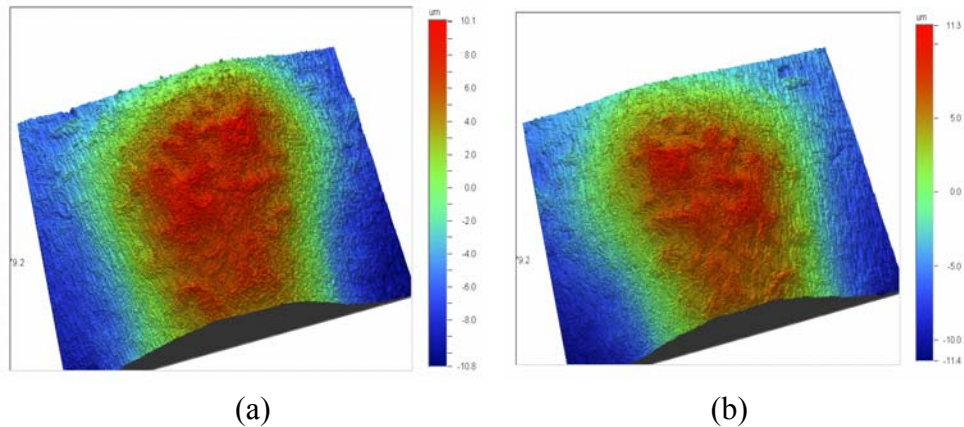


Figure 4.2.6-1. White-Light Interference Microscope Images of President Lincoln's head on a U.S. Penny: (a) the actual penny and (b) the replica. Note the replica is inverted, left to right.

A small scratch was found on this penny and was measured directly on the penny and from the replica. Figure 4.2.6-2 provides cross-sectional profiles of measurements taken directly on the penny and measurements taken from a replica of the scratch on the penny.

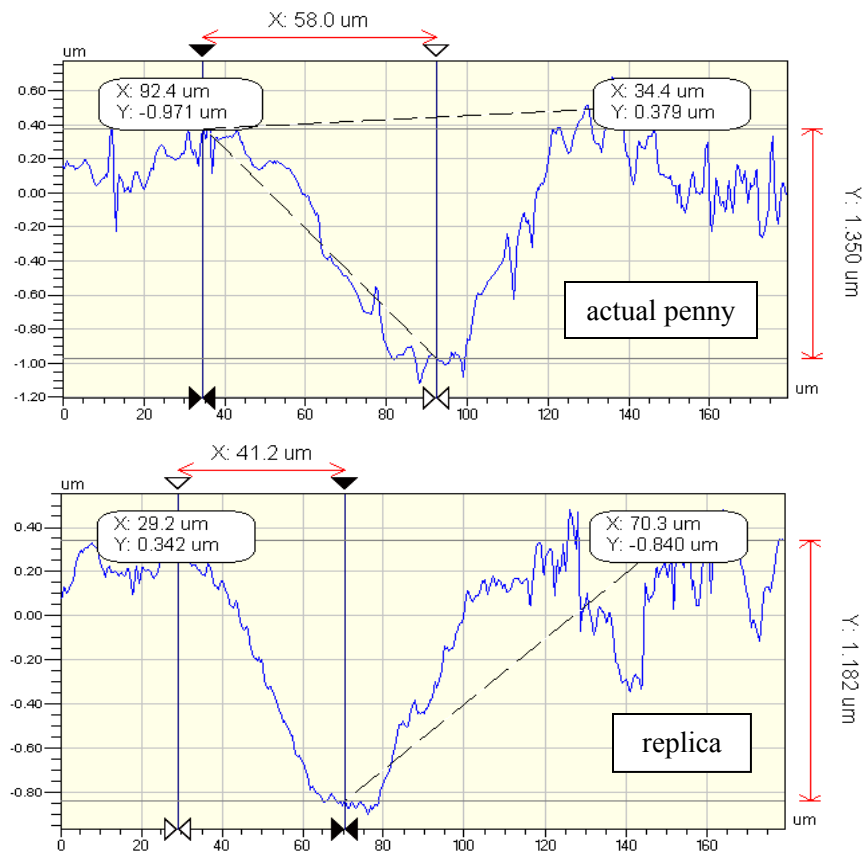


Figure 4.2.6-2. Profiles of Scratch on Penny Taken from White-Light Interference Microscopy Measurements on Actual Penny (Top) and a Replica (Bottom)

These measurements show excellent agreement between the actual scratch and the replica. The measured depth on the actual scratch was found to be 1.35 microns, while the depth determined from the replica was 1.18 microns.

A third test was performed on corrosion induced on an AF1410 wafer. White-light interference microscope images are shown in Figure 4.2.6-3. Very fine details are faithfully reproduced in the replica. Notice the replica image is inverted left to right.

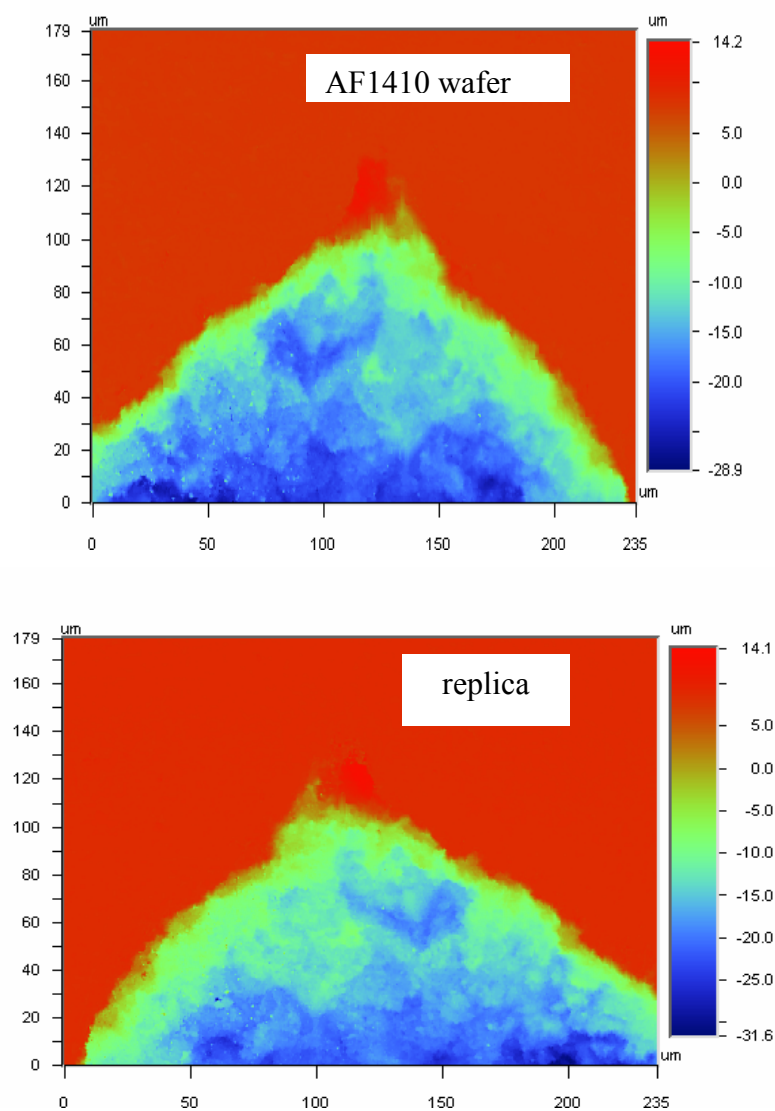


Figure 4.2.6-3. White-Light Interference Microscopic Images of Corrosion Feature Measured Directly from the AF1410 Wafer (Top) and the Replica (Bottom)

From these tests, it can be concluded that the dental paste replication technique works very well. It has a set time for replication of five minutes, with a working time of 2.5 minutes. Resolution is listed as <20 micron, but it is obviously better than this. In the referenced Veeco paper, Reprosil (Dental Wash) was listed as having resolution <0.084 microns. However, for the Navy Corrosion-Fatigue program, we used an alternate product called Aquasil Ultra, which the manufacturer, Dent Supply Caulk, said is made of a more suitable material. Tests on this material indicate that the resolution is in the range of 0.25 microns. This material is quoted as possessing a 98% recovery from deformation. The manufacturer of the dental paste reports a linear dimensional change of 0.50% after the product sets. Furthermore, the replica cleanly separates from the sample, leaving no residue, which was verified by visual inspection using an ultraviolet light microscope. Based on these observations and conclusions, a decision was made to make two replicas of all corrosion patches on the corrosion-fatigue test specimens, as well as the corrosion found on the F-18 arrestment shanks.

4.2.7 Arrestment Shank Corrosion Characterization Study

In the initial phases of this program, it was important to understand the nature of corrosion as found in real arrestment shanks. In order to quantify the characteristics of real corrosion, a small amount of replicating material was applied to the inner surface of a corroded arrestment shank and a glass slide was pressed onto the material until the edges of the slide touched the edges of the arrestment shank. The sample was allowed to cure and was removed and examined with the white-light interferometer. Figures 4.2.7-1 and 4.2.7-2 show white-light interference microscopy images and surface roughness statistics for non-corroded and corroded regions, respectively, on an arrestment shank.

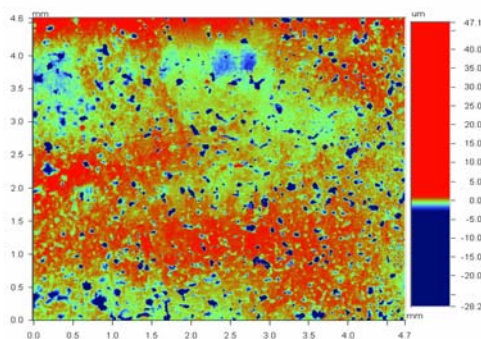


Figure 4.2.7-1. White-Light Interference Microscopic Image of Non-Corroded Arrestment Shank Replica

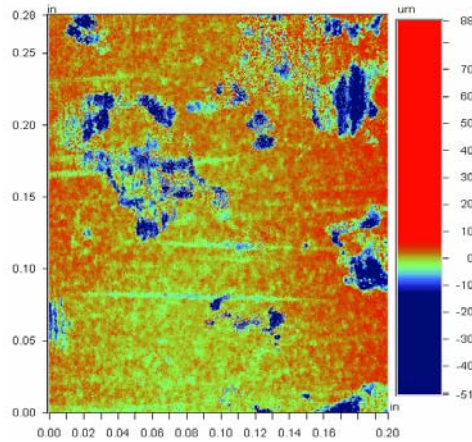


Figure 4.2.7-2. White-Light Interference Microscopic Image of Corroded Arrestment Shank Replica

Since the arrestment shanks will eventually undergo a full fatigue test, it has been critical to analyze these shanks before they are tested. Thus it was necessary to replicate the entire interior region of the shank. This replica will be scanned with the white-light interference microscope and the images will be stitched together.

Table 4.2.7-1. Roughness Metrics for Comparing Corrosion-Fatigue Specimens to Arrestment Shanks

AF1410 A (Exposure Time Hrs.)	Ra	Rq	Rsk	Rku	Rt	NVL (cm ³ /m ²)
3	2.81	4.08	-1.74	30.991	215.754	5.173333333
6	3.35	4.82	-1.28	16.775	200.142	7.118
12	4.03	6.16	-1.54	16.058	263.195	8.425625
	Ra	Rq	Rsk	Rku	Rt	NVL (cm³/m²)
Uncorroded Arrestment Shank	0.75	1.25	-2.51	13.56	11.13	1.38
Corroded Arrestment Shank	2.9	4.8	-2.53	14.56	65.23	10.84

Table 4.2.7-1 tabulates several surface roughness metrics for three corrosion-fatigue test specimens, as well as two regions on an arrestment shank – one with corrosion and one without corrosion. The arrestment shank in the non-corroded region is very similar to the as-machined surface of the corrosion-fatigue specimen, which is supported by Ra and Rq values of 0.75μm and 1.25μm, respectively. Normalized volume loss indicates the amount of material that is missing from a given area. A value of normalized volume loss between one and two denotes a small amount of material loss in this region. The combination of a negative skewness and high kur-

tosis indicates that, where features occur on these surfaces, they tend to be valleys that are sharp in nature. Also, given that the R_t – or the extreme measurement of the non-corroded section – is 11 microns, points to a surface that has little to no damage, as expected.

Examination of the statistics for the corroded region of the arrestment shank gives a picture of the nature of the corrosion damage in these components. The R_a and R_q parameters have almost quadrupled in value compared to the non-corroded shank indicating that a major change has occurred. Since there is a significant amount of surface topography to measure, the kurtosis and skewness measurements become more meaningful. They indicate the same type of features as previously discussed, with the features being slightly sharper as indicated by the small move up in kurtosis. In addition, the extreme values are much larger, which suggests larger features on the surface. Finally, the amount of volume that is lost per-unit quantity of surface area has increased most significantly, which indicates major surface damage compared the non-corroded surface.

Comparisons of the surface parameters of the AF1410 corrosion-fatigue specimens to that of the arrestment shank corrosion bring out the differences between the natures of the corrosion in these two cases. This topic is still under study, so these findings are considered preliminary. First, the two types of corrosion appear to have different topographies, which can be seen by looking at a combination of parameters. In this case, the R_a and R_q numbers are similar in both the 6-hour exposure and the arrestment shank corrosion data; however, normalized volume loss is quite different. One interpretation of this data is that, while the two pieces have experienced similar amounts of damage, the arrestment shank damage was more localized. Also, the skewness of the profile is more negative on the arrestment shank. Apparently, valleys dominate the corrosion found in the AF1410 specimens, but the valleys are not as severe as those found in the arrestment shank corrosion. Both pieces have high kurtosis, meaning that the features are sharp; it is difficult to say which is sharper. R_t holds no real information for the AF1410 specimens since these values are at or above the instrument measurement limits. Finally, visual inspection of the corrosion damage on the arrestment shanks compared to the AF1410 specimens supports the fact that the arrestment shank corrosion is more localized.

4.2.8 Markerband Study

NAVAIR performed a marker band study in order to optimize a method of providing indicators of crack dimensions at given numbers of cycles during the fatigue test. Marker bands are designed to be visible during microscopic examination of the fracture surfaces. The following describes the finalized process for marker band insertion for constant-amplitude fatigue tests.

Constant-amplitude loading was specified for all AF1410 Corrosion-Fatigue plate tests to minimize spectrum effects and to provide a direct comparison to constant-amplitude probabilistic strain-life curves. Prior to corrosion-fatigue testing, the Naval Research Laboratory conducted a fractographic study of marker cycle schemes using AF1410 Compact-Tension test specimens. Several patterns using various combinations of $R = 0.1$ and $R = 0.7$ cycles were investigated, with the peak stress (P_{\max}) held constant for each cycle. The marker cycle scheme that was chosen for use in the Batch A corrosion-fatigue tests gave the most visible marker patterns on the C-T fracture surfaces. Final marker block construction and ordering is as follows:

1. Normal load cycles are completed at the specified maximum peak stress (P_{\max}), with the minimum peak stress (P_{\min}) = $0.1 P_{\max}$.
2. Marker bands are made up of 400 constant-amplitude delay cycles of load ratio (R) = 0.7 , followed by 8 constant-amplitude marker cycles of $R = 0.1$.
3. The maximum stress remains constant at P_{\max} throughout the regular testing cycles and the marker bands.
4. Insertion of the required first block of marker bands are made after the specified number of constant-amplitude fatigue cycles at P_{\max} , with $P_{\min} = 0.1 P_{\max}$ (Table 4.2.8 -1).
5. Subsequent blocks of marker bands are introduced every 1000 cycles in accordance with the specified schedule (Table 4.2.8-1). The maximum number of marker bands in the entire set of marker band blocks is 7 (Table 4.2.8-1).
6. The pattern in Table 4.2.8-1 is repeated until final specimen fracture.

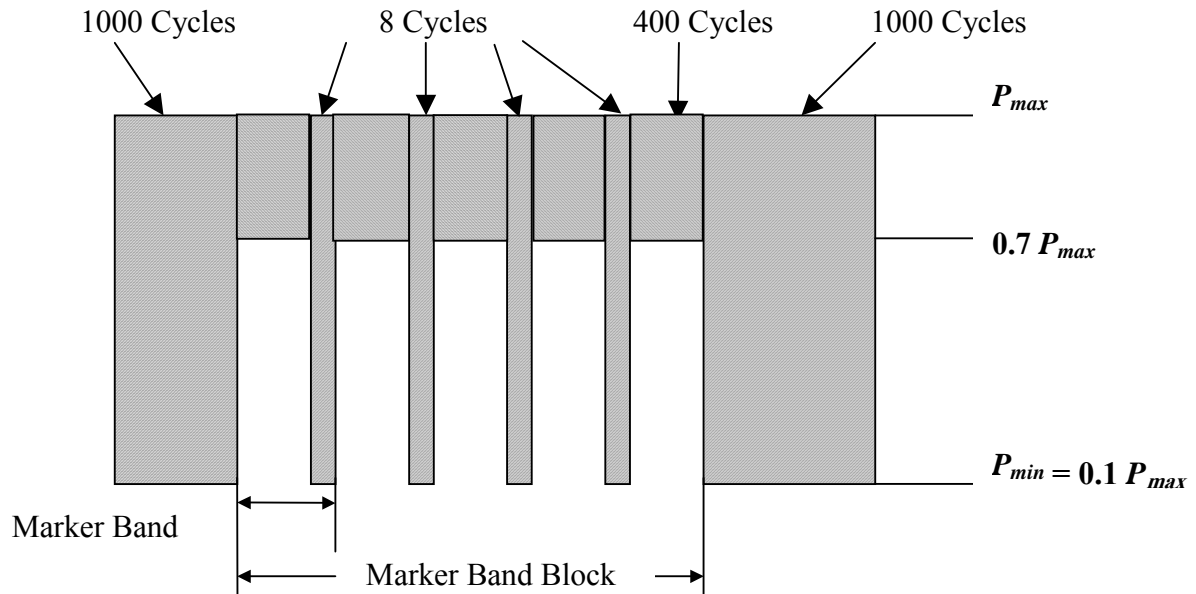


Figure 4.2.8-1. Four Marker Band Pattern

Table 4.2.8-1. Marker Band Schedule

Block Number	Constant-Amp. Cycles	Marker Bands at End of Block	Marker Cycles	Total Cycles
1	1000	3	1624	2624
2	1000	5	2440	6064
3	1000	7	3256	10320
4	1000	4	2032	13352
5	1000	6	2848	17200
Repeat Blocks 1 to 5	1000	Restart pattern at 3		

The number of bands in successive marker blocks is ordered non-sequentially to aid in distinguishing between adjacent block marker values on the fracture surface. An example of the marker block visibility on a fracture surface is shown in Figure 4.2.8-2.

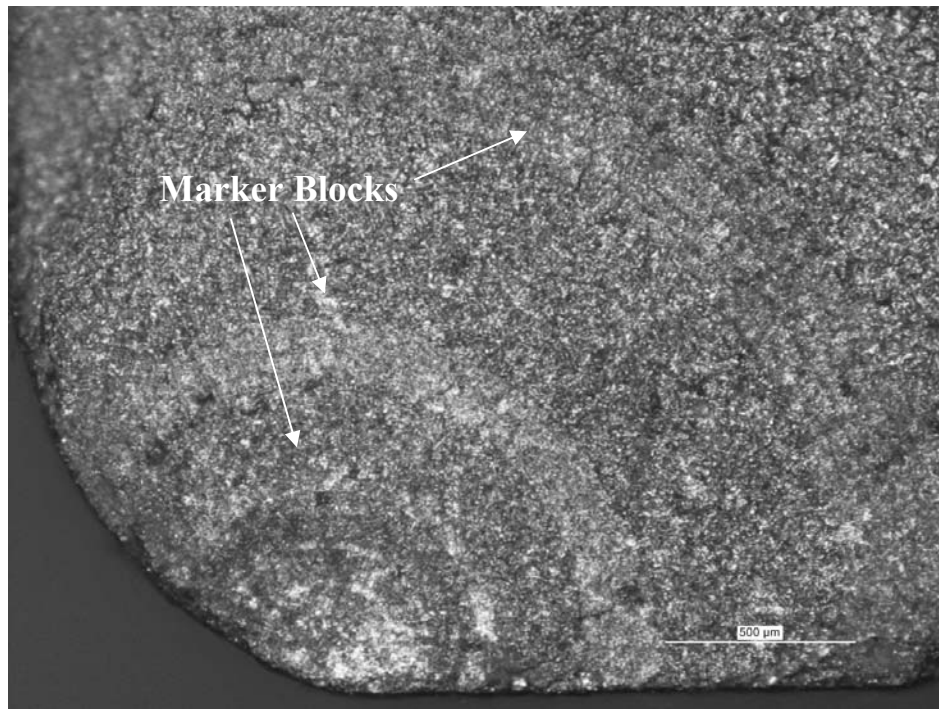


Figure 4.2.8-2. Fracture Surface of Critical Crack on Specimen #19

4.2.9 Quantitative Fractography Study

Quantitative Fractography (QF) was utilized to measure crack depths for estimating the crack initiation life of failed test specimens. The method used to take depth measurements on the specimen fracture surfaces is shown schematically in Figure 4.2.9-1.

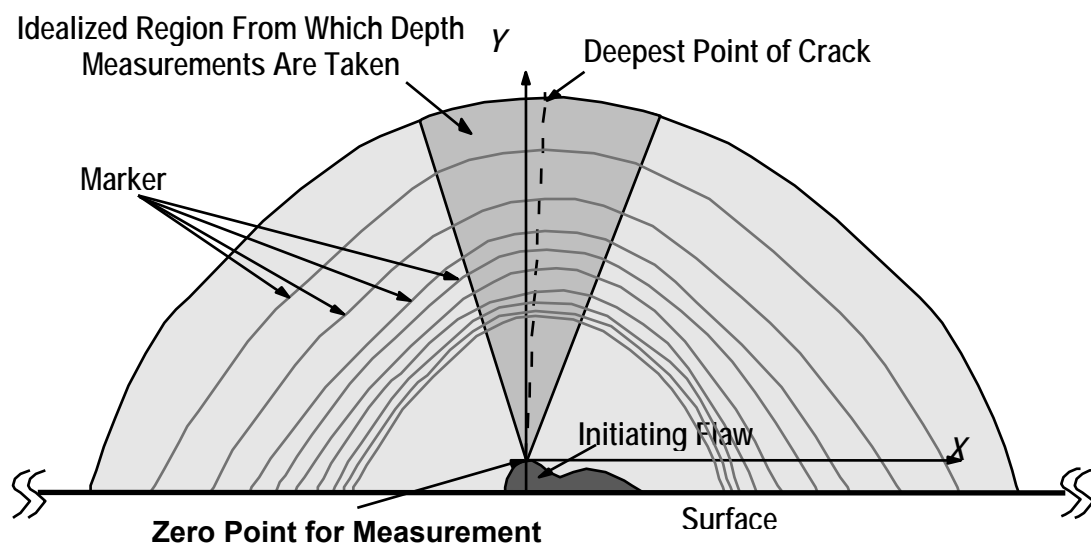


Figure 4.2.9-1. QF Crack Depth Measurement Schematic

For all specimens tested with corrosion on the surface, the origin of the crack depth measurements was set to the maximum depth of the surface flaw that initiated the critical crack in the test specimen. This convention was used to avoid the possibility of double-counting the initiating flaw depth when combining the white-light interferometry data with QF-based life predictions. The same approach was also applied to non-corroded test specimen crack origins. For all specimens, crack depth measurements were taken at the beginning and end of each marker block and from the smallest depths where the marker block boundaries were clearly distinguishable on the fracture surface to the depth that the crack transitions to growth on the shear plane. An example of QF crack depth measurements for a test specimen is plotted in Figure 4.2.9-2.

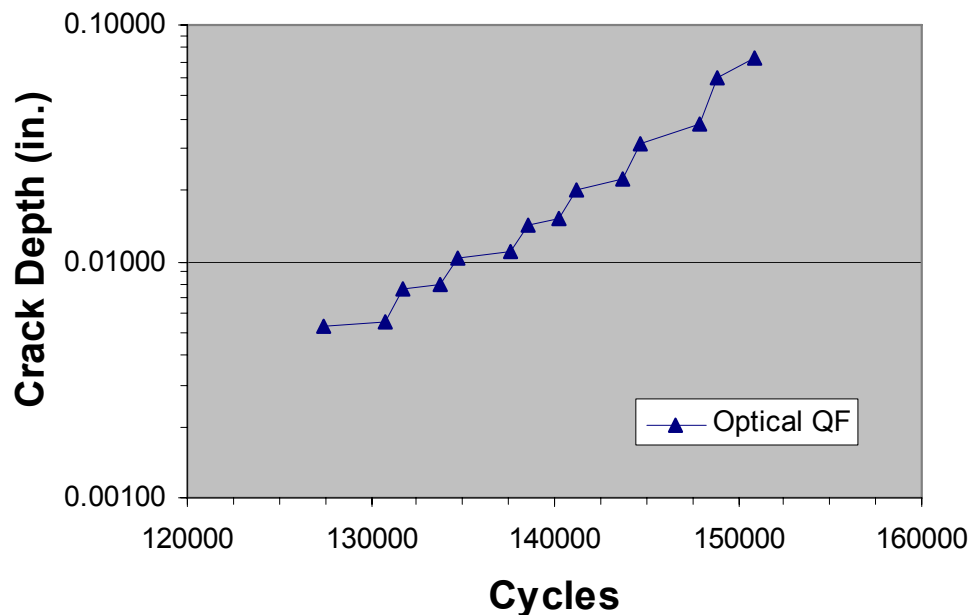


Figure 4.2.9-2. Crack Growth Curve for Specimen #19, 165 Ksi Max. Stress

Crack initiation is defined as the life to a 0.010 in. crack depth. For the Batch A test specimens, the number of cycles to crack initiation is linearly interpolated using the cycle and log crack depth values of the two QF measurements that bracket 0.010 in. All final test results are presented as life to crack initiation.

AF1410 Batch A Test Results

For corroded specimens where the critical crack originated outside the corrosion patch and for non-corroded specimens, the crack origins are at locations where local removal of the material (surface voids) has occurred due to grit blasting of the surface. An example of a grit blast-induced surface void is shown in Figure 4.2.9-3. Dimensions of the surface voids for these specimens were not measured. For corroded specimens where the critical crack originated inside the corrosion patch, the crack origins are at locations where corrosion has caused local removal of material (surface voids) on the order of 70-200 microns in width, 35-120 microns in height, and 20-100 microns deep. An example of a corrosion-induced surface void is shown in Figure 4.2.9-4. Interaction between the corrosion process and the preexisting grit blast surface voids is likely. However, the magnitude of interaction cannot be quantified with the existing test data set.

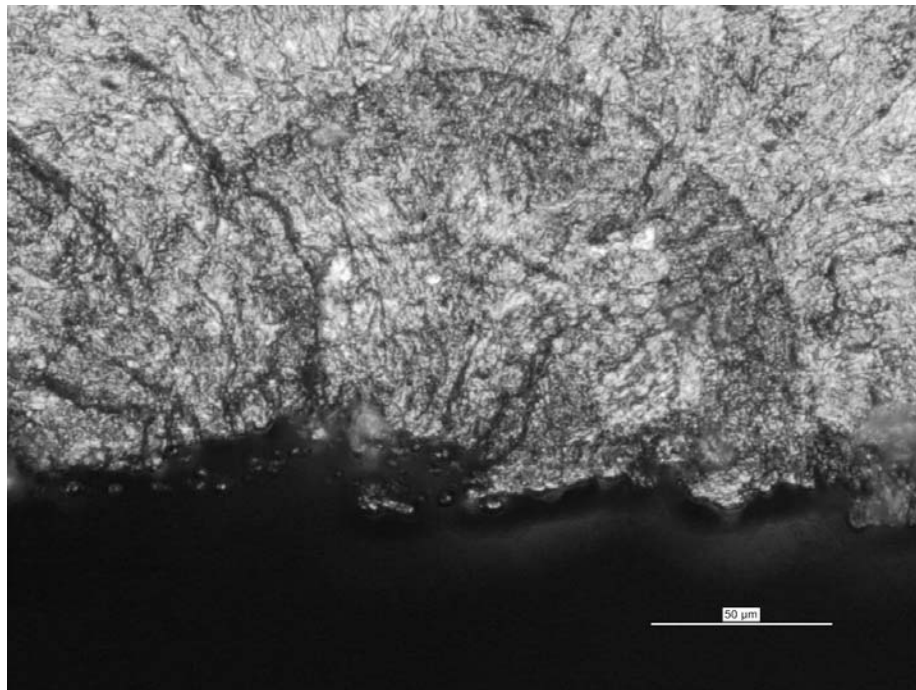


Figure 4.2.9-3. Critical Crack Origin on Specimen #61

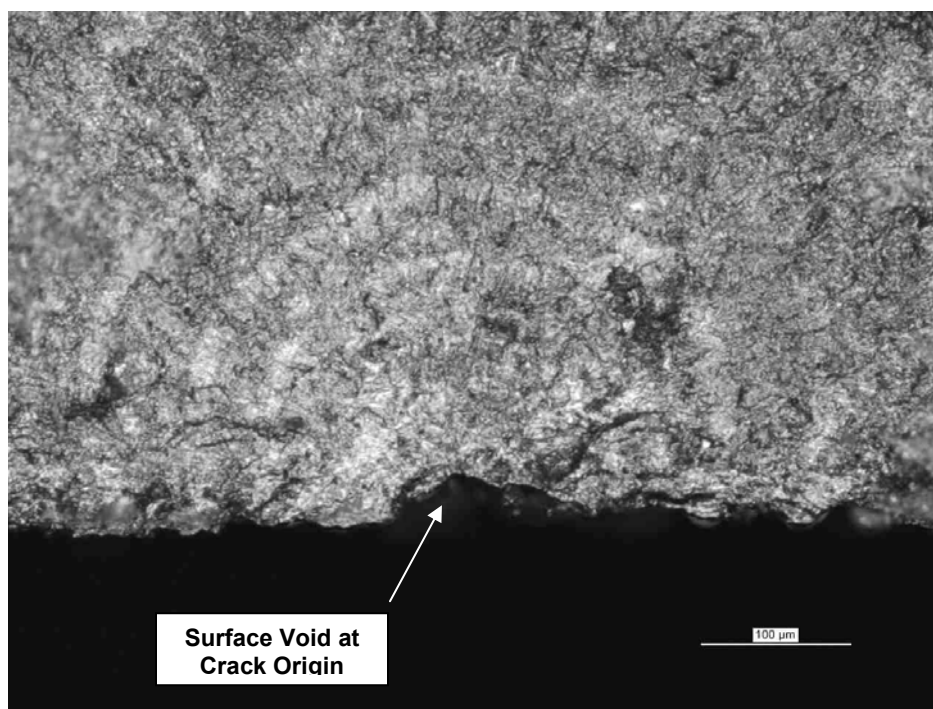


Figure 4.2.9-4. Critical Crack Origin on Specimen #29

4.3 Corrosion-Fatigue Test – AF1410 Set A

An extensive corrosion-fatigue test was conducted to assess the effect that corrosion has on fatigue life in AF1410. Experimental design and data acquisition is described in Section 4.3.1 and analysis and results are found in Section 4.3.2. Complete analysis of these test results were performed as part of the second program contract and will be reported in the corresponding final report.

4.3.1 Summary of Data Acquisition

Batch A Corrosion-Fatigue test specimens were manufactured from 14 bars of 0.375 in. \square 3.5 in. \square 96 in. of AF1410 Steel from Carpenter Technology Corp. All bars were from the same heat (Number 406909) and were delivered in a normalized and overaged condition. Chemical composition of the material is shown in Table 4.3.1-1.

Table 4.3.1-1. Chemical Composition of AF1410 0.375 in. Thick Steel Bars

C	MN	SI	P	S	CR	NI	MO	CO
0.169	0.02	0.03	0.002	< 0.001	2.09	10.19	1.04	14.31
AL	N	TI	O					
< 0.002	< 0.001	< 0.002	< 0.001					

Test plates are 0.375 in. \square 3.5 in. \square 14.0 in., with a 0.125 in. reduced thickness gage section (Figure 4.3.1-1).

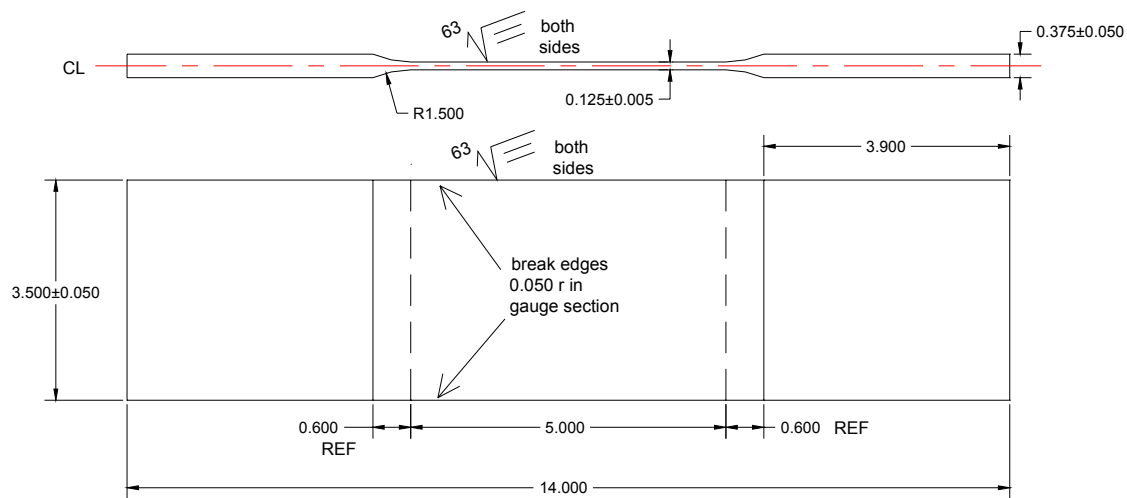


Figure 4.3.1-1. Batch A Corrosion-Fatigue Test Plate Geometry

Test plates were manufactured by Metcut Research Inc. under contract N00421-03-P-0838. The reduced thickness of the gage section was machined prior to heat treatment by peripheral milling of the plate faces with the outer circumference of an end mill. The milling process created a pattern of small ridges along the transverse plate direction, resulting in an irregular surface profile on the machined faces of the plates. The average variation in surface height due to the ridges was 60-80 μ m, depending on the plate being measured.

Because of the thin material stock that was used as a starting point, significant warping occurred on many of the plates due to the milling operation. The warped test specimens were visually classified by NAVAIR into four categories: flat, slightly warped, warped, and very warped. The specimen judged to have the worst warping was measured using an optical comparator, as shown in Figure 4.3.1-2.

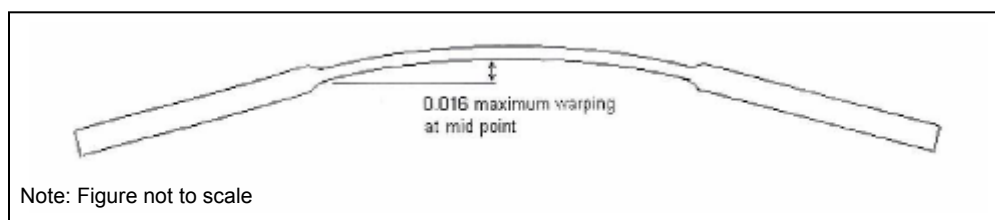


Figure 4.3.1-2. C-F Plate Warping Measurement

Since the warping of the specimens was normal to the orientation of the test machine grips, any testing would apply a significant bending moment and result in non-uniform stresses through the specimen cross-section. To minimize this effect, the specimens were straightened during heat-treat with the goal of minimizing curvature.

The test specimens were heat treated by Hercules Heat Treating Corp. per Boeing PS-15167H specification (preheat to 1100°F for 1Hr, austenitize at 1600°F for 1Hr, quench in Nitrogen, cold stabilize at -100°F for 2 Hrs, age at 950°F for 6.5 Hr.). The straightening was performed in two stages. The first stage occurred during the preheat/austenitizing process. This was accomplished by hanging the specimens in a vertical orientation from a hole drilled in the grip section. Following austenitizing and quenching, the specimens were reevaluated visually for straightness by placing the specimens on a flat surface. Specimens that still exhibited warping were then further straightened during the aging process using mechanical means. These warped specimens were placed into a jig with appropriate spacers to mechanically create the desired shape, and then subjected to the aging treatment with the remaining flat specimens. The specimens were then blasted using 120 aluminum oxide grit at 70 psi air pressure to remove any scale deposited during the heat treat and to prepare the part for plating in accordance with Boeing process specification PS 13144. As a result, the heat-treated specimens had a roughened surface caused by the grit blasting process. Because of the concern in incurring further warping of the test plates, no additional machining or polishing processes were used to try to improve the surface finish.

To evaluate the effectiveness of the straightening process, the surface residual stresses on ten specimens were measured using X-ray diffraction. The measurements were performed by American Stress Technologies, Inc. at three locations in the gage section on both sides of the specimens in the longitudinal and transverse orientations. The measurements indicated the presence of compressive residual stresses on both sides of all specimens, with an average value of 95 ksi in both the longitudinal and transverse directions. Individual measurements for all locations are listed in Table 4.3.1-2.

Table 4.3.1-2. Surface Residual Stress Measurements on AF1410 C-F Plates

Specimen #	Location	Stress (ksi)			
		Longitudinal Direction		Transverse Direction	
		Left Side	Right Side	Left Side	Right Side
41	1	-95.7	-93.5	-95.5	-97.5
	2	-93.3	-98.7	-94.4	-99.9
	3	-97.1	-95.3	-95.2	-95.9
44	1	-94.2	-95.8	-95	-94.3
	2	-97	-97.2	-99.6	-97.3
	3	-92.8	-95.6	-95.3	-99.3
54	1	-92.4	-92.2	-90.6	-92.2
	2	-98.4	-88.4	-101.4	-90.9
	3	-90.7	-91.4	-90.5	-93.9
62	1	-92.9	-92.9	-92.7	-95.5
	2	-91.2	-92	-92.3	-92.5
	3	-99.5	-94.5	-95.6	-97.5
64	1	-94.7	-91.6	-95.2	-93.4
	2	-92.3	-92.2	-90.9	-94.3
	3	-91.8	-91.1	-95.4	-93.7
3	1	-95.3	-101.5	-94.4	-99.5
	2	-96.2	-100.3	-94.7	-99.6
	3	-91.7	-96.5	-90.3	-93.1
5	1	-103.5	-91.7	-102.2	-92.9
	2	-98.5	-98.2	-100.3	-98.8
	3	-97.6	-98.2	-97.1	-98.4
10	1	-97.5	-92.9	-98.2	-90
	2	-98.3	-95.4	-99.8	-92.6
	3	-95.9	-97.6	-92.9	-94.6
11	1	-95.9	-93.5	-95	-92.3
	2	-100.9	-95.8	-100.9	-96.3
	3	-103.6	-84.8	-102.4	-86.5
39	1	-98.7	-97.9	-101.6	-99
	2	-98.1	-100.5	-100.1	-102.1
	3	-99.5	-95.8	-97.7	-97.5
MEAN (Left and Right)		-95.47		-95.8083	

The presence of compressive residual stresses on both sides of the specimens was not considered consistent with the residual stresses expected after the mechanical straightening process (the expected pattern would be a compressive stress on one side and tensile stress on the other). To further evaluate the stress origin, X-ray diffraction stress depth profiles were created on two specimens (#3 and #64). The measurements were taken at three locations in the gage section on the same side of each specimen. Rosette measurements evaluated stress in the longitudinal, transverse, and 45 degree directions. At each location, four depths were evaluated: surface, 0.001 in.,

0.002 in., and 0.003 in. This was done by using electropolishing to remove material prior to the X-ray diffraction measurements at each depth. Plots of the residual stress profiles for each plate are shown in Figures 4.3.1-3 and 4.3.1-4.

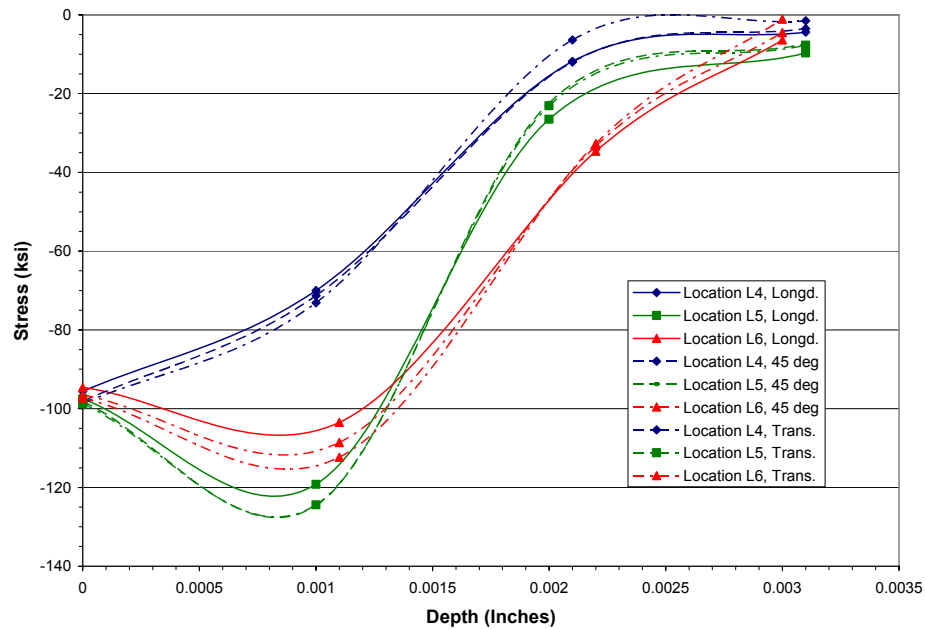


Figure 4.3.1-3. Specimen #3 Post Heat-Treat Residual Stress Profiles

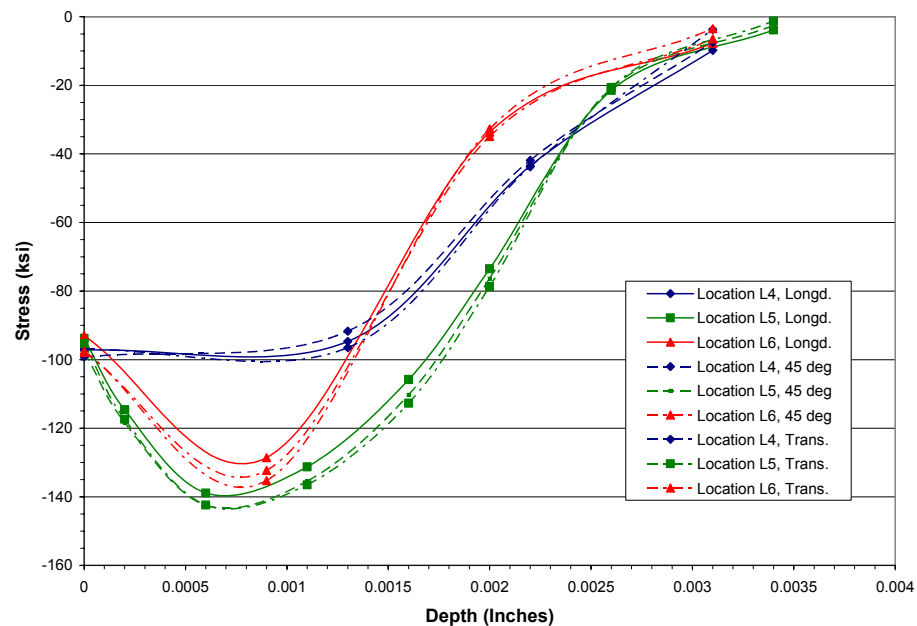


Figure 4.3.1-4. Specimen #64 Post Heat-Treat Residual Stress Profiles

The profiles show a significant residual stress to a depth of 0.001 in. with a rapid stress reduction between 0.001 in. and 0.002 in. At a depth of 0.003 in., the residual stress measurements were small and close to zero. This stress gradient is consistent with residual stresses produced by blasting processes, which typically dissipate at $0.5 \square$ the diameter of the blasting particles (0.0040" for 120 aluminum oxide grit). These two specimens were then further stress relieved by the NAVAIR materials lab by heating for 1hr at 850°F and 1 hr at 900°F, then air cooling to room temperature. Additional X-ray diffraction residual stress profiles were then measured at five depths near the locations of the initial measurements. These results are plotted in Figures 4.3.1-5 and 4.3.1-6.

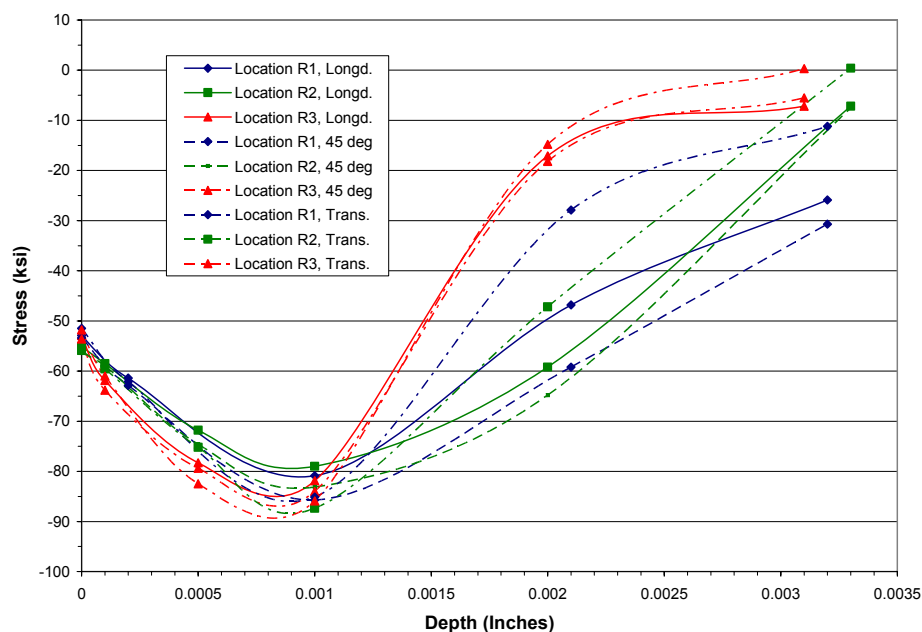


Figure 4.3.1-5. Specimen #3 Post Low-Temp. Stress Relief Residual Stress Profiles

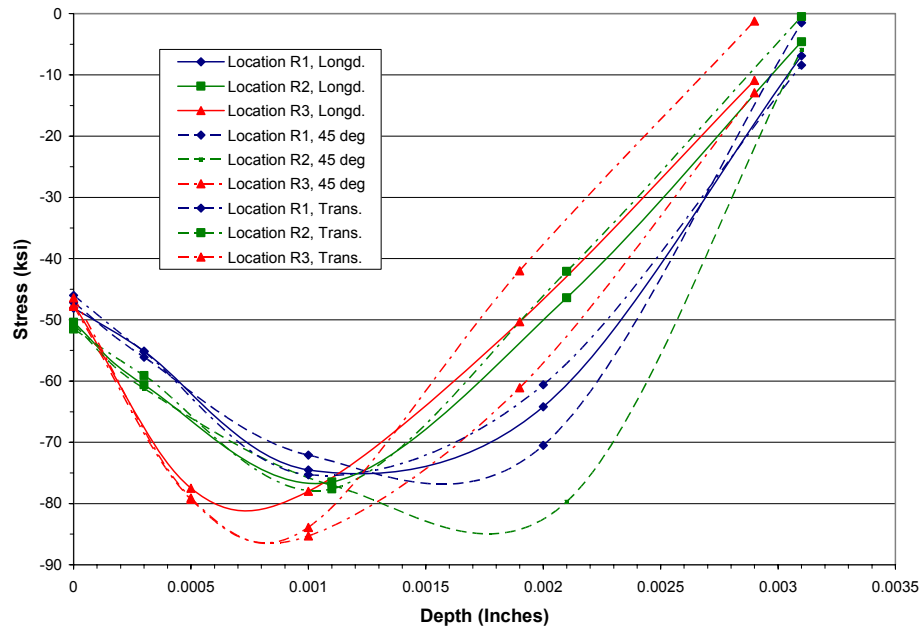
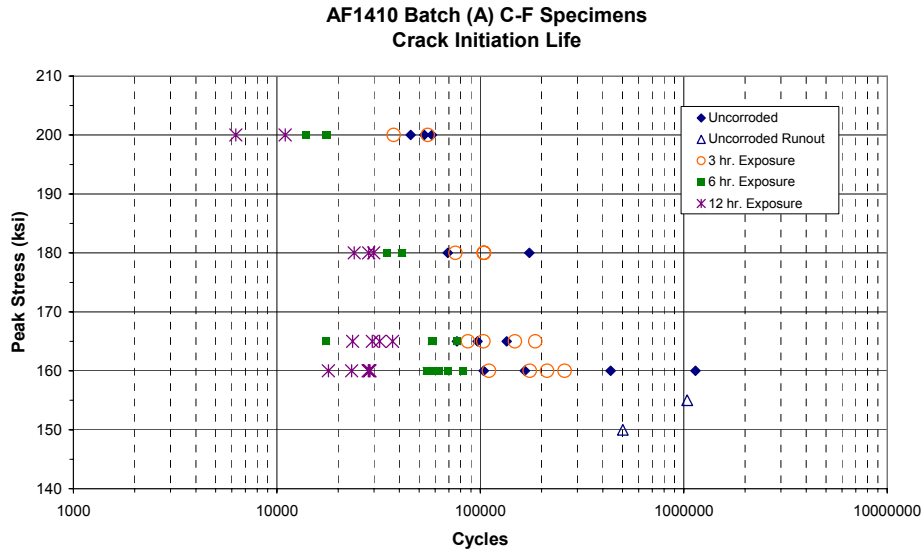


Figure 4.3.1-6. Specimen #64 Post Low-Temp. Stress Relief Residual Stress Profiles

The new measurements show that the maximum residual stress had decreased by approximately 20% and that the location of the maximum stress had shifted to a depth of approximately 0.001 in. This reduction of stress was not considered significant enough to warrant stress relief of the remaining specimens. As a result, all follow-on fatigue testing was performed on the specimens in the as-received condition from Hercules. The two specimens (#3 and 64) that underwent X-ray diffraction profile measurements were destroyed in the process and were not fatigue tested.

4.3.2 Analysis and Results

After specimen failure, each fracture surface was subjected to careful quantitative fractography measurement to ascertain the number of cycles to crack initiation (i.e., a 0.010 inch crack). Figure 4.3.2-1 summarizes the peak stress versus number of cycles to crack initiation. The plot separates specimens by exposure times. The Navy Corrosion-Fatigue Assessment program is not concerned with corrosion growth rates; however, exposure time is expected to roughly correlate to corrosion severity. At this stage in the development of corrosion metrics and models, exposure time was a convenient way to plot the data.



Corrosion-fatigue test results for all corrosion exposure levels are shown in Tables 4.3.2-1 through 4.3.2-4. Results are also plotted in Figure 4.3.2-1.

Table 4.3.2-1. Non-Corroded Corrosion-Fatigue Plate Test Results

Specimen No.	Peak Stress (ksi)	Crack Init. (cycles)	Total Life (cycles)	Critical Crack Location
39	200	57882	68973	Edge
44	200	52985	62148	Surface
55	200	45426	58030	Surface
17	180	69152	85559	Surface & Edge
61	180	174258	192261	Surface
19	165	134646	155157	Edge
50	165	76676	97980	Surface
49	165	96942	120537	Surface
1	160	103915	130829	Edge
28	160	436551	457643	Edge
11	160	1139889	1150097	Surface
40	160	165548	182602	Edge
Runouts				
1	155	1040137	1040137	-
1	150	501567	501567	-

Table 4.3.2-2. 3-Hour Corrosion Exposure Plate Test Results

Specimen No.	Peak Stress (ksi)	Crack Init. (cycles)	Total Life (cycles)	Critical Crack Location
9*	200	37555	48295	Edge
63*	200	55209	67002	Edge
15	180	75508	92805	Corrosion
31*	180	104241	123564	Surface
51*	180	104094	117205	Edge
26*	165	148133	172611	Surface
2*	165	186315	206430	Edge
29	165	86987	109542	Corrosion
62	165	103595	123974	Corrosion
36	160	175012	199784	Corrosion
21	160	110336	134737	Corrosion
33*	160	259542	286100	Surface
7*	160	213161	241575	Surface

* Fractured outside corrosion patch.

Table 4.3.2-3. 6-Hour Corrosion Exposure Plate Test Results

Specimen No.	Peak Stress (ksi)	Crack Init. (cycles)	Total Life (cycles)	Critical Crack Location
66	200	17416	27707	Corrosion
16	200	17580	27896	Corrosion
24	200	13886	23550	Corrosion
41	180	41316	58386	Corrosion
37	180	34688	52888	Corrosion
59	180	41029	57766	Corrosion
14	165	58261	79545	Corrosion
32	165	17470	30764	Corrosion
6	165	57671	79976	Corrosion
12	165	76999	99682	Corrosion
58	160	69243	92031	Corrosion
5	160	82133	103804	Corrosion
20	160	54375	75145	Corrosion
18*	160	62770	82864	Edge
42	160	58514	80041	Corrosion

* Fractured outside corrosion patch.

Table 4.3.2-4. 12-Hour Corrosion Exposure Plate Test Results

Specimen No.	Peak Stress (ksi)	Crack Init. (cycles)	Total Life (cycles)	Critical Crack Location
30	200	10981	17355	Corrosion
65	200	6290	12543	Corrosion
8	180	24014	37259	Corrosion
22	180	28271	39651	Corrosion
57	180	29882	45459	Corrosion
43	165	29423	46598	Corrosion
52	165	23556	43915	Corrosion
56*	165	31979	45140	Surface
47	165	37043	52334	Corrosion
35	160	28104	40937	Corrosion
4	160	23298	40911	Corrosion
46	160	28421	46316	Corrosion
38	160	17918	37270	Corrosion
54	160	28677	48177	Corrosion

* Fractured outside corrosion patch.

It can be clearly seen in the figure that twelve hours of exposure produces a significant drop in fatigue life when compared to zero hours of exposure. Six hours of exposure also introduces a reduction in fatigue life intermediate to twelve hours and zero hours, except possibly in the 180-ksi data. Three hours of exposure does not seem to be distinguishable from the life of those specimens with no corrosion. The severity of corrosion induced in three hours of exposure might be considered cosmetic. The results of this study will influence the test conditions for the second set of AF1410 specimens.

Additional analysis and examination of the corrosion-fatigue test specimens fracture surfaces has indicated that each crack has initiated in some sort of corrosion feature. Characterization of these features and correlations with analysis methods has taken place under the second program contract and will be discussed in more detail in the final report of that contract.

These test results provide the basis for metric development and testing various models that are discussed below. Most of this ensuing work was performed under the second program contract and will not be discussed in this report.

4.4 Continuing and Future Corrosion-Fatigue Tests

As part of the overall Corrosion-Fatigue Assessment program goals, additional tests will be performed on the second and third program contracts. A second AF1410 test will be conducted on specimens without grit blasting, which will eliminate or reduce residual stress and produce a smoother surface than seen on the first set of AF1410 specimens. This will allow the effects of residual stress and surface roughness to be removed as complicating factors in the models.

A set of 300M tests will also be carried out in addition to the AF1410 tests. This experiment will be designed to simply verify the results of the Air Force study on 300M and will only use nine corrosion-fatigue test specimens.

An Aermet 100 test will also be conducted. This material is very similar to AF1410 and is expected to give comparable results. The Aermet 100 experiment is expected to, likewise, consist of a matrix of 60 tests with parallel procedures to the AF1410 experiment.

In addition to the above specimen tests, three AF1410 arrestment shanks will be tested in fatigue. Selected corroded surfaces will be replicated and the replicas characterized with the white-light interference microscope. Predictions will be made based on the proposed model and analysis and will be compared to the actual test results.

Each of these experiments will be conducted on the remaining two program contracts and are not discussed in this report.

4.5 NDE Investigation

It was necessary to apply image-processing techniques to much of the data that were collected for this study. Those techniques will be briefly explained prior to discussing the ultrasonic techniques and the results achieved. ImageJ [8] was used to apply all of the image processing techniques used in the NDI efforts that were performed on this program.

Isolated pixel noise existed in all of the images to some extent. Such noise could distort both the visual and quantitative information. ImageJ's speckle noise removal algorithm was used to remove the isolated pixel noise.

Background intensity variations existed to a significant degree in some of the images. Such variations made it impossible initially to quantitatively compare the results among images from the various ultrasonic techniques, as well as between the ultrasonic techniques and white-light interference microscope image topography data. This variation in background intensity level was removed by first duplicating the image, applying a Gaussian filter with a very large standard deviation, and then subtracting the results of the Gaussian filtering operation from the “denoised”, but unfiltered data.

Ridges produced by the specimen fabrication process were present in some images. These ridges were caused by the initial fabrication processes and were not caused by the corrosion. Therefore, it was believed that they should be removed so that only the corrosion-induced surface variation would be measured. Fourier domain techniques suggested by Russ [9] were used to remove the ridges from the white-light data and from the ultrasonic data. More recent studies (conducted while preparing this report) have indicated that removal of the ridges by the Fourier domain techniques distorts the data in areas between regions. And, the distortions in the ultrasonic data are different from those in the white-light interference microscope data.

Image registration – translation, rotation and scaling – was required before the ultrasonic data could be quantitatively compared with the data from the white-light interference microscope data. The requirement arises because the white-light data and the ultrasonic data were collected at vastly different lateral resolution levels. In addition to that problem, the specimens were aligned somewhat differently relative to the orthogonal scanning directions during data collection. The ImageJ plug-in, TurboReg that was developed by [10], was used to register the images.

Quantitative correlations were accomplished with Image_CorrelationJ, another plug-in for ImageJ. This plug-in was developed by Dr. Gary Chinga [11].

4.5.1 Ultrasonic Technologies

Angle-Beam Backscattered Amplitude

In this technique, the transducer is inclined at a slight angle from the surface normal, and the transducer is raster-scanned in a plane parallel to the surface of the specimen. The specimen must be aligned parallel to the scanning direction to achieve satisfactory results. The advantages of this technique are its considerable sensitivity to changes in surface elevation and relative ease

of application; but, there are a few disadvantages to this technique as well. First, the technique is directional, that is, it detects and images only those features that are aligned nearly perpendicular to the transducer. Second, if the surface is roughened prior to corrosion – as is the case for grit-blasted and shot-peened surfaces – then it can be extremely difficult to image the roughness that is due to corrosion. Finally, this technique does not provide topography information.

UDRI personnel applied this technique to flat AF1410 specimens that had been smoothed and then blasted with grit of various diameters and at different pressures. Stylus profilometer measurements were made at specific locations on each of the grit-blasted regions. The plots in Figure 4.5.1-1 show the relationship between the root-mean-square (RMS) values calculated from the ultrasonic data and the RMS values calculated from the stylus profilometer data.

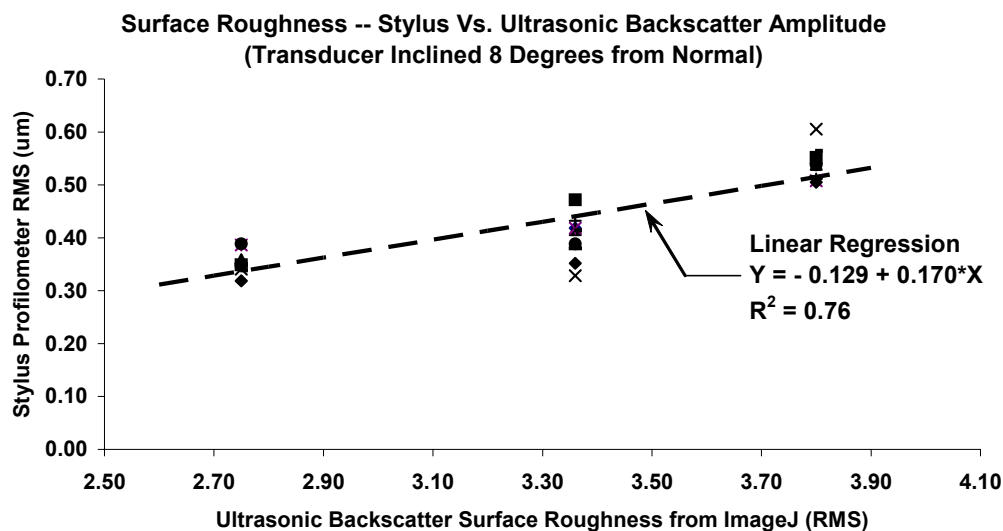


Figure 4.5.1-1. Stylus Profilometer RMS Results vs. RMS Results from Ultrasonic Angle-Beam Backscattered Amplitude from Grit-Blasted Surfaces

The promising results from the application of the angle-beam backscatter technique to grit-blasted specimens led to the application of this technique to one of the 3-hour corrosion-exposure specimens (#23). The topography of the corrosion on that specimen had been precisely mapped with UDRI's white-light interferometric microscope; thus, there would be an excellent standard with which to compare the ultrasonic testing results. The results from the ultrasonic angle-beam backscatter amplitude scan and from the white-light interference microscope examination are presented in Figure 4.5.1-2(a) and (b). It is obvious from these images that the angle-beam backscatter technique has not imaged the corrosion topography. There are two probable reasons for this. First, the surface was roughened by grit blasting prior to corrosion generation; second, many of the corrosion-topography features are not perpendicular to the ultrasonic beam. It appears most likely that the roughness that is due to the grit blasting has masked the roughness that is due to the corrosion topography.

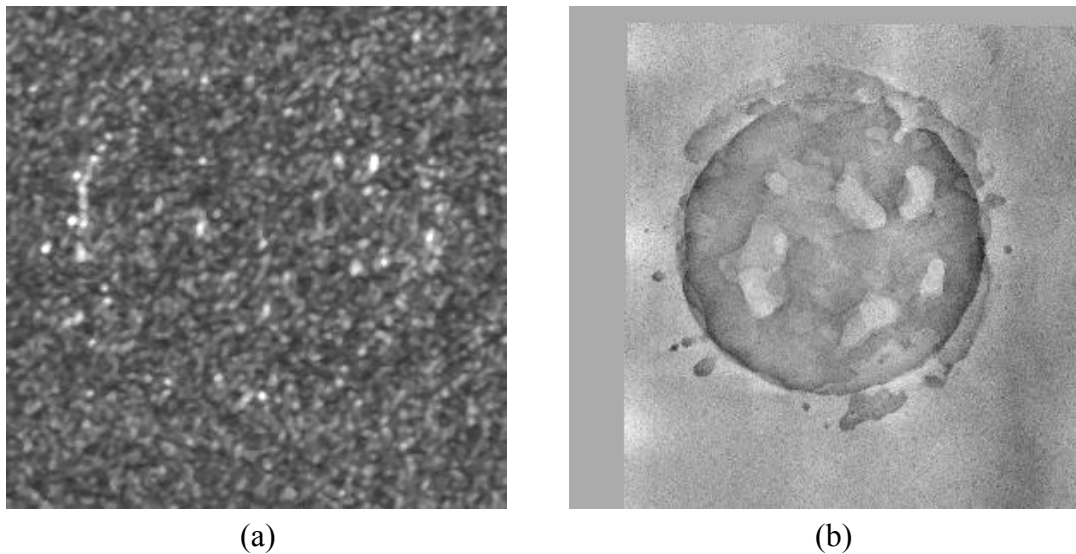


Figure 4.5.1-2. Images of Specimen #23: (a) ultrasonic angle-beam backscatterd amplitude and (b) white-light interference microscope topography

Normal-Incidence Reflected Amplitude

The application of this technique is identical to that used for the angle-beam backscatter technique, except that the ultrasonic beam from the transducer must be aligned perpendicular to the surface that is to be examined. The plane of the specimen must be aligned with the scan plane for precise results. The advantages of this technique are that it is non-directional, easily implemented, and has had decades of use for anomaly detection and location (in two dimensions). Some

of the disadvantages include decreased sensitivity to small changes in elevation relative to that of the angle-beam backscatter technique and a lack of ability to provide topography information.

This technique is normally implemented by capturing a single value or a couple of values (e.g., peak-to-peak values) from the signal that is reflected from the surface that is being examined. In UDRI's implementation for this program, the entire radio frequency (RF) signal was digitized and stored at each sampling location on the specimen. This implementation was chosen because it would allow advanced signal processing techniques to be applied to the signal, such as Fourier spectroscopy. Such applications will be discussed in later paragraphs. For the normal-incidence reflected amplitude technique that is discussed here, only the peak-to-peak amplitude from the signal was used.

The results from the normal-incidence reflected amplitude scan are shown in Figure 4.5.1-3(a). For comparison purposes, the white-light interference microscope image is provided Figure 4.5.1-3(b). It is obvious that the image that was generated from the normal-incidence reflected amplitude data more-closely resembles the image from the white-light data than does the image from the angle-beam backscatter data.

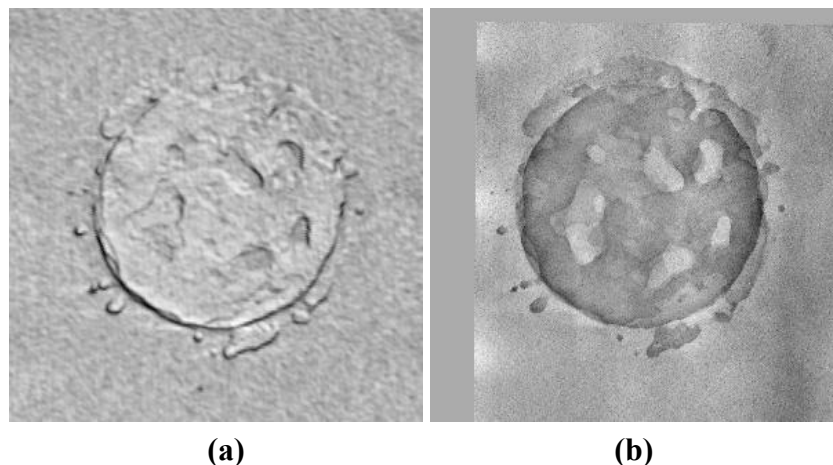


Figure 4.5.1-3. Images of Specimen #23: (a) ultrasonic normal-incidence reflected amplitude and (b) white-light interference microscope topography

Because of the visual similarity of the two images in Figure 4.5.1-3, the images were correlated using Image_CorrelationJ [11] in ImageJ [8]. This correlation procedure can be based on single pixels or local regions of pixels. Regions that consisted of 7 and 14 pixels each were used for the correlation of the images described here. The results for “Normal-Incidence Amplitude” in

Table 4.5.1-1 show that there is no significant correlation between the two images. This would tend to indicate that the visual correlation is due to the edges, which outline the features in the image that were generated from ultrasonic data, as opposed to the topography information that is present in the white-light data.

Table 4.5.1-1. Linear Correlation of Results from Ultrasonic Data with Results from White-Light Interference Microscope Data

Technique	Explained Variance (%)	
	With Ridges Removed	Without Ridges Removed
Region Size = 7 Pixels		
Normal Incidence Amplitude	2	6
Local RMS	2	1
Time-to-Peak	59	87
Phase-Slope	59	88
Region size = 14 Pixels		
Normal Incidence Amplitude	1	4
Local RMS	0	0
Time-to-Peak	56	88
Phase-Slope	56	90

Fourier Spectroscopy (Local RMS) of Ultrasonic Data

Several investigators [12-16] have noted that the Fourier magnitudes of signals that are reflected from rough surfaces decrease as a function of frequency at a much greater rate than do the Fourier magnitudes of signals that are reflected from smooth surfaces. In particular, some [12,13] have demonstrated that the slope of this decrease with frequency of the Fourier magnitudes can be used to generate local RMS values (or at least RMS-related) values at each sampling point during an ultrasonic scan. The advantage of such a technique is that it does provide local RMS estimates of the surface roughness (i.e., at each sampling point). The disadvantages are that it does not provide topographic information and is computationally intensive. It requires the digitization of the normal-incidence RF signal at each sampling point and the subsequent calculation and manipulation of the Fourier magnitude spectra to produce the estimated RMS value at each sampling point.

UDRI developed a software algorithm to calculate the local RMS values and applied it to the digitized ultrasonic RF signals that were acquired for application of the normal-incidence reflected

amplitude technique. The results are presented in Figure 4.5.1-4 along with the white-light image of the specimen. The correlation between these two images was performed in the manner described for the normal-incidence reflected amplitude image in Figure 4.5.1-3. These results are provided in Table 4.5.1-1 above, which are identified as “local RMS”. Once again, whereas there is some visual correlation between the images generated from the two types of data, there is no significant correlation (with or without ridge removal) between the data from which the two images were generated.

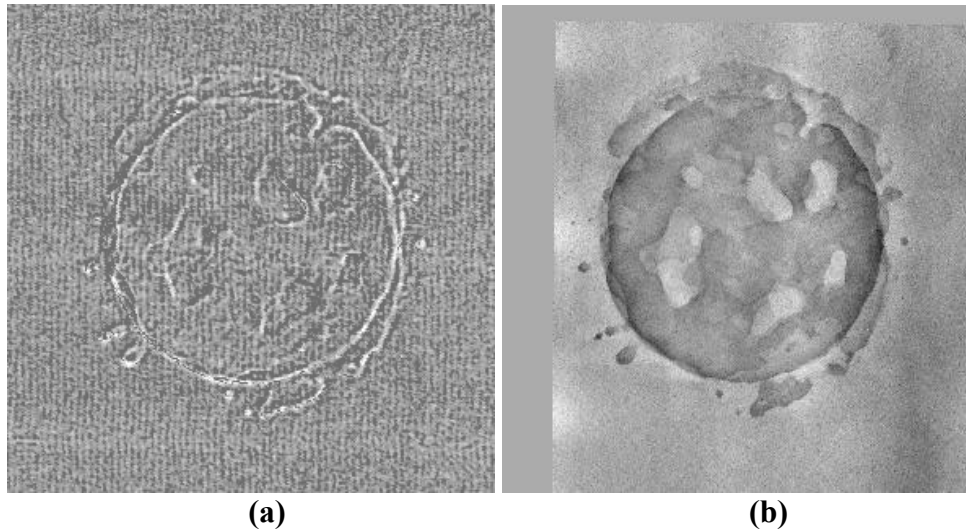


Figure 4.5.1-4. Images of Specimen # 23: (a) ultrasonic RMS and (b) white-light interference microscopy

Topographic Information – Time-of-Flight-to-Signal-Peak Technique

This technique makes use of the digitized ultrasonic RF signals that were acquired for the normal-incidence reflected amplitude technique to generate elevation (topographic) data of the specimen surface. It does so by measuring the time that it takes for the ultrasonic signal to travel to and return from each sampling location on the specimen. That travel time is directly related to the distance between the transducer and the specific sampling location of the specimen. The time is effectively measuring relative elevations (relative to a calibration value) at each location. This is a very simple and long-used technique that requires only the measurement of the time-to-peak-value of the specimen. The uncertainty in time (and, therefore, in elevation) is directly related to the rate at which the signal is digitized and to the ability to precisely locate the signal peak. The major disadvantage of the technique is that it is susceptible to noise.

The image generated from the time-of-flight (TOF) data is shown in Figure 4.5.1-5(a). The visual similarity between that image and the image that was generated from the white-light data is quite good. The correlation results are provided in Table 4.5.1-1 and labeled “Time-to-Peak”. The correlation results without removing the ridges from the two data sets (ultrasonic and white-light) are quite significant – 87% and 88% explained variance depending upon region size. After the ridges are removed by image processing, the explained variances drop to 57% and 59% depending on region size. These results are still significantly better than the analogous results from the local RMS data (2% explained variance for both region sizes). Thus, there is a useful correlation between the time-of-flight-to-signal-peak data and the white-light data, especially if the data are not processed to remove ridges.

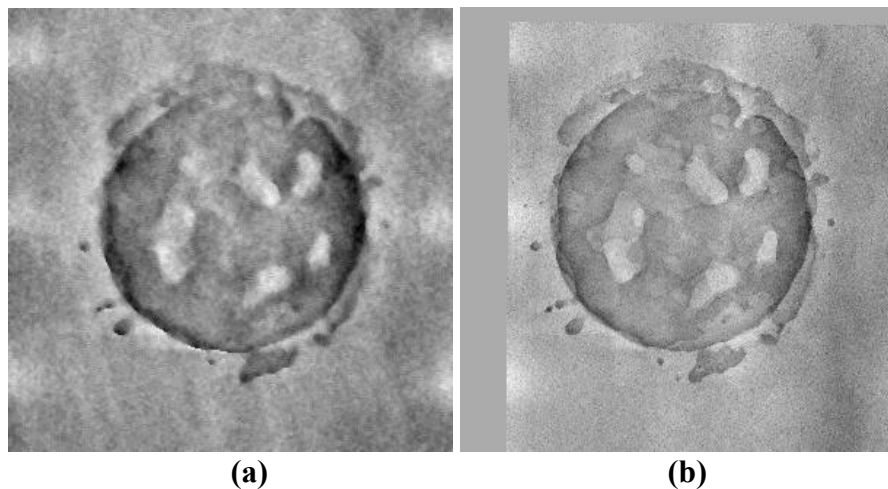


Figure 4.5.1-5. Images of Specimen #23: (a) time-of-flight to peak and (b) white-light interference microscopy

Topographic Information – Fourier Phase-Slope Technique

The data used for the application of this technique is the same as that used in the previous three techniques. As was the case for the generation of the local RMS data, the Fourier transform is applied to each of the digitized signals. Unlike processing for the generation of local RMS data, the technique discussed here makes use of the Fourier phase spectra rather than the Fourier magnitude spectra. As it turns out, the slope of the Fourier phase as a function of frequency provides a direct measure of the time-of-flight (TOF) of the ultrasonic signal from the transducer to the specimen and back again. Unlike the TOF-to-peak data, however, the Fourier phase-slope technique takes advantage of more of the information that is present in the signal. This makes the results less susceptible to noise and somewhat more sensitive to small changes in elevation than the

TOF-to-peak data. It is more computationally intensive than is the TOF-to-peak technique, but not as computationally intensive as the calculation of the local RMS values.

Image results from application of the Fourier phase-slope technique to the normal-incidence RF reflected signals are shown in Figure 4.5.1-6(a) along with the image from the white-light interference microscope data (b), and the image from the TOF-to-peak data (c). The image from the Fourier phase-slope data and the image from the TOF-to-peak data are strikingly similar from a visual aspect. The results from correlating the Fourier phase-slope image data with the TOF-to-peak image data (Table 4.5.1-2) reveal that there is, indeed, a very high degree of correlation between the data from which those images are generated: 97% and 99% explained variance for the two region sizes after removal of the ridges. When the ridges are removed, the explained variance is 99% regardless of region size.

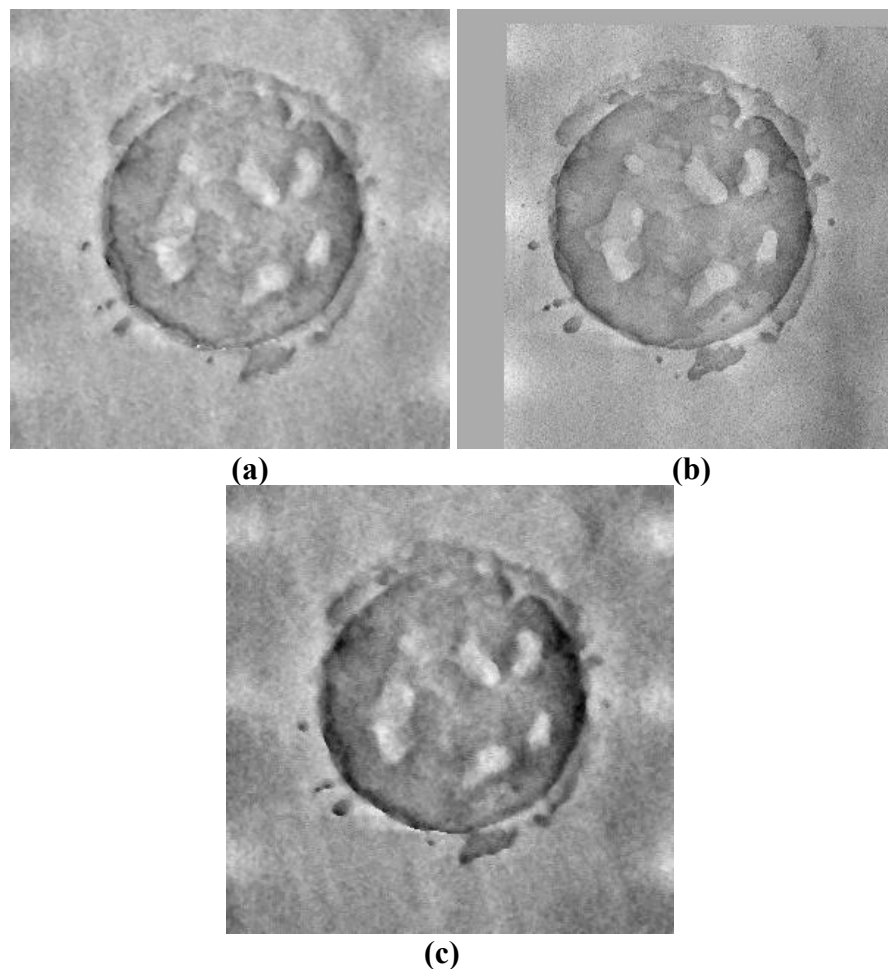


Figure 4.5.1-6. Images of Specimen #23: (a) phase-slope, (b) white-light interference microscopy, and (c) time-of-flight to peak

Table 4.5.1-2. Linear Correlation of Results from Ultrasonic Time-to-Peak with Ultrasonic Phase-Slope Results

Technique	Explained Variance (%)	
	With Ridges Removed	Without Ridges Removed
<i>Region Size = 7 Pixels</i>	97	99
<i>Region size = 14 Pixels</i>	99	99

The explained variance (from Table 4.5.1-1 labeled “Phase-Slope”) for the correlation between the ultrasonic phase-slope image data and the white-light interference microscope image data is 88% and 90%, depending upon region size. After ridge removal, the explained variance drops to 59% and 56% for the two region sizes.

4.5.2 Discussion

Visual observation of the various images generated by applying different signal-processing techniques to the ultrasonic data indicates that the time-of-flight-to-signal-peak and the phase-slope signal processing provide the same, or nearly the same, information. And, the results generated from those two techniques show a highly significant correlation with the topographic data obtained from the white-light interference microscope, so long as the ridges due to machining are not removed by the chosen image processing technique. Apparently, the Fourier-domain filtering technique that was applied for ridge-removal purposes distorts the two types of data sets (ultrasonic and white-light) in different ways.

The other signal-processing techniques (extraction of peak-to-peak amplitude and generation of local RMS values) provide information that emphasizes local changes in elevation (primarily edges), but do not provide actual elevation information. Images that are generated from amplitude and local RMS values, while demonstrating visual similarity to images generated from the white-light interference microscope, do not correlate with the elevation (topographic) information from the white-light interference microscope.

At present, the correlations described here should be viewed with caution, for they result from the analysis of a single 3-hour-exposure corrosion sample (#23). Data have been collected from many other samples with 3-, 6-, and 12-hour exposures, but that data have not yet been analyzed. The remaining data must be analyzed before reliable conclusions can be made. In addition, the metric that will need to be derived from NDI data has not yet been established. Until that metric has been established, the type of NDI information that will be required will remain unknown. The NDI investigation will continue on the subsequent program contracts.

Section 5

Modeling

5.0 Introduction

The objective of the modeling portion of this program was to develop a methodology to model the effect of corrosion on high-strength steel components and to estimate the remaining life of these components based on a suitable metric. The UDRI corrosion modeling efforts consisted of evaluating finite element, boundary element, and elasticity techniques for the prediction of stress concentration factors of corroded surfaces as a means to quantify corrosion severity. The remainder of this section of the report summarizes ESRD and UDRI modeling efforts.

5.1 Analysis of the F-18 Arrestment Shank

As part of a subcontract on the Corrosion-Fatigue Assessment program, ESRD performed a detailed finite element analysis of the F-18 arrestment shank (without corrosion). The objective of the investigation was to develop an approach that would be quick and accurate. ESRD made use of a two-step process to reduce the computational time. First, the number of elements and the number of degrees of freedom were reduced by studying a subdomain of the arrestment shank. A hierarchical model was also used for the cases of interest. Enforcement of proper boundary conditions maintained accuracy of the solution. Three load conditions were considered: hook bounce, cable pickup, and aircraft arrestment. The geometric configuration was adjusted for each case according to the corresponding angle. ESRD studied four cases: 1) a linear analysis, 2) a geometric nonlinear analysis, 3) a multi-body contact analysis using a local subassembly, and 4) a detailed local analysis using multi-body contact solution boundary conditions. Details of these studies are found in Section 6.4 of the ESRD Final report in Appendix A. ESRD found that their proposed approach solved the problem in a fraction of the time required if the entire system were modeled.

5.2 Finite Element Modeling of Corrosion

A central aspect of the Corrosion-Fatigue Assessment program was the development of analysis methods to determine the effect that corrosion has on fatigue life of high-strength steels. ESRD has played a principal role in this regard. Early in the program, ESRD identified an important issue with regard to modeling the fine corrosion details with finite element models. That is, finite element models generally depend on an assumption of continuum mechanics. Section 5.2.1 sum-

marizes the UDRI study to address this issue. ESRD also developed methods to extract k_{teff} from laser profilometry surface maps using StressCheck®. This study is discussed in Section 5.2.2. Section 5.2.3 reviews ESRD efforts to idealize corrosion features to calculate k_t .

In addition to the research conducted by ESRD, several other modeling studies were conducted on the program. In Section 5.2.4, a matrix of simulated corrosion defects is defined. Section 5.2.5 reviews results of analysis on these simulated defects by different analysis software packages as a function of various defect parameters. Section 5.2.6 discusses methods developed to incorporate residual stress into a corrosion model. Section 5.2.7 describes a global-local model that held promise for incorporating corrosion. Each of these studies was based on efforts to employ finite element methods to the problem of corroded situations.

5.2.1 Grain Size and Study of Continuum Assumption

The goal of the modeling effort has been to determine an equivalent stress concentration factor for structural and mechanical components damaged by corrosion. These stress concentration factors will be used for estimation of fatigue life expended using procedures established under this program. In this development effort, there have been several issues for consideration. By definition, the stress concentration factor is the ratio of the maximum stress to the first principle stress that would exist if the corrosion damage were not present. There is an implied scale in this definition of stress concentration factor: that the first principle stress is constant over a representative volume element (RVE). RVE is, by definition, approximately 10 grain sizes. On the scale of RVEs or smaller, the methodology of continuum mechanics should generally be inapplicable. One concern was that the size of corrosion damage might happen to be on the order of 20 microns, while the size of the RVE was estimated to be on the order of 100 microns, meaning that the model assumptions of continuum mechanics might not be valid. If this were the case, then other modeling approaches would need to be considered. Given these concerns over the continuum theory basis for StressCheck® analysis, grain size measurements from optical images were taken on corroded and non-corroded samples from both directions on the samples. Measurements were also taken of the dimensions of corrosion features.

The AF1410 being studied under this program is low-carbon, high-alloy steel. Optimum properties are obtained by multi-step heat treatments, including quenching, to create a highly tempered

martensitic structure with very finely dispersed precipitated austenite particles. This structure is seen in the optical image shown in Figure 5.2.1-1 taken from an etched AF1410 sample. The martensitic microstructure of this material can be hard to characterize. In practice, the parent austenite grains of the material microstructure are widely correlated to the properties of heat-treated steels and, therefore, may be measured. However, in low-carbon steel, the martensite laths form in domains within the parent austenite and, sometimes, a martensite domain size can be defined. One can accentuate the martensite domain or “packet” size, which is related to the prior austenite grain size, by etching and using crossed polarized light as shown in the image.

There are no grains in martensitic materials, but measurements can be made of either the prior austenite grains or the martensite packets (i.e., lath bundles). Table 5.2.1-1 presents results from measurements taken from several different AF1410 samples.

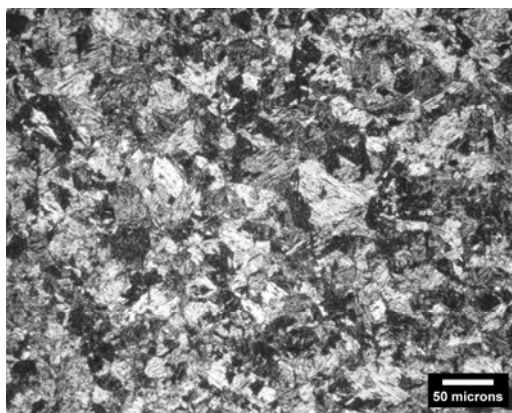


Figure 5.2.1-1. Scanning Electron Micrograph of a Cross-Section of AF1410 Showing Martensitic Packets

Table 5.2.1-1. Measurements of AF1410 Material Martensitic Packets

AF1410 Material	Direction	HRC (avg)	Martensite “packet” size (ASTM number)	Martensite “packet” size (avg microns)
As-received bar stock	Transverse	35.4	15.9	8.8
	Longitudinal		18.9	8.2
Corrosion wafer U3	Transverse	46.1	14.4	9.0 to 9.5
	Longitudinal		15.7	8.9 to 9.3
AF1410-2 (#2)	Transverse	----	15.4	8.8 to 9.4

Similar measurements have been made on 300M. Figure 5.2.1-2 shows an SEM image of a 300M sample. Table 5.2.1-2 shows tabulated measurements of the martensite packets on this sample.

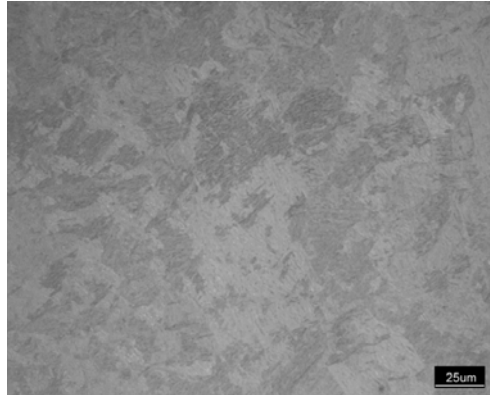


Figure 5.2.1-2. Scanning Electron Micrograph of a Cross-Section of 300M Showing Martensitic Packets

Table 5.2.1-2. Measurements of 300M Material Martensitic Packets

300M Material	Martensite “packet” size (avg microns)	Martensite “packet” size (ASTM number)
Corrosion wafer 300M-2	15.4	9.1

Corrosion features in AF1410 have been found to be on the order of microns, some extending to tens of microns, in depth and width. Essentially, corrosion features occur at all length scales. Some corrosion features are smaller than the martensite packets, as well as some considerably larger. This means that the measurable features of the material microstructure are about the same size as the corrosion features of interest. Based on this observation and after some discussion, it was decided to do additional exploratory experiments using ultrasonic force microscopy to determine the degree of variability of the elastic modulus across this same length scale. If this variability is limited, then the continuum model might still be viable.

A Digital Instruments’ Dimension 3000 Nanoscope IIIa Atomic Force Microscope (AFM) was used to characterize the surface topography of a sample. To map the local, near-surface elastic properties, the AFM was modified to measure the surface displacements generated by propagating an acoustic wave through the sample. When operated in the acoustic-wave mode, the AFM is referred to as an Ultrasonic Force Microscope (UFM). To operate in the UFM mode, the system was configured to measure the surface displacements generated by a piezoelectric transducer that was bonded to one face of the sample. The transducer was excited by a low-amplitude, continuous-wave radio-frequency signal in the range of 400 to 1000 kHz. At low amplitude excitation, the sensing tip is expected to be in contact with the sample at all times. Under this condition, the amplitude detected by the sensing tip is proportional to the elastic stiffness of the material under the tip.

AFM surface topography and UFM amplitude images were obtained at the same location on a polished sample of AF1410. Images were acquired at different magnifications. In these exploratory experiments, only a small region of the sample was imaged. The maximum scan area was limited to $100\text{ }\mu\text{m} \times 100\text{ }\mu\text{m}$. Although it was possible to scan an area as large as this, the features in the images are not very clear. Moreover, flatness of the surface becomes a concern in imaging larger areas with high resolution. Because of these limitations, imaging was limited to a maximum of $20\text{ }\mu\text{m} \times 20\text{ }\mu\text{m}$ and most of the images were acquired by scanning areas that were less than $3\text{ }\mu\text{m} \times 3\text{ }\mu\text{m}$.

Figures 5.2.1-3 through 5.2.1-5 show the AFM surface topography images (left side of each figure) and the corresponding UFM amplitude images (right side of each figure) at different magnifications. Figure 5.2.1-3 shows an image with a scan area of $2.95\text{ }\mu\text{m} \times 2.95\text{ }\mu\text{m}$. The maximum height feature is 20 nm. AFM shows some topographic features that are about 20 nm, while most of the image surface topography is uniform. The UFM amplitude image has uniform contrast indicating very small variations in the elastic stiffness. Figure 5.2.1-4 is an image of a slightly different region on the sample. In this region, the AFM surface topography image shows scratches and a few high spots. The UFM image also reveals the scratches. Other than the scratches, the contrast in the UFM image is quite uniform. The smaller features appear to be precipitates and the variations in elastic stiffness are not significant. Figure 5.2.1-5 shows higher magnification images of areas inside the region of Figure 5.2.1-4. At higher magnifications, a larger contrast in AFM surface topography is observed. The maximum height features are slightly higher than 10 nm. On the other hand, the UFM image shows the precipitates clearly separated from the matrix. It appears that, at high magnifications, significant differences in the elastic properties between the matrix and the precipitates are being observed. Although the UFM contrast shows differences between the matrix and the precipitates, it is a difficult task to provide quantitative information about the elastic properties.

All of the images appear to be within a single packet. No attempts were made to obtain images in a different packet in order to determine the inter-packet variability in the elastic properties. Therefore, these measurements are considered inconclusive. Additional scanning acoustic microscopy measurements might add some value, but it is doubtful that these types of tests can be definitive about the degree of variability in elastic properties at this scale. At this point in time, the issue concerning the validity of the continuum assumption is considered unresolved.

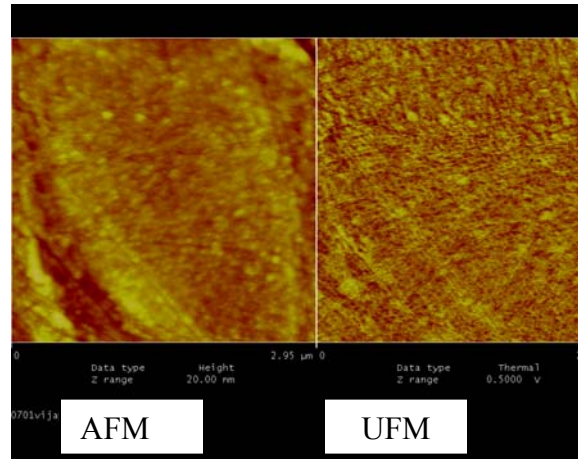


Figure 5.2.1-3. AFM and UFM Images of a Sample of AF1410

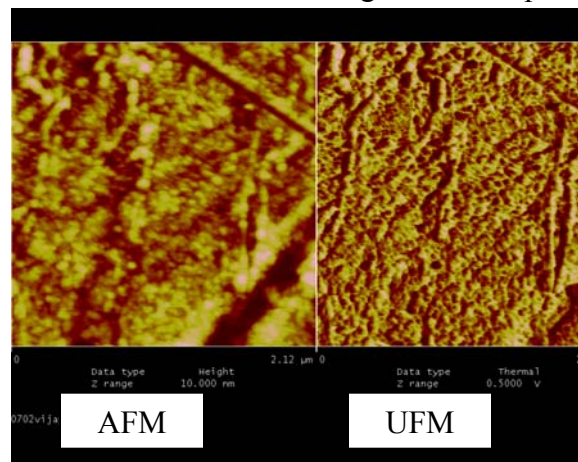


Figure 5.2.1-4. AFM and UFM Images of Different Region of a Sample of AF1410

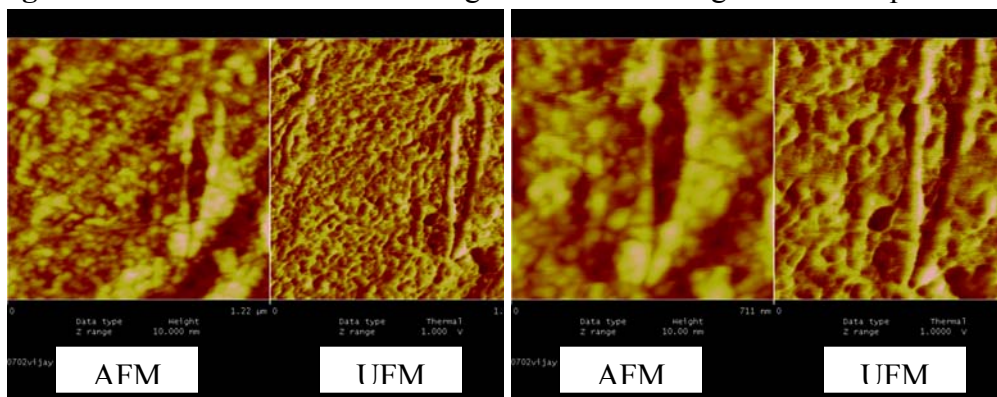


Figure 5.2.1-5. Increased Magnifications of AFM and UFM Images in Figure 5.2.1-4

5.2.2 k_{teff} Extraction Using Laser Profilometry Surface Mapping and StressCheck®

ESRD conducted a study of profilometry data and meshing in the context of StressCheck, their finite element software analysis tool. Early in the program, white-light interference microscopy profiles were not available, so ESRD used laser profile data from a prior Boeing program. Two-

dimensional slices through the corroded surface were processed by spline fitting. It was understood that two-dimensional analysis is unlikely to provide an adequate approximation to real corrosion. An investigation of a two-dimensional model of corrosion was performed to investigate the effects of surface representation on the computed k_{teff} . One significant conclusion drawn from this study was that the complexities of the computational problem increases drastically with increased spatial resolution of the corrosion maps. The problem will only get worse when three-dimensional analysis is attempted unless it can be demonstrated that the smaller scale features are unimportant. Additional details and conclusions from this study can be found in Section 6.1 of the ESRD Final Report located in Appendix A.

5.2.3 Corroded Surface Idealization with Consideration of k_t Sensitivity

ESRD developed an approach to geometrically idealize a corroded surface in StressCheck® by using features actually observed in corroded specimens, such as rings, pits, and waviness. The goal was to simplify a corroded surface into basic Parasolid geometries without adversely affecting, to any substantial degree, the maximum k_{teff} for each geometry. ESRD also included a study of the effects of residual stress on the results. ESRD found that k_{teff} is very sensitive to the details of idealization. Residual stress was modeled as a temperature distribution. They found that residual stress will delay the initiation of fatigue failure, but will tend to accelerate the growth of defects once the defect has penetrated the surface layer where the residual stresses are compressive. Additional details, results, and conclusions of this study are presented in Section 6.2 of the ESRD Final Report found in Appendix A.

5.2.4 Matrix of Simulated Corrosion Defects

Because of the complexity of a true corroded surface geometry, an analysis matrix was generated to compute stress concentration factors for a variety of corrosion-like damage states for both crevice and pitting corrosion. These simplified geometries could be modeled easily and accurately with various commercially-available analysis codes to evaluate each code's potential effectiveness for the modeling of stress concentration factors on corroded surfaces.

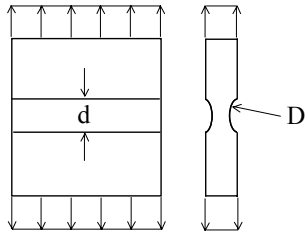
Figure 5.2.4-1 depicts the nine simulated corrosion geometries that were considered. These cases represented a combination of crevice and pitting corrosion states for isolated and adjacent corrosion damage like that anticipated in the actual hardware. Table 5.2.4-1 indicates the particular

combinations of corrosion damage sizes and relative spacings considered, where “D” is the three-dimensional diameter of the feature, “d” is the surface diameter of the feature, and “s” is the spacing between the features. The size of the defects considered in this portion of the UDRI modeling effort was selected to be sufficiently large to enable fabrication of test coupons for which stress concentrations could be measured via x-ray diffraction. However, based on the analysis results discussed in the next section, it was later determined that the experimental verification was not required.

Crevice Corrosion Features

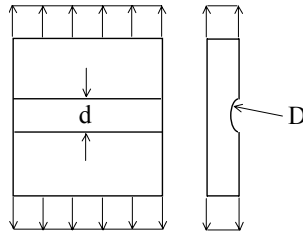
Case 1.

Symmetric Cylindrical Notches



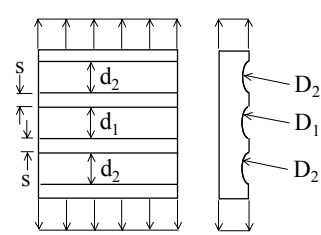
Case 2.

Single Cylindrical Notch



Case 3.

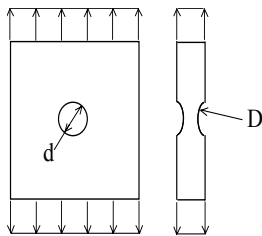
Adjacent Cylindrical Notches



Pitting Corrosion Features

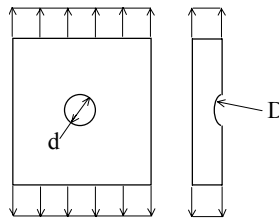
Case 4.

Symmetric Spherical Depressions



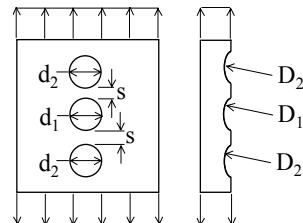
Case 5.

Single Spherical Depression



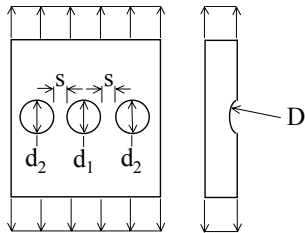
Case 6.

Adjacent Spherica Depressions (Aligned With Loading)



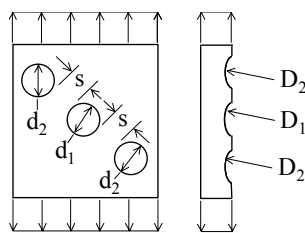
Case 7.

Adjacent Spherical Depressions (Transverse to Loading)



Case 8.

Adjacent Spherical Depressions (Oblique to Loading)



Case 9.

Depressed Surface

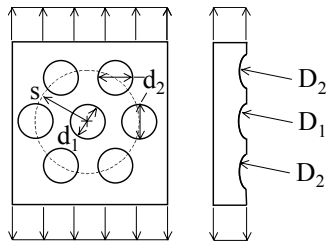


Figure 5.2.4-1. Simulated Corrosion Defect Geometries

Table 5.2.4-1. Simulated Corrosion Defect Matrix

Cases: 1, 2, 4, and 5			Cases: 3, 6, 7, 8, and 9						
D (in)	Depth (in)	d (in)	D1 (in)	Depth1 (in)	d1(in)	D2 (in)	Depth2 (in)	d2 (in)	s (in)
1.000	0.005	0.141	1.000	0.010	0.199	1.000	0.010	0.199	0.025
1.000	0.010	0.199	1.000	0.010	0.199	1.000	0.010	0.199	0.050
1.000	0.015	0.243	1.000	0.010	0.199	1.000	0.010	0.199	0.075
1.000	0.020	0.280	1.000	0.010	0.199	1.000	0.010	0.199	0.100
0.500	0.005	0.099	1.000	0.010	0.199	1.000	0.010	0.199	0.150
0.500	0.010	0.140	1.000	0.010	0.199	1.000	0.010	0.199	0.200
0.500	0.015	0.171	1.000	0.010	0.199	1.000	0.010	0.199	0.250
0.500	0.020	0.196	0.125	0.010	0.068	0.125	0.010	0.068	0.010
0.250	0.005	0.070	0.125	0.010	0.068	0.125	0.010	0.068	0.020
0.250	0.010	0.098	0.125	0.010	0.068	0.125	0.010	0.068	0.030
0.250	0.015	0.119	0.125	0.010	0.068	0.125	0.010	0.068	0.040
0.250	0.020	0.136	0.125	0.010	0.068	0.125	0.010	0.068	0.060
0.125	0.005	0.049	0.125	0.010	0.068	0.125	0.010	0.068	0.080
0.125	0.010	0.068	0.125	0.010	0.068	0.125	0.010	0.068	0.100
0.125	0.015	0.081	1.000	0.005	0.141	1.000	0.010	0.199	0.025
0.125	0.020	0.092	1.000	0.005	0.141	1.000	0.010	0.199	0.050
0.0625	0.005	0.034	1.000	0.005	0.141	1.000	0.010	0.199	0.075
0.0625	0.010	0.046	1.000	0.005	0.141	1.000	0.010	0.199	0.100
0.0625	0.015	0.053	1.000	0.005	0.141	1.000	0.010	0.199	0.150
0.0625	0.020	0.058	1.000	0.005	0.141	1.000	0.010	0.199	0.200
			1.000	0.005	0.141	1.000	0.010	0.199	0.250
			1.000	0.020	0.280	1.000	0.010	0.199	0.025
			1.000	0.020	0.280	1.000	0.010	0.199	0.050
			1.000	0.020	0.280	1.000	0.010	0.199	0.075
			1.000	0.020	0.280	1.000	0.010	0.199	0.100
			1.000	0.020	0.280	1.000	0.010	0.199	0.150
			1.000	0.020	0.280	1.000	0.010	0.199	0.200
			1.000	0.020	0.280	1.000	0.010	0.199	0.250
			0.125	0.005	0.049	0.125	0.010	0.068	0.010
			0.125	0.005	0.049	0.125	0.010	0.068	0.020
			0.125	0.005	0.049	0.125	0.010	0.068	0.030
			0.125	0.005	0.049	0.125	0.010	0.068	0.040
			0.125	0.005	0.049	0.125	0.010	0.068	0.060
			0.125	0.005	0.049	0.125	0.010	0.068	0.080
			0.125	0.005	0.049	0.125	0.010	0.068	0.100
			0.125	0.020	0.092	0.125	0.010	0.068	0.010
			0.125	0.020	0.092	0.125	0.010	0.068	0.020
			0.125	0.020	0.092	0.125	0.010	0.068	0.030
			0.125	0.020	0.092	0.125	0.010	0.068	0.040
			0.125	0.020	0.092	0.125	0.010	0.068	0.060
			0.125	0.020	0.092	0.125	0.010	0.068	0.080
			0.125	0.020	0.092	0.125	0.010	0.068	0.100

5.2.5 Assessment of Various Corrosion Modeling Codes

A series of analyses was performed to compute stress concentration factors for the variety of corrosion-like damage states indicated in the previous section. Three different commercially-available analysis codes having three different solution techniques (h-version finite element analysis in ABAQUS, p-version finite element analysis in StressCheck[®], and boundary element analysis in BEASY) were considered.

The first goal of the analyses was to demonstrate the capability of the various codes to accurately predict stress concentration factors on a variety of representative corroded configurations. The second goal of the analyses was to gain a better physical understanding of the influence of the corrosion surface roughness parameters on the resulting stress concentration factor and change in

fatigue behavior. Once the software tools were validated, analysis efforts could proceed to actual corroded surface geometries and the incorporation of probabilistic techniques to quantify the inherent variability of corrosion phenomena.

The analysis results indicated that all three techniques provided accurate stress concentration factor estimates for a wide variety of corrosion-like geometries. Typical results are presented in Figures 5.2.5-1 and 5.2.5-2 for individual and adjacent spherical pits.

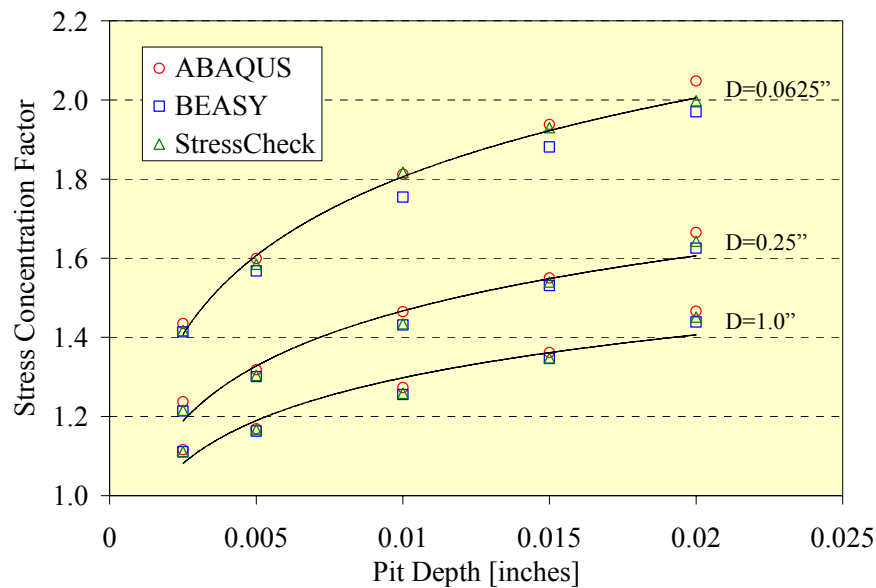
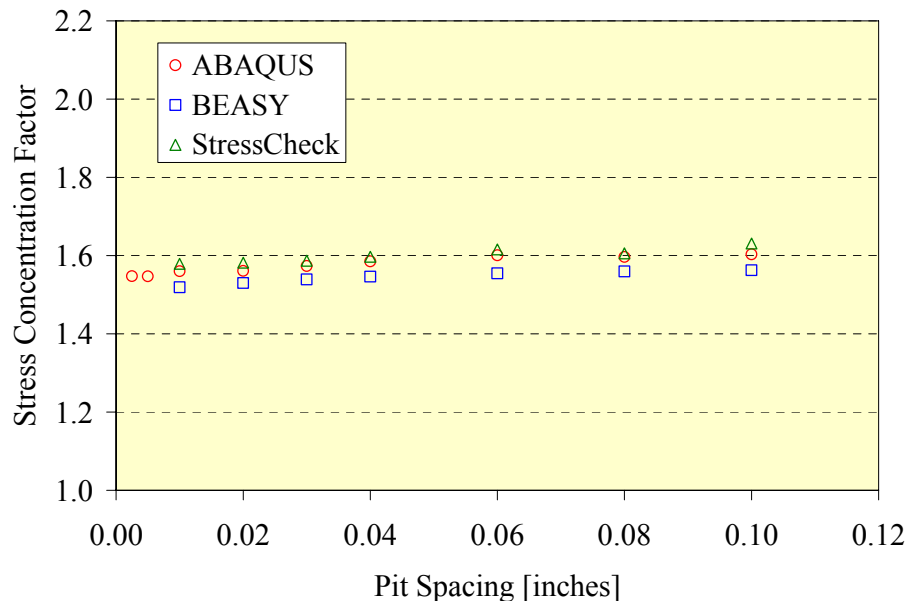


Figure 5.2.5-1. Analysis Results of Various Individual Spherical Pit Geometries (Case 5)



Figures 5.2.5-2. Analysis Results of Various Adjacent Spherical Pit Geometries (Case 6 with, $d=0.01$ inches, $D=0.125$ inches)

Based on the analyses, efforts were made to identify a physical relationship between the corroded surface geometry and the resulting stress concentration factor. Two findings were identified. First, there was a strong relationship between depth and size of the surface defect and the stress concentration factor as indicated in Figure 5.2.5-3, which is the same data as plotted in Figure 5.2.5-1 except normalized by the corresponding pit diameter (d). This was potentially significant for the development of a metric by which to assess corrosion severity in field applications. Second, as was indicated in Figure 5.2.5-2, there was no influence of adjacent defects on the stress concentration factor at each surface defect. This indicated that any potential metric would only have to evaluate the local defect geometry without any far-field influences.

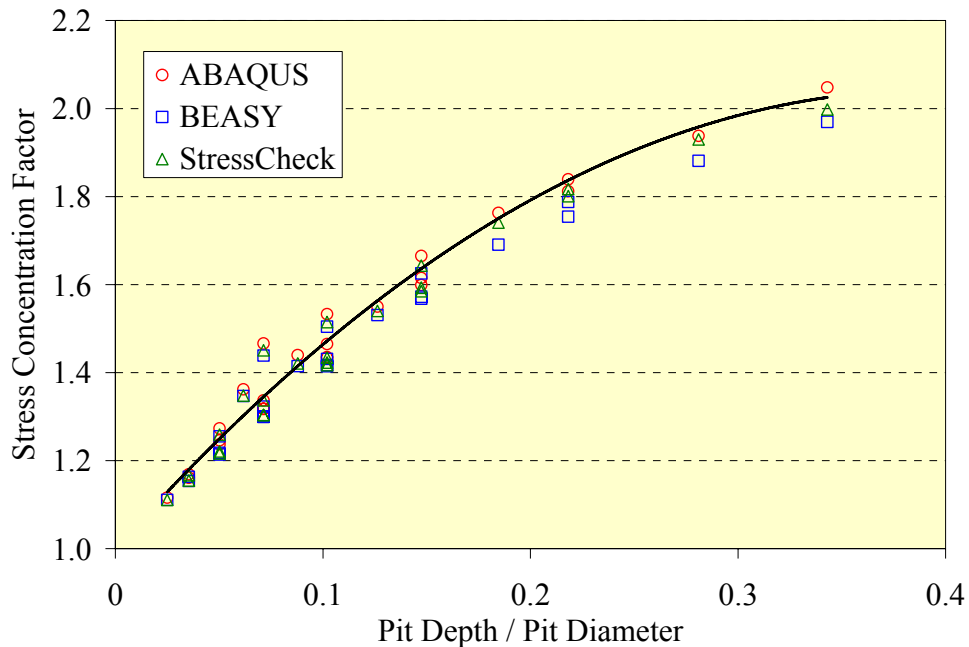


Figure 5.2.5-3. Normalized Analysis Results of Individual Spherical Pit Geometries (Case 5)

5.2.6 Incorporation of Residual Stress Effects

Most aircraft structural components are subjected to shot peening or grit blasting operations as part of the manufacturing process to improve material quality and/or performance. These operations result in a compressive residual stress field on and just below the surface of the material that have a significant beneficial effect on the fatigue life of the component. As such, incorporation of residual stresses is vital to accurately evaluate the severity of a corroded component.

X-ray diffraction measurements of surface and sub-surface residual stresses were taken on the AF1410 specimens utilized in the corrosion fatigue testing portion of the project. These measurements indicated that compressive residual stresses approaching 60% of the yield strength occur and that the residual stresses extended approximately 0.003 inches below the surface.

To account for residual stresses in the model, a temperature field that varied through the thickness of the part was applied to the model. The parameters of the temperature distribution were varied until the equilibrium stress state from the thermal analysis matched the residual stress field. As indicated in Figure 5.2.6-1, a relatively simple exponential function was identified that accurately simulated the residual stress profile.

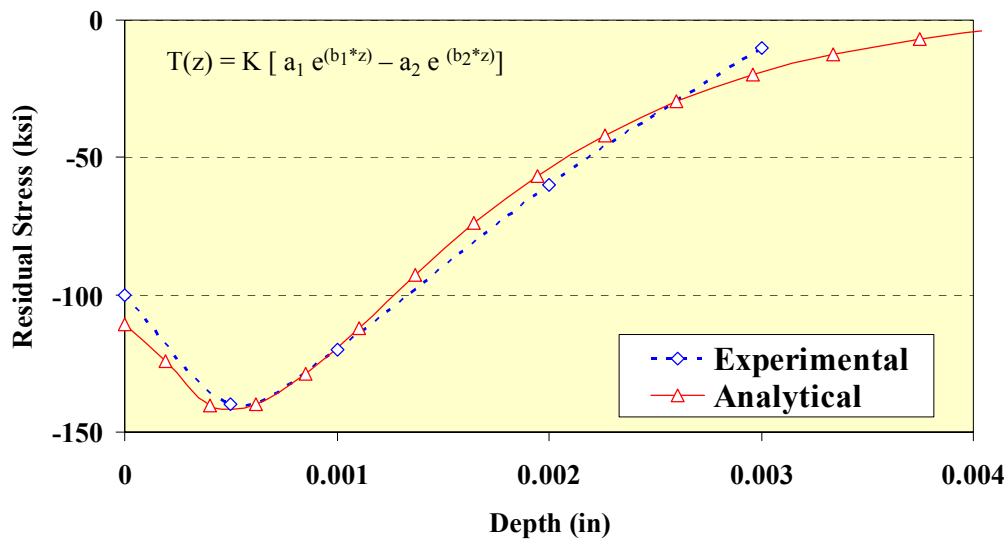


Figure 5.2.6-1. Experimental and Analytical Residual Stress Profile

5.2.7 Global-Local Modeling Technique

In addition to the analyses on simplified surface defect geometries, efforts were made to develop an analysis technique to compute stress concentration factors for actual corroded surfaces. Given the volume of data generated from a detailed mapping of a corroded surface from laser profilometry and/or white-light interferometry, it was not practical to model the entire corroded surface of an actual component or test coupon. Reduced sampling techniques to make the analytical problem tractable, unfortunately, had a significant effect on the stress concentration factor. Thus, in order to obtain accurate stress concentration factors, one must utilize an approach that retained the detailed local surface information as much as possible.

Accordingly, a global-local modeling technique was developed. The global model was used to capture the overall stress field in the part. The local model estimated the influence of the local corroded surface on the stress concentration factor. Displacement boundary conditions from the global model were applied to the local model to account for the remaining structure.

The global-local modeling technique was demonstrated to provide reasonable stress concentration factor estimates of corroded surfaces including residual stress effects. As an example, consider Figures 5.2.7-1 and 5.2.7-2, which depict the global-local model and stress results corresponding to Case 9 ($D_1=D_2=0.125''$, $h_1=h_2=0.005''$, $s=0.010''$) from Figure 5.2.4-1. The local model consisted of just a small region around the geometric features of interest. In the global analysis, the axial loading and residual stress (via the temperature profile discussed in the previous section) were applied to an uncorroded geometry. The results from this analysis were used to drive a local model with corroded surface features. Figure 5.2.7-2 shows the stress variation versus depth at the center pit of the corroded pattern. The presence of the residual stresses reduced the effective stress concentration factor at the bottom of the pit from 1.42 to 1.25.

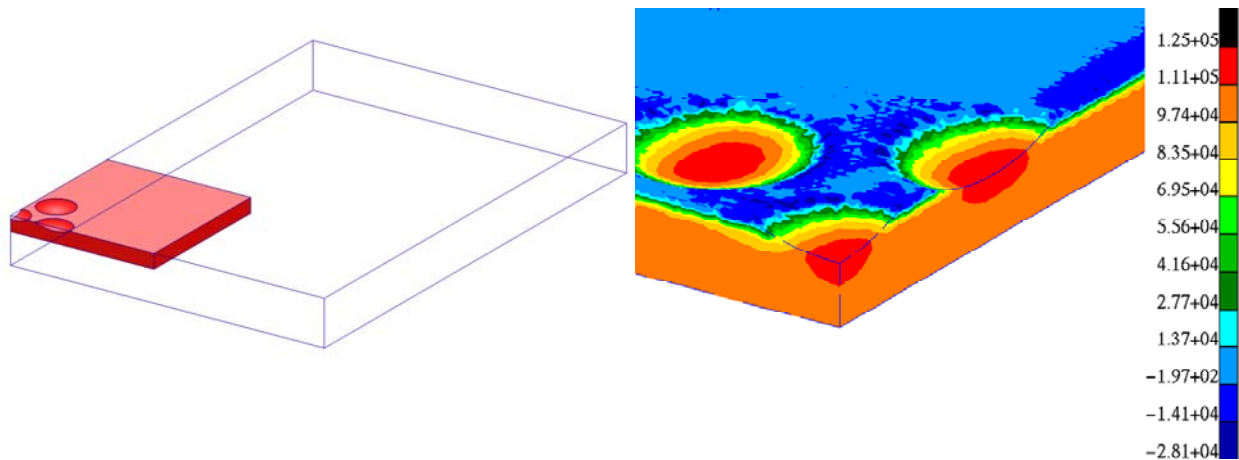


Figure 5.2.7-1. Global-Local Model (Case 9) and Corresponding Stress Profile (Ksi)

Unfortunately, to analyze numerous sites or an entire corroded surface with the global-local technique required a large series of local models that were not practical to evaluate. Alternate means of corrosion surface modeling were required.

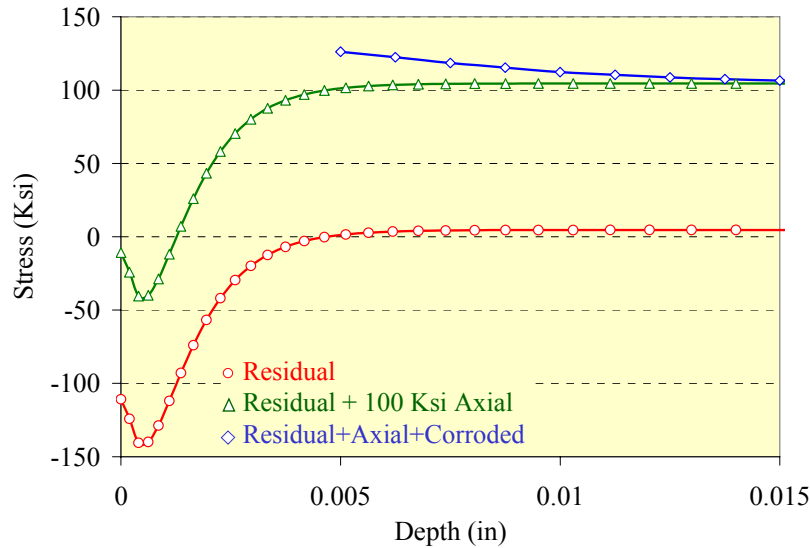


Figure 5.2.7-2. Global-Local Results at the Center of a Corroded Region (Case 9)

5.3 Development of a Pit Metric

Because of the geometric complexity, direct analysis of the corroded surface profile did not appear to be practical, so an alternative approach was developed to estimate the local stress concentration factor via a pit metric based on the local surface geometry. A candidate pit metric was developed as indicated in Figure 5.3-1.

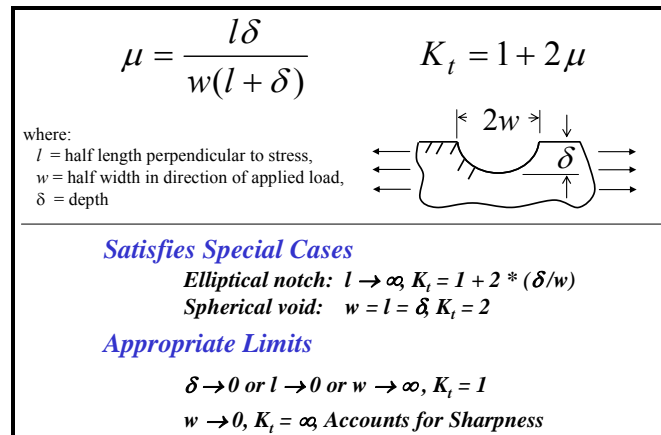


Figure 5.3-1. Candidate Pit Metric for Stress Concentration Factor Estimation

This easily-computed metric provided very accurate stress concentration factors for special cases such as an elliptical notch or spherical void. Additionally, the pit metric had the correct limiting trends so that, for a smooth and shallow pit, the stress concentration factor went to unity; but as the pit became very sharp and deep, the stress concentration factor went to infinity, indicating a crack tip.

A series of analyses was performed to determine pit metric performance on a wide variety of spherical and elliptical notch defects. Results from these analyses showed that the pit metric was accurate when the geometric parameters were precisely known. Unfortunately, efforts to apply the pit metric to actually corroded surfaces were not successful because of the difficulty in computing the pit metric parameters from the chaotic local surface geometry.

5.4 Development of an Elasticity Solution and Limitations

The challenges of applying the pit metric led to the development of an elasticity solution that would not suffer from the difficulties of defining geometric parameters directly from the corroded surface geometry. The elasticity solution approach, shown in Figure 5.4-1, involved performing a Fast Fourier Transform (FFT) of the corroded surface data to represent the actual surface profile as a linear combination of sinusoidal components in the frequency domain. Because each of the frequency components was a smooth, continuous function, one could estimate the stress variation over the surface of each frequency component with an approximate elasticity solution. The stress values corresponding to each frequency component were then recombined, via an inverse FFT, to provide an estimate of the stress field and stress concentration factor over the entire corroded surface.

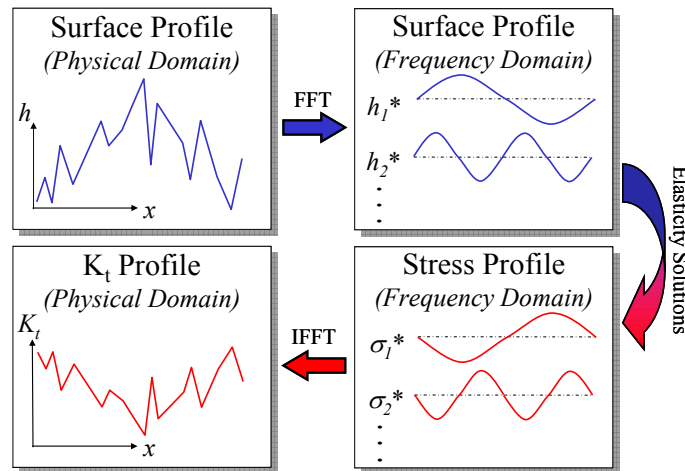


Figure 5.4-1. Elasticity Approach for Corroded Surface Modeling

The elasticity stress function solution, depicted in Figure 5.4-2, was developed based on observations from analyses of axial load components with sinusoidally varying surface geometries. These observations indicated that, for shallow surface height variations, the surface stress varies 180 degrees out of phase from the local surface height. When the surface was low, corresponding to a local pit, the stress was raised; and when the surface was raised corresponding to a local peak,

the stress was reduced. From the elasticity solution, a simple expression was developed that defined the stress variation over a sinusoidal surface in terms of the surface profile parameters (height and wavelength in each surface direction) and the applied axial loading.

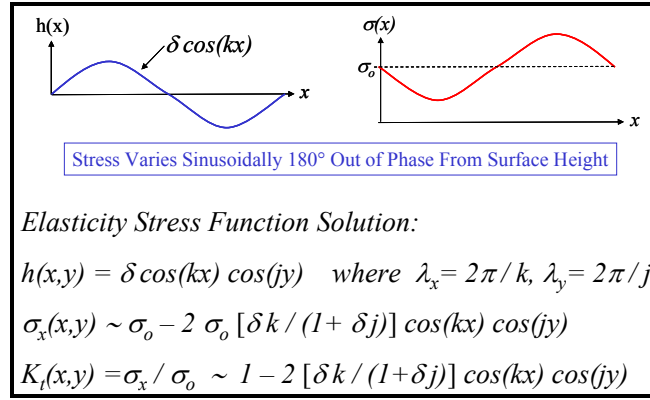


Figure 5.4-2. Elasticity Solution for Each Surface Profile Frequency Component

A series of finite element analyses was performed to estimate the stress concentration factors for a variety of idealized corroded surfaces having increasing complexity. The elasticity solution approach was applied to each of these idealized surfaces and correlated well with the finite element results. As an example, consider Figure 5.4-3, which depicts the elasticity and finite element solutions corresponding to an axial load applied to a surface with a sinusoidal variation in both surface directions. These results indicated that the elasticity solution accurately predicted both the amplitude and spatial variation of the stress profile corresponding to a single frequency component from the FFT of the corroded surface profile.

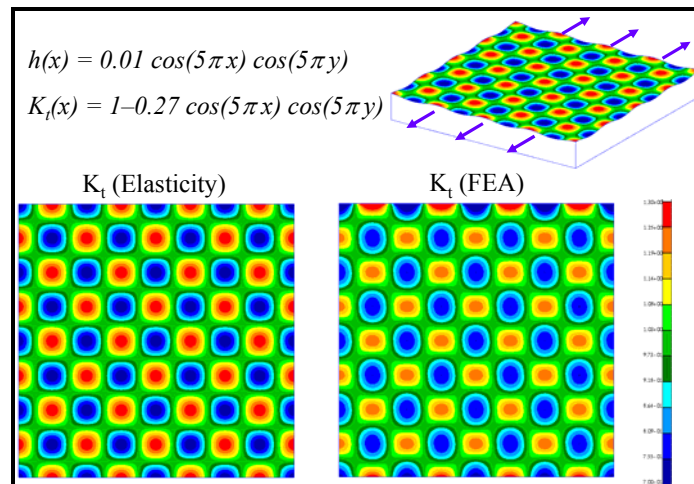


Figure 5.4-3. Elasticity Solution Two-Dimensional Single Frequency Validation Problem

ESRD and UDRI performed a series of detailed finite element analysis to determine the accuracy of the individual frequency component elasticity solutions over a wide variety of conditions. These results, shown in Figure 5.4-4, indicated that the elasticity solution was accurate over most conditions, except when the surface height of one of the frequency components was large compared to the corresponding wavelength. Review of measured surface profile data from actual AF1410 corroded specimens found that the surface heights were significantly smaller than the corresponding wavelengths. This implied that the elasticity solution approach would be used in the most accurate regime and remained viable for estimating the severity of actual corroded surfaces. Details of the parallel ESRD study are found in Section 6.3 of the ESRD Final Report located in Appendix A.

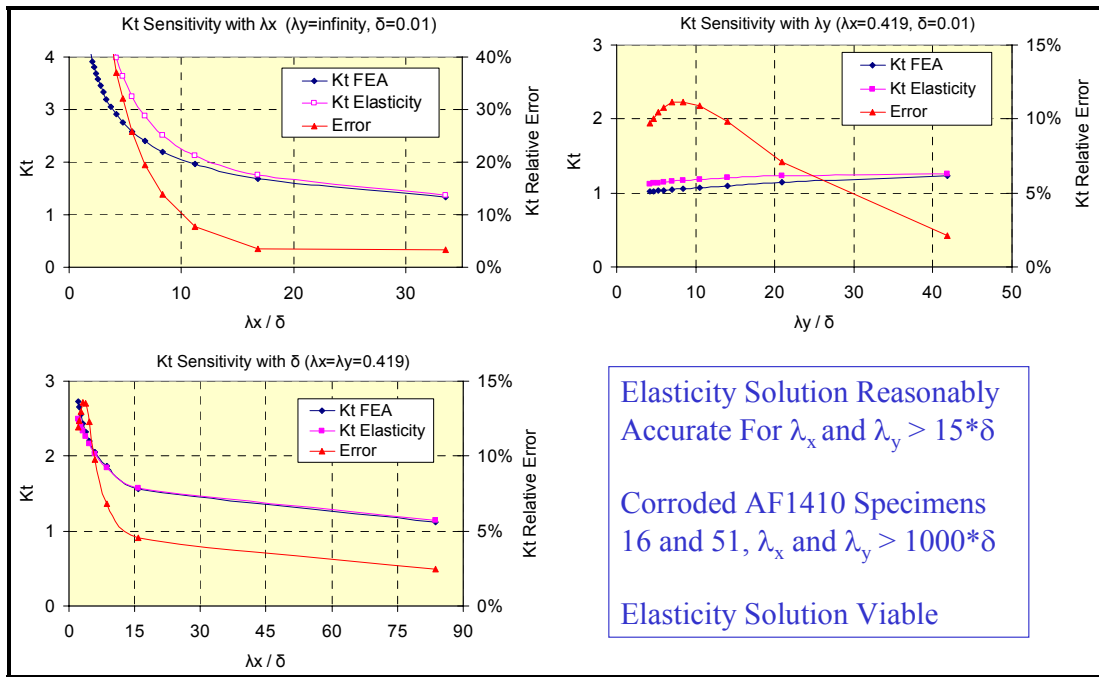


Figure 5.4-4. Accuracy of Individual Frequency Component Elasticity Solutions

Having demonstrated that the individual frequency components were reasonably accurate, a series of finite element analyses was performed to determine if the individual frequency components could be superimposed via an inverse FFT to represent the overall surface stress profile. The justification for superposition was based on the observation that the effects of multiple stress concentrations factors, such as a pit within a pit, were known to combine as the product of the individual stress concentration factors as indicated in Figure 5.4-5. When the individual elasticity solutions were inserted in the product expression and higher order terms were neglected,

the total stress concentration factor was estimated by a summation of terms related to the stress state of the individual frequency components. It was this summation that was computed as a result of the inverse FFT step in the elasticity solution in Figure 5.4-5.

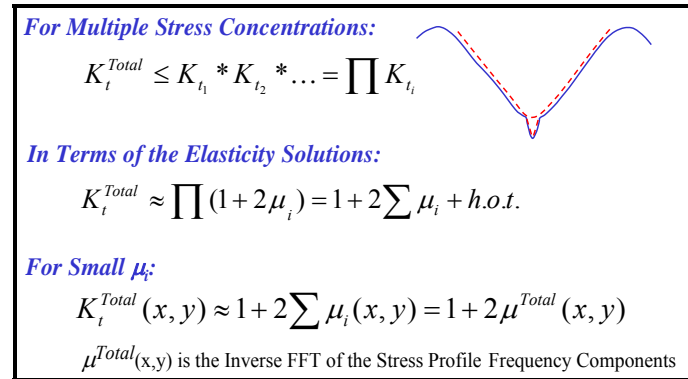


Figure 5.4-5. Combined Stress Concentration Factor Implications

To demonstrate the validity of the superposition approach, consider Figure 5.4-6 which depicts the elasticity (FFT), finite element (FEA), and boundary element (BEM) solutions corresponding to an axial load applied to a component having a surface geometry composed of three different sinusoidal terms. These results indicated that the superposition of the individual elasticity solutions accomplished via the inverse FFT accurately predicted both the amplitude and spatial variation of the stress variation over a complex surface profile.

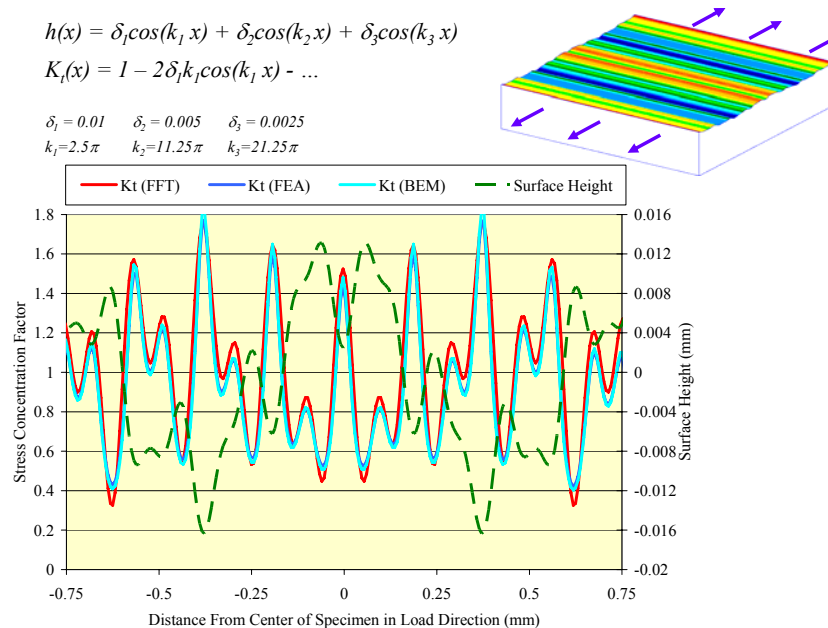


Figure 5.4-6. Accuracy of Elasticity Solution Approach on a Complex Surface

Finally, the elasticity approach was applied directly to an actual AF1410 corroded surface geometry from one of the test specimens. Figure 5.4-7 indicates the post-fracture corrosion surface and the corresponding surface height profile from white-light interferometry. A number of crack locations from the fatigue testing were identified and labeled accordingly.

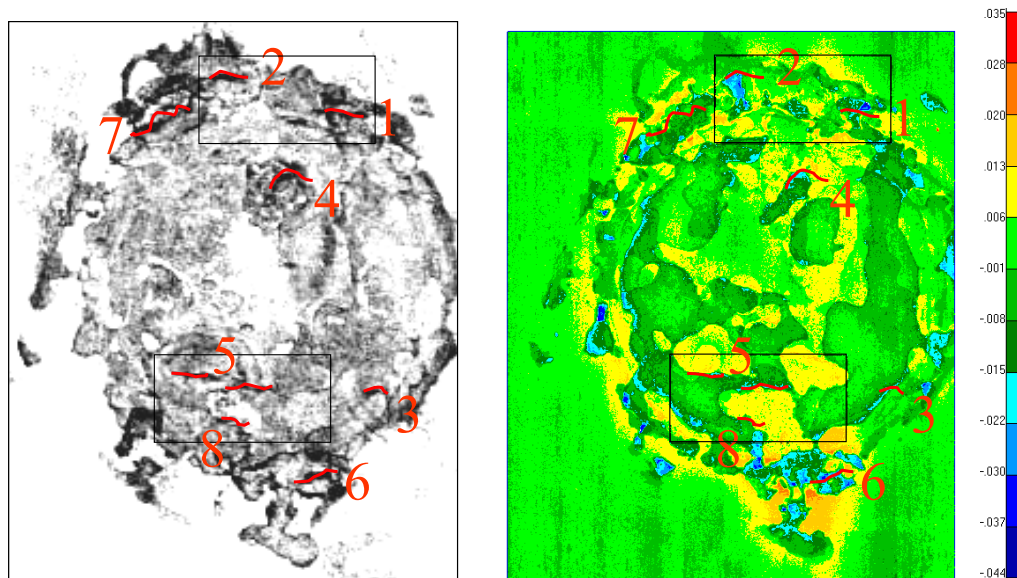


Figure 5.4-7. Corrosion Surface and Surface Height Profiles in AF1410 Specimen #16

Figure 5.4-8 shows the surface height profile and corresponding stress concentration factor estimate from the elasticity solution in the region around Cracks 5 and 8. The loading was applied in the vertical direction and the cracks appeared to form and grow along the step risers between corroded regions of different surface heights. The elasticity solution accurately identified the high stress locations and remained the only practical approach to estimating full-field stress concentration factors of arbitrarily corroded surfaces. Efforts were planned to determine the elasticity solution sensitivity to the spatial resolution and noise content of the measured surface profile, to incorporate residual stress effects, and correlate the elasticity solution results with crack initiation data from testing.

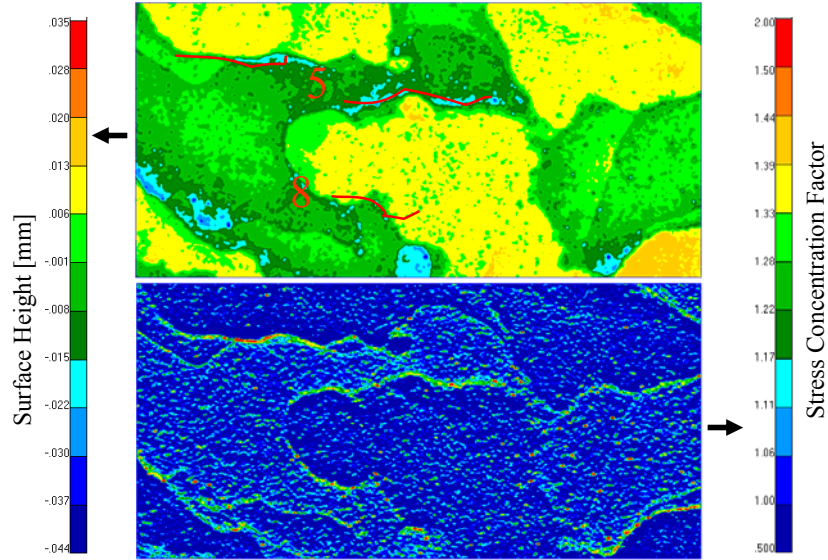


Figure 5.4-8. Zoomed Surface and Stress Concentration Profiles in AF1410 Specimen #16

A comparison was made of maximum k_t values found for each crack on Specimen #16 and the maximum k_t values found in the region of each crack. This comparison is shown in Table 5.4-1. In all cases, the crack contains the region's largest, or nearly-largest, k_t value value. From these observations, it is clear that the elasticity model is identifying true stress risers and candidate crack initiation sites. The elasticity model provides a foundation for further life prediction and disposition decisions.

Table 5.4-1. Comparison of k_t on Each Crack on Specimen #16 to k_t in a Region Around the Crack

Crack	Max k_t in Area	Max k_t on Crack
1	1.82	1.66
2	1.73	1.73
3	1.73	1.73
4	1.84	1.82
5	1.71	1.68
6	1.84	1.84
7	1.84	1.84
8	1.67	1.67
9	1.69	1.61
10	1.85	1.85
11	1.70	1.70
12	1.88	1.88
13	1.71	1.71
14	1.73	1.73
15	1.71	1.70
16	1.81	1.68
17	1.78	1.78
18	1.54	1.54
19	1.61	1.61

Section 6

Correlation

The ultimate goal of this program was to develop tools that can be used to specify the maintenance options for corroded components and to provide a sound engineering basis for selecting the best fleet maintenance options. Essentially, the program was to provide quantifiably justified maintenance criteria for environmentally induced damage (i.e., corrosion) in high-strength steels. In order to meet this goal, a series of corrosion-fatigue tests have been, and are being, conducted. Fracture surfaces have been examined microscopically to ascertain the number of cycles to crack initiation. In addition, white-light interference microscopic measurements have been made on the corrosion surfaces prior to fatigue test. A suite of surface roughness metrics have been calculated for these corrosion patches. Advanced models have also been developed to calculate stress concentration factors for the corroded surfaces. Nondestructive evaluation methods have also been investigated for suitability to this application. At the end of this program contract, the research team moved into the correlation phase of the study. In this phase, correlations are being sought between the various metrics and reduction in fatigue life and between NDI and the metrics. Reliability models are also being developed to make predictions of reduction in life based on detailed corrosion surface height profiles. These activities will be reported in the final report of the second and third program contracts.

Section 7

Conclusion

Under this program, a series of corrosion-fatigue tests have been performed. In order to conduct these experiments, a number of preliminary studies were accomplished. Baseline mechanical tests were carried out. An accelerated corrosion growth study resulted in the development of an electrochemical method that makes use of salt-water soaked filter paper sandwiched between electrodes. This approach provides for generation of corrosion in a local region without masking and associated undercutting at the mask edge. A materials study was performed to ensure that this method for growing corrosion does not produce adverse affects on the underlying steel substrate. Corrosion byproduct removal methods were also studied and a Boeing specification was optimized based on the use of Turco solution. Various profiling techniques were tested and a white-light interference microscope was selected for use on this program. A dental paste method was chosen for replication of each corrosion patch. Various corrosion metrics were studied and several candidates identified that show promise. A marker band approach was optimized for use on AF1410 steel corrosion-fatigue tests. Quantitative fractography methods developed by an Australian team were tested on these specimens and refined for this application. Additional studies were also performed on corroded arrestment shanks, in which the surface roughness characteristics were compared to the characteristics found from the laboratory grown corrosion.

After these preliminary studies were complete, a set of 60 AF1410 corrosion-fatigue specimens were prepared. Corrosion was grown to 3, 6, and 12 hours of exposure on a subset of the specimens. Corrosion was cleaned and the corroded surfaces were measured using the white-light interference microscope. Surface roughness metrics were calculated for each specimen and each specimen was tested in fatigue until failure. Quantitative fractography measurements were made on each fracture surface to determine the number of cycles to crack initiation.

Preliminary steps were also taken to study the effect of corrosion on the fatigue life of 300M components. An Air Force study found that exposure to small amounts of corrosion would lead to a dramatic reduction in life. Consequently, only a small number of corrosion-fatigue tests were planned on 300M with the purpose of confirming the results of the Air Force study. Specimens were prepared and preliminary tests were performed on this contract. This study was completed under the next contract in this program and will be reported in the corresponding final report.

In parallel with these activities, an NDI investigation examined the efficacy of various ultrasonic techniques for measuring surface roughness and topography. Time-of-flight and amplitude methods have shown promise, but ultimate applicability requires selection of the final corrosion metric.

Analytical models were also studied during this program contract. Finite element methods were shown to be ineffective at this time for determination of stress concentration due to the extensive detail required to adequately capture the surface features responsible for the stress risers. Extremely large data maps are required to accurately reflect this geometric detail, which induces a fine model mesh with an associated impractical computation time. Idealizations of the surface profile were shown to be highly sensitive to the idealization parameters. Global/local models were investigated in an effort to work around the computation challenges of this problem. These attempts were unsuccessful. Straightforward finite element analysis of corrosion might not be viable at this time.

In a parallel modeling study, an elasticity approach was developed to approximate the stress concentration factors for corrosion. The limits of applicability of this approach were studied and it was shown that, for the corrosion grown in the laboratory on AF1410 steel corrosion-fatigue specimens, the approach should be within these limits. Maps of stress concentration were compared to crack initiation sites for a few specimens and showed good agreement between experiment and model.

Significant progress has been made towards the development of a maintenance program for high-strength steels that includes the affects of corrosion. Once corrosion has been identified visually, the plan will be to assess the severity of the corrosion with an NDI method based on a corrosion metric. If the corrosion is judged to be cosmetic, the component will be returned to service after removing the damage. If the corrosion is judged to be mild, a replica of the corroded surface will be made and sent to a laboratory for detailed white-light interference microscopic measurements of the profile and subsequent disposition analysis. If the corrosion is judged to be severe, the component will be removed from service until it can be reworked at the depot.

This program contract has met its goals in the overall plan to develop tools that can be used to specify the maintenance options for corroded components and it provides a foundation on which to build the next program contract that will further advance these tools in the development of maintenance practices for high-strength steels.

Section 8

References

1. R. Perez., K.K Sanakaran, and H.G. Smith, Jr., “Structural Life Enhancement – Corrosion Impact on Airframe Total Life Analysis”, The Boeing Company, Final Report submitted to NAVAIR, October 2003.
2. D. Buhrmaster., “Aging Aircraft Corrosion Prevention Compound Standardization Test Development – Final Report 1 – 300M High Strength Steel”, Contract Number F42620-00-D0039-0001, December 2003.
3. R. Fisher, S. Perkins, A. Walker, and E. Wolfart, “Fourier Transform”, 14 September 2004, <http://homepages.inf.ed.ac.uk/rbf/HIPR2/fourier.htm>.
4. S. Barter, “Quantitative Fractography and the EPS Method,” DSTO, June 2002.
5. M. Zecchino and T. Stout, “Replication Enables High Resolution Optical Metrology on Hard-to-Measure Surfaces”, A Veeco Instrument Inc. publication, Copyright 2004.
6. M. Zecchino, “Characterizing Surface Quality: Why Average Roughness is Not Enough”, 7 June, 2004, <http://www.veeco.com>.
7. H. Amstutz, “Surface Metrology Guide”, 8 August 2004, <http://www.predev.com/smg/index.html>.
8. ImageJ was developed by Wayne Rasband of the National Institutes of Health. It is in the public domain.
9. John C. Russ, *The Image Processing Handbook*, CRC Press (1992), ISBN 0-8493-4233-3.
10. TurboReg is an ImageJ plug-in for the automatic alignment of a source image or a stack to a target image. This algorithm was developed by Philippe Thevenaz, Biomedical Imaging Group, Swiss Federal Institute of Technology, Lausanne.
11. Image_CorrelationJ is a plug-in algorithm written for ImageJ by Dr. Gary Ghinga (gary.chinga@pfi.no).
12. N.F. Haines and D.B. Langston, “The Reflection of Ultrasonic Pulses from Surfaces”, *J. Acoust. Soc. Am.* Vol. 76, No. 5, May, 1980, pp. 1443 – 1454.

13. G.P.P. Gunarathne and K. Christidis, "Measurements of Surface Texture Using Ultrasound", *IEEE Trans. On Instrumentation and Measurement*, Vol. 50, No. 5, October 2001, pp. 1144 – 1148.
14. G. Quentin, M. de Billy, F.C. Tenoudji, J. Doucet, and A. Jungman, "Experimental Results on the Scattering of Ultrasound by Randomly or Periodically Rough Surfaces in the Frequency Range 2 to 25 MHz", *1975 Ultrasonics Symposium Proceedings*, IEEE Cat. # 75 CHO 994-4SU, pp. 102 – 106.
15. J. Stor-Pellinen. and M. Luukkala, "Paper Roughness Measurement Using Airborne Ultrasound", *Sensors and Actuators*, A 49 (1995), Elsevier Science S. A., pp. 37 – 40.
16. P.D. Thorne and N.G. Pace, "Acoustic Studies of Broadband Scattering from a Model Rough Surface", *J. Acoust. Soc. Am.*, Vol. 75, No. 1, January 1984, pp. 133 – 144.

Appendix A

ERSD Final Report

US Navy High Strength Steel Corrosion-Fatigue Modeling Program

Final Technical Report

August 30, 2005

Revised December 12, 2005

Barna Szabó¹, Brent Lancaster and Sebastian Nervi
Engineering Software Research and Development (ESRD), Inc.
111 West Port Plaza, Suite 825
St. Louis, MO 63146
314-744-5021 ext. 11
barna.szabo@esrd.com

This report was prepared for the University of Dayton Research Institute, Dayton, OH under subcontract RSC03025, as part of US prime contract No. F42620-00-039-0011. Period of performance: June 24, 2003 – August 30, 2005

¹ Principal Investigator.

TABLE OF CONTENTS

1. SCOPE	4
1.1 ORIGINAL TERMS OF REFERENCE	4
1.2 DELIVERABLES	5
1.3 MODIFICATIONS TO THE TERMS OF REFERENCE	5
1.4 ACCOMPLISHMENTS	6
2. IMPORTANCE	6
3. GOALS	7
4. NUMERICAL SIMULATION	8
5. PLANNING	10
6. APPROACHES/METHODOLOGIES	10
6.1 KTEFF EXTRACTION USING LASER PROFILOMETER SURFACE MAPPING AND STRESSCHECK®	12
6.1.1 Introduction	12
6.1.2 Study Approach and Results	12
6.1.3 Summary	15
6.2 CORRODED SURFACE IDEALIZATION WITH CONSIDERATION OF K_t SENSITIVITY	16
6.2.1 Introduction	16
6.2.2 Study Approach and Results	16
6.2.2a) Residual Stress Effects: Experimental Observations	25
6.2.2b) Residual stress: Analytical considerations	27
6.2.2c) Path Independence	27
6.2.2d) Modeling residual stresses	29
6.2.3 Summary	32
6.3 K_t USING CHARACTERISTIC METRIC FOR APPROXIMATION TO ELASTICITY THEORY (UDRI)	33
6.3.1 Introduction	33
6.3.2 Study Approach and Results	34
6.3.2a) Case 1: 2-D Sinusoidal Surface Function: Single Term Study	38
6.3.2b) Case 2: 2-D Sinusoidal Surface Function: Summation of Differing Terms Study	40
6.3.2c) Case 3: 3-D Sinusoidal Surface Function: Multiplicative, Multi-Variable Terms	44
6.3.2d) Case 3: Validation Study	46
6.3.2e) Case 3: Sensitivity Study	48
6.3.3 Summary	50
6.3.4 Recommended Future Studies	51
6.4 F-18 ARRESTING SHANK (PART-74A480617): SUBMODELING WITH CONSIDERATION OF $K_{t_{EFF}}$	55
6.4.1 Introduction	55
6.4.2 Study Approach and Results	55
6.4.2a) Case a: Linear Study	56
6.4.2b) Case b: Geometric Nonlinear Study	57
6.4.2c) Case c: Contact Subassembly 3D: Local Analysis	59
6.4.2d) Case d: Detailed 3D Subassembly: Local Analysis (no contact)	59
6.4.3 Summary	62
7. IMPLEMENTATION OF STATISTICALLY VARIABLE NON-LINEAR MATERIAL PROPERTIES	62
8. PLAN FOR DEPLOYMENT	62
8.1 THE STRESSCHECK FEA TOOLKIT	63
8.1.1 Toolkit Functions	64
Problem Description	64
Solution Procedures	65
Extraction Procedures	66
Data Delivery	66

9. SUMMARY 67
10. RECOMMENDATIONS FOR FUTURE WORK..... 67
11. APPENDIX..... 68

1. Scope

This report covers the first two years of a multi-year effort, the principal objective of which is achieve significant cost savings and enhanced readiness through the development of definitive corrosion maintenance criteria, the supporting diagnostics and enhanced repair capability to effectively manage structural maintenance of Naval aviation assets. This is a collaborative project among NAVAIR, the University Of Dayton Research Institute (UDRI), Boeing Phantom Works in St. Louis and Engineering Software Research and Development, Inc. (ESRD).

1.1 Original terms of reference

ESRD, Inc. was to provide engineering services in support of this collaborative project.

Specifically, ESRD will perform the following tasks:

1. Perform an investigation of methods designed to transform surface roughness metrics into a form suitable for numerical analysis by the finite element method.
2. Implement modifications needed for the management of surface roughness metrics into the finite element analysis software product StressCheck[®] and provide suitable user-interface for the input and management of surface roughness data.
3. Provide means for the computation of effective stress-concentration factors (k_{eff}) for test coupons from surface corrosion experiments and provide means for verification of computed data.
4. Investigate the sensitivity of effective stress-concentration factors to variations in surface roughness parameters and identify the most critical metrics.
5. Calibrate the mathematical model on the basis of existing experimental data obtained from test specimens and sub-components, with varying degrees of corrosion, measured by laser profilometer, to be supplied by Boeing Phantom Works in St. Louis and NAVAIR.
6. In collaboration with NAVAIR, develop criteria for validation of the predictive capabilities of the mathematical model. The validation protocol is to involve “blind” prediction of the results of experiment. The acceptance criteria shall be based on the characteristics of scatter diagrams of k_{eff} versus surface roughness metrics.
7. Based on the results of validation experiments, develop a plan for improvement of the mathematical model.
8. Enhance StressCheck[®] to enable the use of variable material coefficients over a specified domain in the course of a material nonlinear analysis. The variation of elastic-plastic material coefficients (e.g. modulus of elasticity, Poisson’s ratio, yield strength, etc.) will

- be handled through an external function call. StressCheck[®] will pass the coordinates of the points to the function and receive the corresponding values of the material parameters.
9. Develop a plan for the distribution of the corrosion assessment technology developed under this project to the Navy and its subcontractors, utilizing the COM and Java interfaces of StressCheck[®]. The development of simple-to-use Microsoft Windows desktop and web-based (or cross-platform) applications are envisioned. The interfaces are to provide a convenient communication protocol to integrate the necessary functions of other applications (e.g. MatLab probability and statistical functions) needed to quantifiably assess the useful remaining life of a corroded part. ESRD will expand the COM interface to include new capabilities developed under this contract.
 10. Coordinate the project with NAVAIR, Boeing Phantom Works in St. Louis, and UDRI.

1.2 Deliverables

1. ESRD provided monthly engineering status reports. These reports included descriptions technical program status, accomplishments, issues and concerns and planned activities.
2. ESRD was to provide a draft of the final engineering report thirty (30) days prior to the end of the contract period.
3. ESRD was to provide documentation of the examples that demonstrate the enhanced capabilities of StressCheck[®] and provide guidelines for the proper application of StressCheck[®].

1.3 Modifications to the terms of reference

On 9/10/2004 ESRD was informed by Dimitri Savvas that the AF1410 specimens, fatigue tested at NAVAIR, had substantial residual stresses. He had requested that ESRD investigate the effects of residual stresses on the predictability of failure initiation. Subsequently ESRD was provided data on the distribution of residual stresses obtained by x-ray diffraction measurements. The data indicated that the statistical variation of residual stresses is very large. ESRD understood that the following tasks were to be performed:

- Investigate the effects of surface damage resulting from corrosion in the presence of residual stresses. It is known that residual stresses are induced in high strength steel components through surface treatment. The residual stresses are generally compressive and can reach values as high as 100 ksi². The maximum residual stress occurs at the surface and decays to a negligibly small magnitude over a distance of approximately

² Taking into account the inherent uncertainties and errors associated with x-ray diffraction measurements, the data indicates only a very rough estimate of the residual stresses existing in the specimens.

0.003 inches. Undoubtedly, there is a statistical variability; however statistical data are not available at this time. Corrosion defects remove pre-stressed material. This affects the value of stress concentration factors (K_t); therefore it is expected to have a substantial impact on fatigue life. First, highly idealized models were to be used for the investigation of these effects with the goal to investigate the sensitivity of K_t to the various parameters.

- Collect data from fatigue experiments and interpret the results taking into account the presence of residual stresses.
- Provide consultation in the following areas:
 - a. Review of the overall approach and strategy for integrating these efforts into a comprehensive criterion for future use.
 - b. Assist in tailoring the effort such that it supports the development of the specific requirements to be applied to fleet management of structural parts to which this work will apply.
 - c. Attend Technical Interchange Meetings as requested.
 - d. Propose a conceptual framework for advanced methods for fatigue design and fleet management of airframes.

1.4 Accomplishments

The accomplishments are detailed in the body of this proposal. Certain objectives, originally envisioned at the beginning of the project were modified at project meetings. Other objectives were partially completed and will be addressed in the current phase of the project.

2. Importance

As the naval aviation fleet ages, corrosion and environmental degradation have become major contributors to spiraling naval aviation maintenance costs, burgeoning repair backlog, and increased aircraft failure rates. The corrosion problem is most observable in high strength steels (HSS) which comprise the most critical aircraft components; AF 1410 is one such HSS. In fact, all recent aircraft losses due to corrosion/environmental degradation failures can be traced to a failure of HSS components. Aircraft including F/A-18, F-14, EA-6B and E-2C have been plagued by these corrosion-load cycle failures, forcing the USN the costly measure of grounding these aircraft for extended periods of time.

Much of the increasing cost and risk are attributable to the lack of definitive, clear-cut corrosion maintenance criteria, necessitating the repair and/or replacement of all corroded parts.

Therefore, the USN needs workable corrosion maintenance criteria that can be followed in today's operational environments providing safety and readiness within the limited operations and maintenance resources. With respect to corrosion, maintenance teams must be able to differentiate between corrosion with potential safety impacts and corrosion that does not have substantial impact on life. In other words, maintenance personnel must know what must be removed immediately and what can be tolerated for some time period. The distinction must be justified quantitatively. The USN needs corrosion maintenance criteria that are accessible for routine assessment of corroded components. In short, a reliable and robust geometrically and mechanically defined metric or directive for quantitatively predicting remaining corroded part lives is necessary for a reliable assessment. This approach must be timely and efficient in order to meet USN maintenance scheduling requirements.

Furthermore, it is imperative that workable metrics or executables are properly filtered from those that are not feasible. For example, a proposed executable that takes a very long time to compute a valid numerical result may be too costly because time is a crucial variable in terms of quantitative approaches; therefore it cannot be used as part of a maintenance program and has to be rejected. On the other hand, a complex (more detailed) model may be too costly to be used within a maintenance program but it can be used to generate benchmarks in order to avoid selecting an oversimplified model. An ideal executable may be defined as one that does not imply extended grounding of aircraft during evaluation, yet produces reliable results.

3. Goals

This project was aimed at establishing intervals of inspection based on sound scientific principles and the latest analytical technology to reduce the number of occurrences of in-service failures. It was also hoped that unnecessary inspection procedures could be reduced or eliminated, leading to increased safety and reduced cost. Thus, the focus was on quantitative USN high strength steel corrosion-cycle fatigue modeling and the formulation of reliable predictions for remaining fatigue life. Specifically, developments of prediction models focus on current states of corrosion, as long-term corrosion is highly unpredictable in terms of both extent of damage and location. This is an entirely different problem, and was not considered during the reporting period.

In order to achieve these goals, methodical testing involving validation of proposed metrics and executables must be performed both through laboratory testing and through numerical methods, such as the finite element method (FEM). Verification is a process by which the quality of the numerical solution is ascertained, validation is the process for which a mathematical model is deemed to be an appropriate representation of the physical reality it is intended to represent. Validation of a model is performed through comparison of, independently obtained, experimental and numerical data.

FEM is a numerical method useful for obtaining approximate solutions to the equations of continuum mechanics. The accuracy of the approximate solution can be estimated. The technological prerequisites for verification of a practical, reliable assessment of the remaining service fatigue life of corroded structural components are currently available through the capabilities of StressCheck®.

StressCheck® is the finite element software product of ESRD Inc., of St. Louis, MO. It was chosen as the primary investigative analytical tool for the function of extracting potential mechanical relationships between corrosion and fatigue life. ESRD was to provide detailed mathematical corrosion model verification and validation for the USN and its project team. The results of these verification and validation studies are provided in this report, and are addressed in terms of relevance and feasibility to the maintenance criteria of the USN.

4. Numerical Simulation

Working models are mathematical problems formulated so as to capture the essential characteristics of some physical system with the expectation that the data computed from the solution of a working model will be a reliable predictor of the data of interest. Proper selection of a working model is the most important decision when undertaking finite element analysis. Formulation of a working model involves a theoretical formulation, specification of input data and a statement of objectives.

1. Theoretical formulation. The applicable physical laws, together with certain simplifications, are stated as a mathematical problem in the form of ordinary or partial differential equations, or extremum principles.
2. Specification of input data. The input data are comprised of the following:
 - Data that characterize the solution domain.
 - Physical properties elastic moduli, yield stress, coefficients of thermal expansion, thermal conductivities, etc.

- Boundary conditions (loads, constraints, prescribed temperatures, etc.)
Information or assumptions concerning the reference state (initial conditions).
 - Uncertainties. It is useful to distinguish between two types of uncertainties: When some information needed in the formulation of a working model is unknown then the uncertainty is said to be cognitive (also called epistemic). For example, the magnitude and distribution of residual stresses is usually unknown, some physical properties may be unknown, In addition, there are statistical uncertainties (also called aleatory uncertainties): Even when the average values of needed physical properties, loading and other data are known, there may be very substantial statistical variations. Consideration of uncertainties is necessary in the interpretation of computed data.
3. Statement of objectives. Definition of the data of interest and the corresponding permissible error tolerances.

Associated with each working model is a modeling error. The process by which a working model is evaluated and modified to ensure that it meets necessary conditions for acceptance is called validation. The goal of validation is to ensure that the model is a sufficiently accurate mathematical description of the physical system or process it is supposed to represent³. Validation involves calibration and prediction. The determination of physical properties and other model parameters through correlation with experiments is called calibration. The use of a model to foretell the data of interest corresponding to some set of input data is called prediction.

Working models are solved by numerical means, most commonly by the finite element method. In this process the exact solution is approximated. Determination of the accuracy of data computed from the approximate solution of a particular mathematical model is called verification. In verification accuracy is understood to be with respect to the exact solution of the working model, not with respect to physical reality. Verification is concerned with estimation and control of the discretization error; errors associated with iterative solution procedures and determination that the program is functioning properly.

³ American Institute of Aeronautics and Astronautics, Guide for Verification and Validation of Computational Fluid Dynamics Simulations AIAA G-077-1998 (1998).

5. Planning

As stated, the main objective of this study is the development of metric(s) that characterize HSS corrosion with respect to structural integrity providing viable maintenance guidelines with respect to fatigue life. In the US Navy, it is known that the effective stress concentration factor ($K_{t_{eff}}$) is used as a basis for estimating the FLE.

Therefore, of great interest is the computation and isolation of the maximum effective stress concentration factor of a corroded part as this will limit part life. The definition of $K_{t_{eff}}$ in reference to this study is the ratio of the first principal stress in a corroded part to the local first principal stress in a pristine, or uncorroded, part. The stress concentration in a pristine part will be referred to as K_t .

The goal is to enable USN maintenance personnel to make timely, reliable decisions on the status of flight critical parts through the applications of simple rules. Of course, the effects of corrosion damage on fatigue life expended (FLE) depend on the location of the damage. Therefore inspection must be focused not only on regions of high corrosion, but also where K_t is high in the pristine part.

Since it would be impractical to perform detailed analysis on the effects of corrosion on each part, it is necessary to develop methods that involve two processes: a) the determination of K_t in an uncorroded (pristine) part, and b) based on corrosion metrics obtainable by field observations, or experience based on exposure to various operating environments, estimation of the rate of change of $K_{t_{eff}}$ over time. These methods would provide a basis for evaluating the effects of corrosion on the maximum $K_{t_{eff}}$, as well as determine the rate at which the fatigue life is expended. Process a) can be readily solved using StressCheck[®]; process b) however still remains open. An important question is whether the effects of surface defects caused by corrosion can be analyzed by numerical means.

Since the $K_{t_{eff}}$ is dependent on the geometry of the corroded surface, the corroded surface has to be approximated. The available information is limited by the resolution of the system used for mapping the surface features. The usability of the available information is limited by our ability to represent highly irregular surface features in a mathematical model.

6. Approaches/Methodologies

The approach to HSS corrosion classification centers on formulating the impact corrosion has on a structural component in terms of probabilistic strain life analysis. As stated, the objective was to characterize corrosion with a metric corresponding to $K_{t_{eff}}$ values.

In addition, the sensitivity of these $K_{t_{eff}}$'s when a corroded surface is replaced by an idealized surface is of interest, because simplification of local surface roughness due to corrosion is essential for making the problem accessible to numerical analysis. The reasoning for this plan of approach was that effective stress concentration factors are the basic input to strain life analysis. It is necessary to find a simple, yet reliable, method to quantify these effective stress concentration factors. A series of studies were conducted with the objective to investigate the sensitivity $K_{t_{eff}}$ to details of surface features selected to approximate the main topological features of corrosion induced in a laboratory environment.

In Section 6.1 a preliminary investigation is described which involved two-dimensional analysis of corroded surface representations of varying resolution. The analysis was performed with StressCheck⁴, using the MeshSim⁵ automesh. The results have shown that a relationship between surface roughness and $K_{t_{eff}}$ exists. Extension of this investigation to three dimensions is not feasible at this time due to the very high complexity of corroded surfaces.

In Section 6.2 virtual experiments, involving highly idealized representation of surface features is described. The objective of this analysis was to investigate the sensitivity of maximum $K_{t_{eff}}$ to the choice of idealizations. It was found that $K_{t_{eff}}$ is highly sensitive to the choice of idealizations of the topographical features of corroded surfaces.

In Section 6.3, an examination of an approach proposed by UDRI is described. The main idea is that the corroded surface is idealized by a Fourier series expansion. A K_t value can be associated with each term of the Fourier expansion. UDRI proposed to replace the multiplicative decomposition with an additive decomposition, arguing that the high order terms can be neglected. This is an attractive scheme which, if could be validated, would make corroded surfaces accessible to numerical analysis for the purpose of estimating $K_{t_{eff}}$. Our investigation found that the scheme works well for the low order terms of the Fourier expansion, but its accuracy deteriorates for the high order terms. For this approach to work it is necessary to show that the coefficients of the high order terms decrease at a rate which is much faster than the rate of increase of the approximation error.

In Section 6.4, we showed that for an example HSS part, an F-18 arrestment gear, a subdomain containing localized corrosion can be segregated without affecting $K_{t_{eff}}$, so as long as the appropriate boundary conditions are implemented. This reduces computational time by a significant amount, thus increasing feasibility. The results from each study (Sections 6.1-6.4) are given in the subsequent pages of this report, as well as the implications of each study within the

⁴ StressCheck is a trademark of Engineering Software Research and Development, Inc.

⁵ MeshSim is a trademark of Simmetrix Inc.

global objective, which is to relate a corroded surface to the corresponding maximum $K_{t_{eff}}$ and in effect fatigue life (FLE).

Kteff Extraction Using Laser Profilometer Surface Mapping and StressCheck[®]

6.1.1 Introduction

The focal point of the approach was the development of a relationship between corrosion and surface roughness, and to relate this surface roughness to the effect on fatigue life. Previous ONR 351 funded Science & Technology efforts (Boeing and NAVAIR) indicated such a relationship is possible through the application of a laser profilometer. The key step was the correlation of surface roughness with an effective stress concentration factor ($K_{t_{eff}}$). This was accomplished with the availability of experimental data (test specimens and components, with varying degrees of corrosion as measured by the laser profilometer, tested to fatigue crack initiation) and the implementation of this surface data into StressCheck[®] for processing. Currently, only two-dimensional slices through the corroded surface (i.e. row or column of data) can be processed by spline fitting, as three-dimensional spline fitting is under investigation. Therefore, only two-dimensional cases were considered. It must be noted that for a corroded part it is unlikely that the corrosion pattern will allow the use of a 2-D approximation, which is the case studied in this section. For the case studied in this section, the 2-D model was used for investigating the effects of surface representation on the computed $K_{t_{eff}}$. Since the actual problem is inherently three-dimensional (3-D), the computed values for the 2-D case cannot be compared with values that would be obtained if a 3-D model were used.

Data analysis and reduction of the two-dimensional surface slices resulted in the scatter of $K_{t_{eff}}$ versus surface roughness readings, as well as the approximate location and magnitude of the maximum $K_{t_{eff}}$.

6.1.2 Study Approach and Results

ESRD focused much of its early efforts into integrating Boeing laser profilometer measurements of NaCl/SO₂ fog-corroded specimens into StressCheck[®] through the use of COM pre-processor applications, specifically a Visual Basic (VB) application. This preliminary exercise was centered on the ability to represent surface roughness in a finite element analysis. The VB application was designed to read in the bulk surface measurement data (x, y, and z) from a text file, and optionally filter the data into essential shape characteristics for the purpose of data

reduction and time savings. It was assumed that approximately the same resolution can be seen with fewer data points if only the first and last points, local inflection points, peaks, and valleys are included in the surface location data to be imported into StressCheck. Additionally, the sharpest pit (smallest angle) is considered, as this feature is most likely to influence $K_{t_{eff}}$.

Once the data is read into the VB application and filtered according to the filtering algorithm, a 2-D surface profile in either the x (column) or y (row) direction can be extracted and pit characteristics calculated. From this 2-D surface profile, simply consisting of points in 2-D space, a StressCheck input file (.SCI) consisting of point locations can be written and a spline curve generated through the points. The accuracy of the spline curve to represent the corroded surface is dependent on the point resolution (i.e. the number of points representing surface height). The VB application interface is shown in Figure 1. An example of a mapped surface profile extracted from laser profilometer data supplied by Boeing is shown in Figure 2.

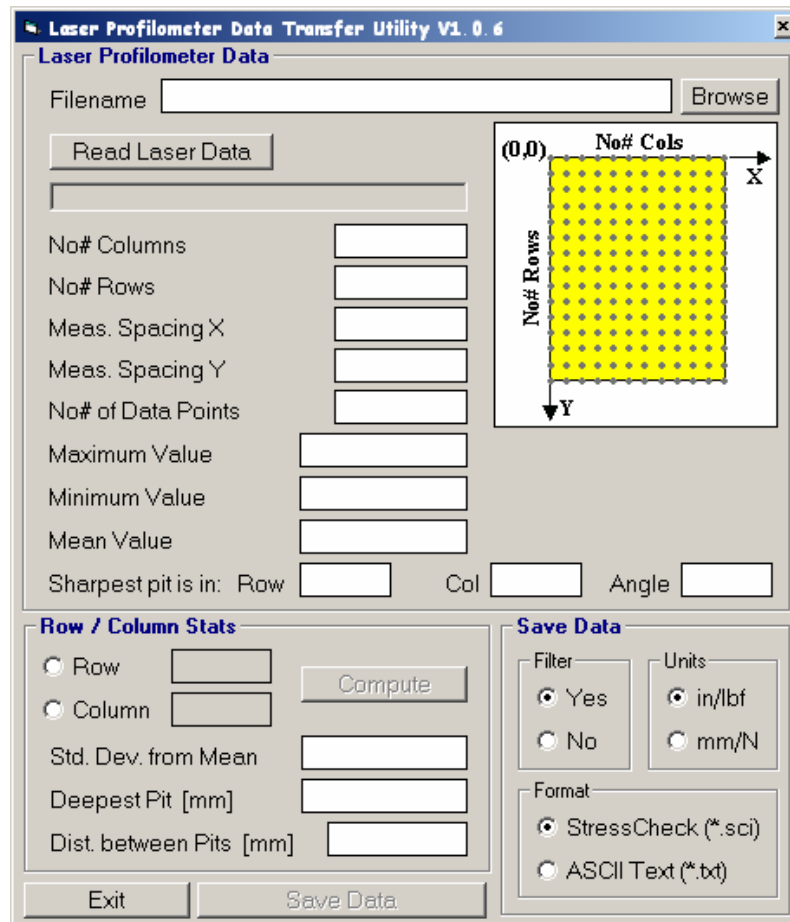


Figure 1. Laser Profilometer VB Application

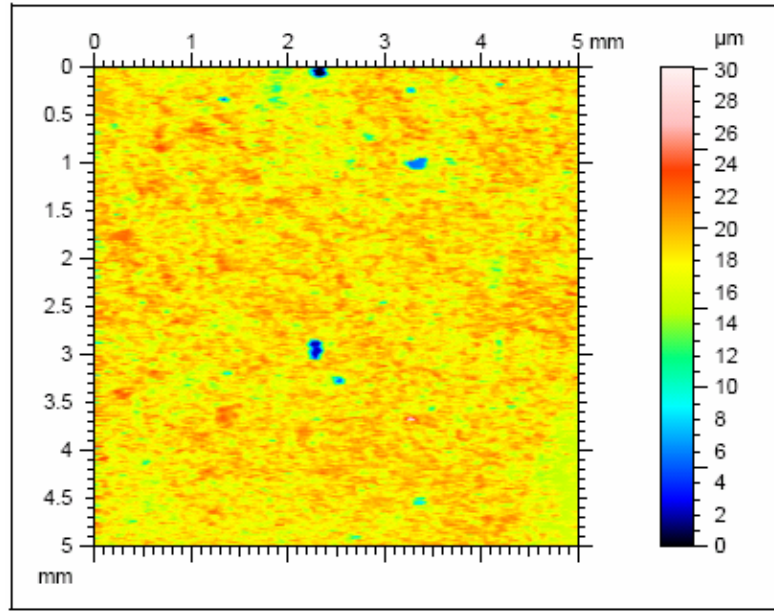


Figure 2. Example Laser Profilometer Mapped Surface Profile

The automatically generated 2-D spline curve produced using StressCheck[®]'s modeling engine represents only the cross-sectional profile at a given row or column of data. The goal, then, is to create an accurate cross-sectional representation of corroded part geometry for automeshing based on the spline curve interpolation. The methodology for filtering example laser profilometer data into key features is shown in Figure 3.

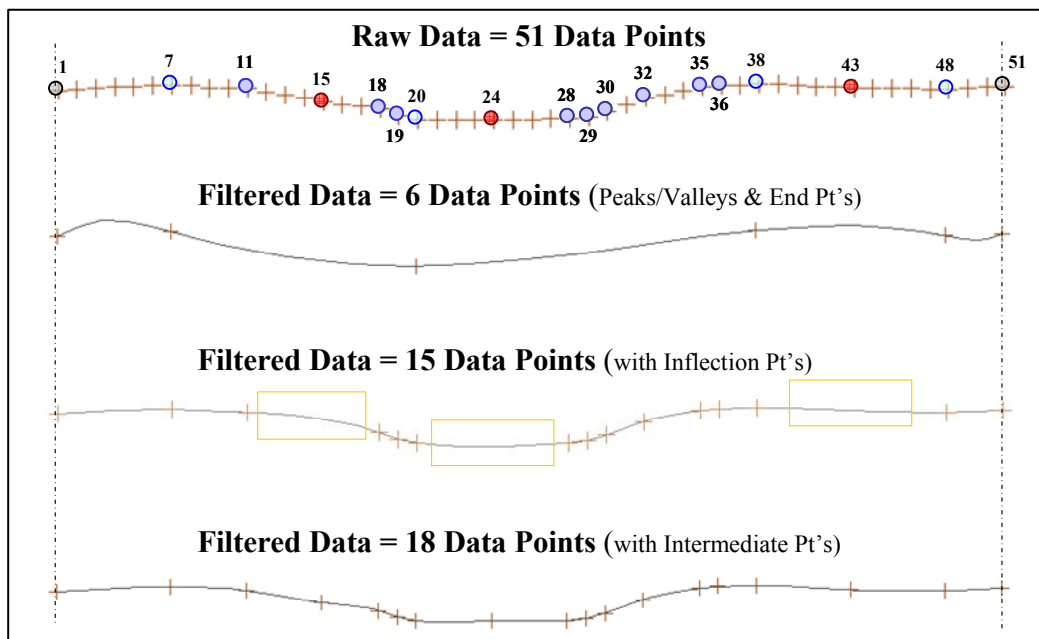


Figure 3. Example of Filtered Spline Curve

The corresponding mesh, generated from the extension of surface data into the given part thickness, along with the corresponding $K_{t_{eff}}$ extraction is shown in Figure 4. It is shown that the $K_{t_{eff}}$ values are exaggerated due to the absence of three-dimensional effects on the stresses. The first principal stress of the uncorroded part is assumed to be 1.0 ksi. Uniform traction load was applied at the ends.

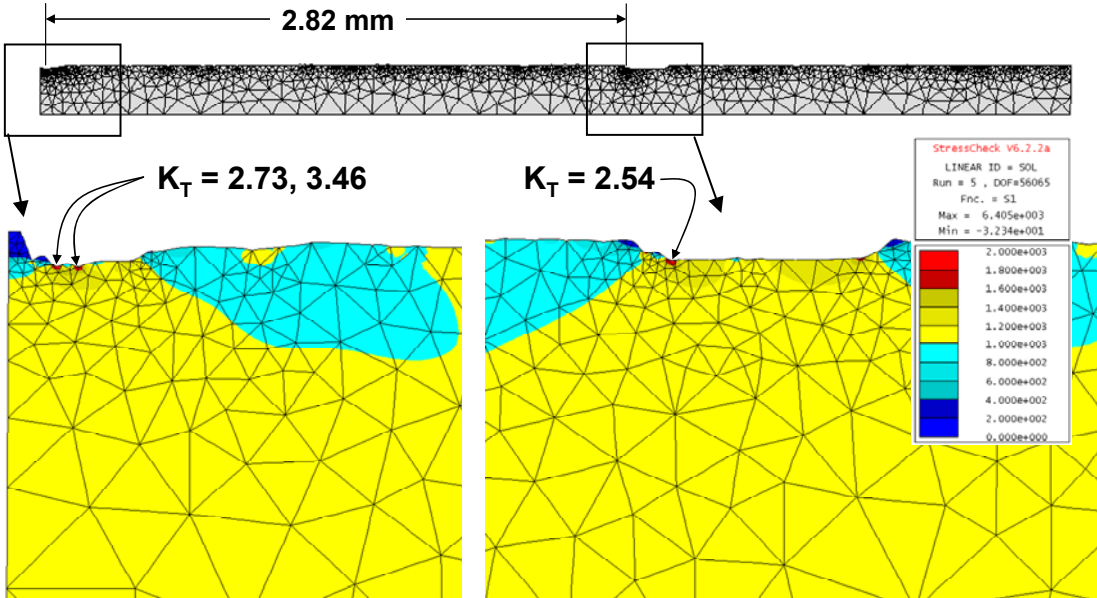


Figure 4. Example of Mesh and $K_{t_{eff}}$ Extraction from Laser Profilometer Data

6.1.3 Summary

The goal of this effort was the development of experience with the management of laser profilometer data and meshing in a simple setting. Assuming that the laser profilometer data contains sufficient surface roughness information to accurately map the corroded surface for quantitative assessment of maximum $K_{t_{eff}}$, and that the filtering does not impact critical regions of the surface, this approach will give a rough indication of the relationship between surface representation and $K_{t_{eff}}$ values. However, owing to the high degree of simplification of the model, the $K_{t_{eff}}$ values extracted from this model are not representative of $K_{t_{eff}}$ values for an actual 3-D corroded surface.

It is clear, that the complexities of the computational problem increase very substantially with increasing resolution of the details of surface features. The size of the problem in three dimensions will require large computational resources unless it can be shown that the short wavelength components of the surface representation can be neglected. The question of feasibility of direct representation of corroded surfaces in a numerical model has to be addressed.

6.2 Corroded Surface Idealization with Consideration of K_t Sensitivity

6.2.1 Introduction

An approach was developed for the purpose of geometrically idealizing a corroded surface in StressCheck[®] by using commonly occurring features observed in actual corroded specimen surfaces. These features included corrosion rings, discernable pits, and waviness characteristics viewed in UDRI experimental AF1410 dogbone test specimens. Of course the features must be highly idealized in order to make them accessible to numerical analysis.

The goal of this approach centered on simplifying a corroded surface into basic Parasolid geometries, without significantly affecting the maximum $K_{t_{eff}}$ for each geometric type. Successful results would indicate substantial savings in time and processing costs, thus allowing USN maintenance staff to quickly convert a corroded surface profile to quantifiable sets of simple geometries and extract the maximum $K_{t_{eff}}$. In addition to $K_{t_{eff}}$ sensitivity to idealization, the effects of residual stresses with respect to dogbone grindouts were investigated in order to quantify the effects of residual stresses in the computed $K_{t_{eff}}$; residual stresses were not considered as part of the model used to study the effect of corrosion on fatigue life. The approach and results are discussed in this section.

6.2.2 Study Approach and Results

UDRI supplied ESRD with corroded AF1410 dogbone specimen surface profiles, measured using White Light technology, each of which was characterized by a central ring of corrosion and a waviness aspect. The dogbones were corroded through the use of filter paper (3.5% NaCl solution). The data was corrected for tilt and curvature removal before any analysis was performed. ESRD then conducted virtual experiments with the objective to determine the sensitivity of $K_{t_{eff}}$ to details of idealization of corroded surfaces under standard conditions. As stated, a limitation of this objective is that replacement of corroded surfaces with idealized ones is permissible only if the maximum $K_{t_{eff}}$ values are not affected substantially by this idealization. Available results, at the time of this report, suggest substantial sensitivity to geometric details implemented for the idealization of corroded surfaces. An example of a corroded surface profile received, Dogbone-66, is shown in Figure 5.

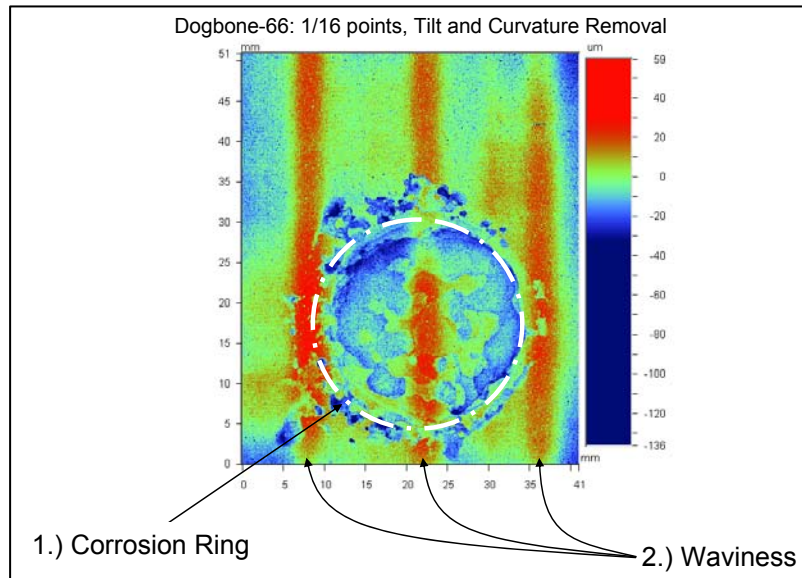


Figure 5. Dogbone-66 White Light Measurement Surface Profile

The geometric details used in the idealization of each corroded surface were designed to include common characteristics or distinctive features of the supplied dogbone profiles. These features include using a toroid to represent the ring of corrosion observed in the experimental surface profile, as well as embedded sinusoidal functions to include the observed waviness of the data. It was reported by UDRI that the waviness could consistently be observed within the majority of test specimens, and described as a sinusoidal wave with a wavelength of ≈ 14 mm and constant amplitude (depth). These features are shown in Figures 6 and 7.

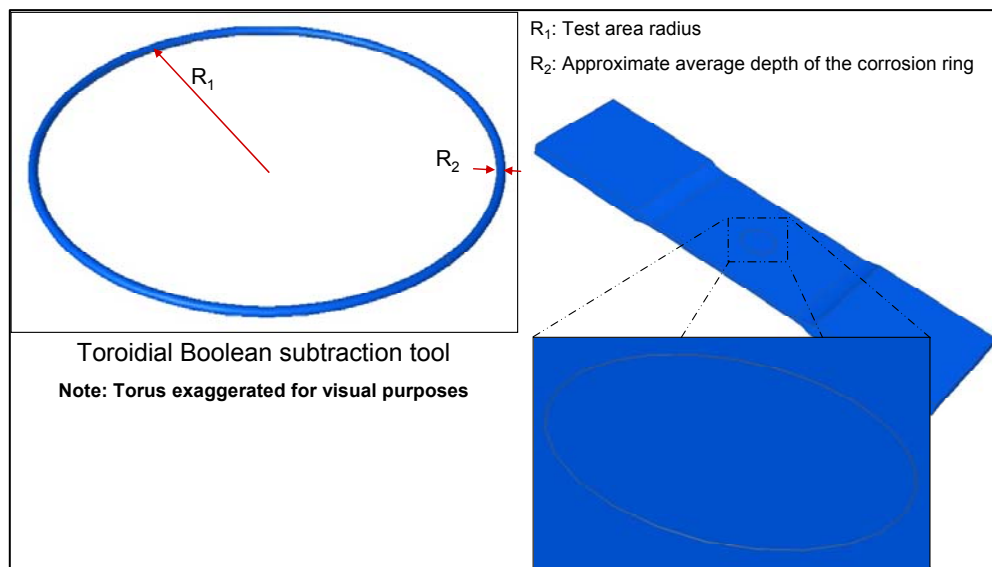


Figure 6. Example Toroidal Geometric Feature for Corrosion-Ring Modeling

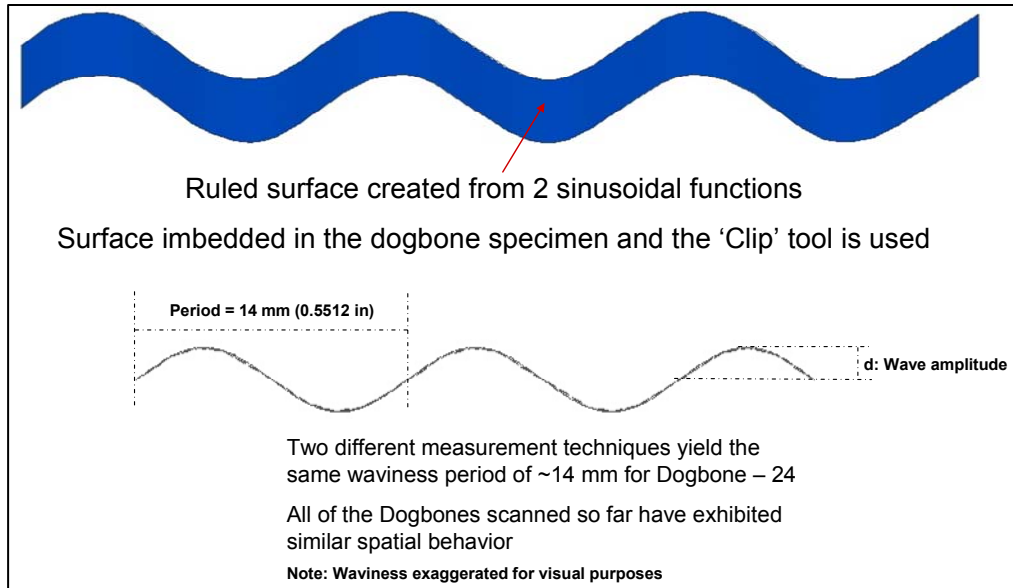


Figure 7. Example Sinusoidal Surface for Waviness Modeling

Before geometric idealization, it was desired to determine the maximum K_t for the pristine dogbone specimen, shown in Figure 8. The model is loaded with uniaxial traction.

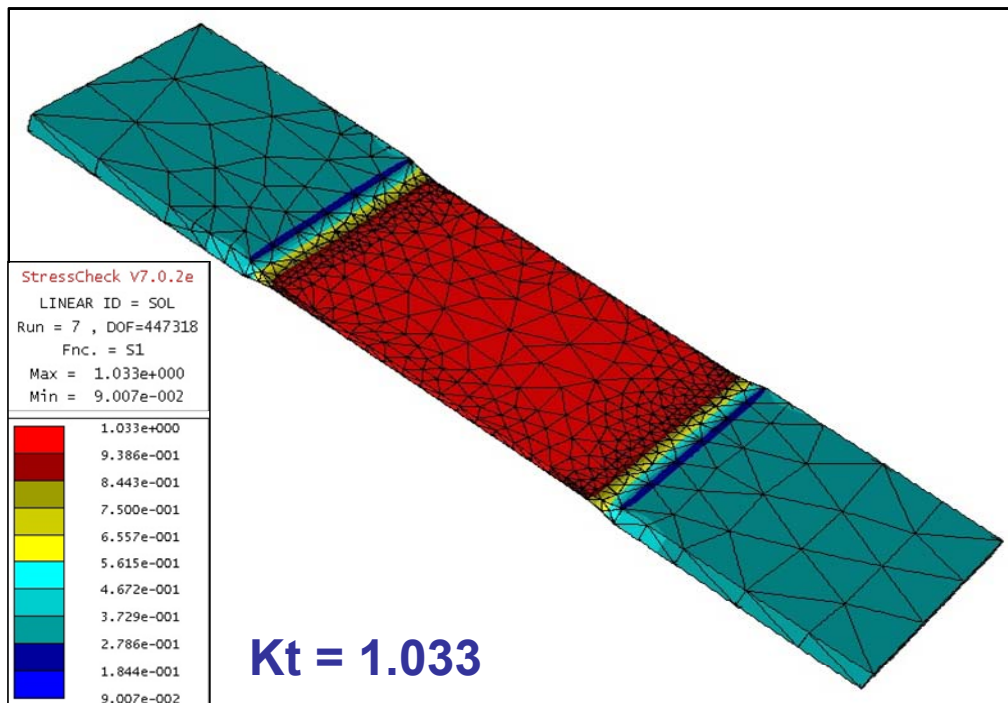


Figure 8. Pristine Case Dogbone Maximum K_t

This model was tested for $K_{t_{eff}}$ sensitivity by the study of three cases: 1) Corrosion-ring only 2) Waviness only and 3) Corrosion-ring plus waviness. From the initial virtual test data, it appears that introducing degrees of waviness in the vicinity of ring-corrosion has a significant effect; the max $K_{t_{eff}}$ may increase or decrease depending on the amplitude of the waviness, indicating some sensitivity. These results are given in Table 1 below.

Table 1. Example Virtual Test Results for Max Kt Sensitivity (Dogbone-66)

	wave amplitude (in)	period (in)	Rt1 (in)	Defect depth (in)	p-level	elements	D.O.F.	max Kt	error %
Torus	N/A	N/A	0.50	0.0025	5	10359	696207	1.980	1.40
Wave	0.003	0.5512	N/A	N/A	6	1252	161229	1.216	1.12
Torus & Wave	0.003	0.5512	0.50	0.0025	5	10852	724167	1.871	0.01

	wave amplitude (in)	period (in)	Rt1 (in)	Defect depth (in)	p-level	elements	D.O.F.	max Kt	error %
Wave	0.003	0.5512	N/A	N/A	6	1252	161229	1.216	1.12
Wave#2	½ Amplitude 0.0015	0.5512	N/A	N/A	6	993	128553	1.116	0.23
Torus & Wave	0.003	0.5512	0.50	0.0025	5	10852	724167	1.871	0.01
Torus & Wave #2	0.0015	0.5512	0.50	0.0025	5	11088	743262	1.947	1.13

In addition to the corrosion-ring and waviness features implemented into the virtual dogbone model, five (5) geometric defects of varying geometric definition were introduced to determine the sensitivity of maximum $K_{t_{eff}}$ to idealized surface perturbations. These defects included spherical, conical, and combined spherical-conical pitting. See Figures 9-12 on the following pages.

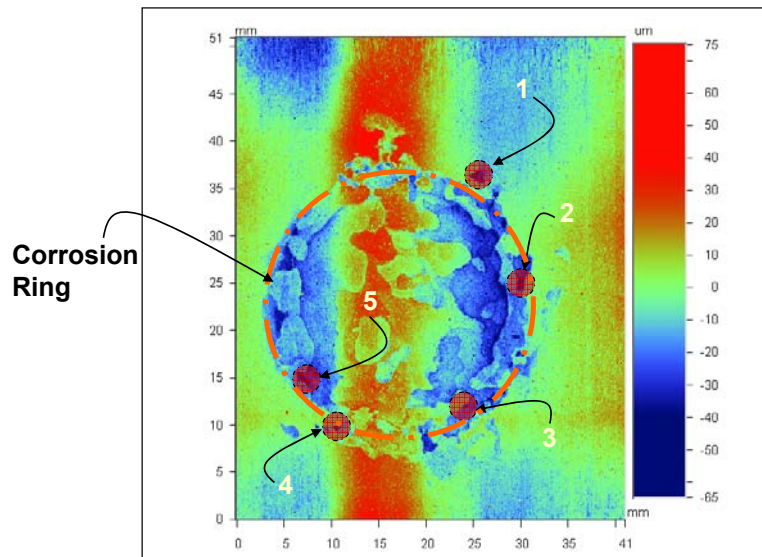


Figure 9. Example Five Key Sites Identified (Dogbone-16)

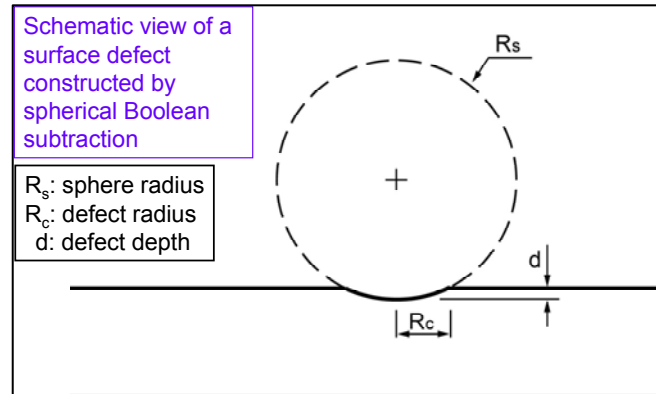


Figure 10. Example Spherical Defect

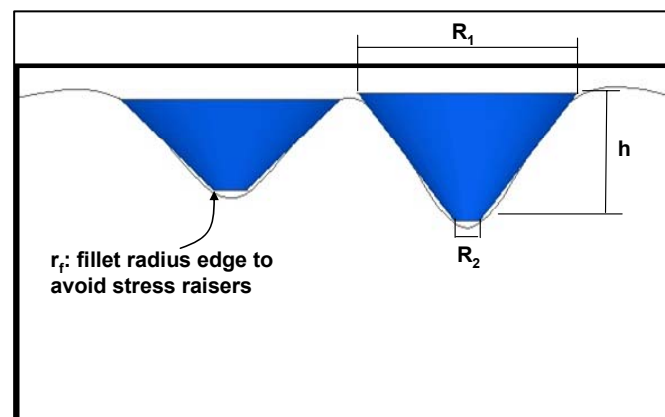


Figure 11. Example Conical Defect

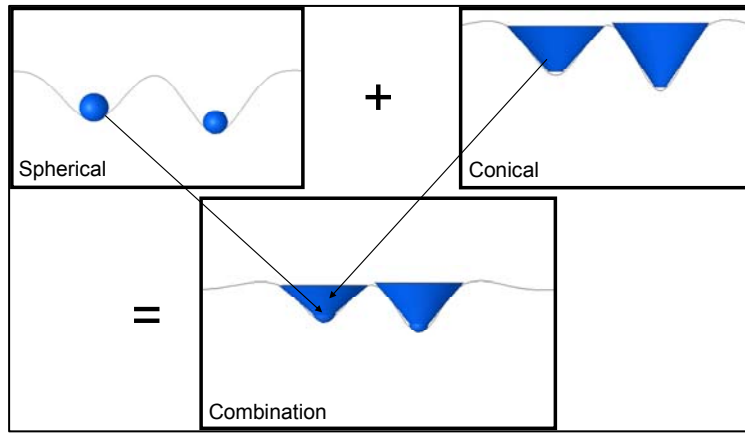


Figure 12. Example Spherical-Conical Defect

Each of these defects was individually assessed, with and without toroidal subtraction of corrosion-ring, for possible idealization to the corroded surface in Figure 9, and was subsequently examined for max $K_{t_{eff}}$ sensitivity under tensile loading. From the initial studies performed, it can be concluded that the maximum $K_{t_{eff}}$ is extremely sensitive to the tested idealized geometric features. By changing the parameters that govern the geometric features (radii, depth, etc), as well as changing the definition of the geometric features (sphere, cone, etc.), the max $K_{t_{eff}}$ varied substantially in both magnitude and location. Therefore, reliable prediction of fatigue performance from topological corrosion data may not be possible, as max $K_{t_{eff}}$ is strongly dependent on the defeaturing and simplifications of an actual corroded surface. This sensitivity can be seen in the example study shown in Figures 13 and 14, for which the toroidal geometry is and is not introduced into the surface.

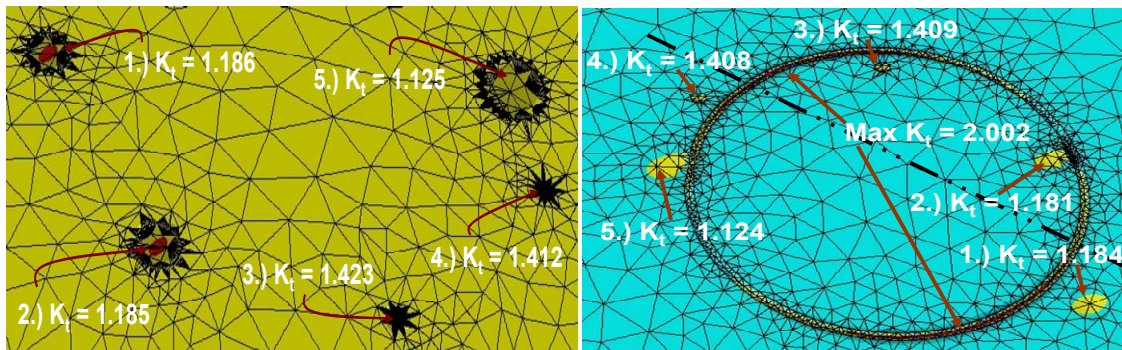


Figure 13. Comparison of $K_{t_{eff}}$ Values for Spherical Pitting and Spherical Pitting plus Toroid

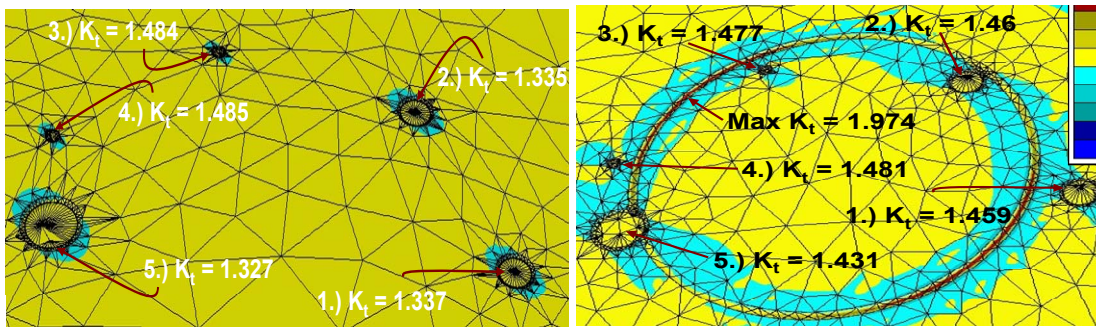


Figure 14. Comparison of $K_{t_{eff}}$ Values for Conical Pitting and Conical Pitting plus Toroid

In addition to the spherical, conical, and spherical-conical defects introduced to the dogbone virtual models in the above study, central disc-shaped defects, as well as circular material grindouts, were applied (please see Figures 15 and 16 below). These additional features were designed to provide further evidence that any geometric surface idealization can cause deviation in the maximum $K_{t_{eff}}$. In Figures 17-18 on the following page, there are examples of disc-shaped defects of differing sharpness (based on parameter r_f , the grindout edge radius) accounting for significant changes in maximum $K_{t_{eff}}$.

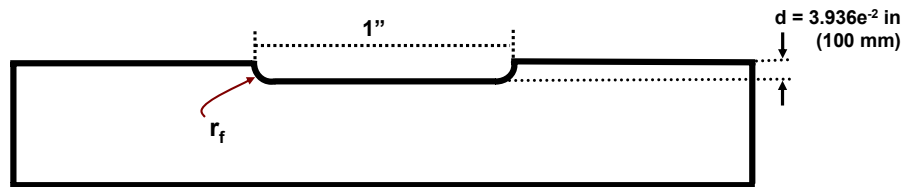


Figure 15. Disc-Shaped Defect

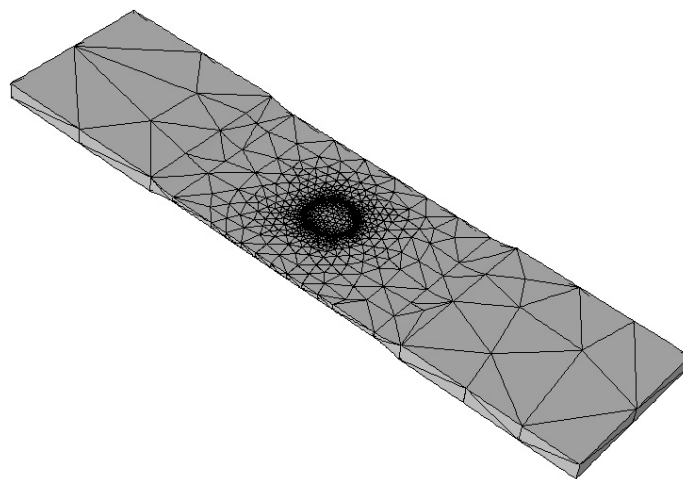


Figure 16. Example Surface Grindout Discretization for Dogbone

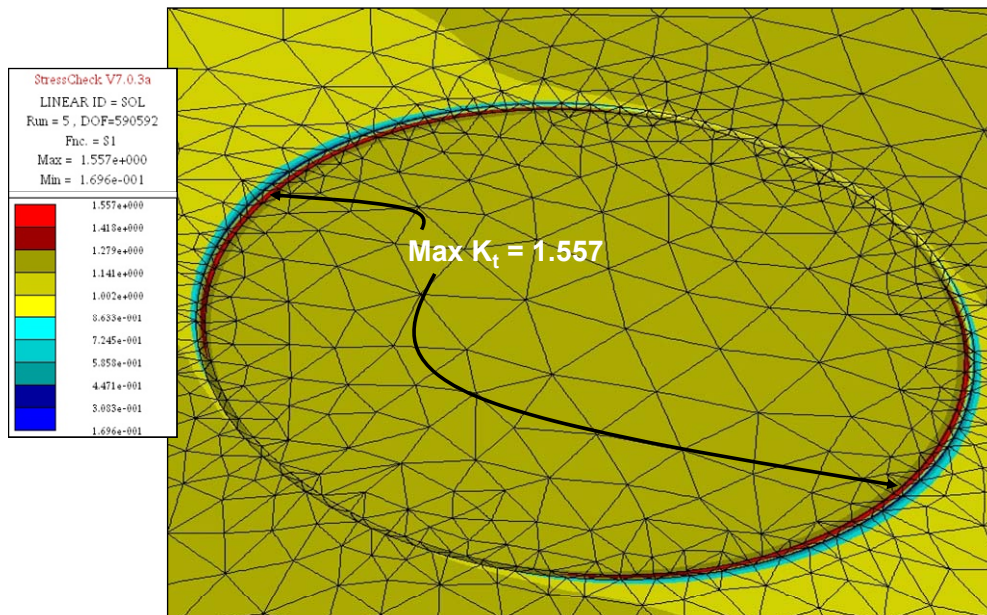


Figure 17. Disc-Shaped Surface Defect of $r_f=0.02''$

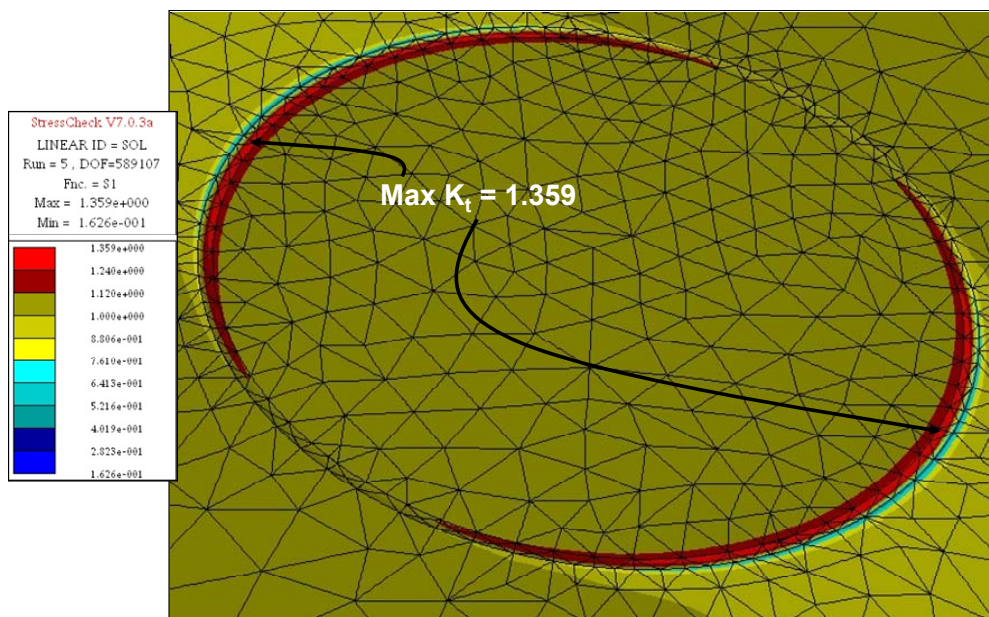


Figure 18. Disc-Shaped Surface Defect of $r_f=0.04''$

As a final investigation into the sensitivity of the maximum effective stress concentration factor, $K_{t_{eff}}$, an arbitrary surface height function $f(x,y)$ was used to construct the surface of an arbitrary square plate. This square plate was subjected to uniaxial loading and studied for two cases: one in which the surface height amplitude A_1 is 0.01 inches, and one in which the surface height amplitude is 0.003 inches (decrease of 70% in amplitude). As can be seen below in Figures 19-20, decreasing the amplitude by ≈ 3.0 (0.01 to 0.003) effectively decreases the maximum $K_{t_{eff}}$ by ≈ 3.0 (4.964 to 1.649) in this case. It is thus emphasized that characterizing corrosion surface features via simple geometric features will rarely, if ever, result in an accurate and reliable way of extracting the maximum $K_{t_{eff}}$ of that corroded surface.

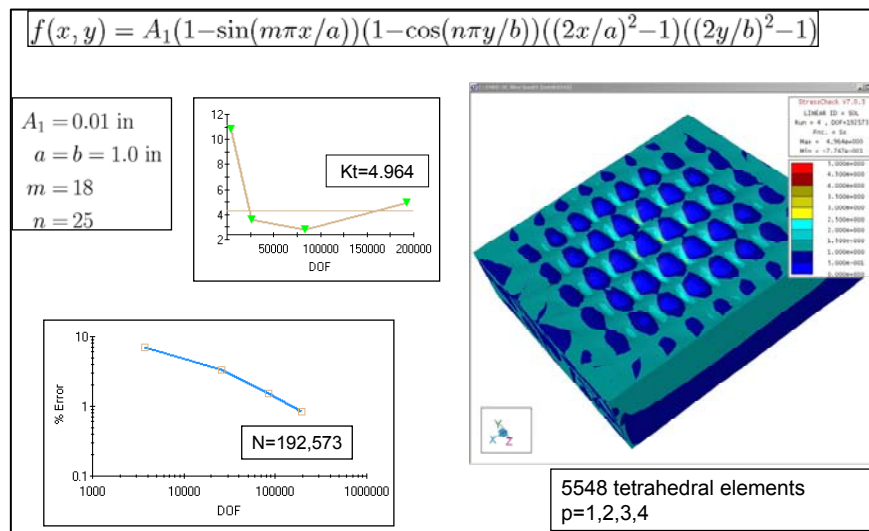


Figure 19. Arbitrary Surface Function with Amplitude=0.01 inches

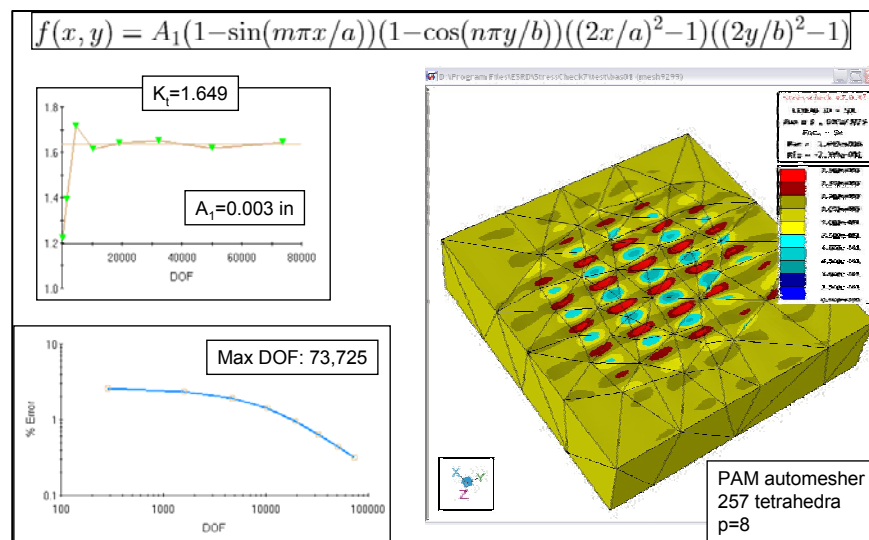


Figure 20. Arbitrary Surface Function with Amplitude=0.003 inches

Sets of circular material grindouts were created by a Boolean surface subtraction of a large radius sphere from the virtual dogbone model. The purpose of using these grindouts was to study the variation of the maximum $K_{t_{eff}}$ for varying radii of circular material removal, R_c . The grindout representation is shown in Figure 21. The StressCheck® model, as well as the sensitivity study data, is shown in Figure 22 and Graph 1. The effect of the grindout radius R_c on the maximum value of $K_{t_{eff}}$ is very small (3% change between extremes).

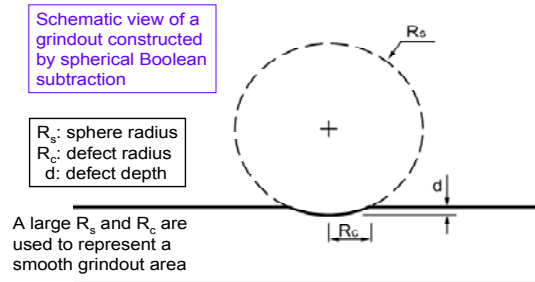


Figure 21. Circular Grindout Sphere Tool

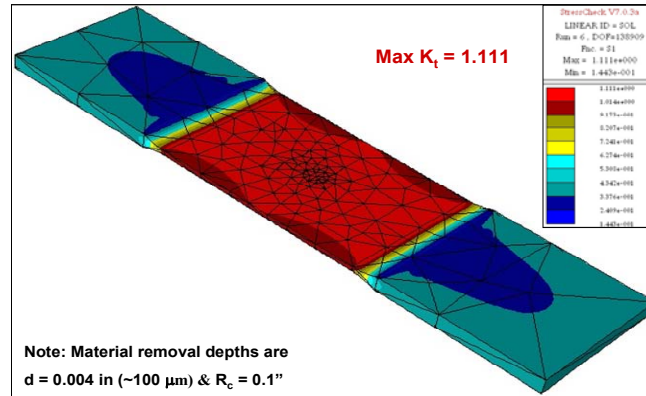
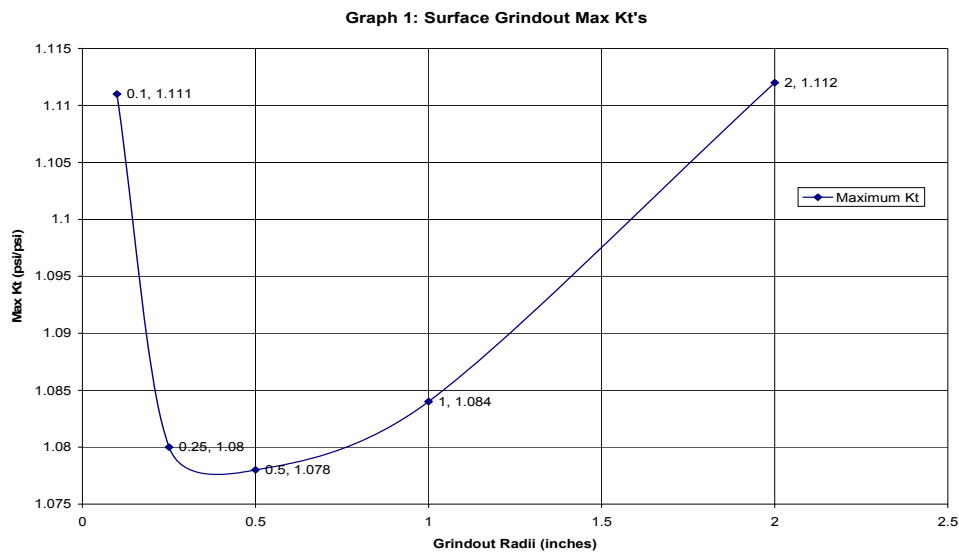


Figure 22. StressCheck® Grindout Model



6.2.
2a)
Res
idu
al
Stre
ss
Eff
ects

Experimental Observations

Residual stress experiments by x-ray diffraction have shown that compressive stresses of ≈ 100 ksi exist for a thickness of 0.003 inches in the test specimens (see Figures 23-24). The goal was to simulate these residual stresses within the virtual corrosion models through thermal loading, and subsequently study the effects of surface grindouts on residual stresses. In addition tensile loading was applied, and the sensitivity of $K_{t_{eff}}$ to variances in surface grindouts was computed.

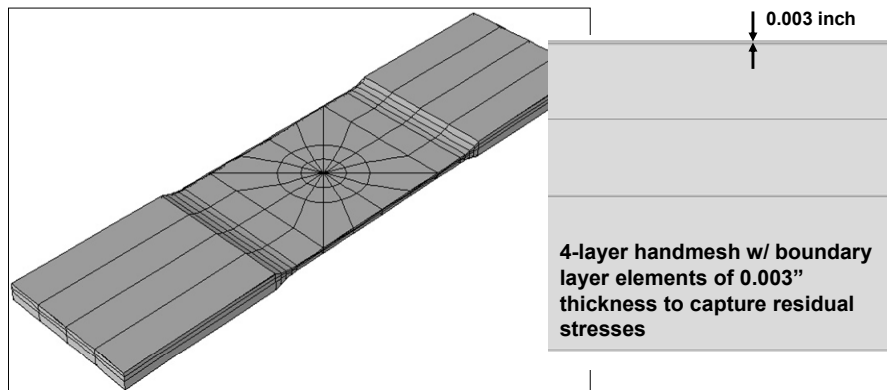


Figure 23. Residual Stress Layer Defined in Dogbone Specimen

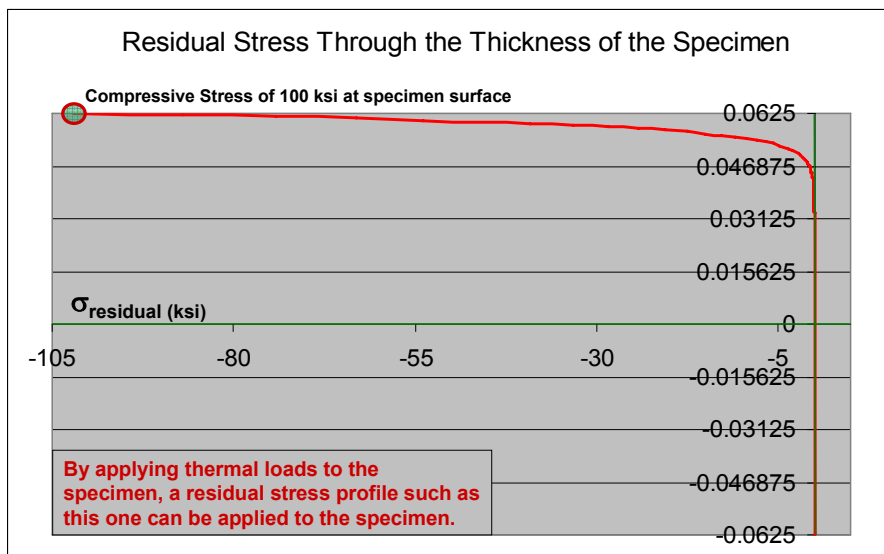


Figure 24. Plot of Residual Stress versus Surface Axis

6.2.2b) Residual stress: Analytical considerations

Modeling the effects of residual stresses by numerical means has three objectives: First, interpretation of laboratory experiments requires consideration of residual stresses because residual stresses affect $K_{t_{eff}}$ values. Second, repair involving removal of corrosion by grinding will affect FLE differently when residual stresses are present. Third, it is conceivable that surface removal by grinding, followed shot peening or other surface treatment to restore residual stresses will be economically feasible since it will increase FLE.

Modeling the effects of residual stresses by numerical means is possible only if the following assumptions are justified

1. Small strain, small displacement theory is applicable
2. The redistribution of stress after material removal occurs elastically
3. The constitutive law is independent of the residual stress
4. The stresses introduced by the cutting tool can be neglected.

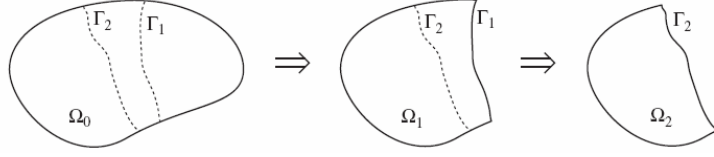
Assumptions 1, 2, and 3 imply the assumption that the principle of superposition is applicable. It is known that the residual stresses must satisfy the equilibrium equation ($\sigma_{ij,j} = 0$ on the body domain Ω), and that the tractions at free boundaries must be zero ($\sigma_{ij}n_j|_{\partial\Omega_0} = 0$ where $\partial\Omega_0$ is the traction free boundary of Ω). It is shown in the following that subject to the stated assumptions, the residual stresses in an elastic body altered by corrosion, grinding or milling depend on the initial residual stress distribution and the current configuration but not on the intervening sequence of configurations. This makes estimation of the effects of residual stresses by numerical means possible.

6.2.2c) Path Independence

We denote the initial body by Ω_0 , its boundary points by $\partial\Omega_0$ and the initial stress state by $\sigma_{ij,j}^0$. The initial stress state satisfies the equations of equilibrium $\sigma_{ij,j}^0 = 0$ on Ω_0 and the stress-free boundary conditions, i.e. $\sigma_{ij}^0 n_j = 0$ on $\partial\Omega_0$ where n_j is the unit normal.

Let us now introduce a cut Γ_1 that produces the domain Ω_1 , and a second cut Γ_2 that produces a domain Ω_2 . Denote the displacement field following the first (resp. the second) cut by U_i^1 (resp. U_i^2). The notation for these cuts is shown in the figure.

Theorem 1: U_i^2 depends on σ_{ij}^0 and Ω_2 but not on U_i^1 or Ω_1 .



Theorem 1. Notation.

Proof: By the principle of superposition U_i^1 satisfies

$$B(U_i^1, v_i) = - \int_{\Gamma_1} \sigma_{ij}^0 n_j v_i dS \quad \forall v_i \in E(\Omega_1) \quad (6.2.1)$$

Where $B(U_i^1, v_i)$ is the virtual work of internal stresses corresponding to the virtual displacement v_i on Ω_1 . $E(\Omega_1)$ is the energy space defined by

$$E(\Omega_1) = \{u_i \mid B(u_i, u_i) \leq C < \infty\} \quad (6.2.2)$$

Denote S_{ij}^1 the stress field corresponding to U_i^1 on Ω_1 and let u_i^2 be the displacement field on Ω_2 corresponding to the tractions $S_{ij}^1 n_j$ acting on Γ_2 , therefore

$$B(u_i^2, v_i) = \int_{\Gamma_2} S_{ij}^1 n_j v_i dS \quad \forall v_i \in E(\Omega_2) \quad (6.2.3)$$

The displacement field corresponding to the second cut is $U_i^2 = u_i^2 + \tilde{U}_i^2$, where

$$B(\tilde{U}_i^2, v_i) = - \int_{\Gamma_2} (\sigma_{ij}^0 + S_{ij}^1 n_j) v_i dS \quad \forall v_i \in E(\Omega_2) \quad (6.2.4)$$

Adding eq. (6.2.3) and eq. (6.2.4) we find that

$$B(U_i^2, v_i) = - \int_{\Gamma_2} \sigma_{ij}^0 n_j v_i dS \quad \forall v_i \in E(\Omega_2) \quad (6.2.5)$$

This proves the theorem for path independence.

Here, we have considered an unconstrained body; hence the displacements are understood to be displacements up to rigid body constraints. We observe, however, that when constraints are applied far from where the material is removed, the same residual stress is obtained after releasing the constraints. If the effect of the constraints is elastic, the result obtained in eq. (6.2.4) remains unchanged, therefore Theorem 1 holds under these conditions also.

We have also assumed that when a body is cut, the cutting operation will not induce stresses. However, in mechanical milling and grinding additional residual stresses are introduced. The magnitude of these stresses is substantial only in a thin layer near the surface.

6.2.2d) Modeling residual stresses

The residual stresses were induced into the model of Figure 23 by the use of thermal loading, which was defined through the thickness by the following exponential function:

$$T_{load} = A \left(e^{\frac{2\beta y}{t_c}} - 1 \right)$$

where: T_{load} is the thermal loading function, A and β are coefficients that control the temperature and hence the distribution of the residual stress, y is the through-thickness coordinate, and t_c is thickness. The induced residual stresses, resulting from the thermal load, are shown in Figure 25.

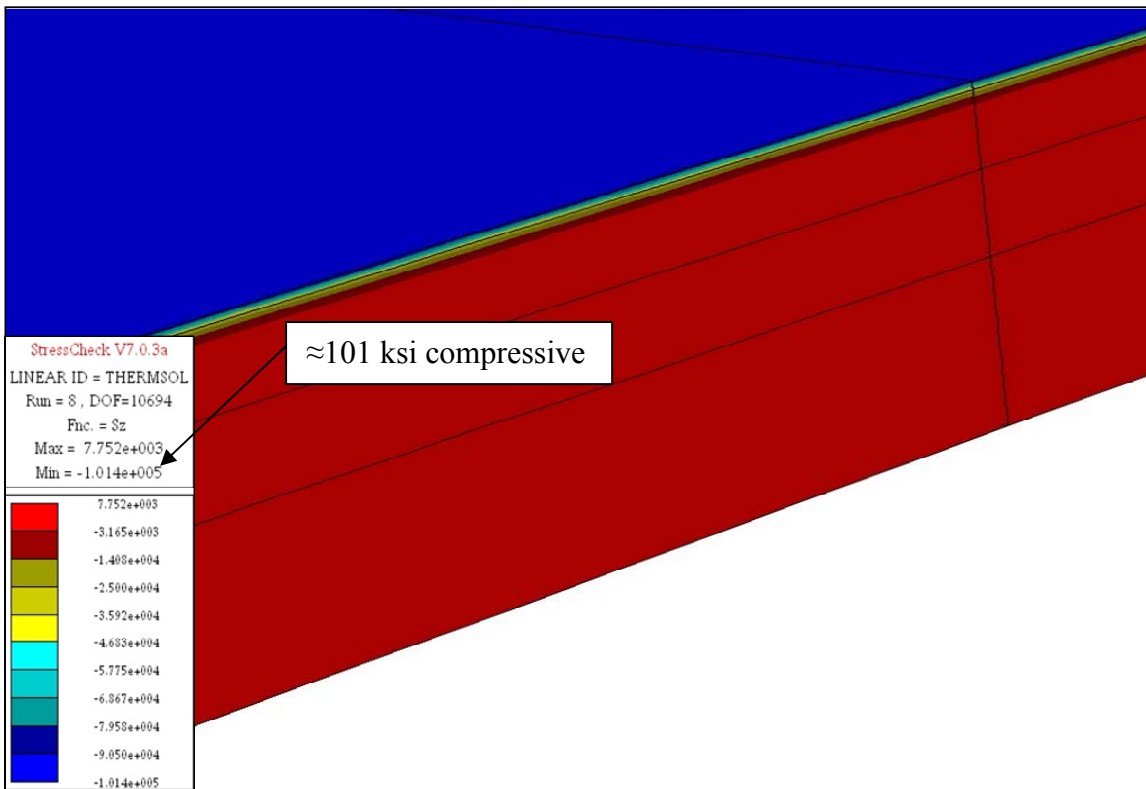


Figure 25. Induced Residual Stresses by Thermal Loading on a Pristine Quarter Specimen

As can be seen in Figure 25, the applied thermal load resulted in a residual stress distribution which closely modeled the behavior of the data in Figure 24. Approximately 101 ksi of induced residual stress is seen at the surface, which decays to nearly zero at a thickness of 0.003 inches. A spherical grindout of 0.004 inches in depth was then applied to the pristine specimen of Figure 25, the results of which can be seen in Figure 26.

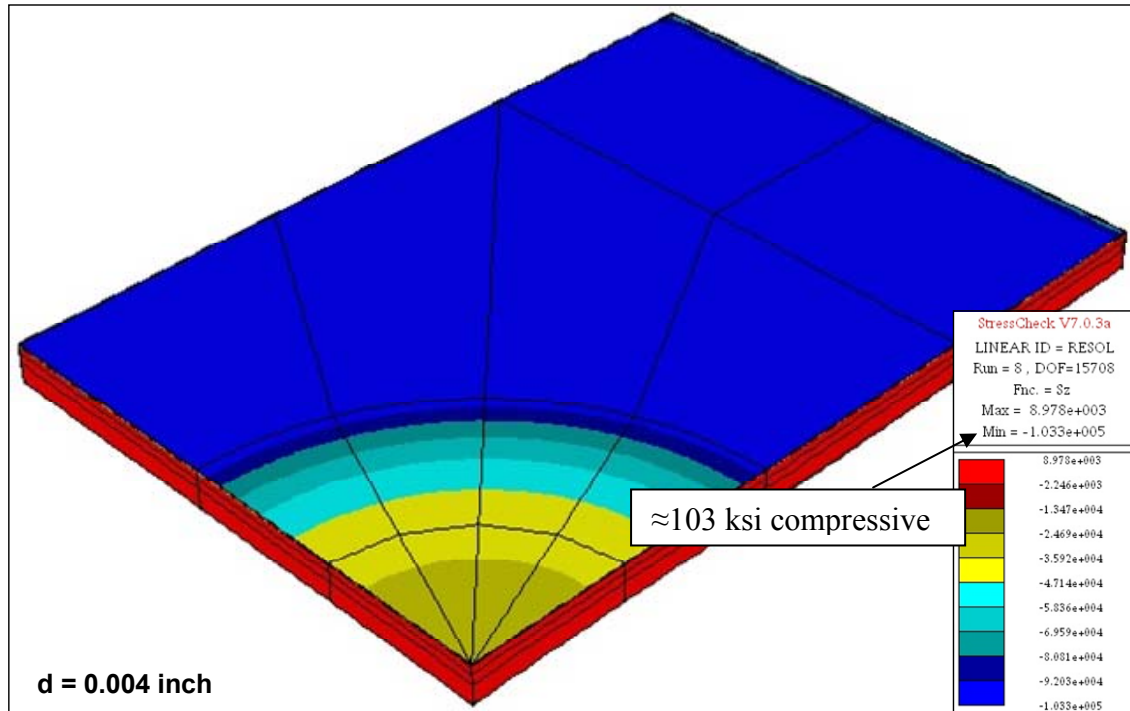


Figure 26. Induced Residual Stresses by Thermal Loading on a Grindout Quarter Specimen

To further illustrate the effects of residual stresses in a specimen, a tensile load of 200 ksi was applied to the specimen in order to observe the combined effects of residual stresses and tensile loading. The addition of stresses, which we assume to be linear, can be determined through the use of superposition. Figure 27 shows the superposition steps, and Figure 28 shows the results of superposition for the specimen of Figure 26. It is noted that the combined effects are clearly visible, as the 200 ksi tensile load superimposed with the -103.3 ksi residual stress shown in Figure 26 is very close (96.7 ksi) to the minimum stress seen in Figure 28 (94.4 ksi).

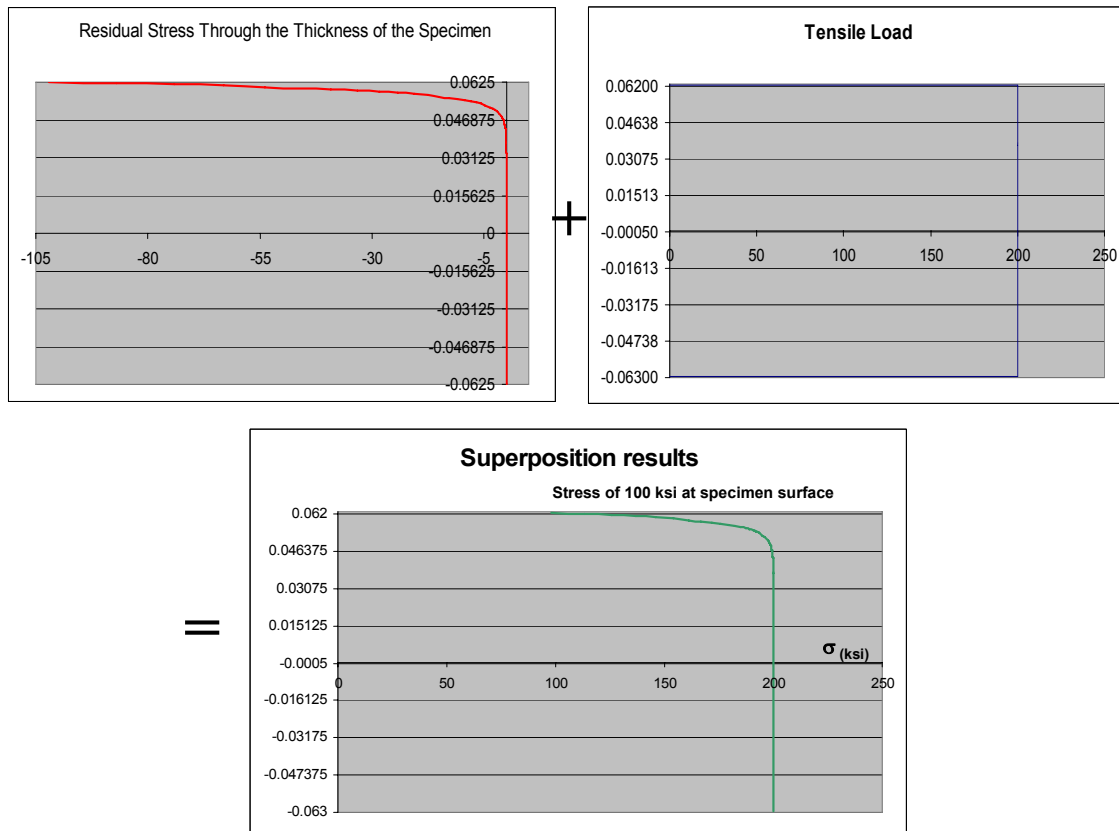


Figure 27. Superposition of Residual Stress and Tensile Loading

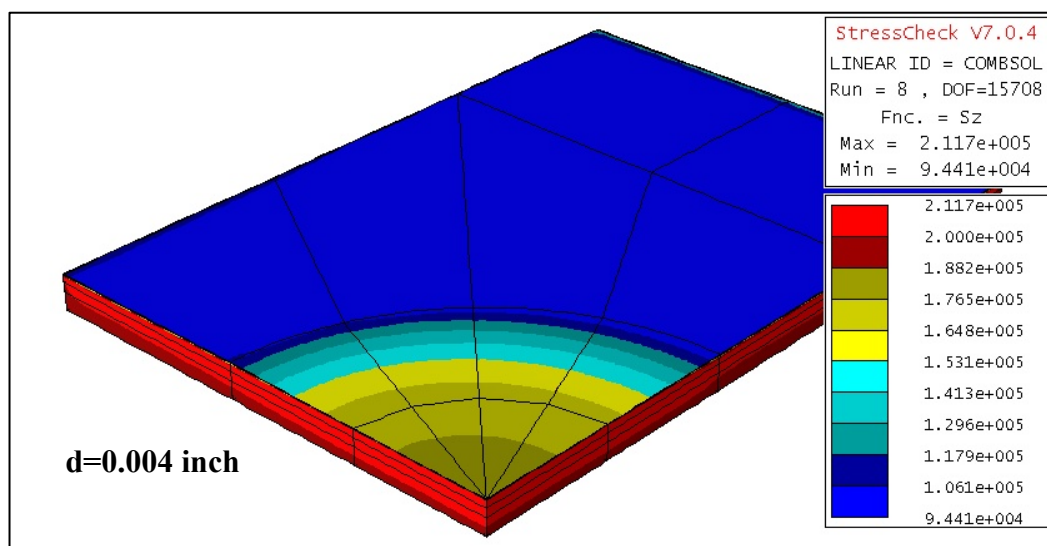


Figure 28. Effects of Thermal and Tensile Loading on a Grindout Quarter Specimen

6.2.3 Summary

The idealized surface defects were characterized by width to depth ratios of order 1. The results of computational experiments show that the maximum normal stress and hence $K_{t_{eff}}$ is sensitive to the details of idealization.

Reliable information is not available concerning the distribution of residual stresses in the AF1410 specimens tested. The x-ray diffraction measurements suggest the magnitude of residual stresses to be close to 100 psi but no information is available concerning their distribution parallel or normal to the surface. In the computational experiments performed the residual stresses were induced by an assumed temperature distribution. This produces nearly uniform stress distribution parallel to the surface, which may or may not be representative of the actual stress distribution. Qualitatively speaking, the presence of residual stresses will delay the initiation of fatigue failure, but tends to accelerate the growth of defects once the surface layer where the residual stresses are compressive was penetrated.

The presence of residual stresses in the AF1410 specimens tested introduces uncertainties that must be taken into consideration in the interpretation of results.

6.3 Kt Using Characteristic Metric for Approximation to Elasticity Theory (UDRI)

6.3.1 Introduction

A heuristic approach for computing an approximation of K_t for a corroded part was proposed by UDRI during the project review meeting held on May 11, 2005 at the Boeing facilities in St. Louis. This heuristic model was developed with the aim to capture the stress concentration (K_t) caused by a hemispherical pit in a 2-D setting. In a second approximation, it was extended to a sinusoidal surface function for a 2-D and 3-D case. A final approximation (involving additional simplifying assumptions) was made to extend the metric to more general cases (any surface) for 2-D and 3-D. The overall objective of this study was to investigate the range of applicability of the simplified model to generalized stress states and corroded surfaces with respect to the maximum K_t ; correlation to fatigue life would then follow. The proposed metric is called the pit metric. The definition of the proposed pit metric for the case of a hemispherical pit is shown in Figure 29.

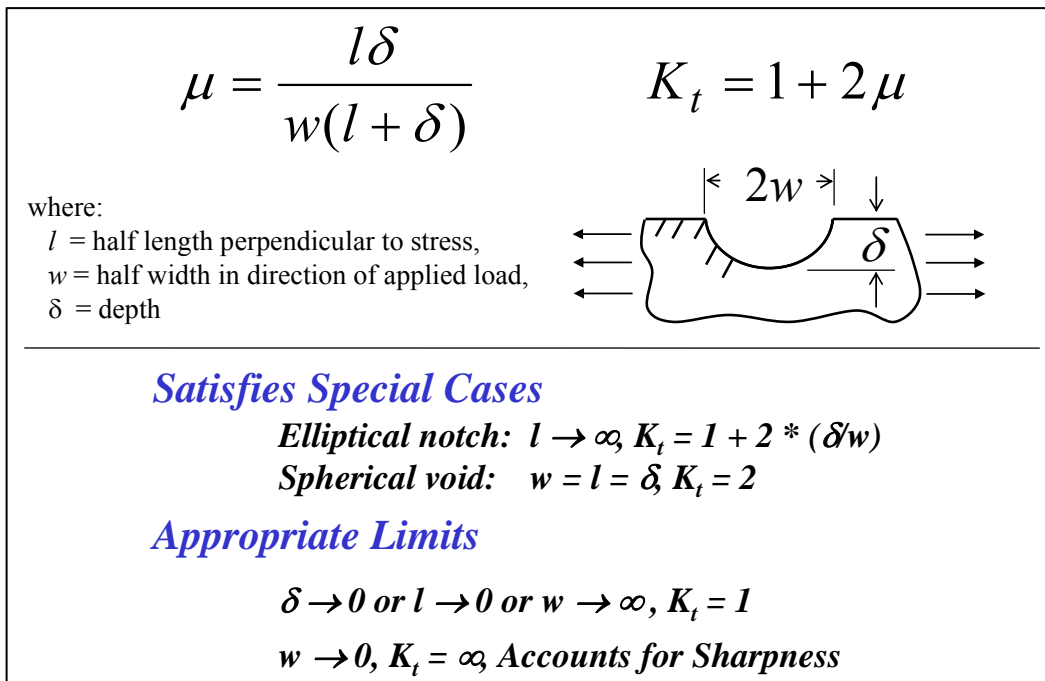


Figure 29. Proposed Pit Metric

6.3.2 Study Approach and Results

This study was performed as a preliminary verification and validation study in which, for a given set of domain parameters and conditions, the pit metric solution for the K_t , considered to be an approximation of the solution to the elasticity equations, was compared with the solution obtained by StressCheck[®], considered to be the exact solution. Currently, the pit metric K_t , denoted as $K_{t_{app}}$, can be compared quantitatively with the exact (FEM) K_t for a set of simple cases, although thorough validation of the pit metric remains incomplete at this time. As will be discussed in the suggested future studies section, the cases of multiaxial stress states as well as curved surface profiles must be examined and validation of these cases proven before the pit metric can be deemed a viable basis for making corrosion maintenance decisions. For the simple cases studied so far the UDRI pit metric exhibits reasonable results, comparing well to the FEM solution for a certain range of input parameters (i.e. width and depth of pit). Each case will be examined and discussed in the following pages of this section.

At the time of writing, an investigation into the validity of the pit metric had been extended into several test cases of varying dimensionality (2-D and 3-D surface functions), all involving uniaxial loading and (simple) smooth geometries. The first case, Case 1, involved the use of a single term, single directional variable sinusoidal function of a defined wavelength (period) to represent an idealized corroded surface height. The second case, Case 2, involved an extension of Case 1 to incorporate a three term expansion of cosine functions, each with differing wavelengths (periods). These additional cosine terms allow for a simple, idealized representation of surface roughness; each was tested individually for contribution to the $K_{t_{app}}$. The third case, Case 3, involved a three-dimensional representation of Case 1 by implementing multiplicative cosine functions. Each case was designed to study the range and applicability of the pit metric. The pit metric formulation is described below.

As mentioned, the approximation utilizes an idealized characterization of a corroded surface through the use of 1-D or 2-D sinusoidal functions. These sinusoidal functions were chosen because of their ability to approximate any periodic function (continuous or non-continuous) through Fourier series term expansion methods (i.e. FFT mapping). It will be noted at this time that corrosion damage is of random nature, possibly such that a reasonable number of periodic terms may not be sufficient to capture a corroded surface profile. This must be an area of future study. An example sinusoidal function of period λ and amplitude A is shown in Figure 30, with key geometric characteristics defined as shown in μ , the pit metric (δ , w , and l).

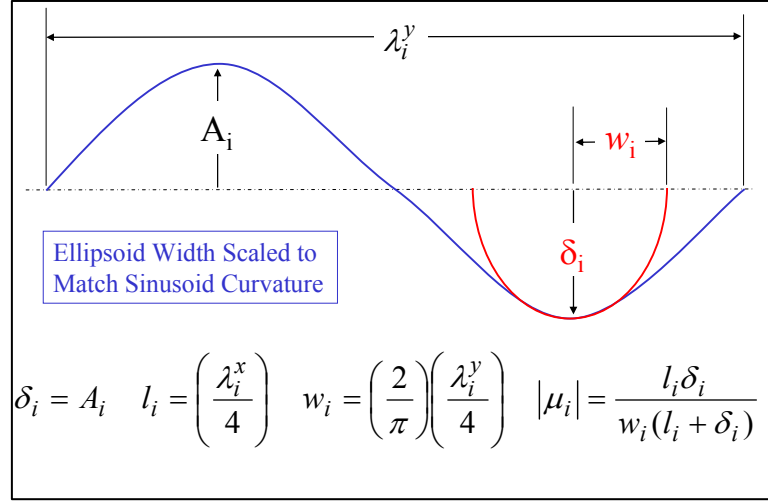


Figure 30. Sinusoidal Function with Pit Metric Characteristics

The introduced pit metric is “fitted” so that the pit corresponds to the coefficients of the sinusoidal function shown in Figure 30. According to UDRI, the above relationships between sinusoidal characteristics (period, amplitude) and the corresponding pit metric parameters (δ , w , and l) provide a simple link between surface height fluctuation and the near-surface stresses. It is shown in Figure 31 that surface height and the corresponding stress are exactly 180 degrees out of phase (inverted about the y-axis). This treatment for the solution of the $K_{t_{app}}$ by the pit metric is intuitive and makes physical sense: the surface height and the corresponding local stress are inversely related. The details of this relationship, however, are dependent on the parameters for the surface representation and the state of loading.

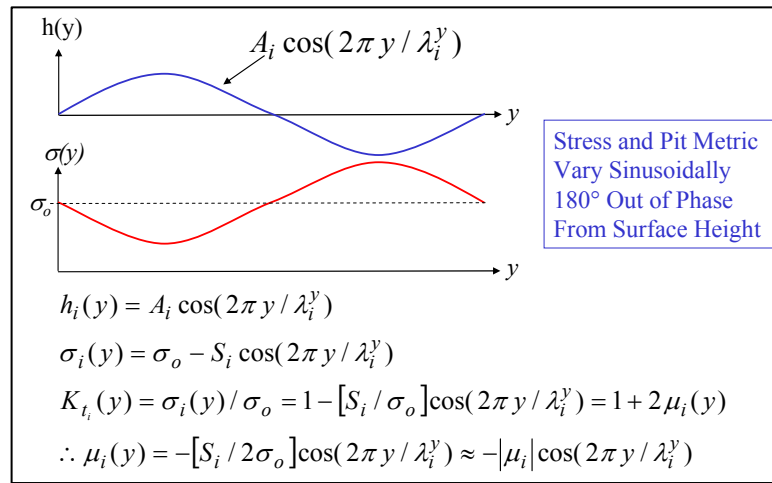


Figure 31. Extension of Surface Function to Pit Metric

Figure 32 shows the extrapolation of the $K_{t_{app}}$ profile from the given surface profile, according to the method proposed by UDRI. To achieve this extrapolation, the physical domain must be mapped into the frequency domain using FFT methods. Once the frequency components necessary to map the physical domain (surface) are determined, within a certain error range, the appropriate pit metric is computed for each frequency component and converted into the physical domain $K_{t_{app}}$ profile.

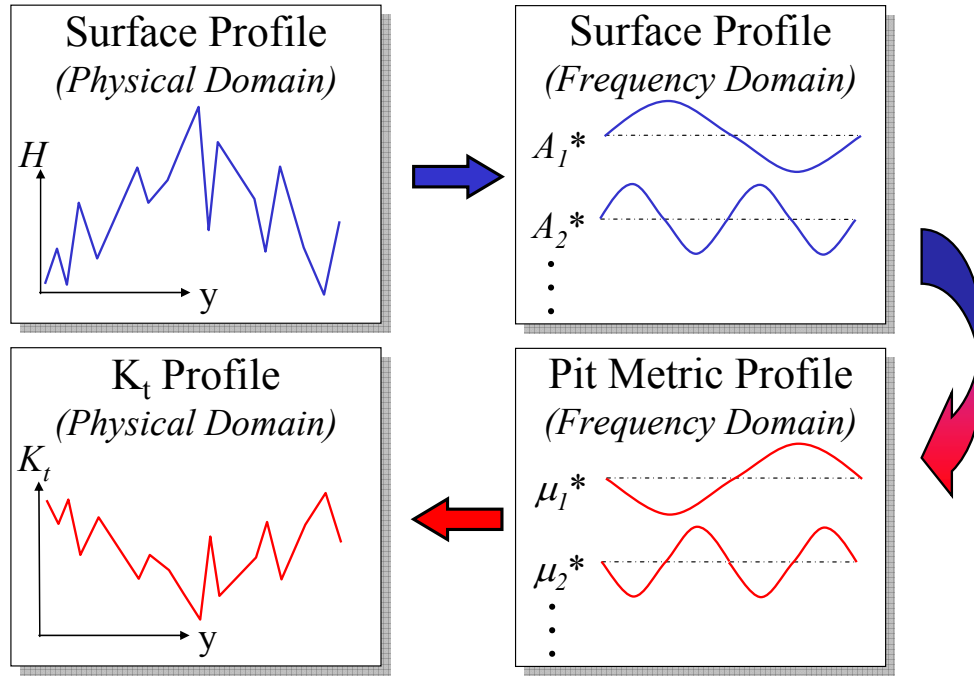


Figure 32. Flow Chart of Conversion of Surface Profile to $K_{t_{app}}$ Profile

There are several assumptions made during the process shown in Figure 32. First, it is assumed that during the conversion of a rough surface profile to the frequency domain through the use of FFT methods, the region(s) of interest do not lose resolution of critical roughness characteristics, as it has been proven that the K_t is very sensitivity to certain geometric variances in the surface profile. As was seen in Section 6.2, it is not likely that the defects caused by field corrosion are periodic in nature or can be described by simple geometries.

Second, it will be shown that the proposed approximation for the stress concentration through the use of the pit metric is valid for specific ranges of application, but may not be a reliable method beyond these specific ranges. This is due to the assumption that the pit metric $K_{t_{app}}$ for a set of sinusoidal surface height functions, as shown in Figure 29 and given as $K_{t_{app}}=1+2\mu$, is similar in approach to the simplified model of the theory of elasticity for an

elliptical notch in a 2-D plate, where the stress concentration is given as $K_t = 1 + 2\sqrt{r/t}$ ⁶. Since both metrics are explicitly defined only for 2-D, it may be limited in complex 3-D cases. Extrapolating the proposed pit metric to the 3-D domain, therefore, may not always yield accurate results when compared to the exact solution due to the improper representation of 3-D effects.

Third, as can be seen below in Figure 33, the total K_t at a surface location for the case of multiple stress concentration terms (given by the product of each successive term) is regarded as the upper bound for K_t . In regard to the pit metric, it is shown that the total $K_{t_{app}}$ is given by $1 + 2\sum\mu_i$ + “higher order terms.” For purposes of simplifying computation, these higher order terms are neglected in favor of only the linear summation terms. This neglect of higher order terms, and the use of $1 + 2\sum\mu_i$ for $K_{t_{app}}$, is valid for the comparison to K_t only if the pit metric, μ_i , is small, i.e. when μ_i^i (where $i > 1$) is negligible in comparison with μ_i .

Each case, as mentioned in a previous paragraph, was studied for accuracy by comparison to the FEM using StressCheck[®]. The modeling assumptions, results and conclusions from each study are described in the following sections.

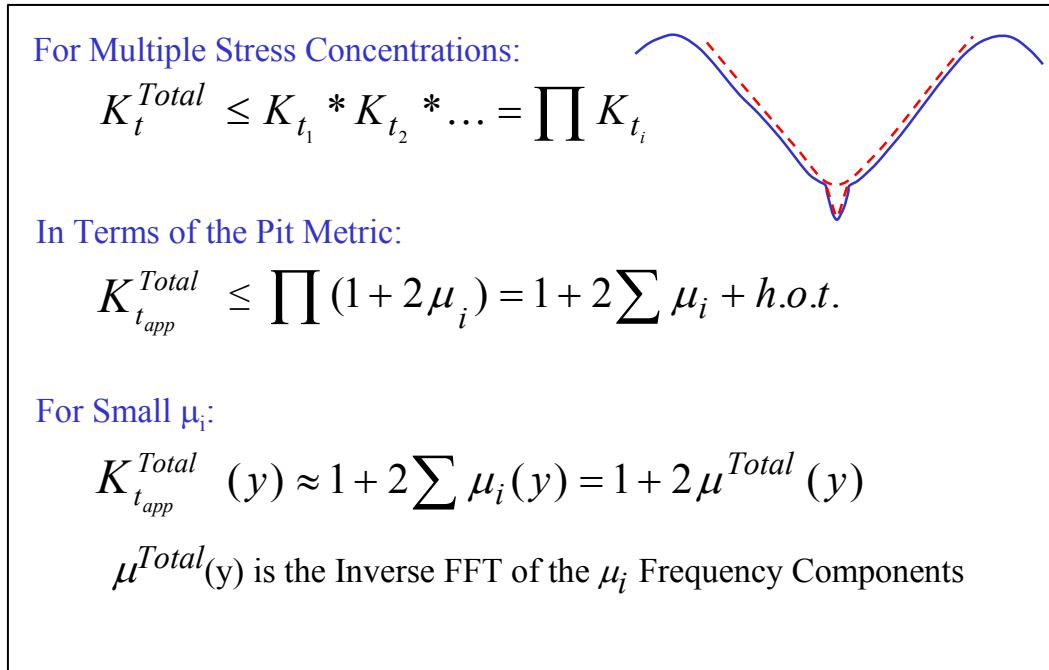


Figure 33. Approximation of the Total Stress Concentration

⁶ Peterson's Stress Concentration Factors (Green Text), p. 22: Equation 44

6.3.2a) Case 1: 2-D Sinusoidal Surface Function: Single Term Study

The model problem is shown in Figure 34, where the surface is represented by a cosine function of wavelength “a”. Due to symmetry, we need only to consider the shaded region indicated in Figure 34. The vertical edges of the domain (shown by parameter d) are subjected to uniform, uniaxial traction loading (σ_∞).

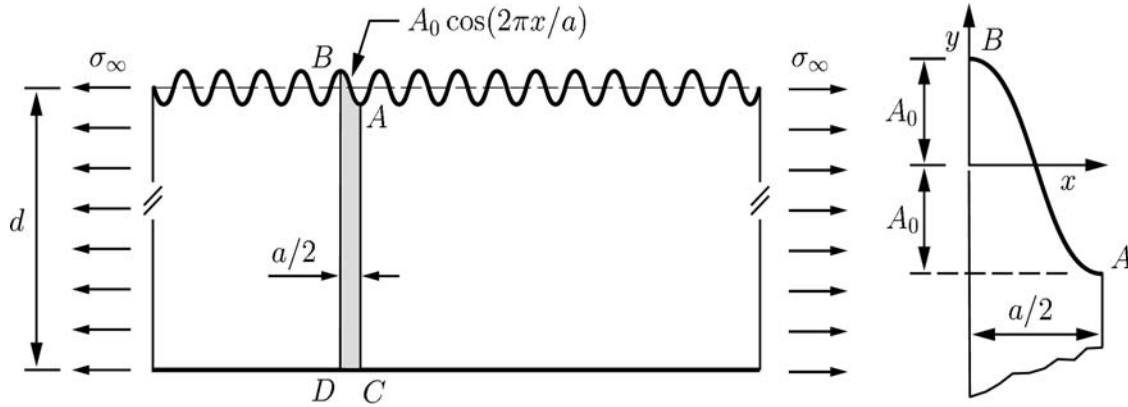


Figure 34. Case 1 Model Problem

The mesh and boundary conditions used for computing the solution are shown in Figure 35. An imposed displacement was used on the vertical edge on the right to define the periodic boundary condition of the uniform traction shown above, while symmetry boundary conditions are prescribed on the opposite vertical edge. The location of maximum Kt is shown as well, as this location does not change during the sensitivity studies.

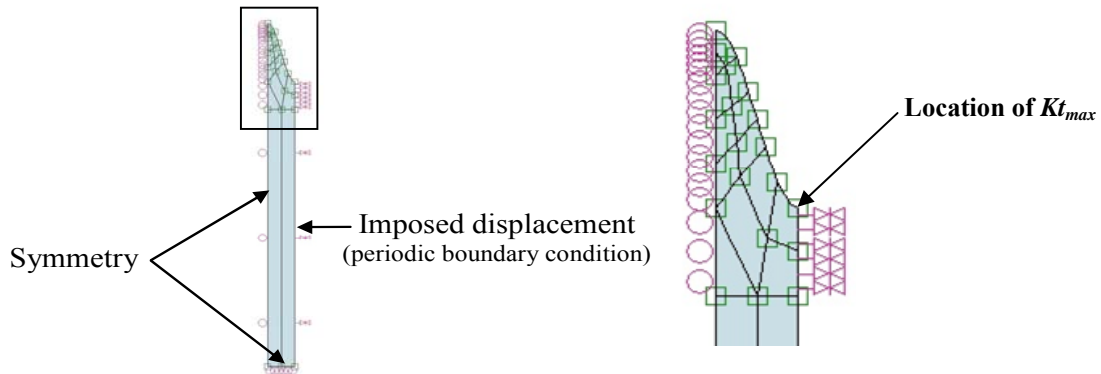


Figure 35. Case 1 Finite Element Discretization and Periodic Boundary Conditions

For this particular case, $A_0 = \delta = 0.01$

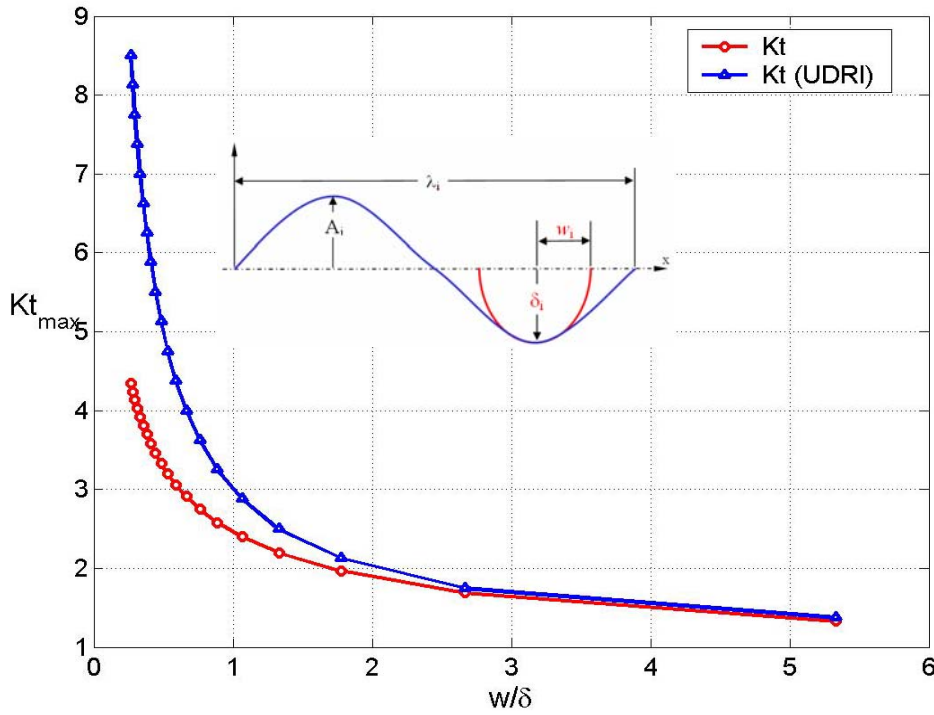


Figure 36. Case 1 Comparison of Exact Kt vs. Pit Metric Kt_{app} for Variable Pit Width

In Figure 36, a comparison between the maximum Kt for the model problem, computed for different values of w (i.e., λ) is shown. It is found that a relative error of 3.8% or higher is obtained when the ratio w/δ is less than $\approx 2\frac{2}{3}$.

The reference Kt values were computed using the FEM via StressCheck[®]. Plane stress conditions were used. All results were verified for error convergence. It is seen that as the ratio w/δ decreases, the error of the estimate obtained by the pit metric formula decreases. However the correspondence between the Kt_{eff} values obtained by finite element analysis and the pit metric formula is very good for large w/δ values.

6.3.2b) Case 2: 2-D Sinusoidal Surface Function: Summation of Differing Terms Study

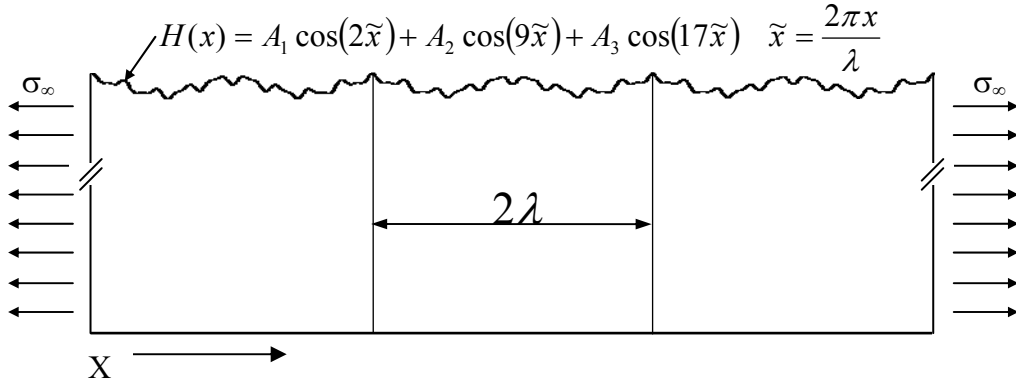


Figure 37. Case 2 Model Problem

Where: $A_1 = 0.01$, $A_2 = 0.005$, $A_3 = 0.0025$, $\delta_{\max} = 0.0175$, $\lambda = 8\pi/15$. The finite element discretization is shown in Figure 38.

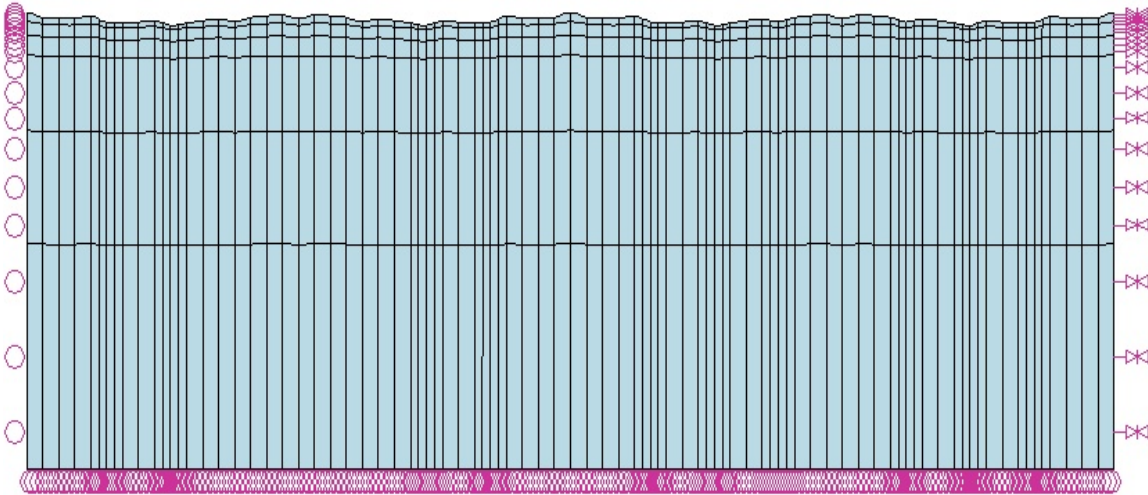


Figure 38. Case 2 Finite Element Discretization and Periodic Boundary Conditions

For this case, the pit metric Kt_{app} is estimated by considering the following upper bound:

$$Kt_{TOTAL} \leq \prod_{i=1}^n Kt_i = \prod_{i=1}^n (1 + 2\mu_i) \approx 1 + 2\sum_{i=1}^n \mu_i + h.o.t \Rightarrow Kt_{TOTAL} \approx 1 + 2\sum_{i=1}^n \mu_i$$

Where the Kt_i , are the stress concentration factors corresponding to each (cosine) component of the surface height. Note that this approximation is completely arbitrary and that the estimate is expected to be close to the actual value of Kt for $\mu \ll 1$. Moreover the expression $1 + 2\sum_{i=1}^n \mu_i$ can no longer be considered an upper bound for Kt_{app} . In Figure 39, the distribution of Kt for the model problem shows that the estimate of Kt_{app} is both overestimating and underestimating the actual value of Kt , over a period.

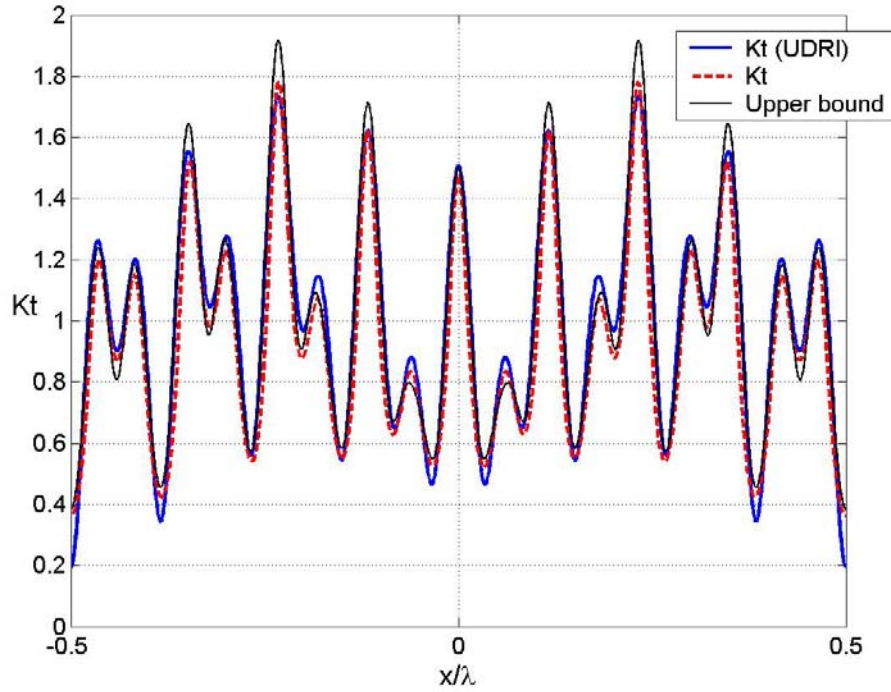


Figure 39. Case 2 Exact Kt vs. Pit Metric Kt_{app} (with Kt_{app} Upper Bound)

For this model problem the accuracy of the pit metric to estimate the actual value of Kt is within a reasonable error (2.63% for Kt_{max}).

The accuracy of the metric was investigated for the case in which λ is changed while keeping all other parameters constant. It is found, as shown in Figure 40, that for this case the metric provides a fairly good estimate of the maximum Kt within its range of applicability⁷.

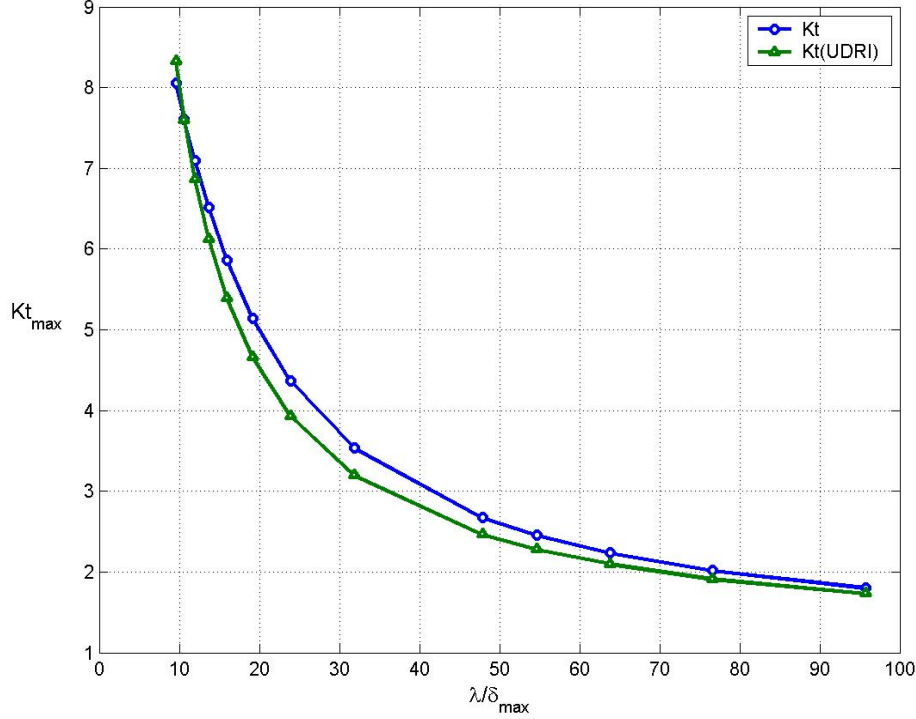


Figure 40. Case 2 Exact Kt vs. Pit Metric Kt_{app} for Variable Wavelength

In addition, an investigation was organized in which the three amplitude coefficients of Case 2 (A_1 , A_2 , and A_3) were randomly varied subject to the constraint that their sum is $\delta_{\max} = 0.005$.

$$A_1 + A_2 + A_3 = \delta_{\max} = 0.005 \quad \begin{cases} 0 \leq A_1 \leq 0.005 \\ 0 \leq A_2 \leq 0.005 \\ 0 \leq A_3 \leq 0.005 \end{cases}$$

The extreme cases ($A_1=0.005$, $A_2=A_3=0$) and its variations (i.e. $A_1=0$, $A_2=0$, $A_3=0.005$) were also included.

⁷ The range of applicability is considered as the range in which Kt is less than or equal to 4, which is considered the range of the majority of practical applications.

This random variation of amplitudes, in which the sum of amplitudes is constant, produced a better understanding of the contribution of each amplitude. As is shown in Table 2, the error contributions vary in sign. See Table 2, which contains the variable amplitudes as well as the corresponding pit metric and actual Kt's. Note that $\lambda = 8\pi/15$.

Table 2. Results of Kt_{app} Term Contributions for $\lambda/\delta_{\max} = 335.1$

Run	A1 (C=2)	A2 (C=9)	A3 (C=17)	Sum	KtmaxSC	KtmaxUDRI	%Error
1	0.0050	0.0000	0.0000	0.0050	1.0749	1.0750	0.0093
2	0.0043	0.0004	0.0003	0.0050	1.1217	1.1187	-0.2675
3	0.0042	0.0006	0.0002	0.0050	1.1235	1.1205	-0.2670
4	0.0025	0.0025	0.0001	0.0050	1.2070	1.2033	-0.3065
5	0.0024	0.0023	0.0003	0.0050	1.2129	1.2083	-0.3793
6	0.0014	0.0026	0.0009	0.0050	1.2909	1.2853	-0.4338
7	0.0018	0.0018	0.0014	0.0050	1.3090	1.2994	-0.7334
8	0.0021	0.0014	0.0016	0.0050	1.3115	1.3014	-0.7701
9	0.0000	0.0050	0.0000	0.0050	1.3310	1.3375	0.4884
10	0.0020	0.0012	0.0018	0.0050	1.3323	1.3223	-0.7506
11	0.0011	0.0023	0.0017	0.0050	1.3627	1.3545	-0.6017
12	0.0022	0.0001	0.0027	0.0050	1.3854	1.3819	-0.2526
13	0.0006	0.0025	0.0019	0.0050	1.4062	1.3976	-0.6116
14	0.0005	0.0022	0.0023	0.0050	1.4415	1.4333	-0.5689
15	0.0007	0.0011	0.0032	0.0050	1.4748	1.4759	0.0746
16	0.0003	0.0017	0.0030	0.0050	1.4995	1.4943	-0.3468
17	0.0005	0.0010	0.0035	0.0050	1.5042	1.5082	0.2659
18	0.0005	0.0005	0.0040	0.0050	1.5295	1.5424	0.8434
19	0.0001	0.0012	0.0037	0.0050	1.5478	1.5509	0.2003
20	0.0000	0.0005	0.0045	0.0050	1.5870	1.6075	1.2917
21	0.0000	0.0000	0.0050	0.0050	1.6010	1.6375	2.2798

As can be seen in Table 2, the dominant amplitude is A3, due to the shorter wavelength of its multiplying cosine term. At the extreme case in which A3 is equal to the maximum, 0.005, the relative error is 2.28%. It is thus assumed that shorter wavelength components, when assessed from Table 2 using the A3 column, will be positively additive in terms of cumulative relative error; the pit metric will overestimate the Kt in this case. For most other amplitude variations studied, it can be seen that the relative error is less than 1%.

6.3.2c) Case 3: 3-D Sinusoidal Surface Function: Multiplicative, Multi-Variable Terms

This case is the three dimensional extension of Case 1. The surface height is defined by the following parametric function:

$$H(x, y) = A_i \cos\left(\frac{2\pi x}{\lambda_x}\right) \cos\left(\frac{2\pi y}{\lambda_y}\right)$$

For this case the pit metric, is given by:

$$\mu(x, y) = -\left|\frac{\delta l}{w(l + \delta)}\right| \cos\left(\frac{2\pi x}{\lambda_x}\right) \cos\left(\frac{2\pi y}{\lambda_y}\right)$$

where: $l = \frac{\lambda_y}{4}$, $w = \frac{2}{\pi} \times \frac{\lambda_x}{4}$, $A = \delta$, $\tilde{x} = \left(\frac{2\pi x}{\lambda_x}\right)$, $\tilde{y} = \left(\frac{2\pi y}{\lambda_y}\right)$, and the pit metric stress

concentration factor Kt_{app} is defined as:

$$Kt(x, y) := 1 + 2\mu(x, y) .$$

For this case, we study the validity of the proposed pit metric in its three dimensional formulation, together with sensitivity studies of Kt_{max} for a range wavelengths in the x and y directions.

The model problem selected for a first study is shown in Figure 41. Figure 42 shows the finite element mesh used for computing the actual Kt , together with the characteristic dimensions of the pit metric. The corresponding boundary conditions are shown in Figure 43⁸.

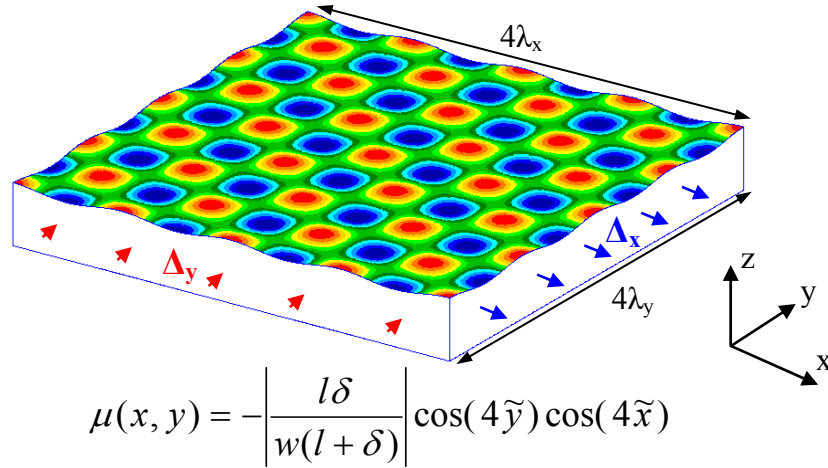


Figure 41. Case 3 Model Problem

⁸ Due to symmetry of the domain, only half a wavelength ($\lambda/2$) in the x and y-direction needs to be modeled.

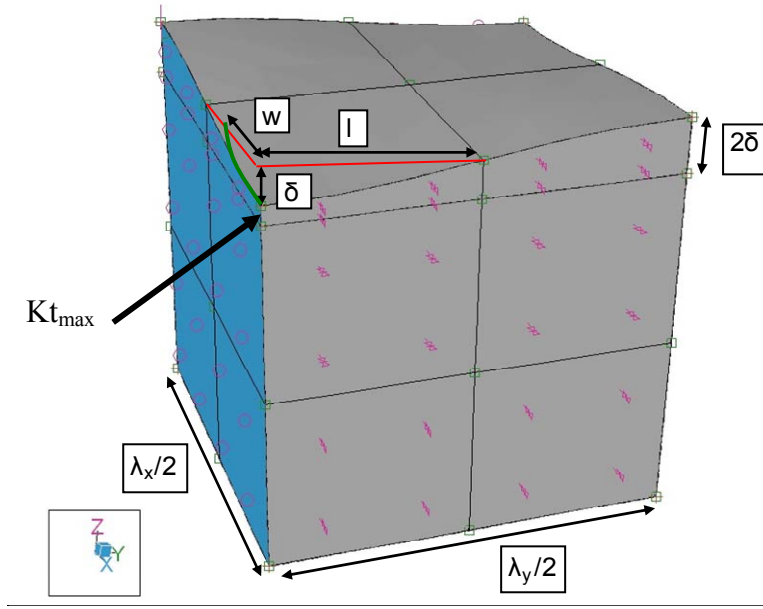


Figure 42. Case 3 Finite Element Discretization and Boundary Conditions

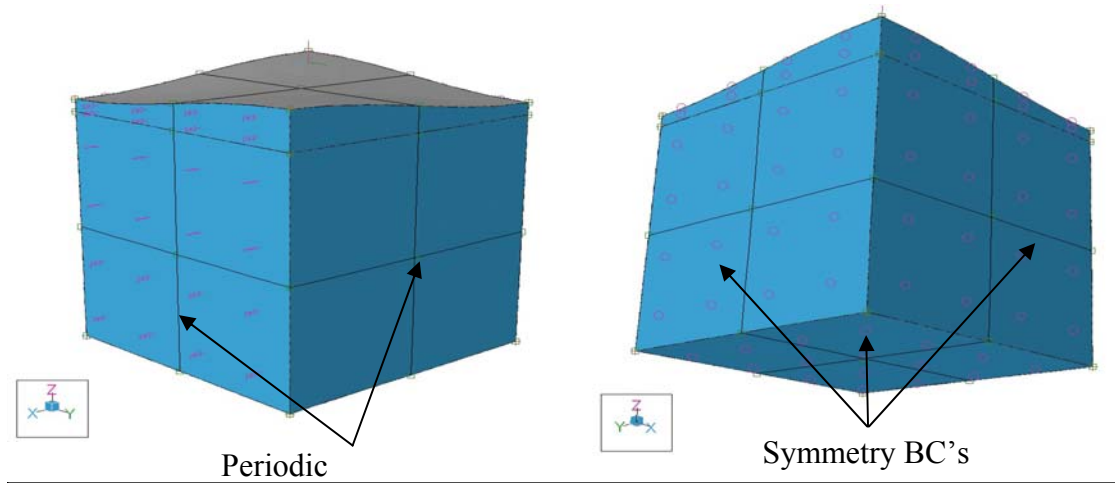


Figure 43. Case 3 Boundary Conditions for Each Model Face

The periodic boundary conditions are given by the imposed displacements Δ_x and Δ_y :

$$\Delta_x = \frac{\lambda_x}{2E}, \Delta_y = -\eta \frac{\lambda_y}{2E}.$$

6.3.2d) Case 3: Validation Study⁹

Two cases were investigated. The first corresponds to a sensitivity study by varying the x-direction and while keeping y-direction constant (Case a)), and the second corresponds to the opposite case (Case b)).

$$\text{Case3a} : H(x, y) = 0.01 \cos(4\tilde{x}) \cos(4\tilde{y}) , x = \text{constant}, y = \text{variable}, \mu = 0.15$$

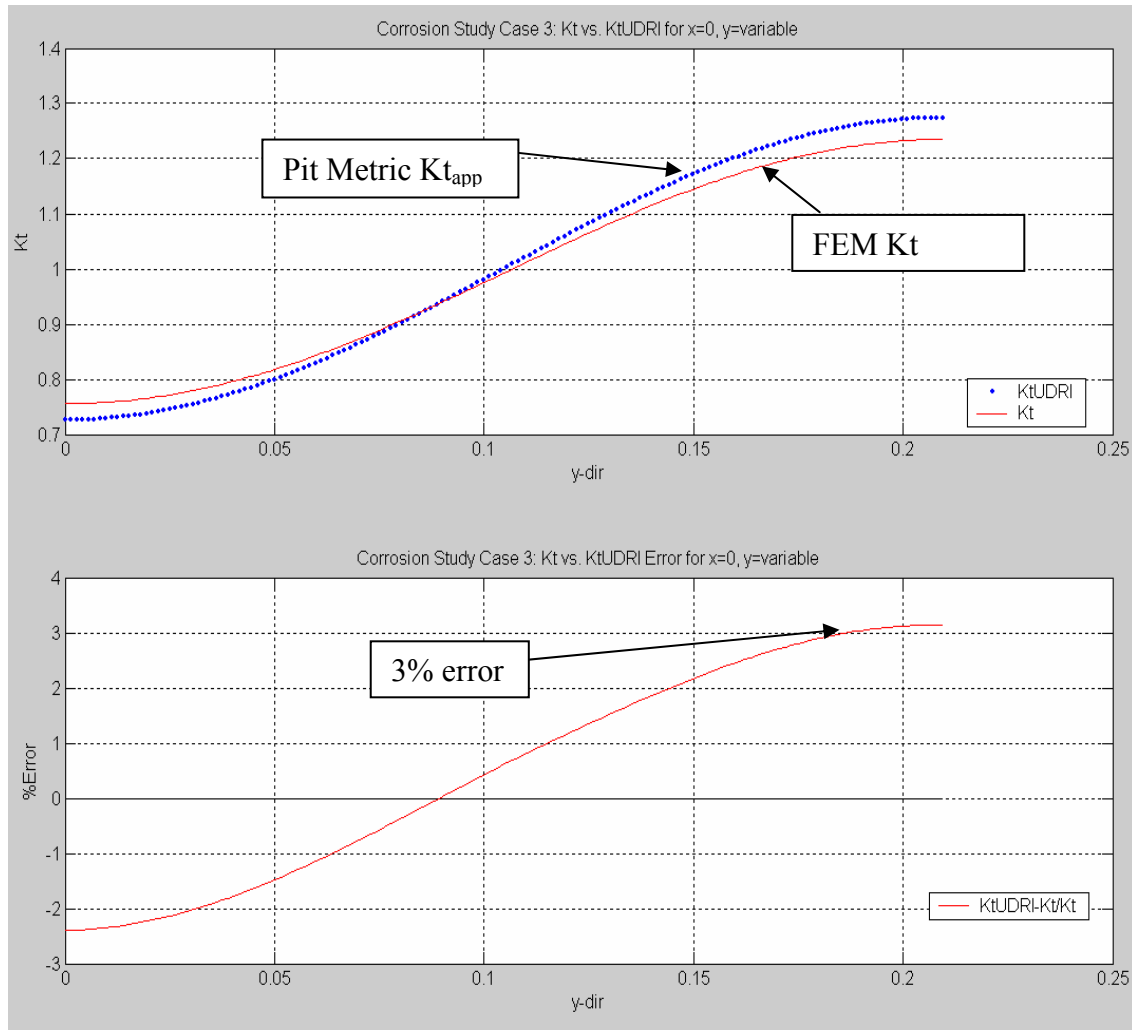


Figure 44. Case3a: Exact K_t vs. Pit Metric $K_{t_{app}}$ for Variation in Y-direction

⁹ In this case, validation was performed with respect to the exact solution of the equations of elasticity

Case3b : $H(x, y) = 0.01 \cos(4\tilde{x}) \cos(4\tilde{y})$, $x = \text{variable}$, $y = \text{constant}$, $\mu = 0.15$

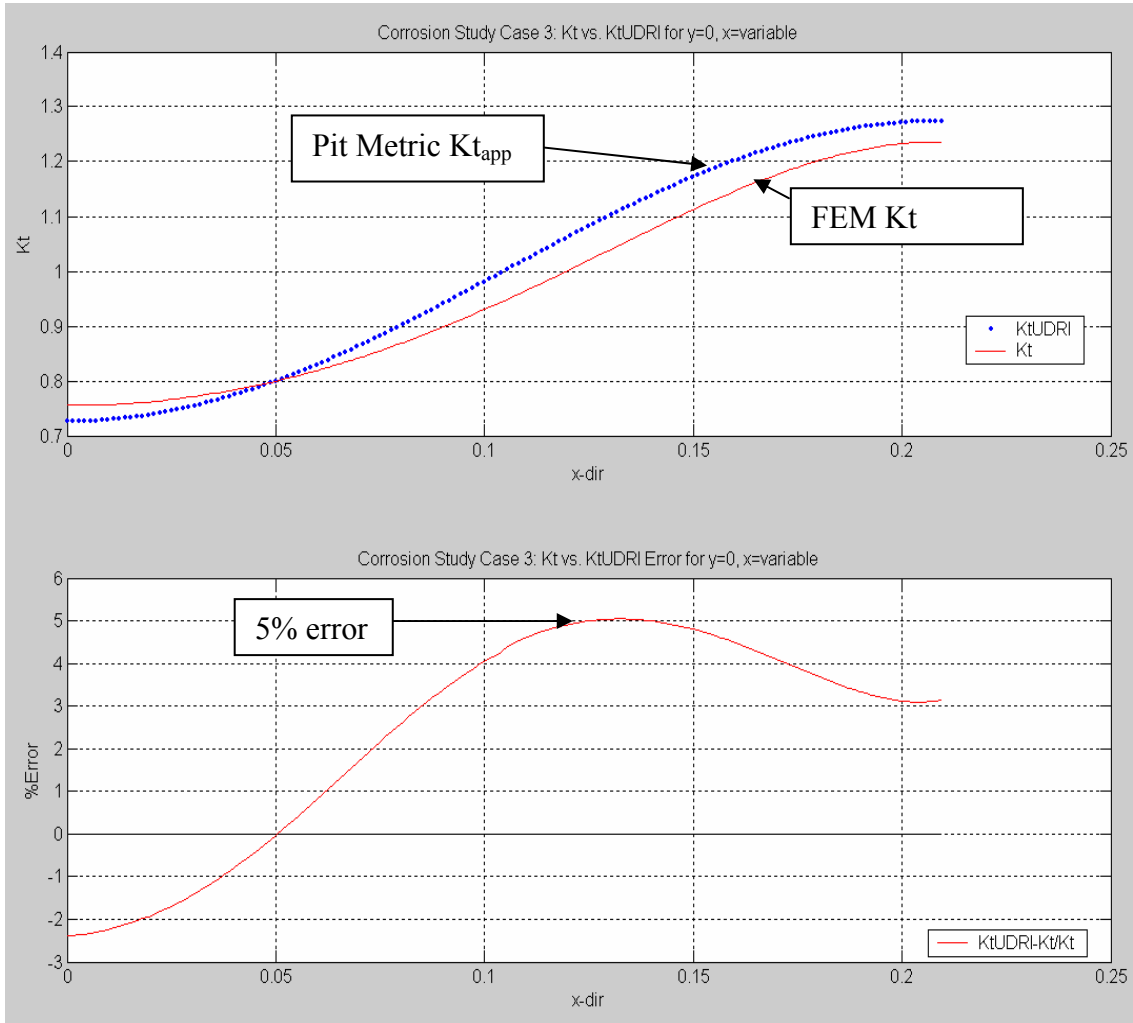


Figure 45. Case3b: Exact Kt vs. Pit Metric Kt_{app} for Variation in X-direction

It can be seen from Figures 44 and 45 that the maximum relative error between the estimated and actual Kt is 3% and 5% for cases a) and b) respectively. This indicates a fairly close correlation of Kt between the pit metric approximation and StressCheck[®] for low amplitude, long wavelength cases. More extreme cases will be estimated for sensitivity.

6.3.2e) Case 3: Sensitivity Study

A sensitivity study was performed in which both λ_x (w parameter) and λ_y (l parameter) were varied through a range of values to test the validity of the proposed UDRI method in computing an estimate of Kt_{\max} . The sensitivity parameters used in the study were: amplitude A , λ_x and λ_y ; the amplitude A was in fact held constant for these studies, as it was shown that it has the same effect as varying the wavelength λ_y . The pit metric function used in this sensitivity study is the equation shown below, and the parameters used in the sensitivity study are shown in Table 3:

$$\mu(x, y) = -\left| \frac{lA}{w(l+A)} \right| \cos\left(\frac{2\pi x}{\lambda_x}\right) \cos\left(\frac{2\pi y}{\lambda_y}\right)$$

Sensitivity Parameters			
Variable	Min	Max	Runs
A	0.0050	0.2000	10
λ_x	0.0419	0.4190	10
λ_y	0.0419	0.4190	10

Table 3. Case 3 Sensitivity Parameters

In Figure 46, both λ_x (i.e., $2\pi w$) and λ_y (i.e., $4l$) increased simultaneously and equally from 0.0419 to 0.419, with $A = \delta = 0.01$. Low wavelength terms cause divergence, as predicted.

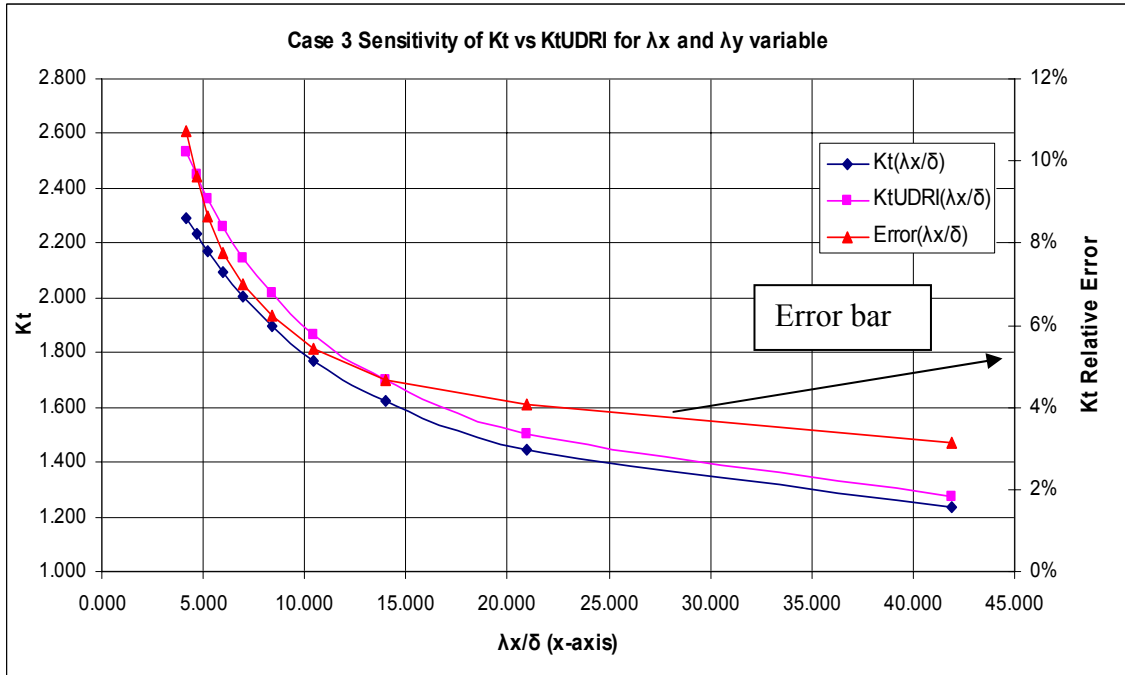


Figure 46. Case 3: Exact Kt vs. Pit Metric Kt_{app} for Variable λ_x

As can be seen in Figure 46, a relative error of ~5% is not reached until λ_x/δ is ~13.82.

This case indicates a fairly good range for wavelength λ_x .

In Figure 47, λ_x (i.e., $2\pi w$) is held constant at 0.0419 and λ_y (i.e., $4l$) is increased from 0.0419 to 0.419, with $A=\delta=0.01$. The error is fairly high for even longer wavelength ratios.

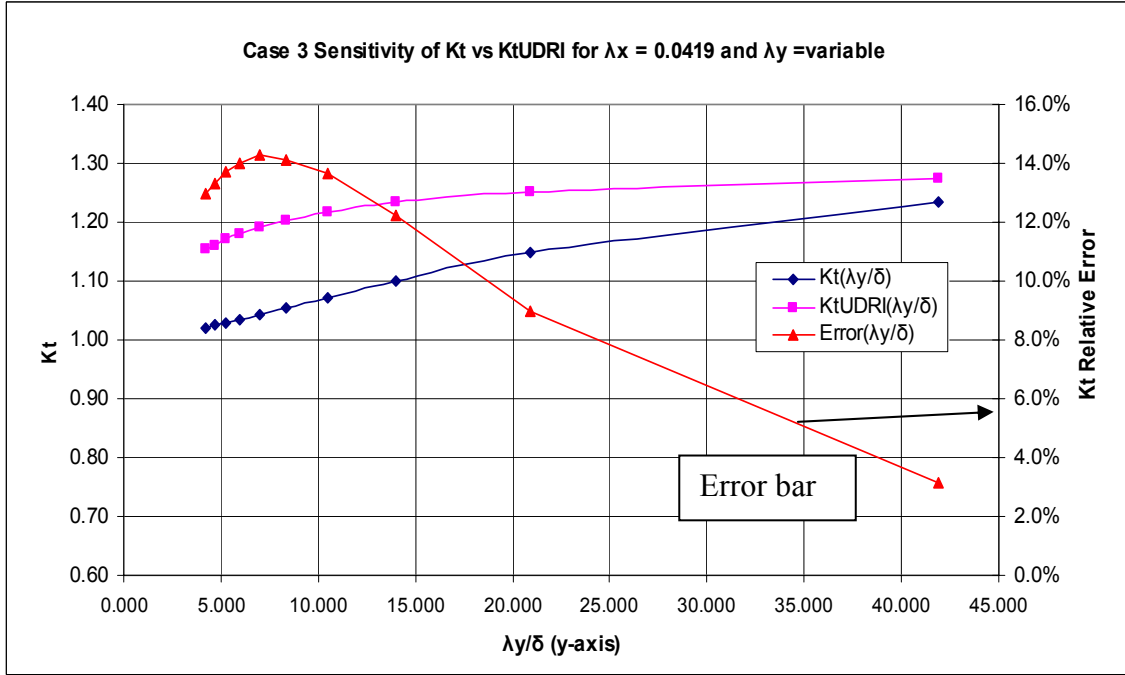


Figure 47. Case 3: Exact Kt vs. Pit Metric Kt_{app} for Variable λ_y

As can be seen in Figure 47, a relative error of ~5% is reached between $\lambda_y/\delta = 36$ and 40. This case indicates that shorter λ_y with respect to Ktmax results in high sensitivity.

In Figure 48, λ_x (i.e., $2\pi w$) is increased from 0.0419 to 0.419 and λ_y (i.e., $4l$) is held constant at 0.0419, with $A=\delta=0.01$. Very low error is observed until $K_t \approx 2.0$.

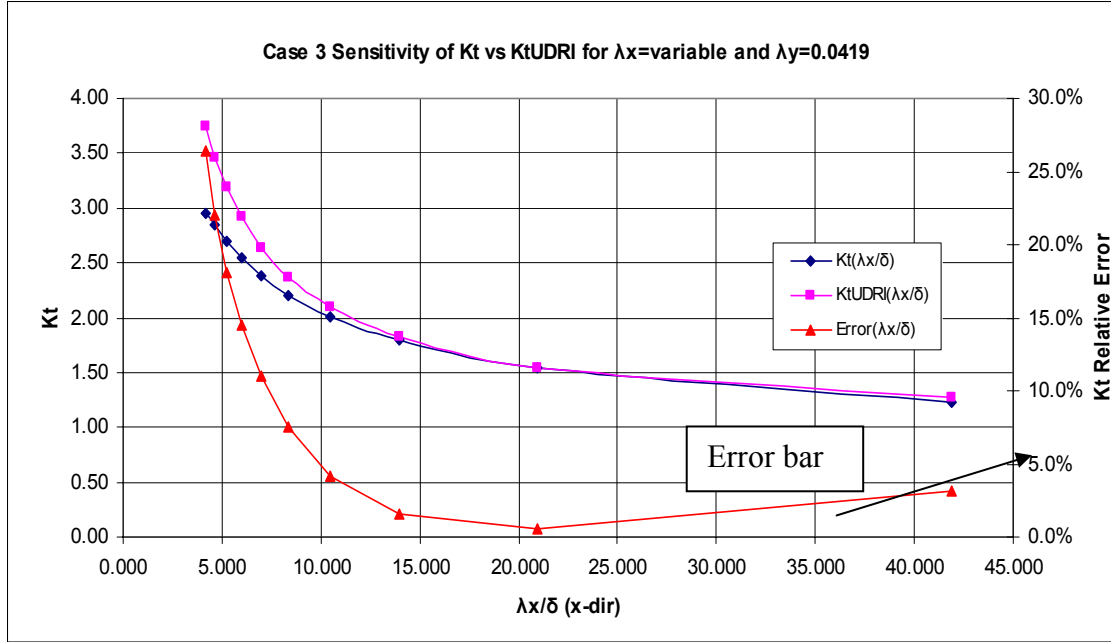


Figure 48. Case 3: Exact K_t vs. Pit Metric K_{tapp} for Variables λ_x and λ_y

As can be seen in Figure 48, a relative error of $\sim 5\%$ is reached between $\lambda_x / \delta = 8.2$ and 10.0. After $K_t \approx 2.0$, there is a strong divergence, the relative error being 25% when the actual $K_t \approx 3.0$.

6.3.3 Summary

The pit metric for estimating the stress concentration factor K_t , as proposed by UDRI, provides a good approximation, when the ratio w/δ is greater than approximately 2.7 (or, equivalently, the wavelength λ is greater than 16 times the amplitude) under uniaxial stress conditions. The quality of the approximation rapidly deteriorates with decreasing w/δ ratios. Therefore the success of using the pit metric in a manner proposed by UDRI depends on whether the measured corroded surface can be accurately represented without including an excessive number of terms, including short wavelength components. It was observed in previous studies (see Section 6.2) that neglecting the smaller wavelength components may result in improper idealization and misleading results. Therefore, special attention has to be given to this issue. Additionally, it has yet to be determined whether the pit metric is valid for multiaxial stress states and curved surfaces. This investigation is a subject of recommended future study, and is described in 6.3.4.

6.3.4 Recommended Future Studies

In order to determine whether the procedure developed by UDRI is a reliable indicator of fatigue life, it will be necessary to perform a series of laboratory and computational experiments. The laboratory experiments would involve testing of corroded specimens on one hand, and specimens micro-machined to represent the idealized surfaces on the other. It will be necessary to collect baseline data to determine the statistical variation of fatigue life of identical specimens. In order to provide for repeatability, the specimens are required to have identical features (representing a corroded part). For this reason, it is proposed that the features be micro-machined. The stochastic/FEM experiments would employ the data from these experiments, implementing necessary filtering and treatment processes before comparing the pit metric maximum $K_{t_{app}}$ to the FEM maximum K_t for more general cases.

All sources of error attributed to both measurement error and error of data manipulation, such as point rotation-translation with regard to specimen location, as well as the location of the reference surface, must be identified and incorporated accordingly into the current working model. These are crucial components for determining the inherent error bounds and contributions to the maximum K_t .

The initial filtering process will involve finding the minimum grid size for input into a mathematical analysis software tool; this is simply due to the large size of the ASCII file containing a sufficient resolution of experimental data points. Knowing this minimum grid size, the “worst case” or more explicitly the most extreme (i.e. depth, angle of feature, apparent roughness) region of corrosion must then be identified and partitioned for mapping. An example of the partitioning of a critical region is shown in Figure 49.

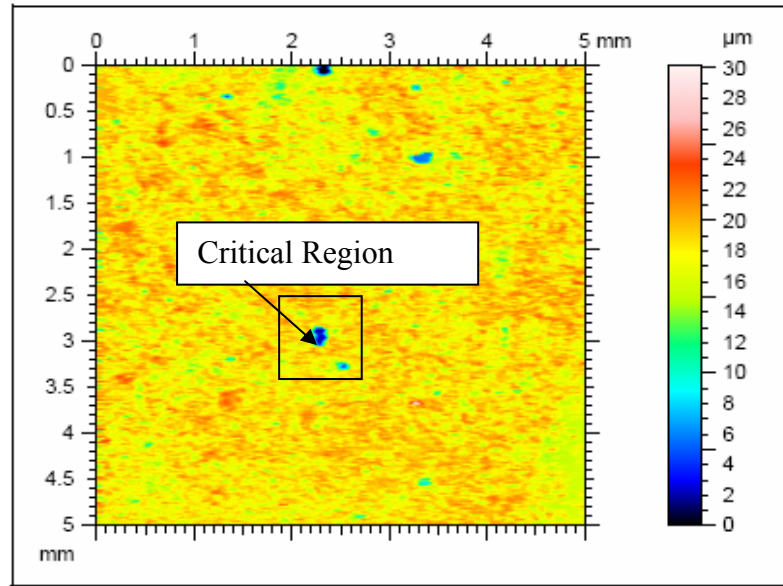


Figure 49. Partitioning of a Critical Region for FFT Mapping

This “worst case” partition must be properly mapped from the physical domain (surface feature heights and angles, surface roughness profile) into the frequency domain (amplitudes and wavelengths, surface representation) using, for example, the MATLAB FFT function. Once the significant amplitudes and frequency components, or those most likely to contribute to the K_t , have been identified from the data, the frequency domain pit metric μ can be approximated for each frequency component and the approximate maximum effective $K_{t_{app}}$ for the partitioned region can be determined. After this step, the $K_{t_{app}}$ values computed from the FFT and pit metric treatments can be compared to the FEM results using StressCheck[®], but will remain devoid of noise effects (incorporation of random noise into experimental data will be discussed separately). See Figure 50 for a review of the pit metric $K_{t_{app}}$ algorithm for a set of given surface heights.

As shown, three main steps are required to produce a $K_{t_{app}}$ using the pit metric: 1) Perform Spatial FFT on surface height data (White Light, Laser Profilometer), 2) compute a pit metric, μ , for each frequency component resulting from FFT, and 3) compute the local $K_{t_{app}}$ by summing the results for each pit metric frequency component, μ .

Given Surface Height Data, $H(x,y)$, Perform Spatial FFT:

$$H(x, y) = \sum h_{ij} \cos(2\pi x / \lambda_i^x) \cos(2\pi y / \lambda_j^y)$$

For Each Frequency Component, Compute Corresponding Pit Metric Frequency Component:

$$\delta_{ij} = h_{ij} \quad l_{ij} = \lambda_i^x / 4 \quad w_{ij} = (2 / \pi)(\lambda_j^y / 4)$$

$$|\mu_{ij}| = l_{ij} \delta_{ij} / w_{ij} (l_{ij} + \delta_{ij})$$

$$\mu_{ij}(x, y) = -|\mu_{ij}| \cos(2\pi x / \lambda_i^x) \cos(2\pi y / \lambda_j^y)$$

Inverse FFT Pit Metric Frequency Components to Obtain:

$$K_t^{Total}(x, y) \approx 1 + 2 \sum \mu_{ij}(x, y) = 1 + 2 * \mu^{Total}(x, y)$$

Figure 50. Algorithm for the Determination of Pit Metric $K_{t_{app}}$ from an Arbitrary Domain

Random noise fluctuations may now be introduced into the selected partition data, allowing for the development of the “experimental error” bound, within which the computed $K_{t_{app}}$ should lie. These noise effects must be bounded by both the measurement error as well as the data manipulation error. The goal of this investigation is to determine what effect these random noise fluctuations have on the computed pit metric $K_{t_{app}}$ (i.e. how robust is the pit metric in the presence of random noise).

Additionally, the pit metric must be validated for the cases of multiaxial stress states and curved surfaces. Noting that the pit metric was developed for the cases of uniaxial stress in a planar surface, the direction of the stress being given by the selected spatial direction used in the FFT mapping, it is necessary to determine whether a change in the remote multiaxial stress field of a 3-D flat plate with a central oval pit results in a local disturbance of the directions of principal stresses around the pit. Since the pit metric $K_{t_{app}}$ is controlled by the directions of the FFT mapping, local disturbance of the directions of the principal stresses around the pit will produce invalid results. Furthermore, introducing curvature of surface into which pitting will occur must be studied also, as the pit metric has been investigated on flat surfaces.

The theoretical basis of small variations in the solution domain of problems of two-dimensional elasticity is discussed in a paper published in 1961¹⁰. The main point is that the K_t 's can be estimated with good accuracy using simple formulae, subject to the assumption that the surface is sufficiently smooth. This paper claims improvements on the results presented earlier by Neuber¹¹. The results presented herein are consistent with those results.

¹⁰ Ivo Babuska and Jaroslav Kautsky, "Ein Beitrag zur Theorie der Kerbspannungen", ZAMM **41** (1961) 11/12 420-427.

¹¹ Heinz Neuber, *Kerbspannungslehre*, (1937) Springer-Verlag, Berlin.

6.4 F-18 Arresting Shank (Part-74A480617): Submodeling with Consideration of $K_{t_{eff}}$

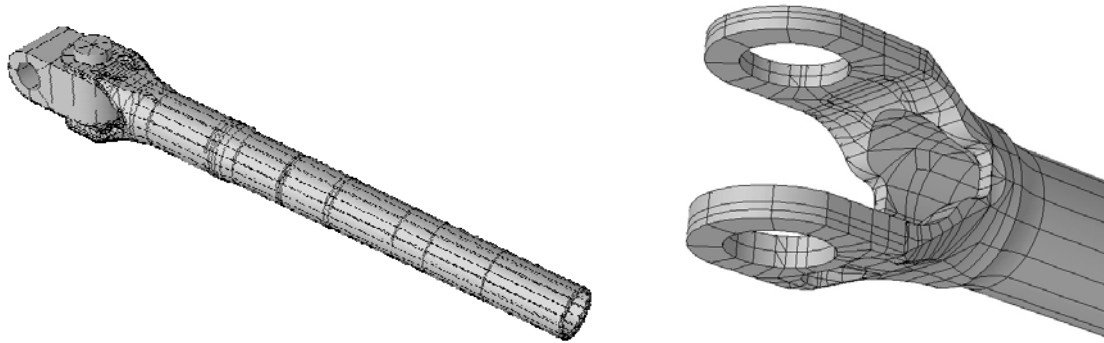


Figure 51. Hand-meshed F-18 arresting hook shank with detailed lug view

6.4.1 Introduction

The objective of this investigation was to develop a modeling approach that will allow for fast computation of the parameters of interest, in this case the $K_{t_{eff}}$, while maintaining the accuracy of the solution. The chosen part is the F-18 arresting hook shank of Figure 51. The reduction of the computational time is attained by a two-step process: the first is based on studying a subdomain of the arresting hook, therefore decreasing the number of elements and the number of degrees of freedom, and the second is based on a hierarchic modeling approach on which the proper model is determined for the cases of interest. The accuracy of the solution is achieved by proper enforcement of the boundary conditions. This investigation focuses on three load conditions, denoted as hook bounce, cable pickup, and aircraft arrestment load case (load cases 1 to 3 respectively). For each load case different geometric configurations depending on the angle θ (see Figure 52) were investigated. This modeling approach is discussed in some detail for the aircraft arrestment load case (load case 3) for $\theta = 0$ in the following.

6.4.2 Study Approach and Results

Within this study, there were four cases of primary interest: a) a linear study, b) a geometric nonlinear study, c) multi-body contact study using local subassembly, and d) detailed, local analysis using boundary conditions obtained from multi-body contact solution. Each case approach and result is described in detail in the following pages.

6.4.2a) Case a: Linear Study

Objective: The load case is statically indeterminate at the connection between the arm, the pivot and the pivot damper; therefore a contact solution is required in order to obtain the load transfer and the stresses. The objective of this study is to determine the stresses acting on the boundaries of the zone of interest in order to apply these to a reduced domain, therefore avoiding the necessity of modeling the contact between components. A linear beam model (see Figure 53) was used for estimation of the moment, shear, and axial loads acting at section A-A.

The resulting value of the maximum stress acting on section A-A (shown in Figure 53) is larger (≈ 334 ksi) than the ultimate value (245 ksi). This indicates that a linear model is overestimating the actual value of the stresses, and a geometric nonlinear model is required to properly account for bending-axial coupling.

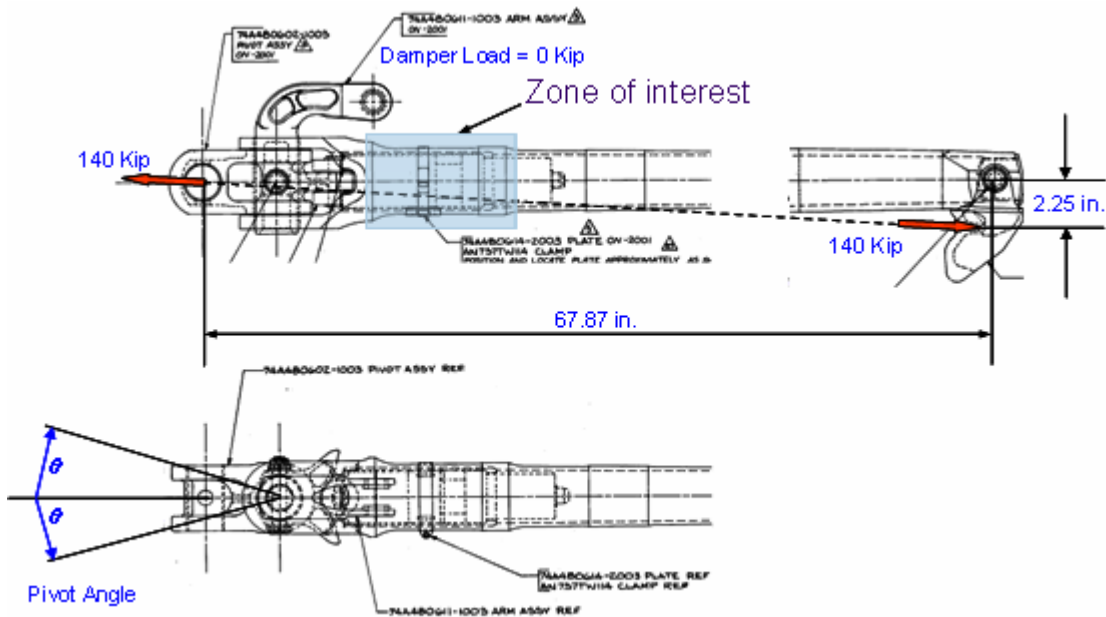


Figure 52. Load scheme

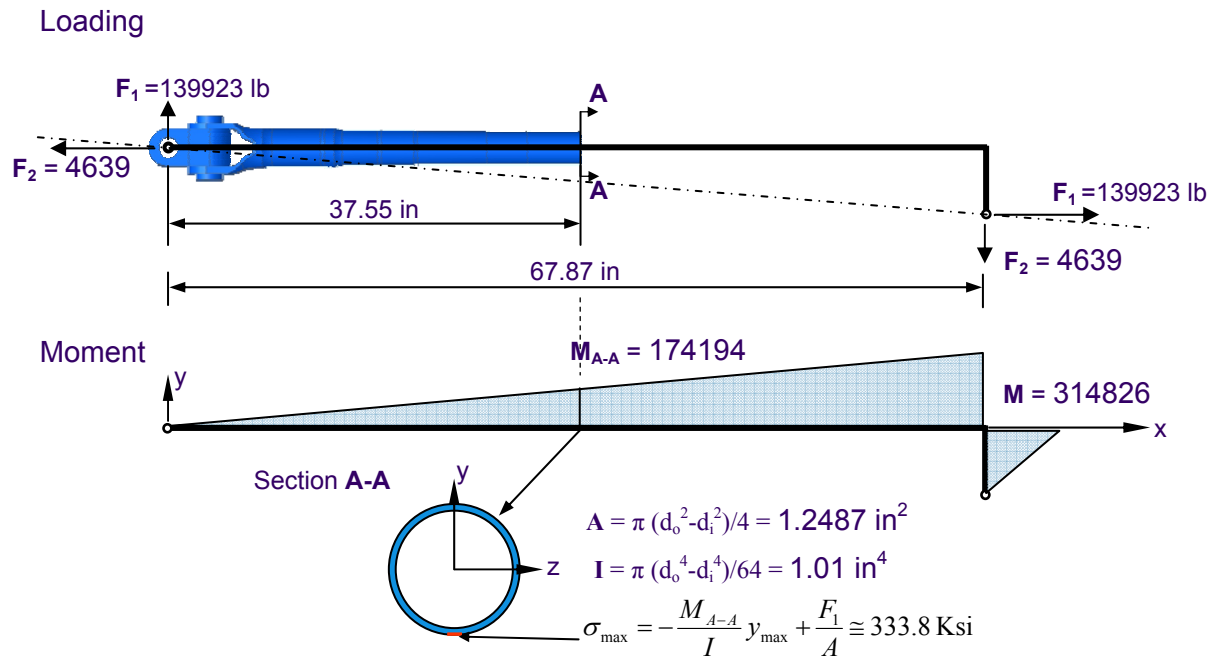


Figure 53. Loading diagram and moment diagram for the beam model

6.4.2b) Case b: Geometric Nonlinear Study

Objective: Geometric nonlinear analysis to determine the moment, shear, and axial loads distribution along the shaft. Select the local region for a 3D linear analysis based on the results of the geometric nonlinear analysis.

In this study a two-dimensional plane-stress model was used (see Figure 54) where the height and thickness of each section was adjusted to maintain the same area and moment of inertia of the original section. This is a structural model intended only for obtaining the deformed configuration, the moment, axial force and shear force.

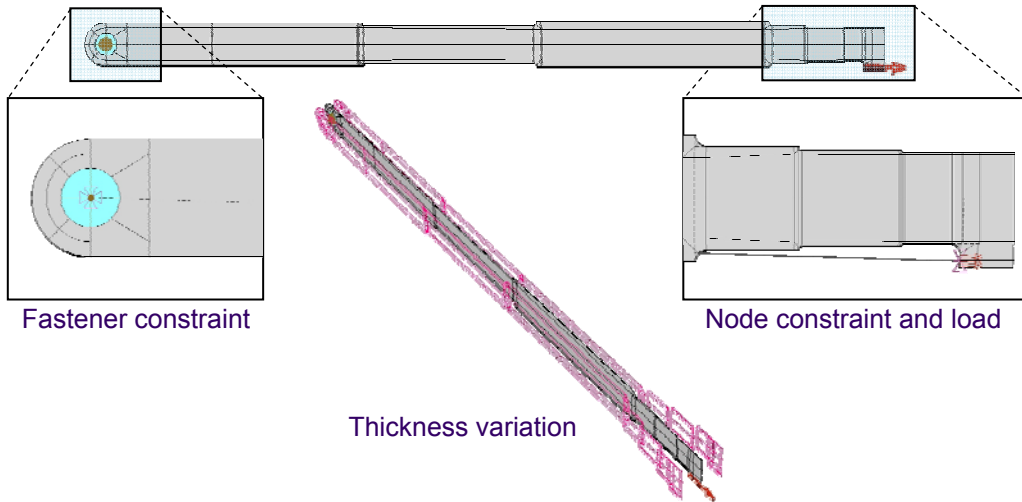


Figure 54. General nonlinear model

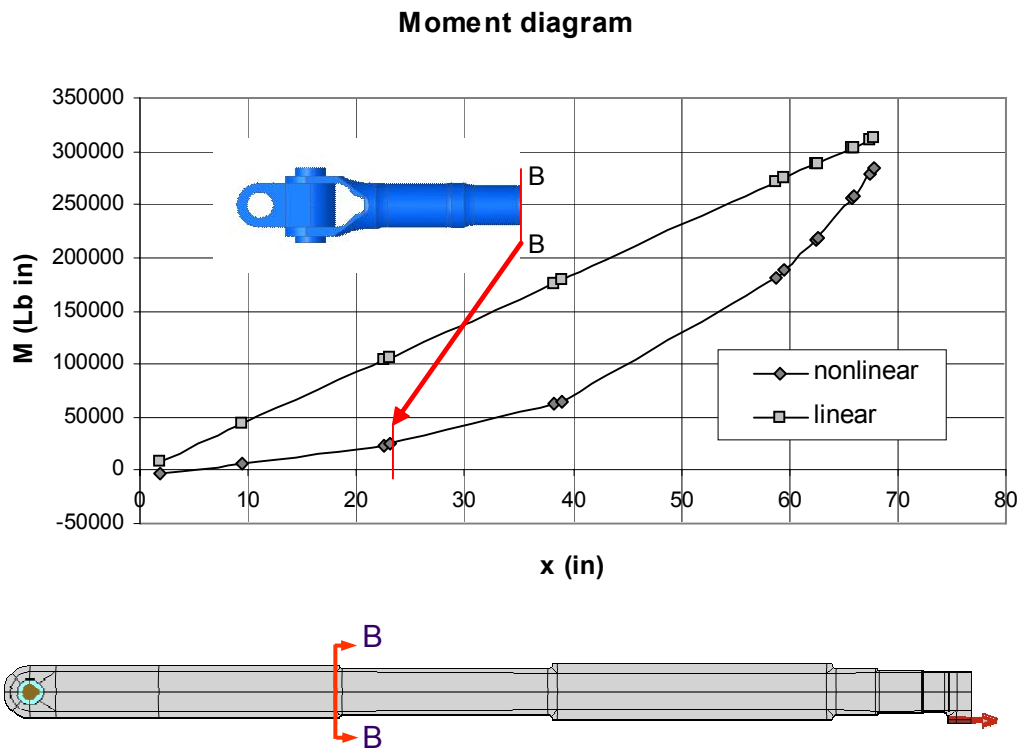


Figure 55. Moment diagram for the linear and nonlinear models.

Since the moment variation is nearly linear from the pin connection to section B-B and the deflection in that region is quite small (see Figure 55), the stress state of the arresting arm can be well approximated by a 3D linear solution.

6.4.2c) Case c: Contact Subassembly 3D: Local Analysis

Objective: obtain load transfer, and stresses for subsequent detailed 3D study.

With the moment and axial load computed from the 2D geometric nonlinear model, the three-dimensional contact solution was obtained to find the stress distribution in the region of primary interest (see Figure 56).

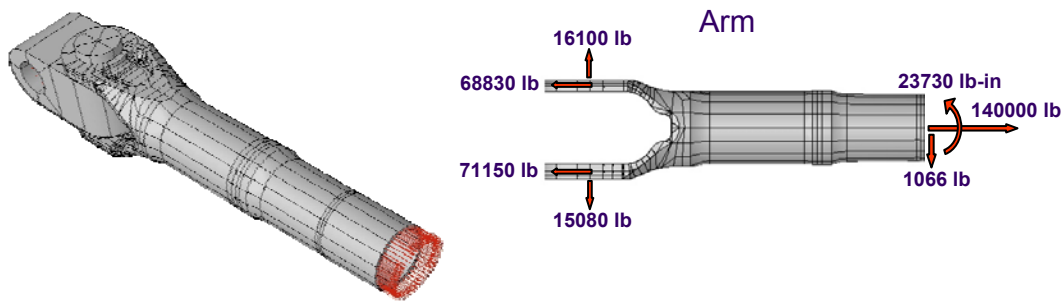


Figure 56. Force distribution computed from the contact model.

Once the load transfer in the contact region was determined (Figure 57), further simplification of the model was considered. The stresses computed in this study for the zone of interest are to be compared with the stresses obtained in the next study.

6.4.2d) Case d: Detailed 3D Subassembly: Local Analysis (no contact)

Objective: Reproduce the stress distribution obtained using contact.

The comparisons between the model cases can be seen on the following page. The interior and exterior stress distributions for the contact and non-contact solutions are shown in Figures 58-59.

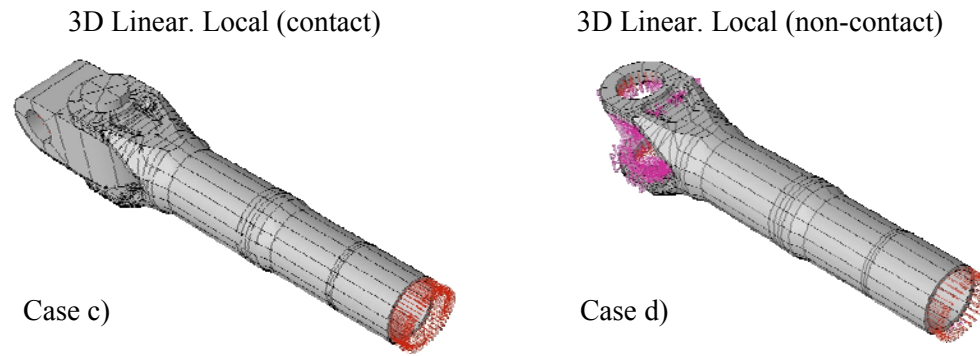


Figure 57. Three dimensional model for contact (Case c) and its simplified version (Case d)

Stress distribution (exterior)

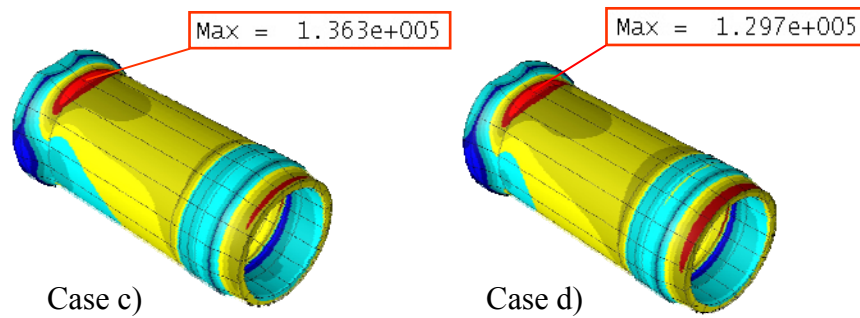


Figure 58. Stress distribution at the exterior of the zone of interest. Case c) Contact solution, Case d) non- contact solution

Stress distribution (interior)

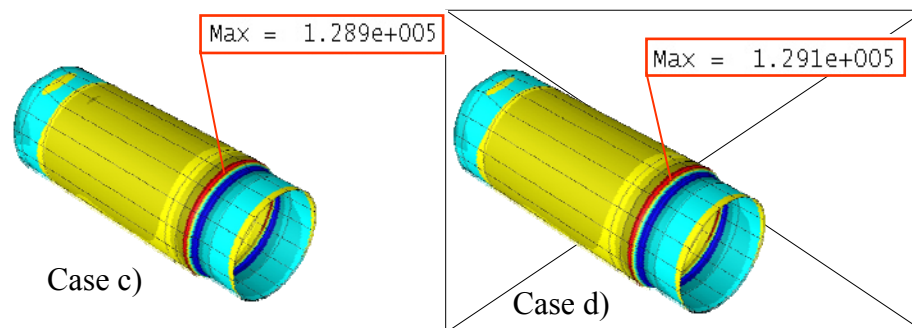


Figure 59. Stress distribution at the interior of the zone of interest. Case c) Contact solution, Case d) non- contact solution

Finally, Case (e) shows one additional model simplification, consisting of removing the clevis region of Case (d) and constraining the section using springs. Please see Figure 60 for this case.

In Figure 61, the interior stress distribution obtained from the contact case (Case c) is compared with the solution obtained for Case e.

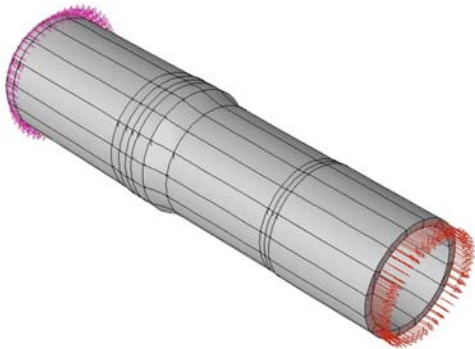


Figure 60. Case e: Simplified version of Case d

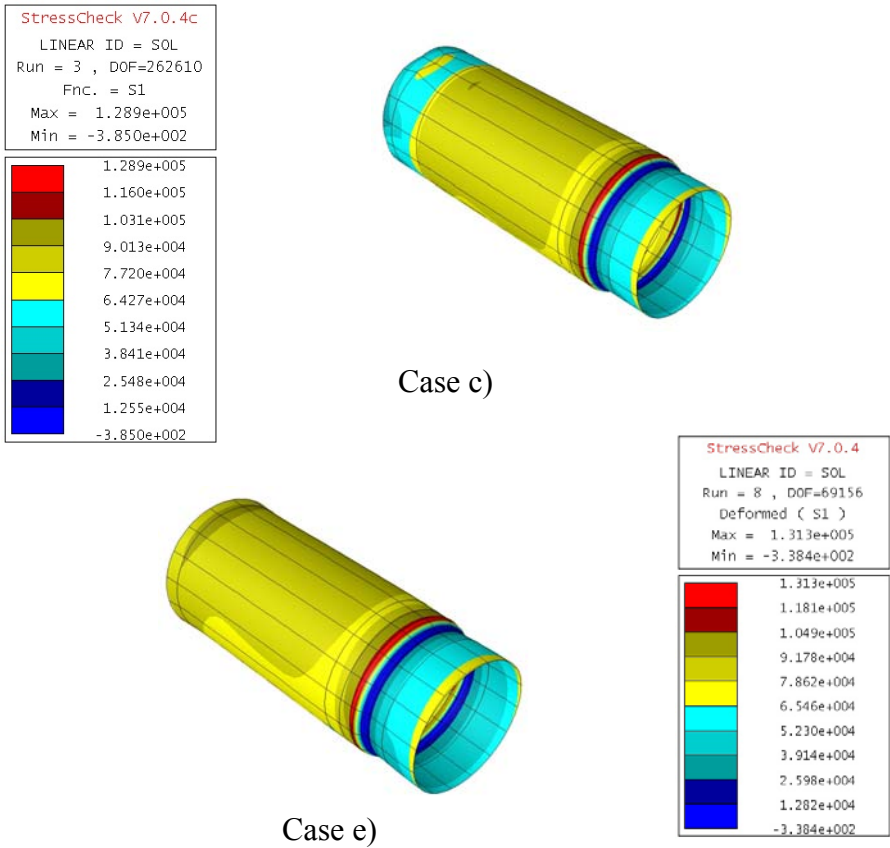


Figure 61. Stress distribution at the interior of the zone of interest. Case c) Contact solution, Case e) non contact solution with further simplified domain.

6.4.3 Summary

It can be seen from Figures 58, 59, and 61 that the proposed approach provides practically the same stress distribution in the region of primary interest for all cases. The advantage of this approach is that the problem can be solved in a fraction of the time that would be required if the entire system was to be modeled.

7. Implementation of Statistically Variable Non-Linear Material Properties

ESRD implemented variable coefficients for material properties for linear and nonlinear isotropic materials into StressCheck. For linearly elastic materials the modulus of elasticity and Poisson's ratio can be defined by functions of the spatial variables specified either in local or global coordinate systems. For elastic-plastic materials additional coefficients can be formula-based: the yield strength, the Ramberg-Osgood parameters, etc. The formulae can be defined internally in StressCheck, or can be provided through external function calls. In the latter case StressCheck will pass the formula name and the global coordinates to the external function and receive the corresponding values of the coefficients. The external function call is implemented in Windows OCX so that the user may write a subroutine in Visual Basic and communicate with StressCheck without having to re-compile or re-link. This required modification of the element stiffness matrices, load vectors and extraction (i.e., post-processing) procedures. The functionality is ready for testing. ESRD is waiting for NAVAIR to provide a set of test cases. Therefore this work is not yet complete, so ESRD is not in a position to provide examples that demonstrate these enhanced capabilities of StressCheck. ESRD expects to complete this project during the current phase.

8. Plan for Deployment

ESRD is engaged in the development of a framework for the distribution the corrosion assessment technology developed under this project to the USN and its subcontractors, utilizing the COM and Java interfaces of StressCheck®. The development of simple-to-use Windows desktop and web-based (or cross-platform) applications is envisioned. The interfaces are to provide a convenient communication protocol that integrates the necessary functions of other applications (e.g. MATLAB probability and statistical functions). A brief description follows:

8.1 The StressCheck FEA Toolkit

The capability for integration of StressCheck's simulation functions, into a user-developed application, is referred to by ESRD as "Toolkit FEA". StressCheck provides a toolkit of functions for the construction, solution by the finite element method, and post-processing of mathematical models representing mechanical parts.

StressCheck V7 can be deployed as an engineering analysis application server capable of supporting a wide variety of requirements related to the automation of engineering analysis functions. The simulation functions provided can be incorporated directly into problem-specific software tools, or integrated with other similar application services to be deployed from within an engineering design and analysis environment. The ultimate goal of the StressCheck FEA Toolkit is to make advanced technology in computational mechanics readily accessible to practicing engineers in a form that minimizes the level of expertise required to benefit from the technology.

In order to achieve the goal of not having to regain expertise in FEA analysis methodology, it is necessary to add an intermediate layer of development between the technology provider, and the user of the technology. For purposes of this discussion, we will refer to these intermediate development activities as application integration. These activities encompass the integration of various tools into forms that address a particular design or analysis problem that will hide the complexities that would ordinarily be encountered by a user of conventional general-purpose analysis tools when trying to solve such problems. In order for these problem-specific tools to be used successfully, they must focus on the solution of specific engineering problems, and require little or no training in FEA.

Problem-specific applications access the functionality of the FEA Toolkit by utilizing an Application Programming Interface (API) that is exposed to the application integrator, based on a commonly accepted inter-process communication protocol, the Microsoft Component Object Model (COM). COM makes it possible to give a large population of tool developers access to advanced software technology that has been developed by experts in a variety of fields, making it possible to integrate these technologies into a single customized application, or into an integrated design and analysis environment.

Among the most generally applicable tools available today for the solution of problems in engineering analysis are the finite element method and the boundary element method. These technologies involve the use of a well-defined sequence of steps that may be applied to the solution of a wide variety of engineering problems. Although it is possible that other solution methods (such as closed form techniques) can be used to solve individual problems, or classes of

problems, there are many reasons why the finite element method is preferred. One particularly important factor that favors finite element analysis is the ability of the technology to deliver accurate results for a wide range of problems, with automatic evaluation of the quality of the computed results. In a typical scenario, where an analyst is intimately involved in the solution of a particular engineering problem, we rely on that analyst's expertise and familiarity with the tools to give us confidence in a solution produced by a particular tool. However, when analysis functions are automated, and the analyst is effectively removed from the quality assessment loop, it is essential that the application server produce information about solution quality automatically.

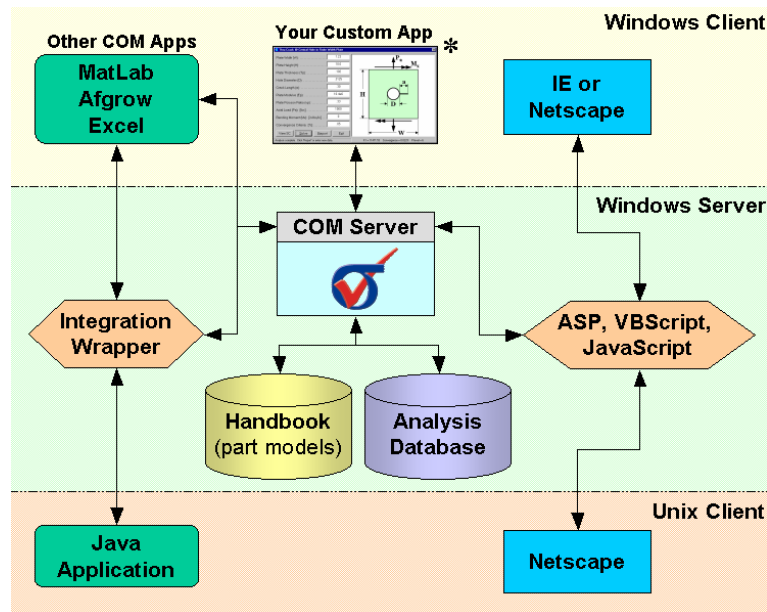


Figure 62. Integration using the StressCheck COM Server

8.1.1 Toolkit Functions

The functions that are exposed by the StressCheck FEA Toolkit are organized into the following four categories: problem description, solution procedures, extraction procedures, and data delivery.

Problem Description

Describing a problem to be solved by StressCheck involves three steps: construction of a geometric description of a physical domain in one, two, or three dimensions; discretization of the

domain into sub-domains for which a system of equations can be readily constructed for later solution, the description of material properties and boundary conditions.

Today, solid modeling is the most powerful technique for the description of a general geometric domain. StressCheck's analysis engine utilizes Parasolid as its solid modeling kernel and exposes a complete set of API functions that permit the construction of a general family of geometric primitives including points, curves, surfaces, and solids, as well as a variety of methods for manipulating these primitives such as Boolean operations, edge blending, extruding, spinning, sweeping, etc. Not only is it possible to construct geometry, but also the geometric definitions are fully parametric and associative, so that updating one or more design variables easily modifies the location, dimension, and orientation of individual features within the domain.

Once the geometric domain of a problem was described in a parametric form, it is necessary to discretize the domain by means of manual meshing, mapped mesh construction, or fully automatic mesh generation. Depending on the type of analysis performed, and on the complexity of the domain, one or another method of discretization may be preferred. StressCheck's API supports each type of mesh construction for 1D, 2D, and 3D problem domains. It is also possible to choose whether to regenerate the discretization in response to changes in design variables, or to simply adjust the existing discretization to fit the new configuration of the domain. It is also possible to choose whether or not to re-mesh, depending on whether the adjusted mesh satisfies prescribed criteria related to element quality such as distortion and aspect ratio.

Material properties and boundary conditions may be specified through the API for defining problems in heat transfer, elasticity, and thermal-elasticity for a wide variety of isotropic and orthotropic materials as well as laminated composites. Elasticity loading conditions include tractions, body forces and spring boundaries, in global or local coordinate systems, specified by constant, parameter, or design variable based expressions. Elasticity constraint conditions include built-in, symmetry, anti-symmetry, soft-simple support conditions, and imposed displacements specified by constant, parameter or design variable based expressions.

It is the responsibility of the application integrator to apply modeling assumptions that are appropriate for the problem in question, and to define the problem accordingly using the API functions provided by toolkit.

Solution Procedures

The toolkit provides a variety of procedures for solving the set of simultaneous equations that represent the engineering problem. It is possible to define a set of instructions (via the API) that

will direct the solution procedure by defining the type of solution to be performed (linear elastic, heat transfer, modal/buckling analysis), and the convergence criteria to be used in evaluating the quality of the solution. Certain classes of problems may also require advanced solution procedures involving material and/or geometric nonlinear analysis. Once again, it is the responsibility of the application integrator to decide which solution procedure is appropriate for the problem at hand, and to exercise his or her choices via the API.

Extraction Procedures

One of the most important classes of API functions made available to the application integrator is that associated with the extraction of engineering data from a numerical solution. The StressCheck FEA Toolkit provides access to raw engineering data for displacements, stresses, strains, etc. at any desired location in the domain. It also provides convergence information that verifies the accuracy of any computed information.

Specifically, the API provides extraction functions for the computation of engineering quantities at user-defined points, along curves, and across surfaces. API functions provide for the evaluation of minimum and maximum quantities over the complete domain or for meaningful sub-regions of the domain. It is possible to obtain resultant forces and to evaluate overall model equilibrium, and to compute such quantities as the area, undeformed volume and deformed volume of the solution domain or meaningful sub-regions. Fracture mechanics quantities are available for both 2D crack tips, and along 3D crack fronts. All extracted data are available in the context of a parametric design study such that computed quantities are provided as a function of the variation in a selected design variable.

Data Delivery

StressCheck makes all computed data accessible in a form suitable for direct viewing, for insertion into reports and database records, or for transmitting to other integrated applications. API functions are provided that retrieve requested raw data in tabular form. Qualitative solution information such as deformed shapes and contour fringe images can be obtained in static graphic formats such as Windows bitmap, jpeg, etc., or in a form which is conducive for dynamic three dimensional graphical viewing via a HOOPS Stream File.

9. Summary

At the close of the second year of the USN High-Strength Corrosion Fatigue Modeling Program progress can be reported in the following areas: (a) Completion of preliminary numerical experiments concerned with the utility of simplified techniques for the estimation of K_t values, (b) completion of structural and strength analysis of a prototype tailhook assembly, including consideration of geometric nonlinear effects and mechanical contact, (c) progress in the development of a deployment strategy of simplified models through ESRD's Web Book product and (d) enhancements of StressCheck, incorporated in V7.0.5, that include mechanical contact and improved methods of surface representation.

10. Recommendations for Future Work

The original goal of this project was to develop corrosion metrics, compute K_{teff} values for specific corrosion-damaged surfaces and, using those values, estimate FLE of HSS structural components with a reasonable degree of reliability. At this point it appears doubtful that this approach will lead to the desired results within the time and resources available to this project. The main difficulty is that extensive validation experiments will have to be performed that require a substantial amount of time and may result in the rejection of some or all of the proposed metrics.

The goal of validation is to determine whether it is possible to justify replacement of corroded surfaces with idealized surfaces for the purpose of determination of K_{teff} values needed for estimation of the fatigue life expended (FLE). Assuming that the results of validation experiments will justify simplification, the next important goal will be to develop a classification system for corrosion defects that will allow correlation of field observations with the definition of equivalent defects.

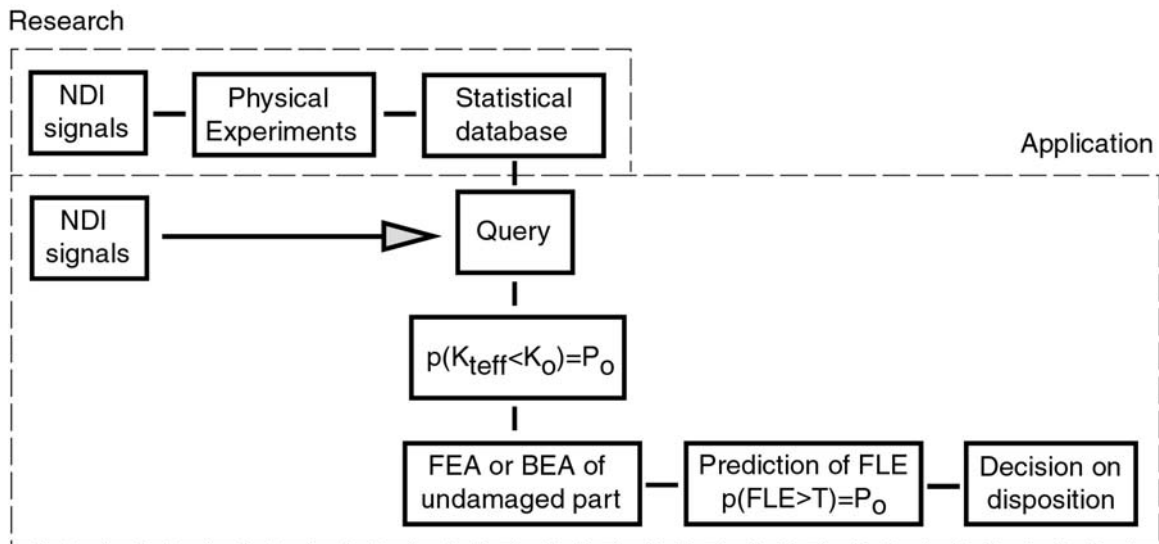


Figure 63. Schematic representation of the recommended approach

While this remains a worthwhile long-term goal, consideration of an alternative, phenomenological approach is recommended. An outline is shown schematically in Fig. 63. The goal is to correlate NDI signals of coupons damaged by various degrees of corrosion, representative of field conditions, with K_{teff} values using low cycle fatigue experiments. The results of these experiments would be stored in a statistical database.

The database would be queried for statistical information in terms of the probability that the K_{teff} values corresponding to a given set of NDI signals are less than a certain value K_o . The undamaged part would be analyzed. Using the available statistical information and the probability that $K_{teff} < K_o$, the probability that FLE is greater than some time T could be estimated. This would lead to rational decisions concerning the disposition of corrosion-damaged parts. It is essential that the statistical database correlating NDI signals with K_{teff} be representative of corrosion damage occurring in actual service. Therefore the relationship between corrosion damage induced under laboratory conditions and corrosion damage that occurs in the field should be established.

11. Appendix

The appendix contains an annotated list of StessCheck input files used in the numerical work described in this report. The files are made available on a CD enclosed with this report.

	Filename	description
2A:	FCL2001_0003_Dogbone	parameterized dogbone corrosion specimen
2B:	ResidualStress1a_update	Handmeshed quarter specimen with various residual stress formulations
	Residual_1b(defects)	Handmeshed quarter specimen with various residual stress formulations and a single spherical defect
2C:	65_col590_.....	SC input files for column 590 (spec-65) w/ the various filtering techniques
	tenscale_.....	2-D models of spec-65 and the various filtering
2D:	66_col138_.....	SC input files for column 138 (spec-66) w/ the various filtering techniques
	tenscale_.....	2-D models of spec-66 and the various filtering
2E:	1_fivedefect_spec16	3-D model of corrosion specimen-16 w/ 5 conical defects of the same depth
	1_torusfivedefect_spec16	3-D model of corrosion specimen-16 w/ 5 conical defects and edge corrosion of the same depth
	1conedefect_spec16	3-D model of corrosion specimen-16 w/ 1 conical defect
	1conedefect_spec27	3-D model of corrosion specimen-27 w/ 1 conical defect
	1conedefect_spec27_2	3-D model of corrosion specimen-27 w/ 1 conical defect
	2conedefect_spec16	3-D model of corrosion specimen-16 w/ 2 overlapping conical defects
2F:	1_fivedefect_spec16	3-D model of corrosion specimen-16 w/ 5 spherical defects of the same depth
	1_torusfivedefect_spec16	3-D model of corrosion specimen-16 w/ 5 spherical defects and edge corrosion of the same depth
	1defect_spec27_trial1	3-D model of corrosion specimen-27 w/ one spherical defect
	1defect_spec27_trial2	3-D model of corrosion specimen-27 w/ one larger spherical defect
	2defect_spec27_trial1	3-D model of corrosion specimen-27 w/ two larger and overlapping spherical defects
	2defect_spec27_trial2	3-D model of corrosion specimen-27 w/ two spherical defects
	2_fivedefect_spec16	3-D model of corrosion specimen-16 w/ 5 spherical defects of the same depth and waviness
	2_torusfivedefect_spec16	3-D model of corrosion specimen-16 w/ 5 spherical defects and edge corrosion of the same depth and waviness
2G:	combedefect_27_trial1	3-D model of corrosion specimen-27 w/ one combination defect
	combedefect_27_trial2	3-D model of corrosion specimen-27 w/ one combination defect
	1combedefect_16	3-D model of corrosion specimen-16 w/ 1 combination defect
	1_fivedefect_spec16	3-D model of corrosion specimen-16 w/ 5 combination defects of the same depth
	1_torusfivedefect_spec16	3-D model of corrosion specimen-16 w/ 5 combination defects and edge corrosion of the same depth
	2_fivedefect_spec16	3-D model of corrosion specimen-16 w/ 5 combination defects of the same depth and waviness
	2_torusfivedefect_spec16	3-D model of corrosion specimen-16 w/ 5 combination defects and edge corrosion of the same depth and waviness
2H:	discdefect_spec	3-D model of corrosion specimen-16 with disc defect (rf = 0.02")
	2discdefect_spec	3-D model of corrosion specimen-16 with disc defect (rf = 0.05")
	3discdefect_spec	3-D model of corrosion specimen-16 with disc defect (rf = 0.1")
	4discdefect_spec	3-D model of corrosion specimen-16 with disc defect (rf = 0.2")
	5discdefect_spec	3-D model of corrosion specimen-16 with disc defect (rf = 0.4")
	6discdefect_spec	3-D model of corrosion specimen-16 with disc defect (rf = 0.475")
2I:	grindout	3-D model of corrosion specimen-16 with grindout feature (large sphere) (rc = 0.1")
	2grindout	3-D model of corrosion specimen-16 with grindout feature (large sphere) (rc = 0.25")
	3grindout	3-D model of corrosion specimen-16 with grindout feature (large sphere) (rc = 0.5")
	4grindout	3-D model of corrosion specimen-16 with grindout feature (large sphere) (rc = 1")
	5grindout	3-D model of corrosion specimen-16 with grindout feature (large sphere) (rc = 2")
2J:	16_1a_toruswave	3-D model of corrosion specimen-16 with edge corrosion and waviness
	16_2a_torus	3-D model of corrosion specimen-16 with edge corrosion
	16_3a_wave	3-D model of corrosion specimen-16 with waviness
	halfamp_16_1b_toruswave	3-D model of corrosion specimen-16 with edge corrosion and half amplitude waviness
	halfamp_16_3b_wave	3-D model of corrosion specimen-16 with half amplitude waviness
2K:	24_1a_toruswave	3-D model of corrosion specimen-24 with edge corrosion and waviness
	24_2a_torus	3-D model of corrosion specimen-24 with edge corrosion
	24_3a_wave	3-D model of corrosion specimen-24 with waviness
	halfamp_24_1b_toruswave	3-D model of corrosion specimen-24 with edge corrosion and half amplitude waviness
	halfamp_24_3b_wave	3-D model of corrosion specimen-24 with half amplitude waviness

2L:	30_1a_toruswave	3-D model of corrosion specimen-30 with edge corrosion and waviness
	30_2a_torus	3-D model of corrosion specimen-30 with edge corrosion
	30_3a_wave	3-D model of corrosion specimen-30 with waviness
	halfamp_30_1b_toruswave	3-D model of corrosion specimen-30 with edge corrosion and half amplitude waviness
	halfamp_30_3b_wave	3-D model of corrosion specimen-30 with half amplitude waviness
2M:	65_1a_toruswave	3-D model of corrosion specimen-65 with edge corrosion and waviness
	65_2a_torus	3-D model of corrosion specimen-65 with edge corrosion
	65_3a_wave	3-D model of corrosion specimen-65 with waviness
	halfamp_65_1b_toruswave	3-D model of corrosion specimen-65 with edge corrosion and half amplitude waviness
	halfamp_65_3b_wave	3-D model of corrosion specimen-65 with half amplitude waviness
2N:	a1_onlytorus_defect	3-D model of corrosion specimen-66 with edge corrosion
	66_1a_toruswave	3-D model of corrosion specimen-66 with edge corrosion and waviness
	66_2a_torus	3-D model of corrosion specimen-66 with edge corrosion
	66_3a_wave	3-D model of corrosion specimen-66 with waviness
	halfamp_66_1b_toruswave	3-D model of corrosion specimen-66 with edge corrosion and half amplitude waviness
	halfamp_66_3b_wave	3-D model of corrosion specimen-66 with half amplitude waviness
2O:	3a_BoundaryLayer_Mesh	3-D model of corrosion specimen with parameterized boundary layer thickness, grindout radius, and grindout depth
	No_Defect_Compress_Residual	Quarter model of pristine corrosion specimen with parameterized values, applied thermal and traction loads
	Defect_Compress_Residual	Quarter model of corrosion specimen w/ grindout, parameterized values, applied thermal and traction loads
2P:	back_arrestinghandmeshBCs	Backup to handmeshed arresting hookshank
	bakbackhandmesh	Seconde backup to handmeshed arresting hookshank
	backup_74A480617_new_final	Backup to final arresting hookshank solid model
	Residual_1b_defectsbackup	Backup to Residual_1b(defects) (see 2B)
2Q:	no input files in folder	
2R:	case1	Parametric model for UDRI Pit Metric Case 1 configuration
2S:	case2base	Hand-meshed parametric model for UDRI Pit Metric Case 2 configuration
	case2automesh	Automeshed parametric model for UDRI Pit Metric Case 2 configuration
2T:	Case3_BL_final	Hand-meshed parametric model for UDRI Pit Metric Case 3 configuration

Appendix B

Boeing Final Report

HIGH STRENGTH STEEL CORROSION - FATIGUE MODELING

Final Report

R. Perez, D. Rich, K. K. Sankaran and H. G. Smith, Jr.

The Boeing Company
St. Louis, Missouri

April 2006

Final Report for the Period January 2004– April 2006

Table of Contents

	Page
Table of Contents	ii
Acknowledgments	iii
1. Introduction	1
2. Test Plan Definition	2
3. Corrosion Characterization	3
4. Corrosion Metrics	7
5. Finite Element Methods Requirements	18
6. Progression of Corrosion Pit and Fatigue Crack Growth Ending in Failure	18
7. Laboratory Simulation Techniques for In-Service Corrosion	21
8. Potential of Micro-machining to Simulate Corrosion	23
9. In-Service Experience of Steel Corrosion	27
10. Effective Stress Concentration Factor	30
11. Software Tool for Profilometry Roughness Analysis.	32
12. Corrosion Metric Development	35
13. Round Robin Evaluation of Fractured Specimens	41
References	47

Acknowledgments

This effort was sponsored by the University of Dayton Research Institute (UDRI) under subcontract no. RSC03024. Mr. Wally Hoppe was the Technical Monitor at UDRI. The following Boeing personnel worked on this project: Dr. Rigo Perez, Mr. Daniel Rich (Program Manager till August 2005), Mr. Albert Neal (Program Manager), Dr. K.K. Sankaran and Dr. Herb Smith, Jr. Other Boeing participants included Mr. Gary Weaver, who performed the scanning electron microscopy. This report is an update of the final report submitted in December 2005 and covers work accomplished between January 2004 and April 2006 and includes the interim report submitted in June 2004.

1. Introduction

Corrosion increases the stress in an airframe part by reducing the effective cross sectional area of the structure carrying the load. Corrosion also causes stress concentrations, which can result in premature fatigue crack initiation. Therefore, the presence of corrosion reduces fatigue life and can result in greater risk of component failure. The prevention and repair of corrosion is a major maintenance cost for the U.S. Armed Services.

Corrosion-fatigue modeling and analysis are essential to determining the impact of corrosion on structural integrity. Efforts have focused principally on aluminum alloy applications and more recently on steel alloys (Reference 1). This report documents the results of the Boeing effort, which is part of a high strength steels corrosion-fatigue modeling program conducted by UDRI. The Boeing Company tasks cover the following:

1. Assisting UDRI in corrosion simulation, exposure and characterization procedures including specimen preparation and masking to avoid crevice corrosion.
2. Characterizing the magnitude of corrosion on specimens provided by UDRI by laser profilometry and spot check measurements using microscopy.
3. Determining the adequacy of laser profilometry to obtain valid corrosion metrics for use in life prediction models and developing software tool to provide these metrics.
4. Examining the laser profilometry data obtained previously and performing a comparative statistical and probabilistic fatigue life prediction analysis to determine the efficacy and adequacy of using this technique.
5. Defining the requirements for finite element analysis methods, which use the metrics to calculate stress concentrations caused by corrosion. These stress concentrations shall be applicable in fatigue life analysis procedures.
6. Identifying aircraft parts that have corroded in service, defining issues involved in correlating various corroded parts removed from in-service aircraft and selecting an in-service part for component testing with UDRI/USN concurrence.
7. Developing plans for testing the in-service parts and gathering of corroded and non-corroded parts for use in simulation tests.

These activities support the overall program goal to quantify corrosion and conduct sufficient tests to obtain lives from specimens with various levels of corrosion. Presently different and inconsistent definitions of corrosion exist. The approach is to determine K_t 's and distributions/grouping of K_t 's and to analytically accomplish the following:

- Define corrosion categories with respect to K_t grouping
- Define characteristics for each corrosion category
- Correlate NDI signals to corrosion metrics, and
- Develop maintenance plans/practices/processes based on categories

2. Test Plan Definition

As part of the planned effort in defining test plans including fatigue test coupon and specimen configuration definition, selection of stress levels, specification of corrosive environments, and data requirements, information was provided to UDRI on Boeing's experience with the cleaning of corroded steel coupons and the effects of the corrosion exposure environment.

Cleaning of Corroded AF 1410 Coupons - Boeing had provided the corroded and tested AF 1410 fatigue coupons from the previous program (Reference 1) to UDRI for corrosion characterization using white light profilometry. In response to an inquiry from UDRI regarding why the Boeing-cleaned corrosion fatigue specimens did not look very clean and what could be done to clean the specimens further, it was noted that the specimens appeared dark and not shiny because the specimens were fabricated from AF 1410 bar stock heat treated and processed exactly as the production F/A-18 parts to simulate the effects of actual production conditions. As such, the specimens discolor during heat treatment and are further lightly blasted to remove any adhering scale. The cleaning procedure and the solutions are designed to remove the "rust" and generally remove the corrosion products without affecting the corroded surface morphology and topography. Therefore, the "dark" areas will remain in the cleaned specimens. However, the specimens are not dirty and do not discolor with time.

Effects of Corrosion Exposure Environment - Under the previous program (Reference 1), Boeing had investigated the effects of exposure to salt spray in a neutral salt fog chamber (ASTM B117) as well as in SO₂ modified salt fog chamber (ASTM G85 Annex A4) on the fatigue lives of AF 1410 steel coupons. UDRI exposed the AF 1410 material to alternate immersion in salt water and was not sure if 60 days of such exposure would create a noticeable change in fatigue life. Boeing had found that the tests with exposures of up to 100 hours in neutral salt fog failed at locations outside the corroded area so it could not be determined if it had an effect on fatigue lives. A noticeable decrease in fatigue life was observed after exposure for 100 hours in SO₂ modified salt fog.

One difficulty with steel alloys such as AF 1410 and 300M is that they do not passivate and hence do not nucleate discrete pits, which grow and decay as in aluminum alloys and stainless steels. The corrosion is of a more general nature and the alloys tend to "rust" and show tendency toward exfoliation. However, in the early stages of corrosion the surface topography of the corroded surface can be characterized like that of the pitted surface. As corrosion progresses, the local "pit" like areas quickly spread uniformly making pitting characterization meaningless. The corrosion then would have to be characterized by other techniques such as weight loss or thickness loss measurements. The challenge then is to control the corrosion exposure in such a way that one could quantitatively measure the corrosion, but still obtain reduction of fatigue lives.

3. Corrosion Characterization

The objective of this task was to characterize the magnitude of corrosion on specimens provided by UDRI using laser profilometry and perform spot checks using optical microscopy to verify the laser data.

We received from NAVAIR twenty one (21) flat wafers of AF 1410, four (4) flat wafers of 300 M and three (3) cylindrical specimens of 300M steel exposed to neutral salt fog for the durations listed in the Figure 3-1.

Figure 3-1 Specimens used to Characterize Corrosion

Material	Wafer #	Surface Finish	Exposure
AF 1410 Flat Wafer	U 21	As is	96
	22	As is	240.5
	25	As is	507
	10	Polished	96
	11	Polished	96
	13	Polished	96
	15	Polished	240.5
	18	Polished	240.5
	23	Polished	240.5
	U 16	Polished	507
	U 23	Polished	507
	U 25	Polished	507
	16	Sand Blast	96
	21	Sand Blast	240.5
	28	Sand Blast	507
	3	Polished	48
	6	Polished	24
	2	Polished	168
	5	Polished	312
	8	Polished	216
	9	Polished	264
300 M Flat Wafer	3	As is	24
	4		24
	6		72
	7		192
300 M Cylinder	xx		24

Boeing's Engineering Laboratories cleaned all of the corroded AF 1410 and 300 M material in hot caustic solution to remove the corrosion products. Prior to immersion in the solution, all of the wax that had been used as a maskant was removed from the specimen surface.

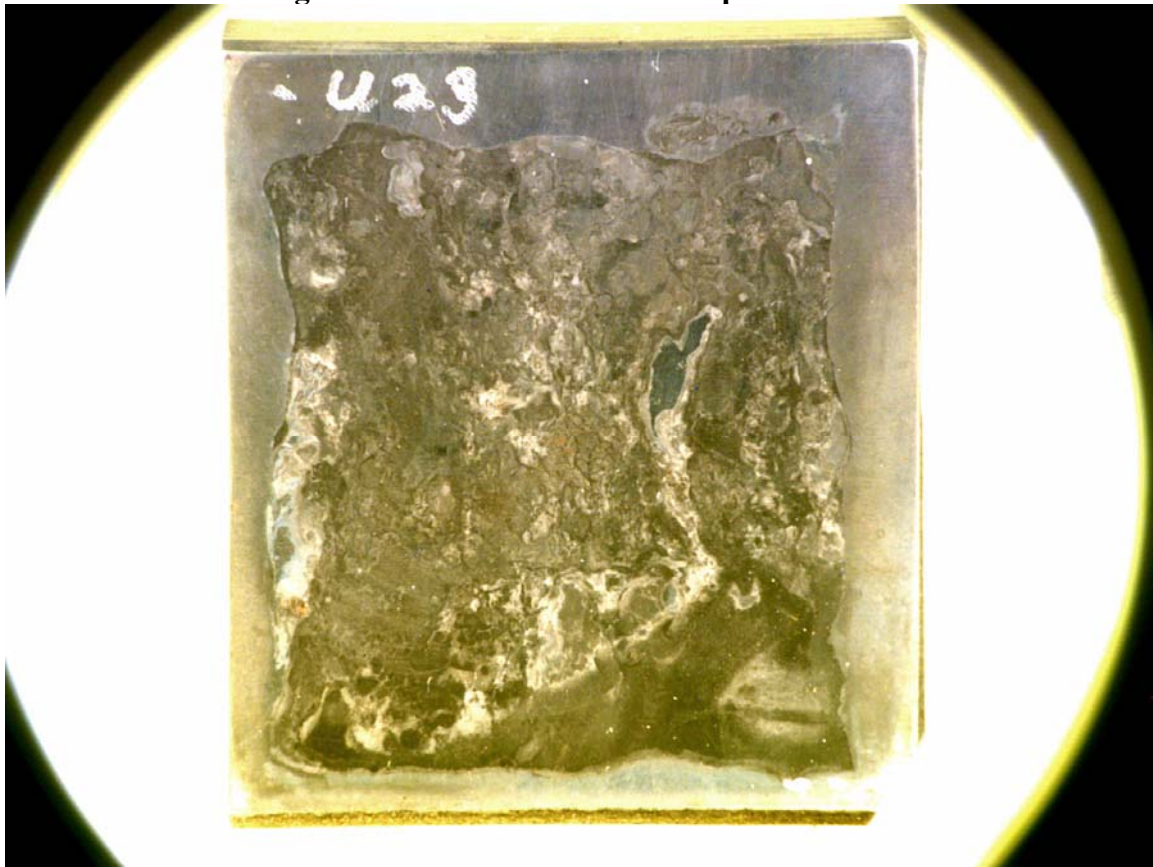
A preliminary optical microscopic evaluation of several of these wafers showed similar type of corrosion and depth in local "pit" like areas, as observed previously (Reference 1) in the corroded AF 1410 specimens. Six of the flat AF 1410 wafers (15, 18 23, U16, U23 and U25), the four flat 300M steel wafers as well as one cylindrical 300M steel wafer

were characterized by laser profilometry by Solarius. In addition, two of the AF 1410 wafers (2 and 5) were sent to UDRI for their characterization.

The purpose of this characterization was to compare the pitting characteristics resulting from these exposure times to those from the exposure to 100 hours in SO₂ salt fog in the previous program (Reference 1). The 100 hours of exposure in SO₂ salt fog had a measurable impact on the fatigue lives of AF 1410 steel compared with the baseline uncorroded condition.

The flat AF 1410 and 300 M wafers were photographed and scribed with identification marks in preparation for laser profilometry characterization by Solarius. A photograph of the corroded surface of wafer U23 is shown in Figure 3-2. The wafers were indented (as shown for U23) to provide a reference for identification of the locations that were characterized.

Figure 3-2 Corroded Surface of Specimen U23



For each of the six AF 1410 and the four 300 M wafers, laser profilometry was performed with three measurements in 5 mm x 5 mm areas with 10 micron spacing between x and y. In each specimen, the profilometry was performed in highly corroded regions whose locations were identified by using a coordinate system. In addition, one measurement of the entire corroded region (25 mm x 25 mm) was also performed for

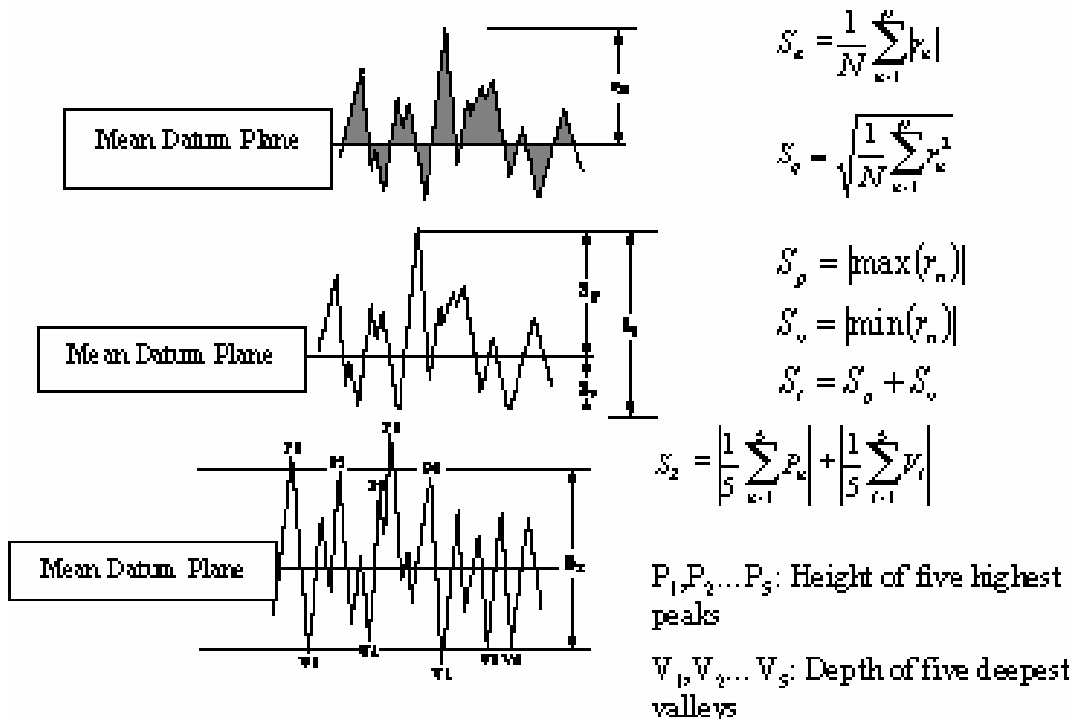
wafer U23. The purpose was to assess whether statistically equivalent results are obtained by characterizing randomly chosen smaller corroded areas. For the 300M cylindrical specimen, only one measurement in a 5 mm x 5 mm area with 10 micron spacing between x and y was performed. The purpose of this measurement was to determine the effects, if any, of the specimen curvature on the measurements.

Solaris provided ASCII text as well as the following surface roughness indicators for all of the measurements.

Sa – Arithmetic mean deviation of the surface, units - μm
 Sq – Root Mean Square deviation of the surface, units - μm
 Sp – Maximum height of summits, units - μm
 Sv – Maximum depth of valleys, units - μm
 St – Total height of the surface, units - μm
 Sz – Ten point height of the surface, units - μm
 Sds – Density of summits of the surface, units – peaks/ mm^2

These measurements are defined in Figure 3-3 (provided by Dimitri Savvas of NAVAIR).

Figure 3-3 Definitions of Surface Roughness Measurements



The values obtained from profilometry measurements are the distance from the sensor head to the surface of the corroded material. The average of all these measurements defines the "mean datum plane" or "baseline". This distance is just the average

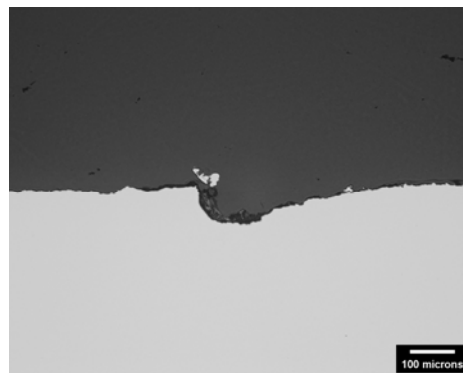
measurement of all those taken and has no significance with regard to any geometric feature. This distance is subtracted from all measurements to give a smaller value relative to the mean plane, which is then used in the computation of the other surface roughness calculations. Thus, the laser profilometry measurements do not provide a true measure of the “material loss” due to corrosion. However, they do provide several statistical parameters, which may be of use in defining corrosion metrics, as discussed in the next section.

In the previous section it was stated that the challenge in the development of methods to obtain corrosion metrics for steel alloys is to control the corrosion exposure in such a way that one could quantitatively measure the corrosion, but still obtain reduction of fatigue lives. Corrosion fatigue coupons tested under the previous program (Reference 1) exhibited three different types of fracture.

- For low levels of corrosion, the fatigue crack initiated and propagated to failure away from the corroded area.
- For some specimens, at intermediate levels of corrosion exposure in neutral salt, the fatigue crack propagated thorough the corroded area.
- For most specimens exposed for 100 hours in SO₂ salt spray, fatigue cracks appeared to nucleate and propagate along the trenches representing the creviced area underneath the edge of the maskant.

When maskants are used, there is always the possibility of crevice formation resulting in trenches from which fatigue cracks can nucleate and grow. An example of such a trench is seen in the Figure 3-4, generated by UDRI from a specimen provided to them, which shows the surface of a fractured AF 1410 specimen.

Figure 3-4 Crevice or Trench Formation at Base of Maskant



Methods must be developed to mask the specimens in ways that avoid the formation of such crevices around the edges.

4. Corrosion Metrics

The purpose of this task is to develop metrics, based on the laser profilometry data, which can be used to quantify the effects of the corrosion on the fatigue life. Although the test coupons are tracked based on the elapsed time of exposure to the corrosive environment, it was shown in previous work (Reference 1) that the exposure time is an unreliable metric. This is a result of several factors. First, the degree of corrosion is dependant upon the quality of the exposure to the corrosive environment in the test chamber and can vary depending upon placement in the chamber and possible shielding from other coupons, etc. Longer time in the chamber does not necessarily correlate to a more advanced corrosion state. Second, different corrosive environments cause different levels of corrosion for the same exposure time. Comparisons across environments are therefore not possible. Lastly, there is no direct correlation between exposure time and in-service corrosion levels, and thus exposure time cannot be used as a metric for corrosion found in the fleet.

Therefore, a metric based directly on the attributes of the corroded surface is required. In the previous work cited, we developed a characteristic pit norm that worked very well for the aluminum specimens under consideration. It was somewhat conservative in that it assumed a completely uniform spread of corrosion, which was not the case particularly in the early stages. Also, steel products do not pit as aggressively as aluminum alloys do and therefore the usefulness of the pit norm for the steel parts was unclear. Measuring the pit sizes requires a microscope and is a somewhat tedious process that would not lend itself to service in the fleet. We sought a metric that could be obtained easily in the field and would address the shortcomings of the pit norm.

Laser profilometry (LP) offers the promise of addressing these issues. There are a number of standard surface roughness parameters that are determined by LP, and the intent is to evaluate their utility in serving as a metric for the effects of the corrosion on fatigue life. These were described in detail in the previous section of the report. In addition, it may be that some combinations of the standard parameters, or some new, as yet undefined parameter, might correlate more directly to the fatigue life. This possibility would be considered in a follow-on effort.

Figures 4-1, 4-2, and 4-3 show that the profilometry parameters for the AF1410 show a definite trend with respect to exposure time. It is also clear that some of the parameters show a tendency toward higher scatter at the longer exposure times. The data obtained in this program (marked as New Data) correlates well to the data from Reference 1 (marked Existing Data).

Figure 4-1 Profilometry Parameters versus Exposure Time

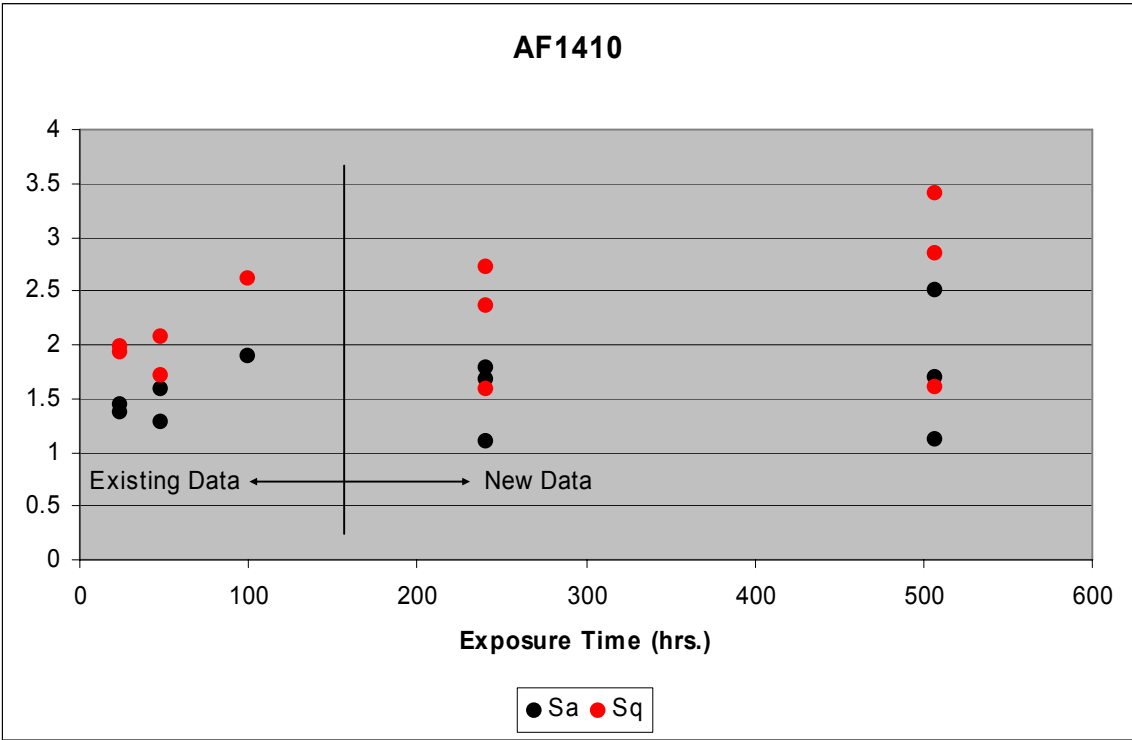


Figure 4-2 Profilometry Parameters versus Exposure Time

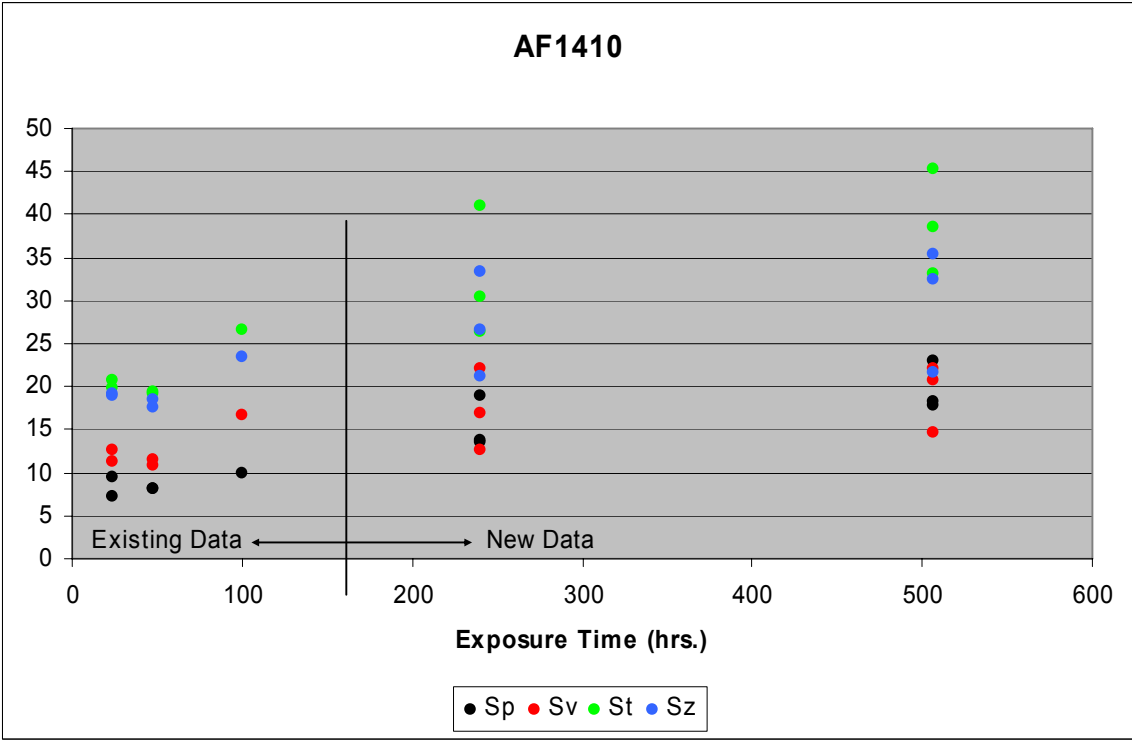
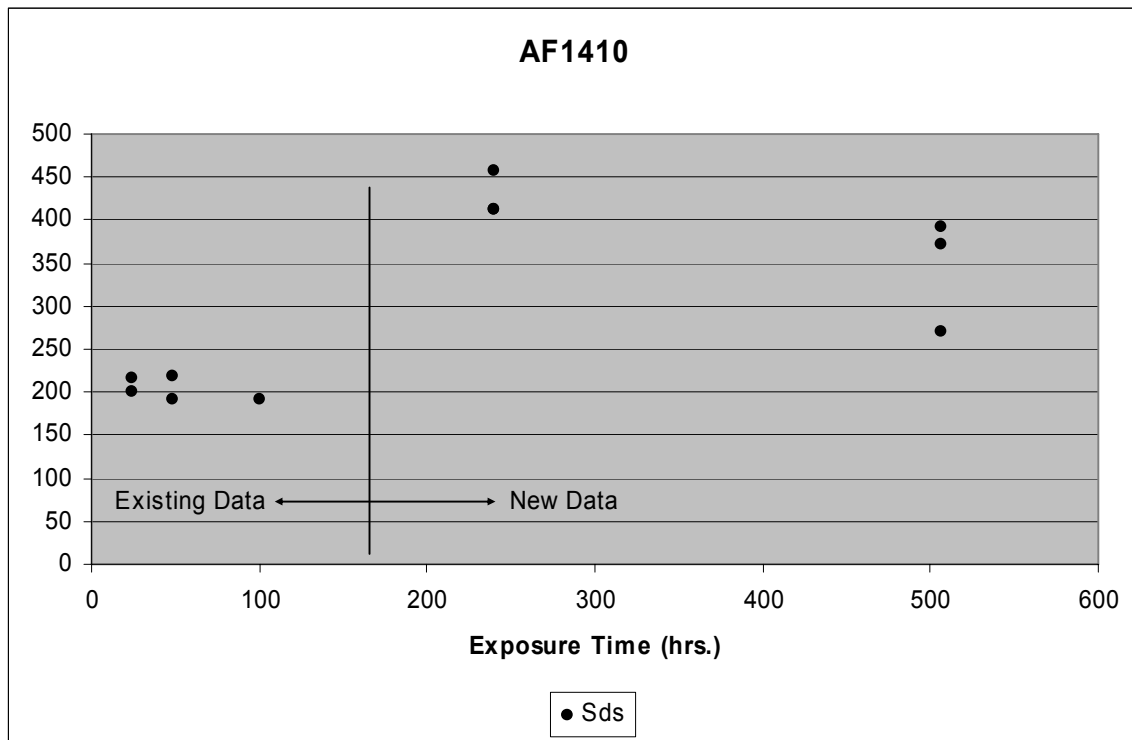


Figure 4-3 Profilometry Parameters versus Exposure Time



Similar trends can be seen in the profilometry data for the 300M specimens. In this case, there is no existing data. All the data was generated in this program. These results are shown in Figures 4-4, 4-5, and 4-6.

Figure 4-4 Profilometry Data for 300M Specimens

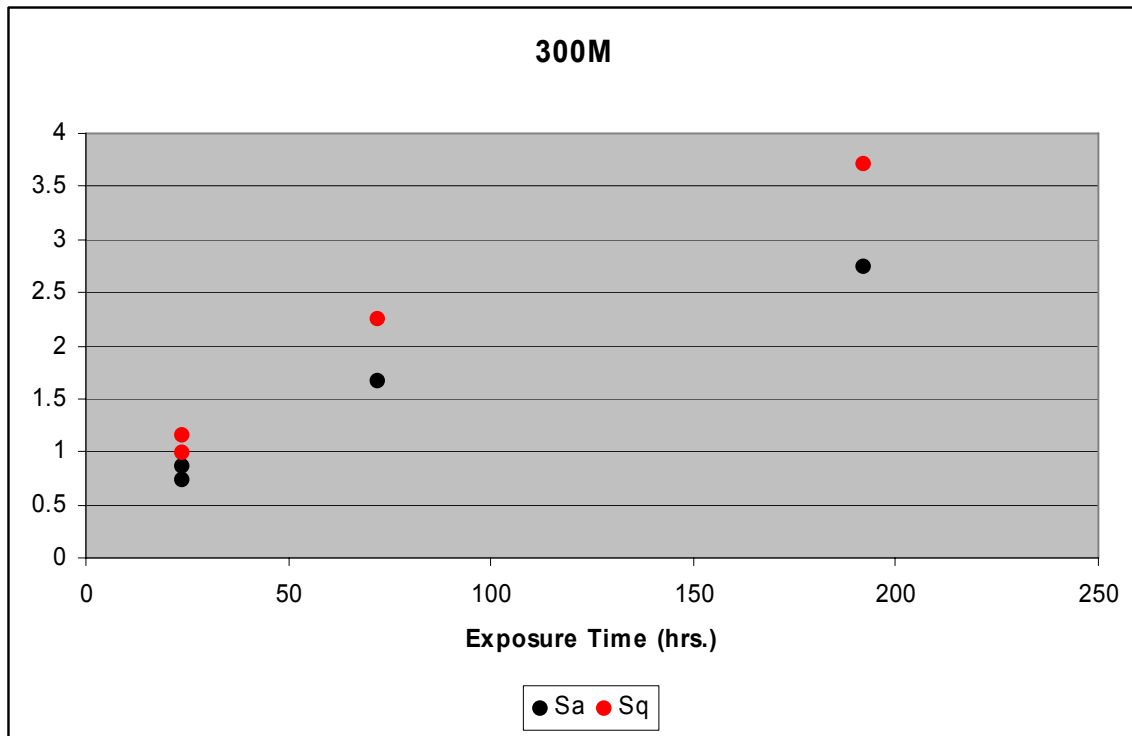


Figure 4-5 Profilometry Data for 300M Specimens

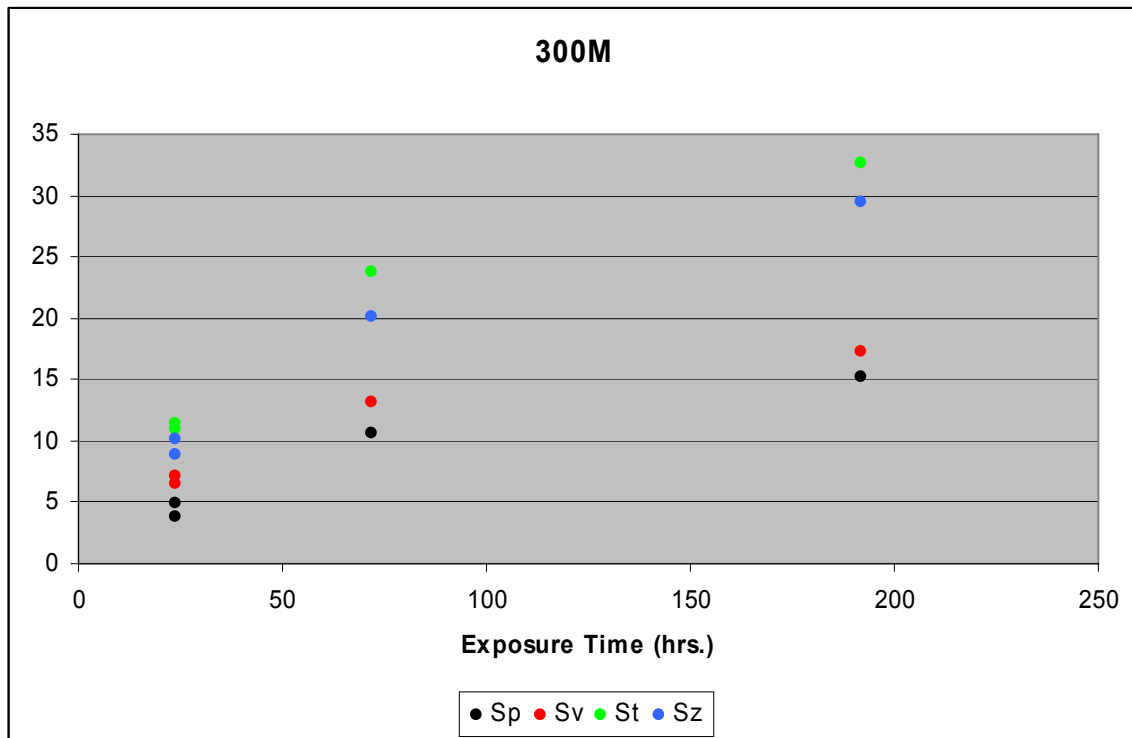
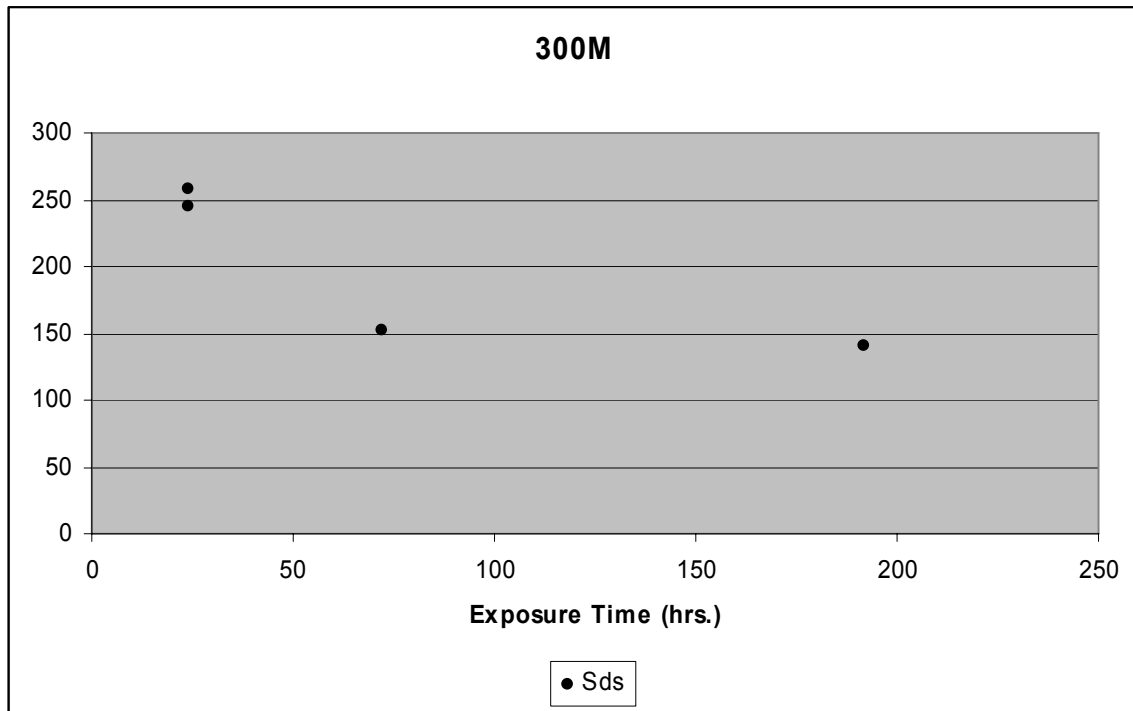


Figure 4-6 Profilometry Data for 300M Specimens



The real goal, however, is to correlate the various parameters to some effect on fatigue life. There was no fatigue data, however, obtained in this part of the program. Some limited fatigue data was obtained in the work cited in Reference 1; however, only part of those specimens had profilometry data available. Figure 4-7 shows the complete test matrix and results from that effort.

Figure 4-7 Test Results from Reference 1
(Failure Location is from the end of the Specimen)

ID	Exp, Hrs	Add. Exp. Hrs	Total Exp. Hrs	Max Stress, ksi	Life	Failure Location
Baseline						
Base-1	0	0	0	200	12,336	5.25
Base-2	0	0	0	160	29,848	5.25
Base-3	0	0	0	140	20,247	4.5
Base-4	0	0	0	180	13,382	4.5
Base-5	0	0	0	180	22,023	4.5
Base-6	0	0	0	170	53,671	4.75
Base-7	0	0	0	140	71,205	4
Base-8	0	0	0	170	35,006	5
Base-9	0	0	0	180	12,806	3.75
Base-10	0	0	0	170	22,504	4
Base-11	0	0	0	200	13,856	4
Base-12	0	0	0	160	22,001	5.25
Base-13	0	0	0	150	41,750	4.25
Base-14	0	0	0	170	13906 (Invalid test)	N/A
Base-15	0	0	0	200	10,457	4
24 Hours Neutral Salt Fog						
24-1	24	0	24	140	66,133	5.1
24-2	24	0	24	200	8,962	5.1
24-3	24	0	24	180	17,823	4.2
24-4	24	0	24	160	31,871	5.6
24-5	24	0	24	140	23,745	3.7
24-6	24	0	24	200	9,596	5.2
24-7	24	0	24	160	52,816	4.9
24-8	24	0	24	140	44,433	5.15
24-9	24	0	24	170	37,492	4.15
24-10	24	0	24	170	25,985	4.1
24-11	24	0	24	180	12,441	4
24-12	24	0	24	200	14,039	4.1
50 Hours Neutral Salt Fog						
2-1	2	48	50	200	11,301	4.5
2-2	2	48	50	170	29,283	2.3
2-3	2	48	50	140	30,579	4.6
2-4	2	48	50	140	64,678	5.05
2-5	2	48	50	140	40,436	5.7
2-6	2	48	50	140	57,648	3.6
2-7	2	48	50	170	21,554	5.65
2-8	2	48	50	170	17,079	5.6
2-9	2	48	50	170	30,086	4.2
2-10	2	48	50	200	12,888	4.05
2-11	2	48	50	200	10,855	4.18
2-12	2	48	50	200	10,634	3.1
100 Hours Neutral Salt Fog						
4-1	4	96	100	140	30,444	5.25
4-2	4	96	100	170	15,883	5.75
4-3	4	96	100	200	8,099	5.25
4-4	4	96	100	140	42,990	5.2
4-5	4	96	100	170	15,386	5.25
4-6	4	96	100	200	10,188	4.53
4-7	4	96	100	140	27,442	5.25
4-8	4	96	100	170	15,733	5.75
4-9	4	96	100	200	9,746	5.12
100 Hours SO2 Salt Fog						
100-1	0	100	100	140	14,259	5.25
100-2	0	100	100	140	13,267	5.25
100-3	0	100	100	140	15,204	5.25
100-4	0	100	100	170	5,617	5.25
100-5	0	100	100	170	7,966	5.25
100-6	0	100	100	170	6,735	5.25
100-7	0	100	100	200	3,487	5.25
100-8	0	100	100	200	4,649	5.25
100-9	0	100	100	200	4,000	5.25
4-10	4 (in neutral salt)	96	100	140	13,519	5.25
4-11		96	100	170	6,306	5.25
4-12		96	100	200	3,855	5.25

Profilometry data had been obtained for seven of the specimens (2-1, 2-3, 4-8, 4-11, 24-3, 24-7 and 100-8). These specimens represented a mix of exposure times and exposure environments and, in addition, they were fatigue tested at different stress levels. Whereas this was useful in obtaining some basic idea of behavior, it was not possible to build a definitive picture of the relationships. In an effort to fill in the gaps we developed a plan to obtain profilometry data for a number of the remaining specimens (indicated by the orange color coding). We believed that this would give the ability to get a more complete picture of the relationship of fatigue life to corrosion level and stress.

One problem that we had in the previous work was the fact that for some of the higher corrosion levels the crack developed at the transition from the corroded to the non-corroded areas. This transition was a test-induced artifact that would not appear in the service environment. We also planned a series of profilometry measurements on this transition area in an effort to determine a compensation factor that could be applied to the test results to account for this artifact.

In addition to accounting for the induced edge, the measurements would allow the determination of the effective thickness loss of the surface. As the profilometry measurements are relative to the mean plane, there is no way to measure the thickness loss. These transition measurements would allow the overall thickness loss to be determined as an important additional factor. The steel shows a propensity for general corrosion much more than aluminum, and therefore the overall thickness loss can contribute to a general increase in stress and a reduction in fatigue life.

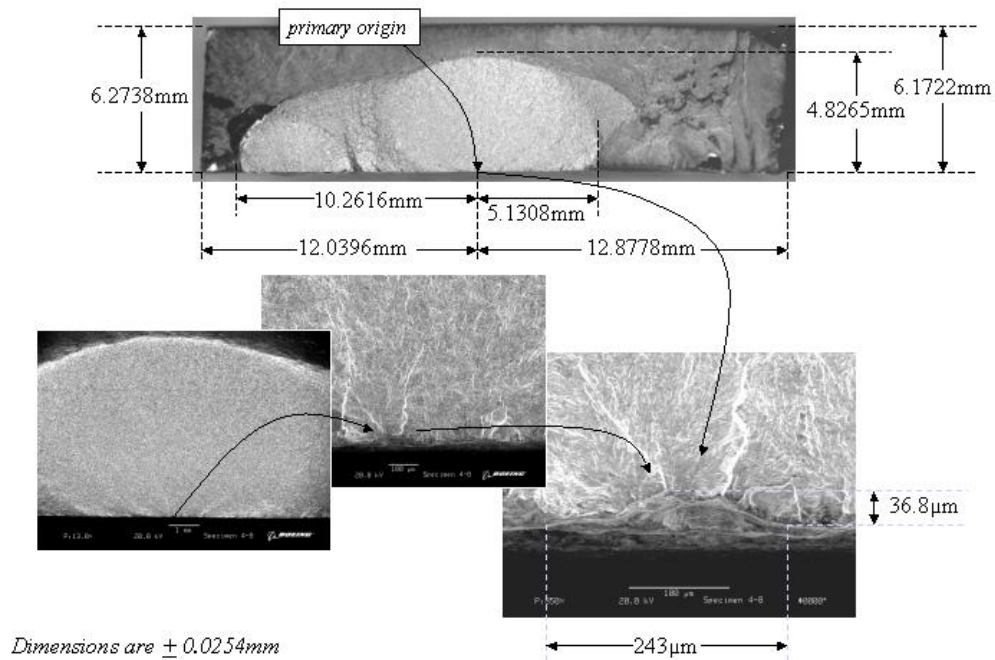
A fractographic analysis was conducted of Specimen 4-8 to determine the failure progression. Specimen 4-8, see Figure 4-8, had been tested to failure under constant amplitude loading, stress ratio = 0.02 and a maximum stress of 170 ksi, for 15,733 cycles. The specimen had been previously exposed to a salt-fog environment to develop a central corroded area. The specimen had been masked to keep the environment from the edges and the ends of the specimen leaving a rectangular corroded zone. One-half of the fracture surfaces were used for analysis with the Scanning Electron Microscope, SEM. The following is information observed from review of the fracture surface.

The fracture surface of specimen 4-8 is shown in Figure 4-9. The failure was due to fatigue with the primary fatigue origin being at a 0.0368 mm by 0.243 mm corrosion pit. The corrosion pit was located close to the center of the corroded area. The crack grew in a semi-circular fashion till failure at a critical depth of 4.83 mm. A secondary fatigue origin was located slightly inside of masked area demarcation line with no discernable corrosion pit.

Figure 4-8 Test Specimen 4-8



Figure 4-9 .Specimen 4-8 Fracture Surface Showing Fatigue Origins and Fracture Dimensions



Collages of pictures are provided in Figure 4-10 to better describe the failure characteristics. At the top center is the fracture surface with the next picture being a side view of the specimen. The lines of corrosion demarcation can be seen on side and at the bottom of the test sample.

The left uppermost picture is an angle view showing the fracture surface on top and the side of the specimen below. Again the line of corrosion demarcation can be seen on the side surface.

The left and right bottom pictures show that the “steps” at the demarcation line was 0.0353 mm and 0.275 mm for the left and right sides, respectively. No explanation is possible at this time as to why these steps are so different in size.

Figure 4-10 SEM Photos showing Relation of Corrosion Demarcation Lines to Fracture Surface

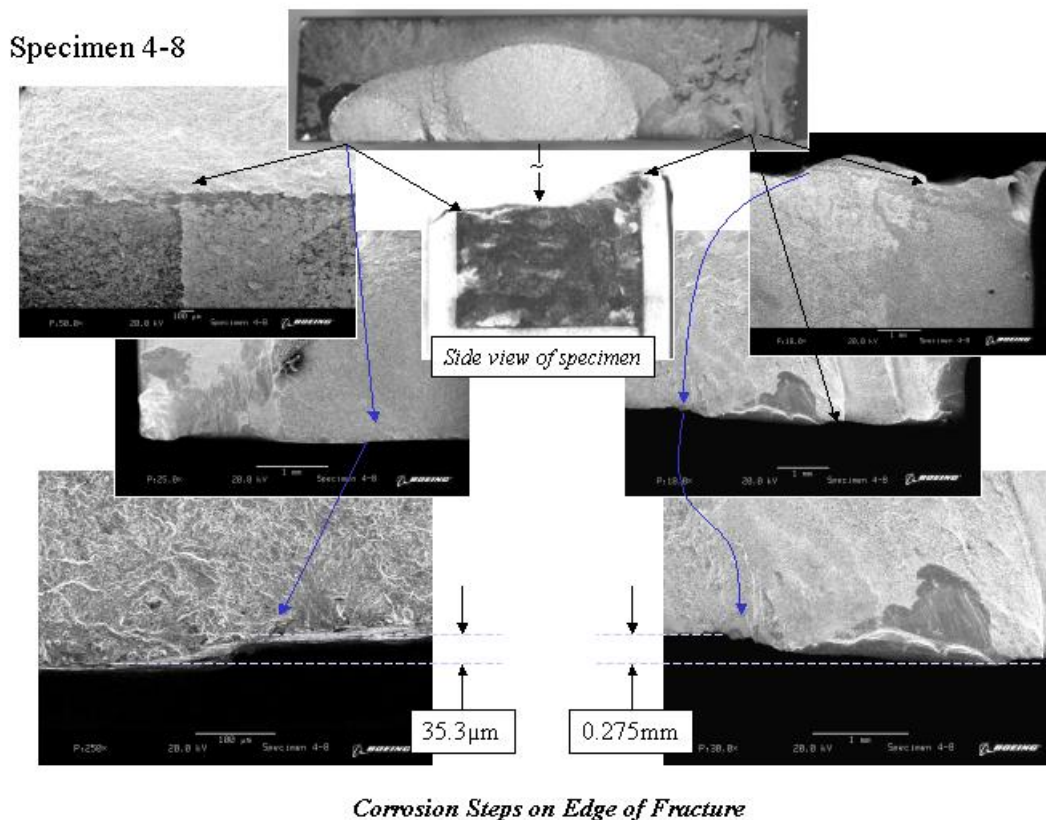


Figure 4-11 documents the features seen on the fracture surface of Specimen 4-8. Again fatigue striations were found emanating from a corrosion pit. There was also some overload fracture when the specimen broke in two pieces. Striation density measurements, as shown in Figure 4-12, were made as a function of distance from the primary origin. The striation density relationship was integrated to provide an estimation of the crack growth behavior as shown in Figure 4-13. Notice that this suggests that it took 11,195 cycles to grow to failure of the 15,733 total cycles applied to the specimen.

Using the definition of crack initiation as the time to a 0.01-inch crack, there was approximately 40% (6,000/15733) of the time spent in crack initiation and 60% of the time in crack growth.

Figure 4-11 Specimen 4-8 Fracture Surface Showing Fatigue and Overload Zones

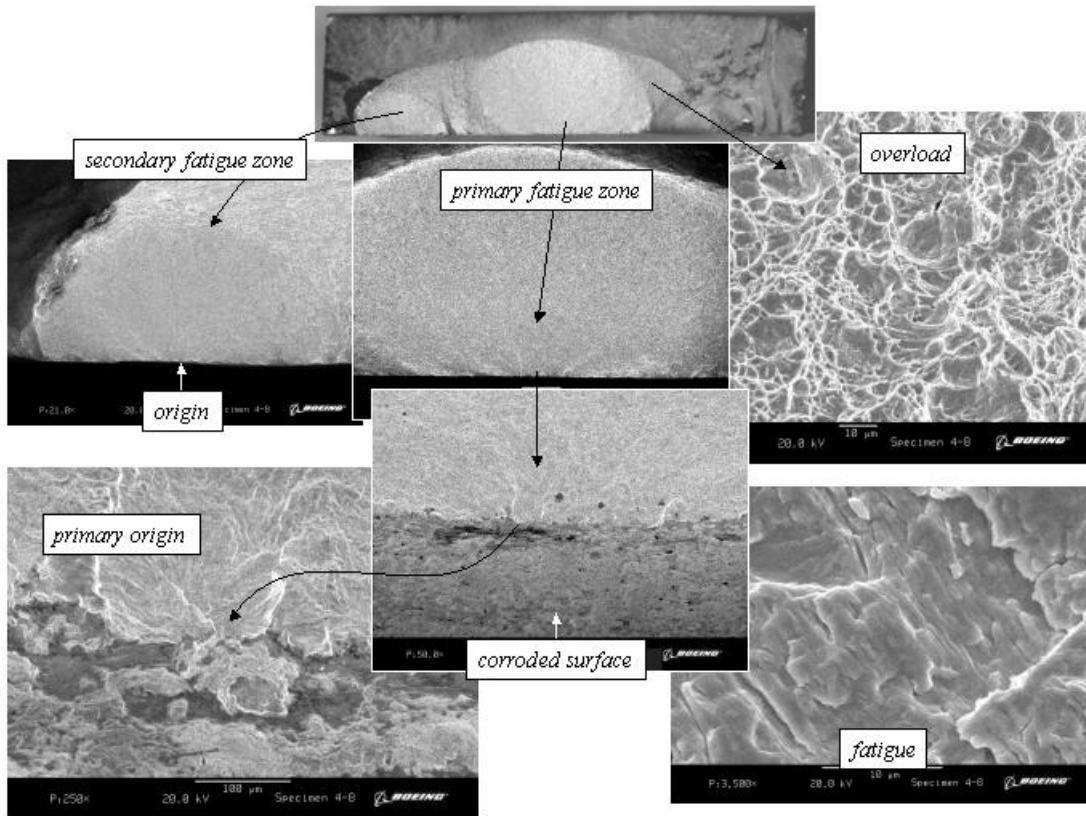
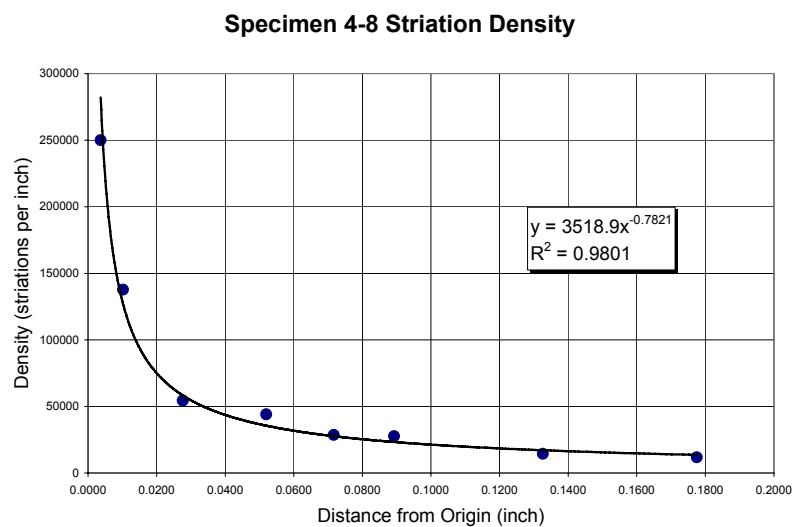
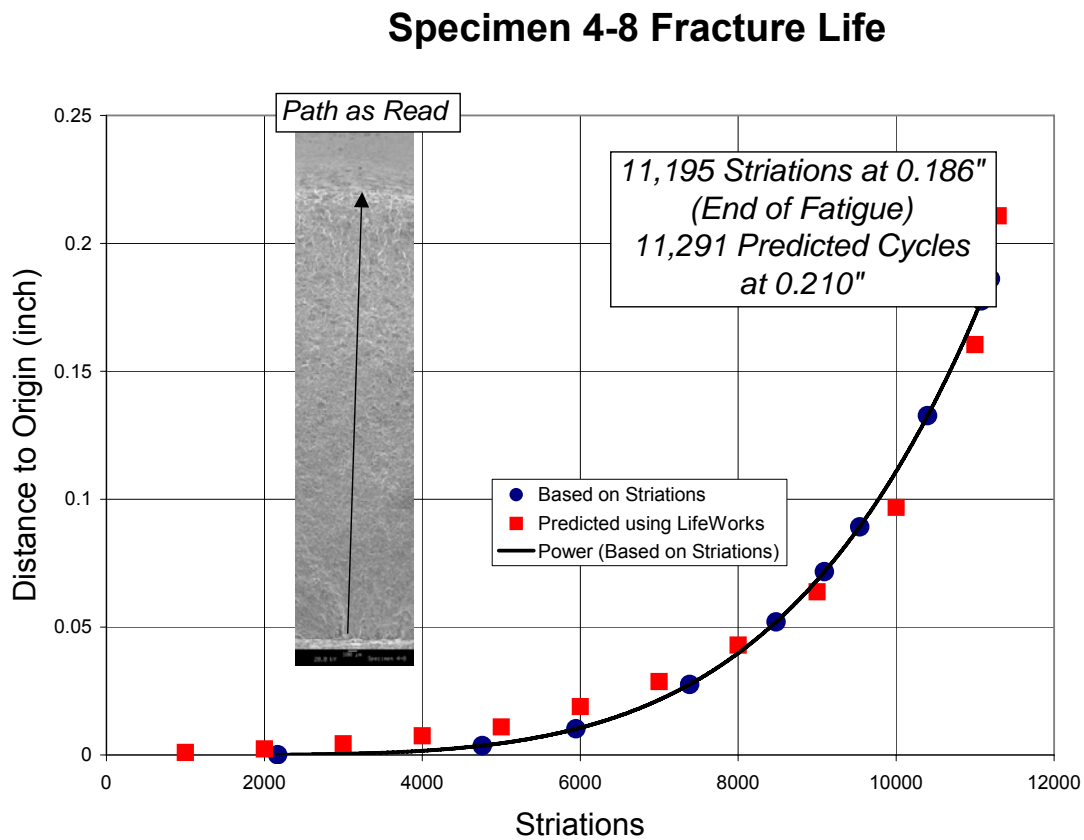


Figure 4-12 Striation Density Plot for Specimen 4-8



Crack growth predictions were made using Boeing durability and damage tolerance software *LifeWorks*. As shown in Figure 4-13 the predictions were in excellent agreement with the SEM striation measurements.

Figure 4-13 Specimen 4-8 Crack Growth Behavior



5. Finite Element Methods Requirements

Modeling of the corroded surface was to be accomplished by ESRD. In support of their effort, Boeing provided ESRD with the raw profilometry data files for the aluminum 7075-T6 and AF1410 samples collected on the previous program. The aluminum samples 43-2, 47-2, 49-2, 52-2, 57-1, 59-2 and 62-2 all had associated fatigue life data as did the AF1410 samples 2-1, 2-3, 4-8, 4-11, 24-3, 24-7, and 100-6. Boeing conducted several conversations with ESRD representatives to explain and clarify the information in the files. Also one should exercise caution about the use of elastic stress concentration in fatigue life predictions as discussed in Section 10.

6. Progression of Corrosion Pit and Fatigue Crack Growth Ending in Failure

The normal fatigue damage progression has four phases as shown by Curve A in Figure 6-1. These are: 1) time for crack initiation, 2) time for short crack growth, 3) time for long crack growth, and 4) failure.

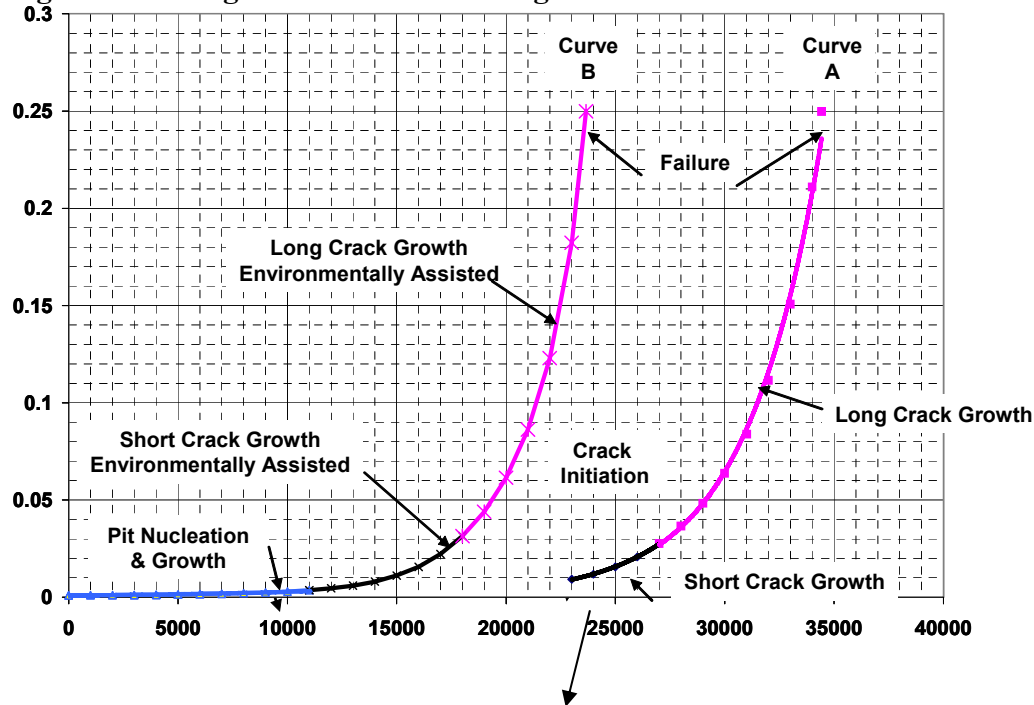
The progression of damage in parts subjected to both corrosion and fatigue is a complex subject and has been investigated by many researchers, References. 2-7. A theory that has gain in popularity in recent years is one that divides the time to failure into five phases as shown by Curve B in Figure 6-1. These phases are: 1) time for pit nucleation, 2) time for pit growth, 3) time for short crack growth, 4) time for long crack growth, and 5) failure.

Fatigue Damage Progression - Fatigue damage in a structure begins on the microscopic level. Cyclic stresses at discontinuities such as dislocations, grain boundaries, etc. cause the development of an actual crack. The time for this crack to reach a somewhat arbitrary size of 0.01 inch has become known by some investigators as the time to crack initiation. The 0.01 inch crack size was selected to be a crack that could be reliably found using eddy current inspection in a hole.

The methodology to predict this time to crack initiation is most often based on strain based procedures. The strain based method, unlike the stress-based method, analytically accounts for the residual notch stress-strain effects that the previous cycles may have on subsequent cycles. However, it still requires extensive element tests for the foundation for the analysis.

Strain based methods are now the basis for most fatigue calculation programs used in the aircraft industry today. The procedure used at Boeing was developed by Rich under the direction of Impellizzeri in 1975 as reported in References 8 and 9. The program was shared with several throughout the industry including NAVAIR. The program has undergone several iterations since that time, some within the company and some from by others in the industry. The Program LOOPIN used by many within the industry is a derivative of the original Impellizzeri/Rich program.

Figure 6-1 Progression of a Nucleating Pit to Crack Growth and Failure



Short Crack Growth - Crack growth for crack sizes less than 0.03 inch is referred as short crack growth and should be based on small flaw theory. It has been established that crack growth rates for small flaws are considerably faster than for larger flaws and thus places limitations on linear elastic fracture mechanics. Dr. Jim Newman, formerly of NASA, and others have discussed this behavior in the literature. However, this 'small flaw' effect is generally not considered by analysts throughout industry. There are many reasons for typically ignoring it – not the least of which is the difficulty in properly accounting for it. There is little da/dN data collected for small flaws and there is no known analytical technique available to smoothly transition between small-flaw analysis and typical analysis. Compounding the problem is the fact that residual stresses often exist adjacent to stress concentrations which also must be considered.

Long Crack Growth - Linear elastic fracture mechanics provides good agreement with observed crack behavior once the crack is larger than 0.03 inch. This region of crack growth is referred as long crack growth and extends till the critical crack size is achieved. At the 0.03 inch depth, the effect of residual stress from normal applied loads is usually minimal.

Failure - Failure is controlled by the material's inherent fracture toughness, applied loading, crack size and geometry.

Environmentally Assisted Damage Growth

Time to Pit Nucleation - The first phase, time for the corrosion pit to nucleate, is perhaps the most difficult to establish since it is related to many parameters. The surface

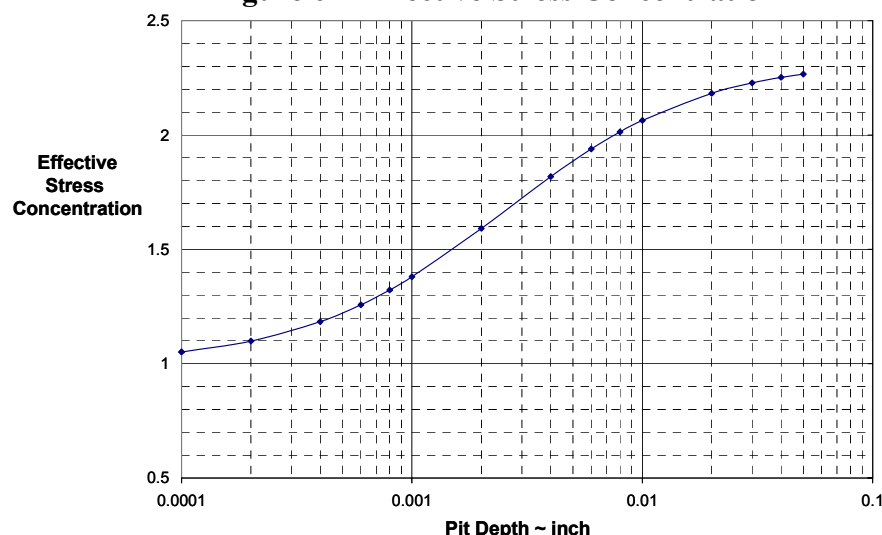
finish and the barriers to the corrosive environment are the first thing to be considered, next is the base material's resistance to corrosion and lastly the surrounding materials and their electrical properties.

The barriers to corrosion are usually applied in layers. A variety of barriers to environment such as cadmium and nickel plating have been used as the first line of defense to protect steel. Ion vapor deposited aluminum has also been used for protection and more recently High Velocity Oxygenated Fuel, HVOF, thermal spray powder coatings are becoming the barrier of choice. On top of this barrier there is usually a paint system as the outside barrier. Fasteners are often installed with a wet sealant to minimize conductivity differences in the joint to avoid galvanic corrosion.

The breakdown of these barriers is often associated with abrasion or fretting of surfaces so as to destroy sections allowing the environment to impinge on the base metal. Clearance joints or loose fitting pins and bushing which allow movement with high contact stresses can lead to breakdown of the barrier. Also runway debris can chip away the barrier on the undercarriage and lower surface adjacent to the landing gear. Proper evaluation of this first phase of damage progression must, by reasons of the complexity, be determined by experience and by considerable in-service data.

Once the barrier is broken, a pit nucleates and the pit begins to grow. The effective stress concentration for a small pit is slightly greater than 1.0 as shown in Figure 6-2, (see Section 10 for the development of Figure 6-2), so the crack initiation time remains long. Also as the pit grows, the material that was at the base of the pit is "eaten away" by the corrosion action thus destroying the cyclic damaged microscopic material thereby zeroing out the cyclic damage. Kondo, Reference 2, refers to this as a competition between pit and fatigue crack growth. This phenomenon continues as the pit grows under the environmental conditions until it reaches a size that the effective stress concentration is large and crack growth rate fast enough that a fatigue crack actually forms and starts to grow. The transition from pitting growth to fatigue crack growth occurs when the fatigue crack growth outruns the pit growth.

Figure 6-2 Effective Stress Concentration



The development of the pit and the time for the pit to grow is basically a function of the environment and breakdown of the barriers to corrosion. For this reason the cyclic effect is often ignored during this phase.

Environmentally Assisted Short Crack Growth - Once the crack begins to grow, the short crack growth mechanism takes over. The short crack growth rate is influenced by the environment but mostly by the cyclic loading. The crack grows according to the small flaw theory until it reaches a 0.03 inch crack size. Starting with this damage phase, the time for a new pit to initiate at the bottom of a fatigue crack is so long that during this period of crack growth, further pit growth is usually ignored. As each cycle of loading produces some amount of crack growth, the next cycle comes before further pit development.

Environmentally Assisted Long Crack Growth - Linear elastic fracture mechanics again provides good agreement with observed crack behavior once the crack is larger than 0.03 inch provided one uses the environmentally affected da/dN curve. This region of crack growth is influenced primarily by the cyclic loading but the influence of the environment can be significant. This crack growth region extends till the critical crack size is achieved.

Environmentally Assisted Failure - Failure is controlled by the material's inherent fracture toughness, applied loading, crack size and geometry. The environment has little influence on the critical crack size.

7. Laboratory Simulation Techniques for In-Service Corrosion

Service testing or long-term simulated service testing in the laboratory is the only sure means to accurately determine the susceptibility, type and extent of corrosion of systems in service. However, such tests are not practical, and short term accelerated laboratory tests are used under controlled conditions to simulate service behavior. Accelerated corrosion test methods by definition are designed to approximate, in a short time, the deteriorating effect under normal long-term service conditions. Standardized ASTM tests have been developed for evaluating various types of corrosion observed in service such as general, pitting, crevice and exfoliation corrosion.

In the aerospace industry, accelerated laboratory corrosion tests have primarily been used for screening of materials and for quality control. The validity of these tests for generating corrosion metrics data for fatigue life prediction has not been verified. The selection of a valid accelerated laboratory test depends on the material to be evaluated and the type of corrosion to be simulated. The design of the components and assemblies are also important factors as their geometry and in-service maintenance actions provide additional sites and causes for inducing in-service corrosion.

The available accelerated corrosion test methods for corrosion simulation can be divided into non-electrochemical methods where no excitation is applied to the coupons and electrochemical methods where external excitation is applied. Electrochemical tests are

of great value in investigating almost all types of corrosion and aspects of corrosion behavior such as passivation and barrier coatings. These tests offer a direct measure of the kinetics of the corrosion process for a given material/electrolyte combination. In contrast, non-electrochemical tests, particularly the spray tests, have been in use a lot longer and are well suited for a comparative evaluation of the corrosion susceptibility of materials and coatings.

For aerospace applications, spray tests are used extensively to evaluate the corrosion susceptibility of alloys and coatings. Several atmospheric-type environments are currently being evaluated in spray corrosion tests with the intention of simulating service environments. The oldest and most commonly used of these is the neutral salt spray environment consisting of a 5% NaCl solution (ASTM B117). The SO₂/Salt spray test (ASTM G85, Annex 4) was developed to simulate the performance of alloys in aggressive environments such as aircraft carriers. The prohesion test (ASTM G85 Annex 5), a modified salt spray test that combines a wet-dry cycle with a dilute environment of lower Cl ion concentration, is already recognized as providing a more realistic simulation of corrosion attack in service (Reference 10).

Both electrochemical and non-electrochemical methods have been used to simulate corrosion in the laboratory. Unlike aluminum and stainless steel alloys, high-strength steel alloys such as 300M, AF 1410 and HP-9-4-30, which are commonly used to fabricate aircraft components, do not develop passive films and hence do not naturally and readily develop pits in corrosive environments. In such cases, electrochemical methods have been used to induce pits, as recently reported for example in bare D6ac steel (Reference 11). In alloys that do not naturally form pits, their formation in service is due to the breakdown of the corrosion protection system. This breakdown allows pit nucleation and growth in environments that will not otherwise promote pitting.

Non-electrochemical methods such as salt spray environments have been used to cause pitting in HP-9-4-30 steel protected by various coatings such as cadmium, electroless nickel, etc., (Reference 12). Without coatings and their breakdown, non-electrochemical methods will only cause general corrosion (red rust) and not discrete pits.

Superimposition of alternating wet/dry cycles during corrosion exposure has been shown to simulate in-service corrosion exposure better than continuous exposure tests. In the HP-9-4-30 steel corrosion study cited above, the exposure was alternated with baking and freezing of the coupons. The accelerated corrosion test, designated GM9450P, used by General Motors provides a combination of cyclic conditions (salt solution, various temperatures, humidity and ambient environments) and is used to evaluate assemblies and components (Reference 13). This test is effective for evaluating a variety of corrosion mechanisms. The test durations can be individually tailored to achieve any desired level of corrosion exposure.

The need for the development and validation of reliable accelerated corrosion tests for simulating corrosion and generating metrics for life prediction cannot be overstated. In

this context, there continues to be a need to evaluate and validate corrosion simulation tests, test environments and corrosion characterization methods.

Assumptions in Simulated Corrosion Testing - In order to make calculations on the effects of corrosion, at least three assumptions have been made. First, there is an assumption that the development of the pit is independent of the cyclic load. The second is that one can take the pit geometric size parameters and determine its time to fatigue crack initiation. Lastly this time to crack initiation is based on the cyclic loading and the effective K_t of the pit.

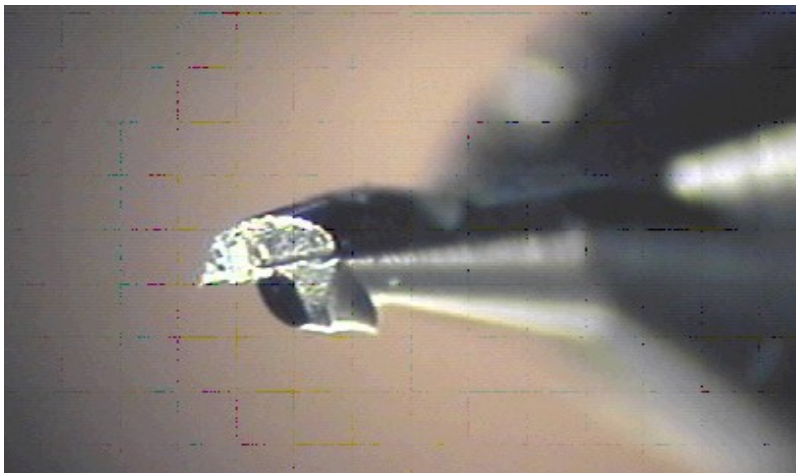
The specimens that are presently being tested by NAVAIR under this program and those described in Section 9.1 are really tests of *Previously Corroded Specimens*. At the time that the cyclic test was begun the specimens were taken out of the environment and all pit growth was stopped. The pits sizes that existed at the time they were taken out of the environment thus determines the times to initiate a 0.01 inch crack. The inherent assumption is that the cyclic crack growth rate will dominate. While this may be true for the largest pits it will likely not be true for the smaller pits.

8. Potential of Micro-machining to Simulate Corrosion

Micromachining of simple geometric features was investigated as a potential technique to simulate corrosion. Mechanical micro milling and laser micro machining were examined for their potential feasibility.

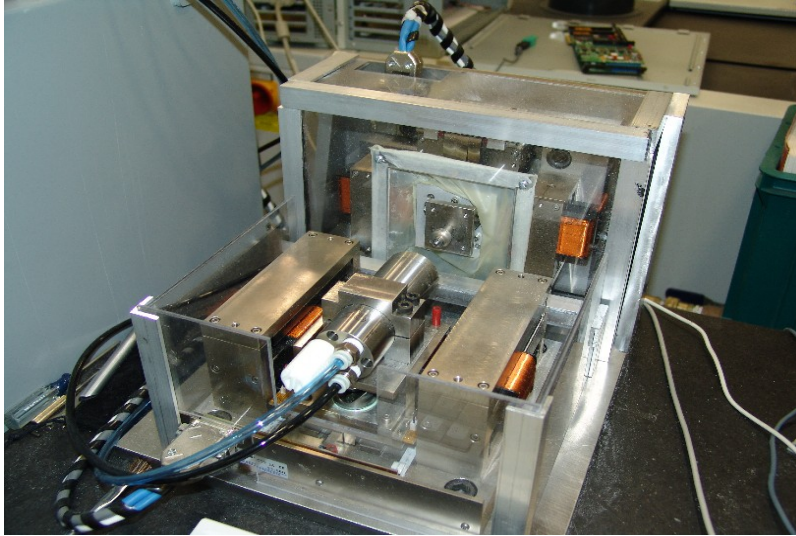
Mechanical micro milling is a relatively new process with several types of meso-scale to micro-scale milling machines commercially available. Micro milling is performed by rotating a carbide cutting tool and cutting and removing material to form the desired shapes in a finished part. The micro-scale processes are similar to large scale milling operations, except the machine accelerations and spindle rotational speeds are much higher than large-scale machines. Currently, carbide cutting tools are commercially available down to 5 microns in diameter (See Figure 8-1).

Figure 8-1 Micro End Mill 250micron diameter



High speed air turbine, air bearing spindles operate up to 250,000rpm with 150,000rpm commonly available (See Figure 8-2).

Figure 8-2 High Speed Mechanical Micro Milling Machine



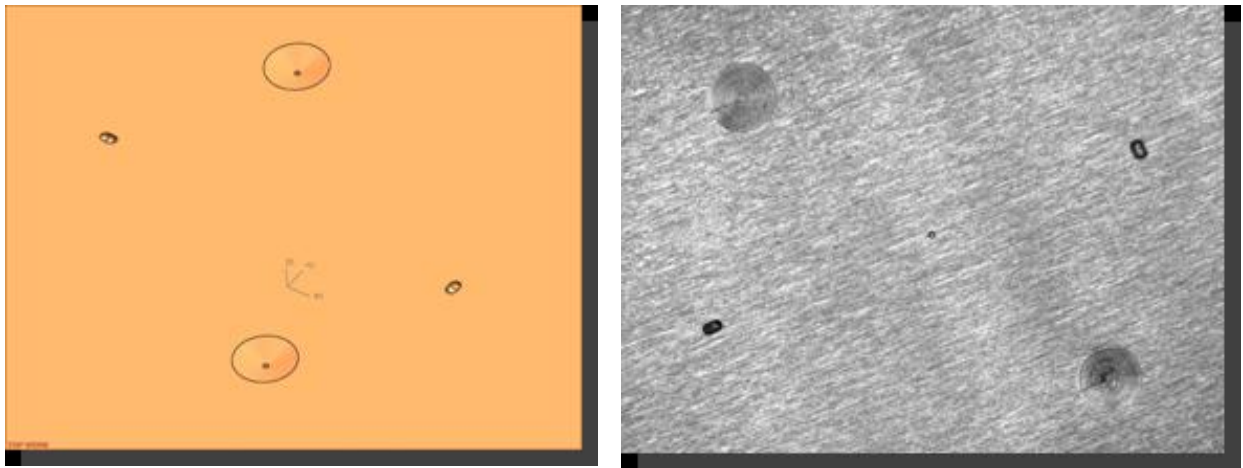
These tools and machines can be used to generate simple geometric features such as holes, dimples or internal or external conic sections on the order of 50 to 500 microns in size (See Figure 8-3).

Figure 8-3 Micro-machined Gear on a Penny



We micro-mechanically milled AF 1410 steel coupons with conical, cylindrical and spherical geometrical features using 0.005 in. (125 microns) radii tools. Five samples were machined to test the reproducibility of the process. Figure 8-4 shows the solid model and a photograph of the micro-machined features. The features were characterized by UDRI using white light profilometry.

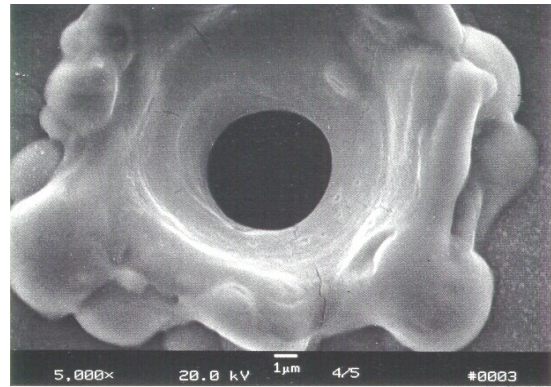
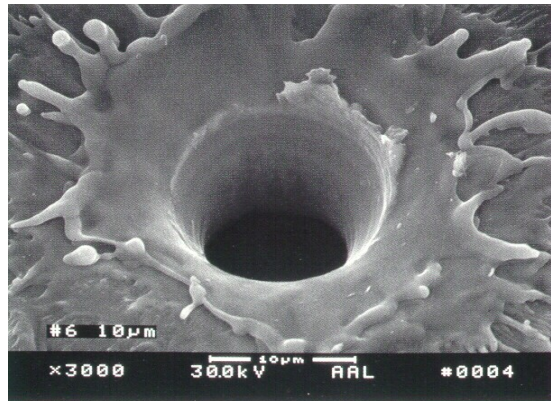
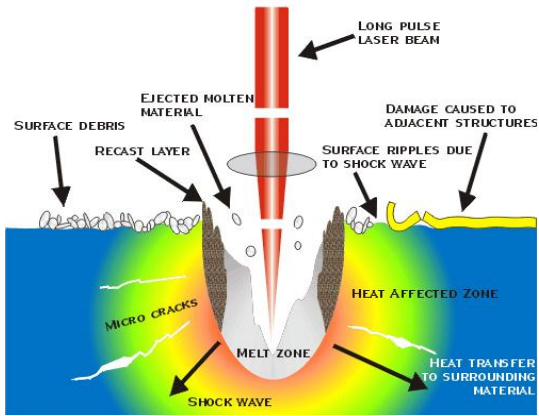
Figure 8-4 Micro-machined Features on AF 1410 Steel



Laser micro machining machines and techniques are also commercially available. Laser machining ablates or vaporizes material to facilitate material removal. High energy density is achieved by focusing to a small spot size and pulsing the laser. Higher frequency pulses result in higher energy density and a smaller spot size. Lower energy density typically results in higher material removal rates, but larger heat affected zones and reduced precision. Lasers are currently available with pulse trains in the Femto second scale. Features can be laser micro-machined to similar length scales as the mechanical micro milling operations (See Figure 8-5). Both machining operations could potentially leave residual stresses in the machined surface that might influence fatigue. The mechanical cutting operations generate surface heating and localized melting as well as mechanical compression of the machined surface. The mechanical milling-induced residual stresses are typically lower for sharper cutting tools, but for micro machining the relative sharpness of the cutting tools is typically much less than macro-milling tools. The laser ablation of the surface creates localized heating, which is typically much smaller for higher energy densities. The machining-induced stresses are usually isolated to a thin surface layer can typically be removed with light chemical milling. When studying fatigue behavior or mechanical properties, these machining-induced surface residual stresses may have an effect.

The scale of the corrosion features may be smaller than current micro-machining capabilities and the machining-induced residual stresses may corrupt a corrosion and fatigue life study. Further review of these issues is necessary for determining the feasibility micro machining techniques to simulate corrosion.

Figure 8-5 Laser Micromachined Features
(Courtesy University of Missouri Rolla: Hai Lung Tsai)



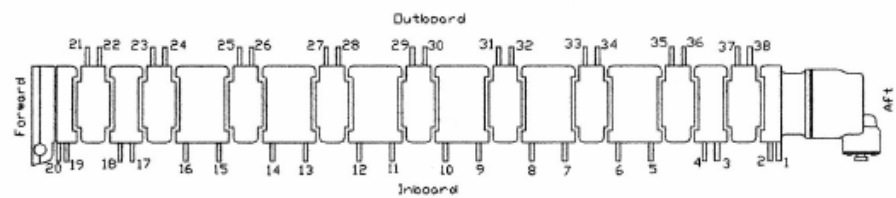
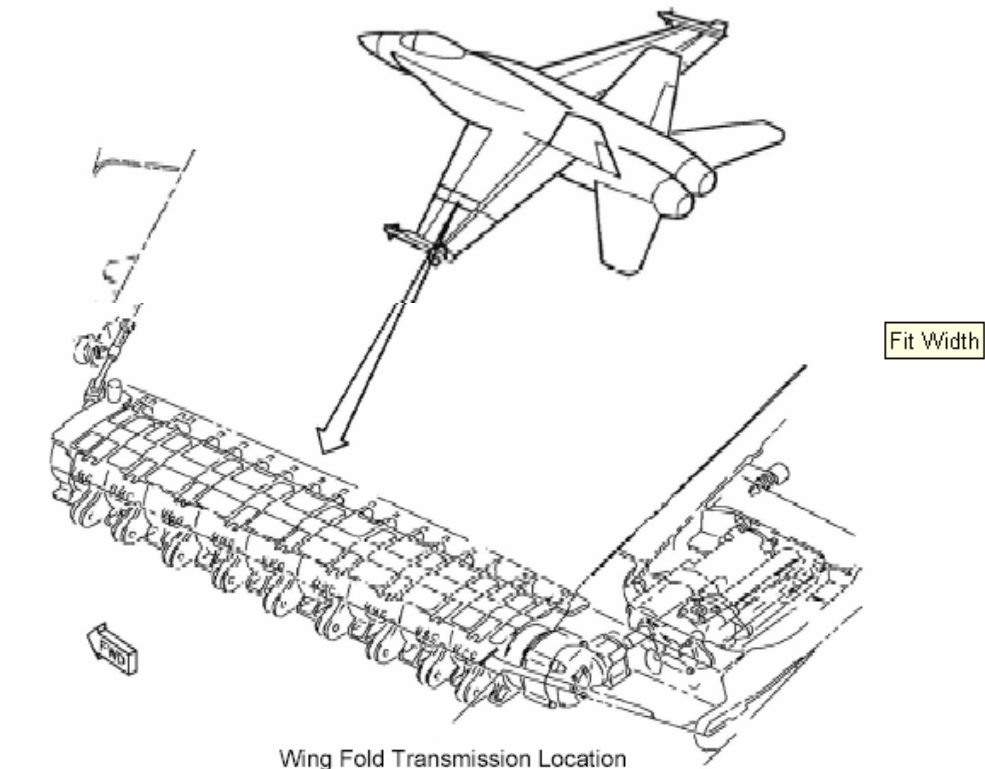
9. In-Service Experience of Steel Corrosion

A survey of Boeing St. Louis engineering organizations was made to determine instances of corrosion of steel structure in service aircraft. Corrosion of steel parts has been found on: the F-15 nose landing gear cylinder; the F/A-18 shock strut cylinder; the F/A-18 arresting hook; the F/A-18 main landing gear lever; and the F/A-18 wingfold transmission. While none of these parts have failed such that an aircraft has been lost, they have lead in to in-service inspection and maintenance and in some cases failure has caused secondary damage. Corrosion in the F/A-18 arresting hook has led the USN to aggressive inspections and repairs due to criticality of this structural element, even though there are no reported instances of a fatigue crack emanating from the corrosion. Several engineering investigations have been made of corrosion of the F/A-18 wingfold transmission that will be summarized in the following paragraphs.

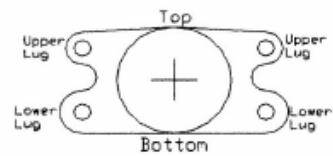
Wingfold Transmission - Data obtained from prior work conducted by NADEP North Island, Allied Signal, and Boeing under separate contract, References 14-16, may serve as a basis for follow-on work with UDRI/USN/USAF.

The wing fold transmission housing / lugs are HP 9-4-30 Steel, heat treated to 220 KSI. The location of the wing fold transmissions and the lug numbering system used are shown in Figure 9-1. As reported in Reference 14, three lugs failed with fatigue crack initiation from corrosion pits at the lug hole. See Figure 9-2 for the conditions of the corrosion on the lugs. No material anomalies were detected other than the cadmium plate protection was worn / corroded away from the lug hole areas. Further, the absence of chlorine and high sulfur content within the corrosion byproduct material indicates a unique corroding ion: sulfide. Sulfides have been known to greatly accelerate pitting corrosion in steels.

Figure 9-1 Wingfold Transmission



WingFold Transmission P/N 2022308-7/8-1/3 (viewed from above)



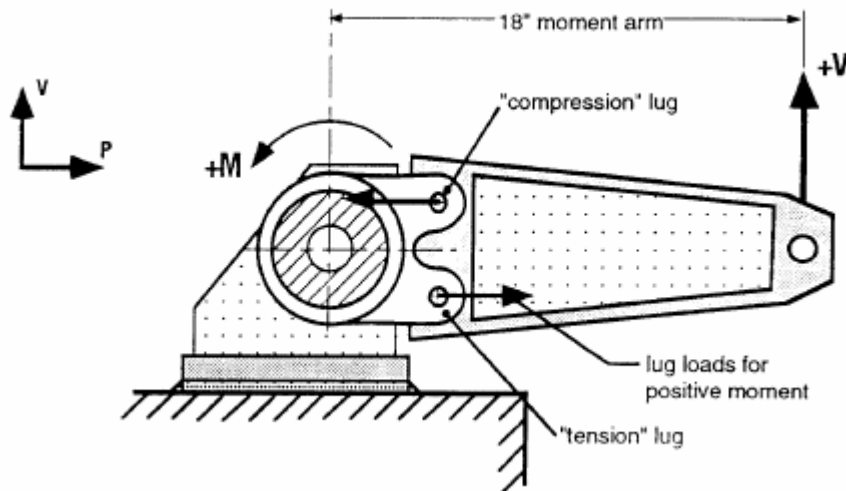
Wing Fold Transmission Lug Identification - TEI F18-0002-01

Figure 9-2 Corroded Transmission Lugs



A fatigue assessment was undertaken on the F/A-18 program to evaluate the effect of corrosion on the fatigue life of the wing fold transmission parts. Included were tests of baseline non-corroded parts, corroded parts that had seen approximately 10 years of service, and corroded parts that had been repaired. The tests were conducted at Allied Signal Aerospace the subcontractor for the transmission. The complete discussion of the testing is contained in an Allied Signal Report 93-67123, Reference 16. All specimens were tested using the F/A-18C/D usage spectrum in the test fixture shown in Figure 9-3. The spectrum or profile represented 300 equivalent flight hours with 20 profiles equal to one service life (i.e. 6000 hours). Each specimen was tested to failure or until a crack developed sufficient to cause the test stand deflection and/or load to exceed established limits.

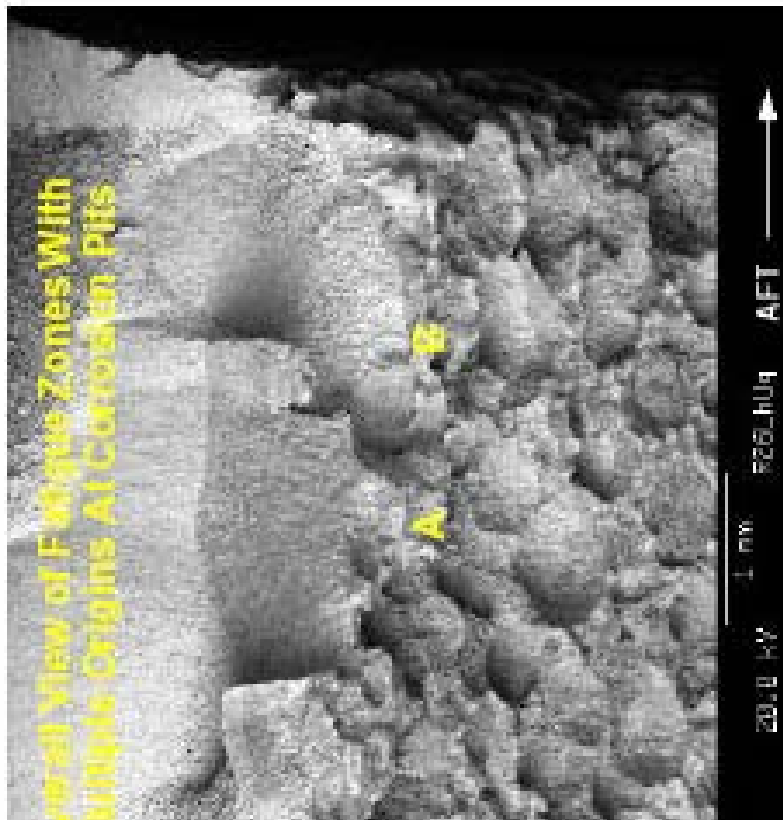
Figure 9-3 Element Test Fixture



10. Effective Stress Concentration Factor

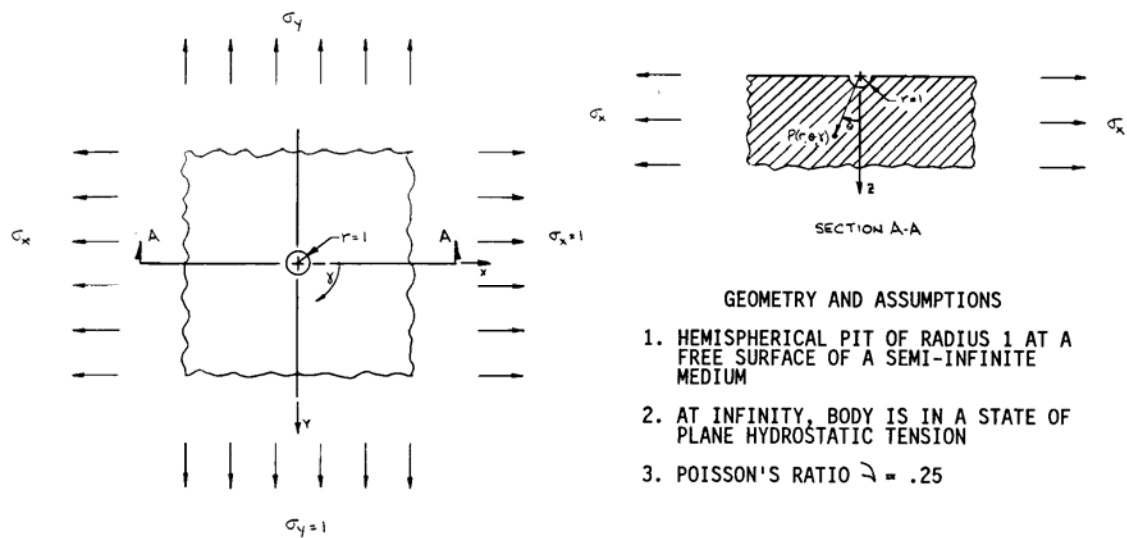
In an attempt to characterize the effectiveness of pits as a stress concentration, work from R. A. Eubanks and R. E. Peterson were combined. Eubanks of the Illinois Institute of Technology developed the stress concentration of a hemispherical pit at the free surface of a semi-infinite solid. Reference to Figure 10-1 shows that simulation of corrosion with a hemispherical shape is reasonable.

Figure 10-1 Pits on Lug Hole Wall Surface



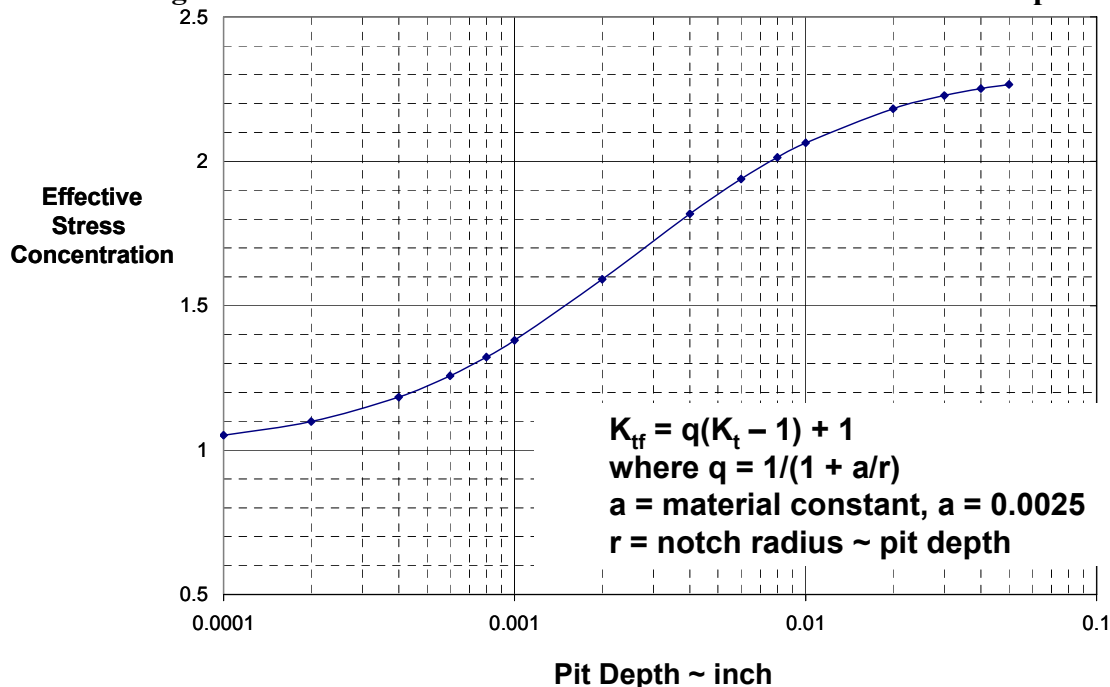
The solid is in a state of plane hydrostatic tension as shown in Figure. 10-2 and a Poisson's ratio of 0.25. Eubanks found the maximum stress to occur at the bottom of the pit and to be 2.23 times the body stress. At one radius away from the bottom the stress concentration was reduced to 1.04 so the stress gradient is very steep.

Figure 10-2 Stress Concentration of a Hemispherical Pit



Use of the elastic stress concentration has been found to over predict fatigue damage due to an effect of notch sensitivity. Peterson discusses notch sensitivity in his Book ***Stress Concentration Factors***, Reference 17. Figure 10-3 shows the use of his notch factor equation to determine an effective stress concentration as a function of pit depth assuming the hemispherical pit. A material constant of 0.0025 for quenched and tempered steel as suggested by Peterson was used in the equation shown in Figure 10-3 to arrive at the effective stress concentration as a function of pit depth. For very small pits the stress concentration is ~ 1.0 and for large pits the stress concentration is ~ 2.33 .

Figure 10-3 Effective Stress Concentration as a function of Pit Depth



11. Software Tool for Profilometry Roughness Analysis

The development of corrosion metrics based on profilometry data required some sort of tool for processing the raw data, applying various levels and types of filtering, and computing the standard suite of roughness parameters. A generic tool that would allow the flexibility to create new metrics was not available, so a Java application was developed that would provide the foundation upon which a complete profilometry analysis tool could be built. The current tool has some basic functionality and can be easily modified to include new capability. Figure 11-1 shows a screen shot of the main GUI configured for the analysis of a data file from Solarius.

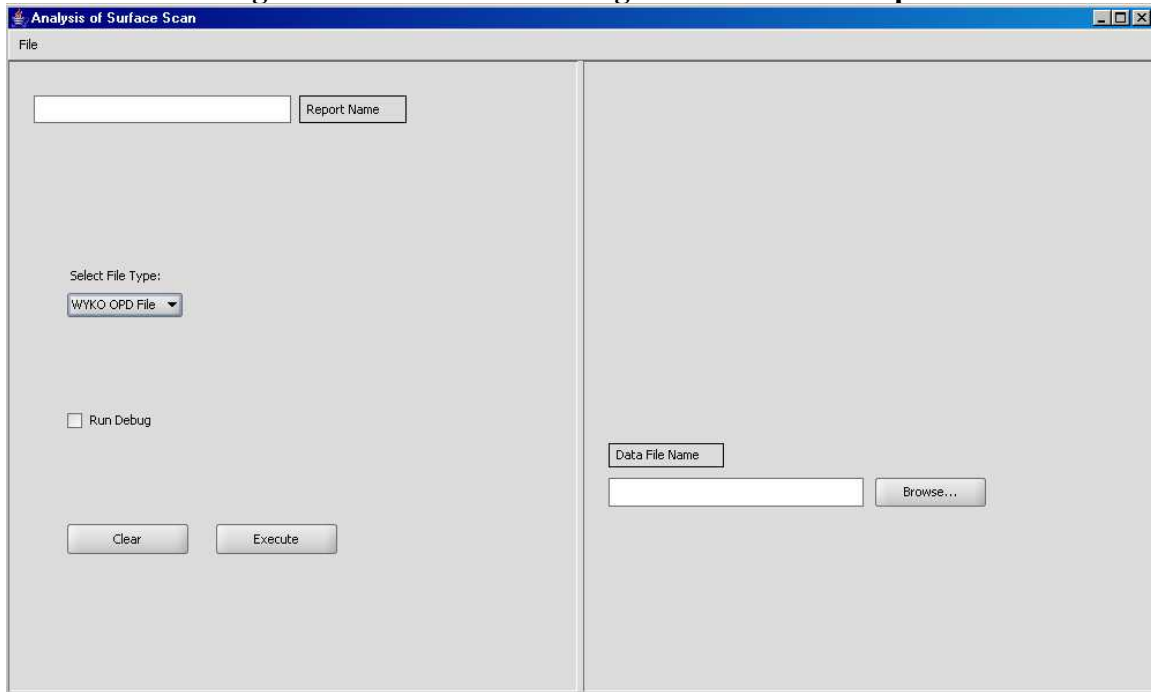
Figure 11-1 Surface Scan of Solarius File

The screenshot shows a Java GUI titled "Analysis of Surface Scan". The interface is split into two main sections. The left section includes a "Report Name" text field, a "Select File Type:" dropdown menu currently showing "Solarius File", a "Run Debug" checkbox, and "Clear" and "Execute" buttons. The right section contains several input fields: "Beginning Line Number" (0), "Ending Line Number" (500), "Number of title lines" (4), and "Number points per scan line" (501). Below these are three dropdown menus for "Size of x increment" (10 cm), "Size of y increment" (10 cm), and "Units of z measurements" (cm). There are also radio buttons for "XY" and "Raw" (which is selected), and a "Data File Name" text field with a "Browse..." button.

Figure 11-2 Surface Scan of Solarius File

The files from Solarius are text files and come in two variants. There is a radio button that allows the user to specify which type of file is under consideration. The WYKO profilometry instruments produce a binary file which is much different from that received from Solarius. The main GUI configured for the WYKO file input is shown in Figure 11-2. The only input required for the WYKO case is the file name as all the descriptive information is contained in the file itself.

Figure 11-3 Main GUI Configured for WYKO Input



The profilometry file is processed to determine the waviness and roughness components of the surface. This is accomplished using a 0.8mm cutoff wavelength Gaussian filter. The standard suite of roughness parameters, (see Section 3 for a discussion of these parameters), for the resulting surfaces is computed and displayed in a text report. In addition to two dimensional views of the various surfaces, a three dimensional view is generated that can be rotated to allow a unique perspective to be obtained on the nature of the surface being analyzed.

The leveled profile is shown in Figure 11-3. The results of the Gaussian filtering are shown in Figure 11-4 and the three dimensional view is shown in Figure 11-5. The three dimensional view allows the user to rotate the image to get the clearest view of the corrosion features.

Figure 11-4 Leveled Profile

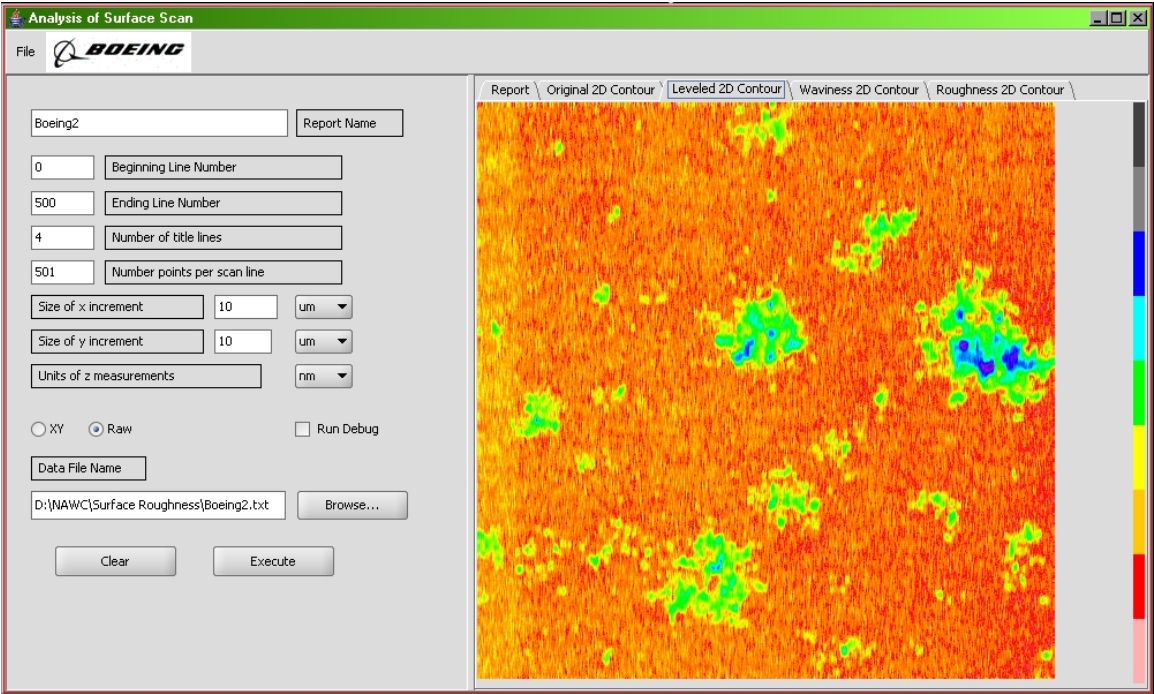


Figure 11-5 Filtered Profile

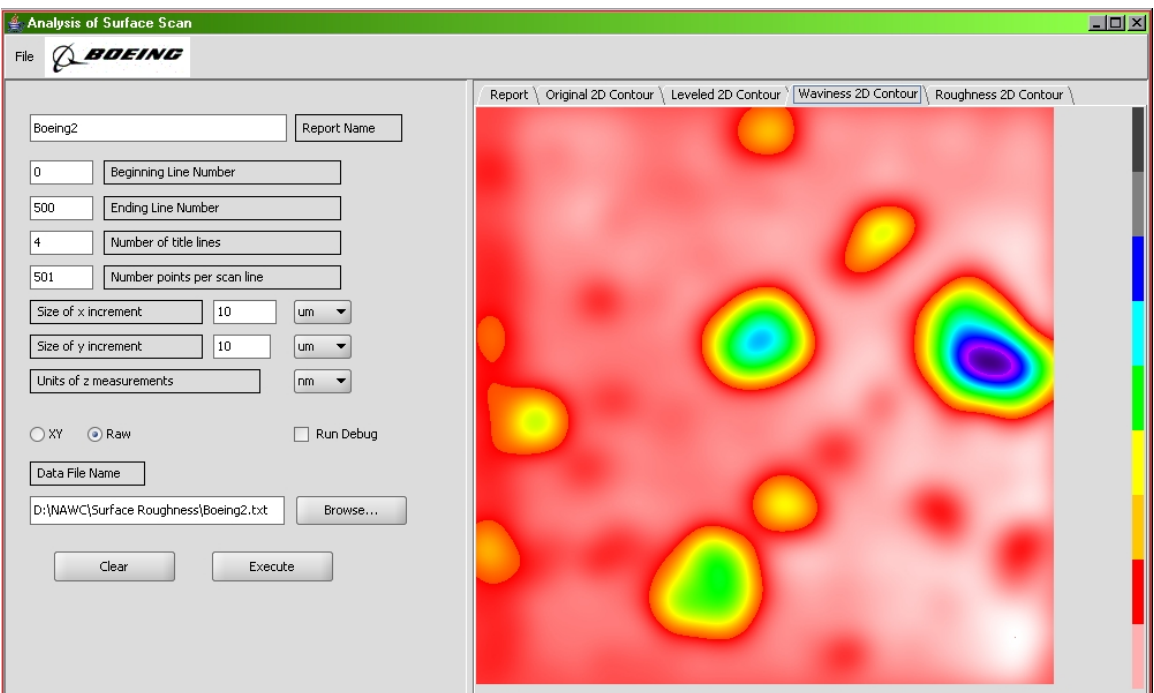
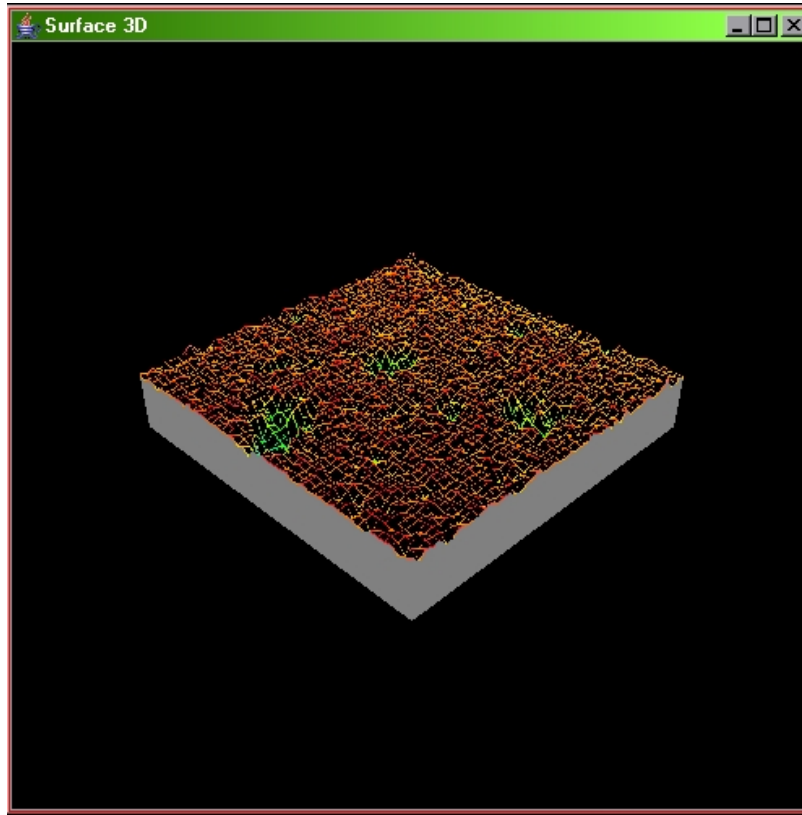


Figure 11-6 Three Dimensional View



Several additional features could be added to make the tool provide more comprehensive output. These additional features include: flexibility in the selection of filtering types and cutoff frequencies; and Fast Fourier Transform analysis capability. It is recommended that these additions be considered for future work to provide the greatest capability to generate metrics that can be correlated with fatigue life.

Work on this tool was stopped in view of the program's decision to use the ImageJ software and the suite of associated plug-ins that provide a rather complete range of filtering and roughness processing. All corrosion metric development was conducted with the ImageJ program.

12. Corrosion Metric Development

Correlations between measures such as the surface roughness, deepest valley and highest peak and the lives of fatigue specimens at various stress levels were performed to determine if a metric for corrosion can be obtained based purely on the geometry of the corrosion. Our initial work began with the complete images as we received them from UDRI, however, we noticed some roughness values that did not correlate well to the overall pattern in the data. Upon closer examination, it was noted that the scanned

images covered an area of the coupon the encompassed the corroded spot as well as a significant portion of the uncorroded plate. This is shown in Figure 12-1.

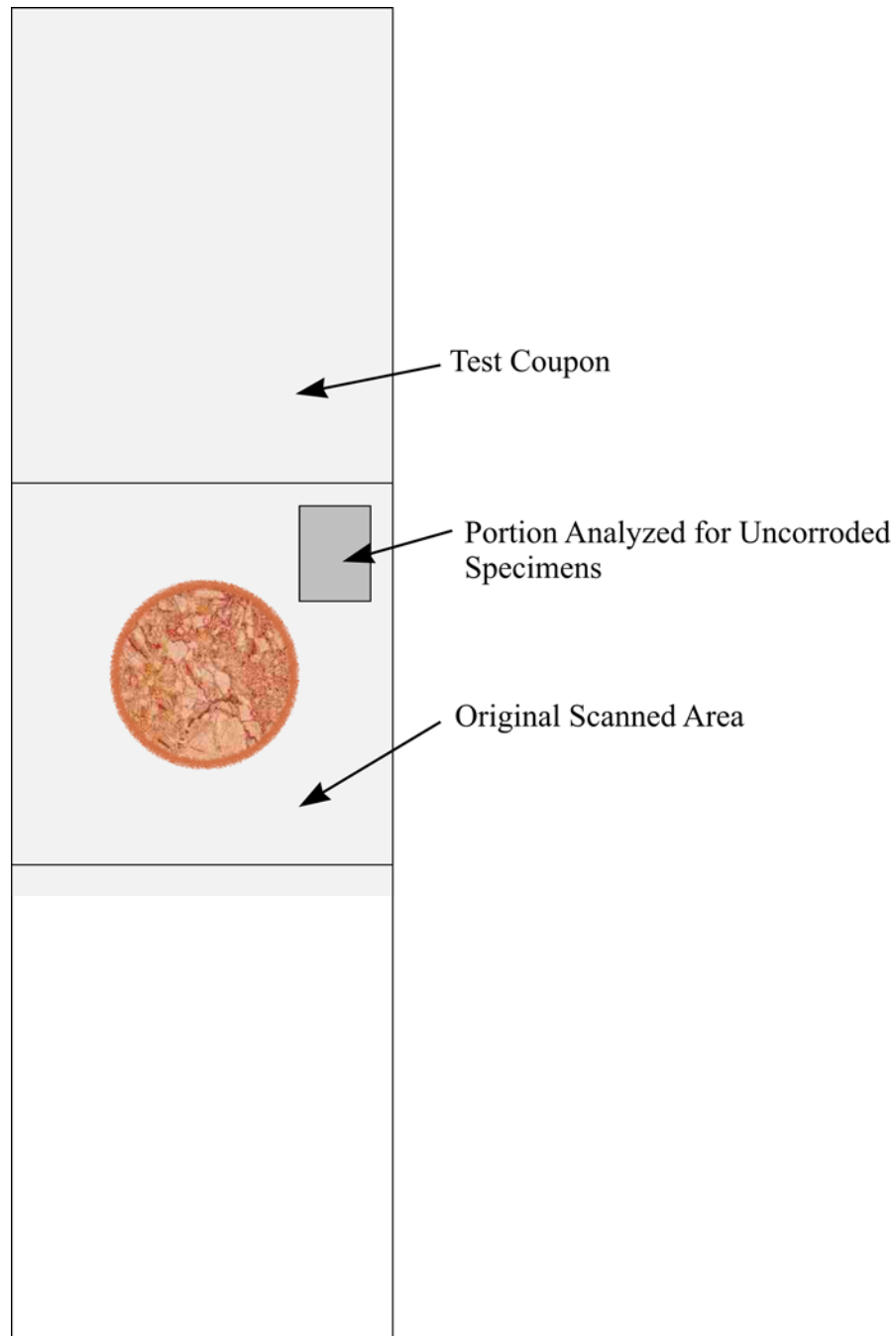


Figure 12-1 Coupon Showing Overall Scanned Area

Several smaller regions were examined and the data was compared. The regions examined were the four quadrants inside the corroded surface, the center quadrant-sized area, the largest inscribed square and the smallest circumscribed square. This is illustrated in Figure 12-2.

In most cases it was found that the interior measurements were the same, within about 1%. In two cases, in particular for specimens 16 and 66, the UDRI measurements were higher than the center measurements that we reported. Upon closer examination, our inscribed square and circumscribed square measurements were vastly different and the latter measurement corresponded to the UDRI measurement much more closely. This seems to be due to the very aggressive corrosion in the circular boundary where a crevice effect seems to be present. In all cases it appeared that the center quadrant measurements were equivalent to the average of all the interior measurements. We decided that this measurement would be used as representative of the specific corrosion morphology.

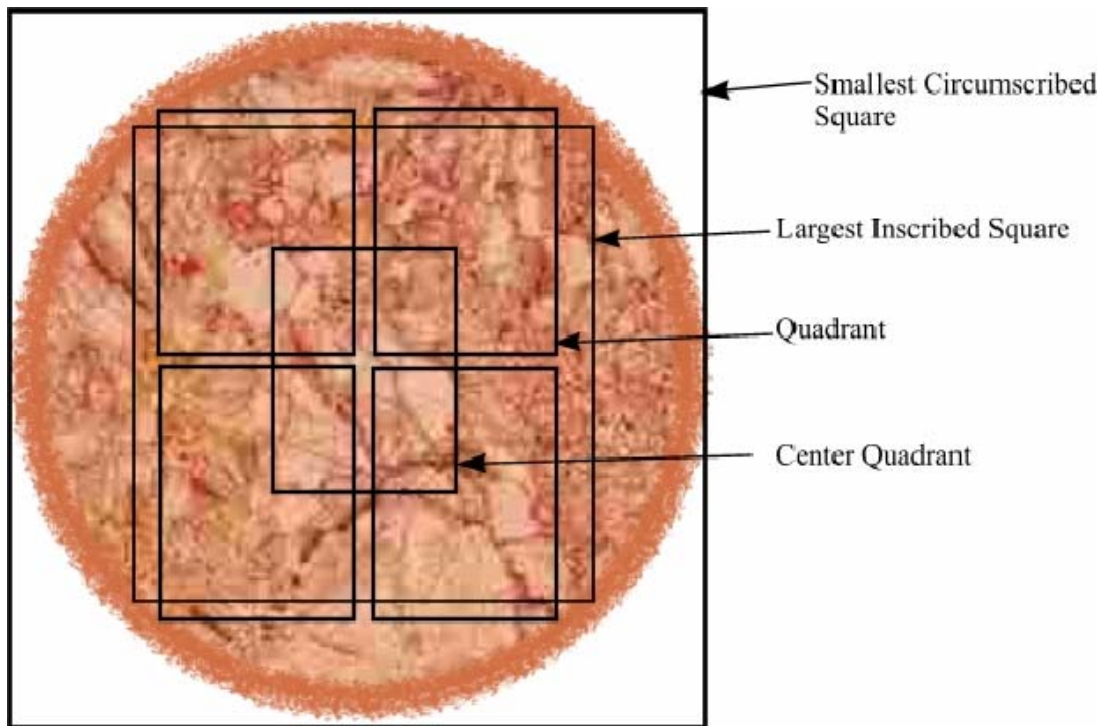


Figure 12-2 Detail of Corrosion Spot Showing Areas Used in Roughness Analysis

We observed anomalies in the plot of the unfiltered data from specimens tested at 160 ksi. This is clearly seen in Figure 12-3 where some of the specimens corroded for 3 hours showed very deep valleys but had essentially the same fatigue life as the specimens without such features. Subsequent filtering removed the anomalous data. In addition, there was no difference in fatigue life between the non-corroded specimens and those corroded for 3 hours.

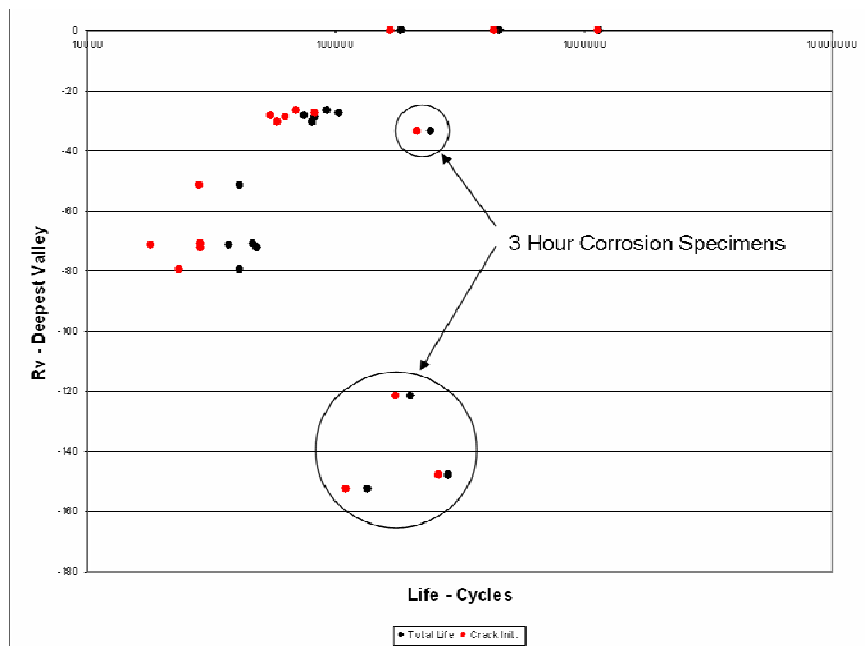


Figure 12-3 Rv versus Life for Specimens Tested at 160 ksi – Unfiltered Data

Figure 12-4 plotted with filtered data, also shows similar results, except that the specimens corroded for 3 hours fall in a more appropriate range. The uncorroded data was plotted against average roughness parameters that were obtained by characterizing an uncorroded portion of the images from the other cases. The values from

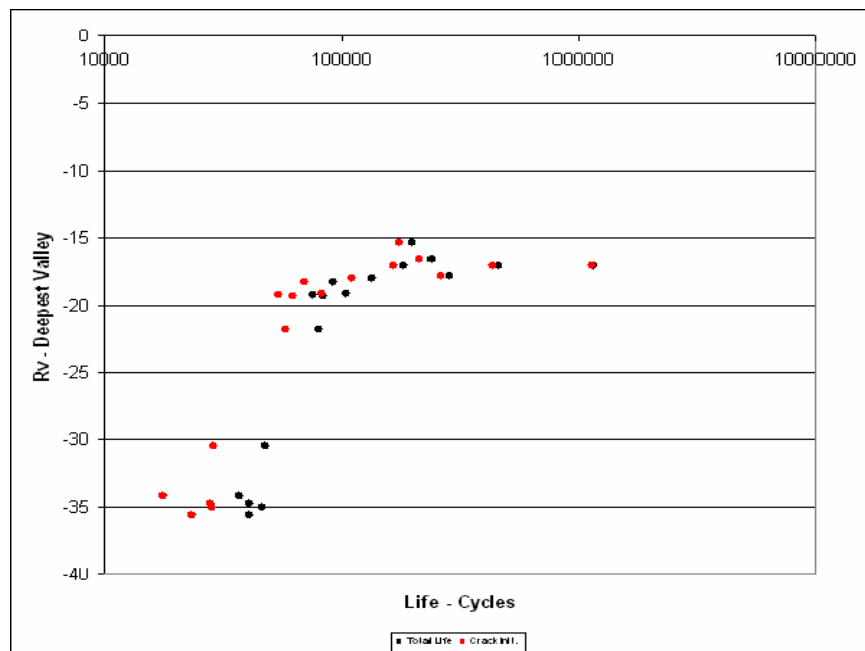


Figure 12-4 Rv versus Life for Specimens Tested at 160 ksi – Filtered Data

Filtering had a significant impact on the Rv and Rp values (the lowest valley and the highest peak). However, the overall roughness values, Ra, were not significantly affected. Figure 12-5 shows a plot of the roughness versus the fatigue life for the specimens tested at 160 ksi.

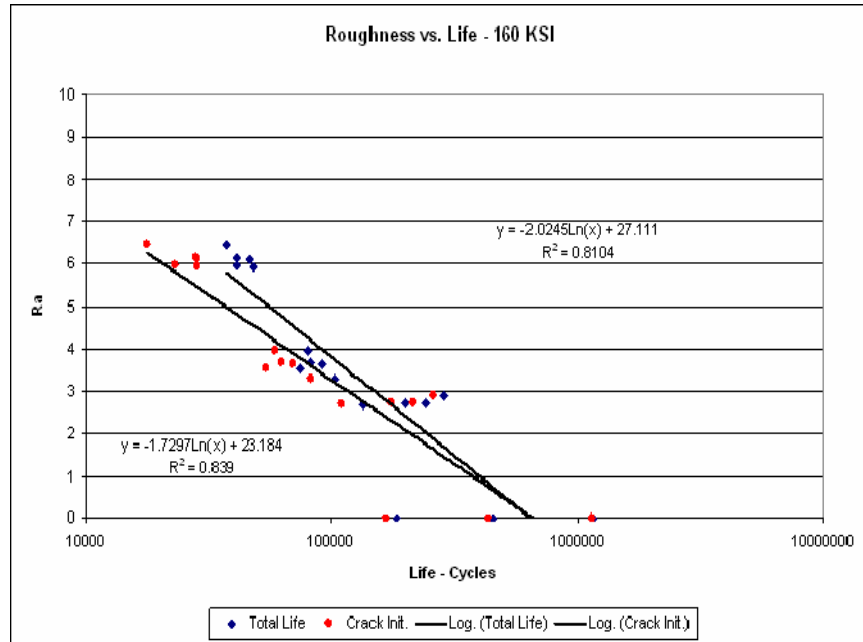


Figure 12-5 Ra versus Life for Specimens Tested at 160 ksi – Unfiltered Data

It should also be noticed that the values for the non-corroded specimens were plotted at a roughness value of zero and do not seem to fit the trend of the other data as well. The slopes of the two trend lines are very similar between the crack initiation life and the total lives. This would be expected as the cracks that initiate earlier would reach final failure earlier as well. Improvements of the results resulting from data filtering are shown in Figure 12-6

The values for the non-corroded specimens were set to the average that was obtained for the non-corroded areas of the corroded specimens. The area used to obtain these measurements is shown in the schematic in Figure 12-1. The data in Figure 12-6 is plotted with a linear trend line to provide a direct comparison to the unfiltered data in Figure 12-5. The same data is also plotted in Figure 12-7 with a power curve fit. While neither of these two fits is ideal, the analysis demonstrates a potential for roughness analysis parameters to be further explored to obtain a definitive corrosion metric.

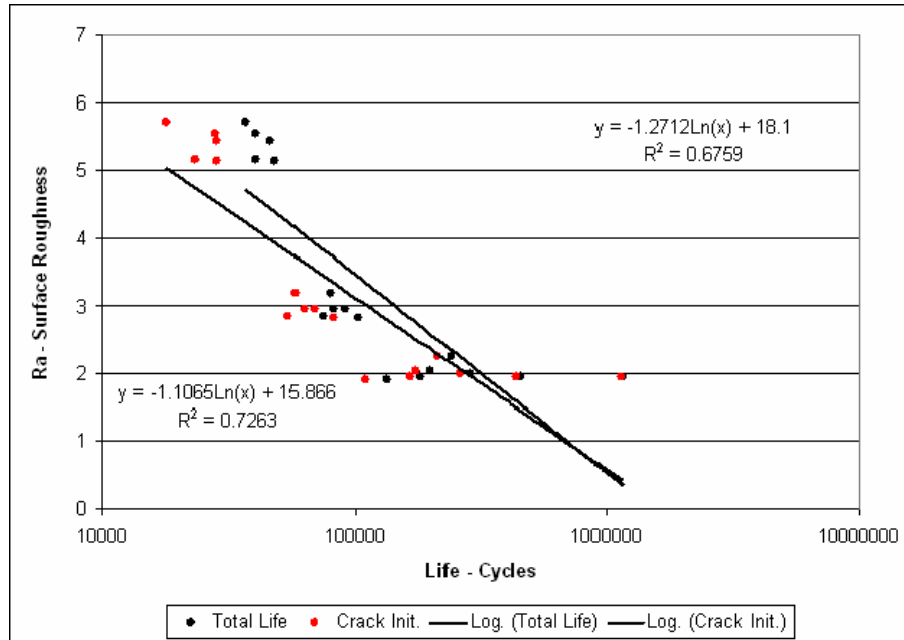


Figure 12-6 Ra versus Life for Specimens Tested at 160 ksi – Filtered Data

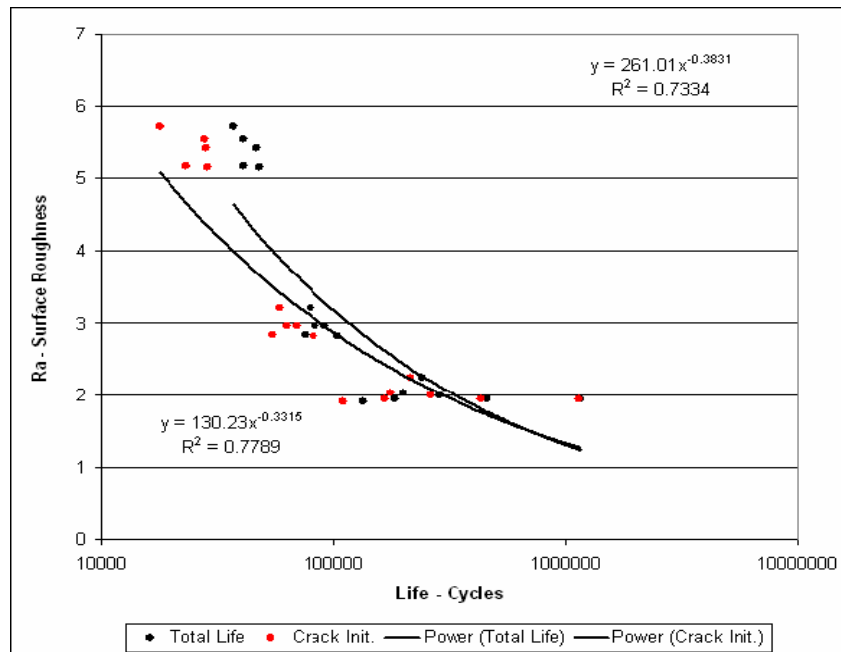


Figure 12-7 Ra versus Life for Specimens Tested at 160 ksi – Filtered Data and Power Curve Fit

Very similar behavior is seen in the 180 ksi plot of life versus roughness. This is shown in Fig. 12.8. The base value of the curve fit is different, as you would expect due to the decrease in nominal life as stress is increased, however, the exponent on the power curve is very similar.

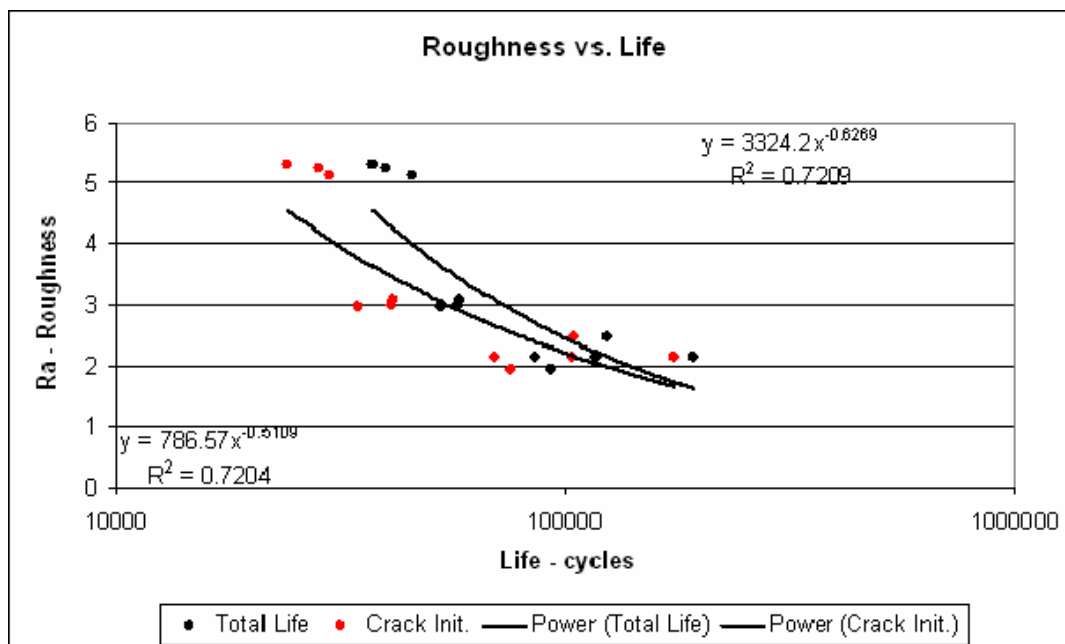


Figure 12-8 Ra versus Life for Specimens Tested at 180 ksi – Filtered Data and Power Curve Fit

The corrosion roughness shows promise as a metric. Additional work is required to correlate it more fully with life and to explore the implications of some of the other roughness measures such as Rv, the deepest valley. In some cases an average of the 10 deepest points is used as a measure, which may give a better idea of the extent of more serious corrosion.

13. Round Robin Evaluation of Fractured Specimens:

Fractography of AF1410 corrosion fatigue specimens 19, 27, 30, 39, 49, 50 and 55 using optical microscopy has been completed for determining crack initiation. The cycles to initiate a 0.01” size flaw determined from this characterization are shown in the following table along with the values obtained by NAVAIR on the same specimens. There is excellent agreement between the two sets of measurements.

Specimen #	Corrosion exposure (hours)	Maximum Stress (ksi)	Cycles for 0.01” Crack Determined by Boeing	Cycles for 0.01” Crack Determined by NAVAIR
19	None	165	136,832	137,386
49	None	165	99,074	99,467
50	None	165	80,443	80,250
39	None	200	56,545	56,961
55	None	200	45,573	45,673
44	None	200	52,985	47208
27	12	200	3,704	
30	12	200	7,515	6,735
65	12	200	5,641	3,484

Figures 13-1 through 13-9 show the fracture surfaces of the nine specimens.

Figure 13-1 Fracture Surface of Specimen 19

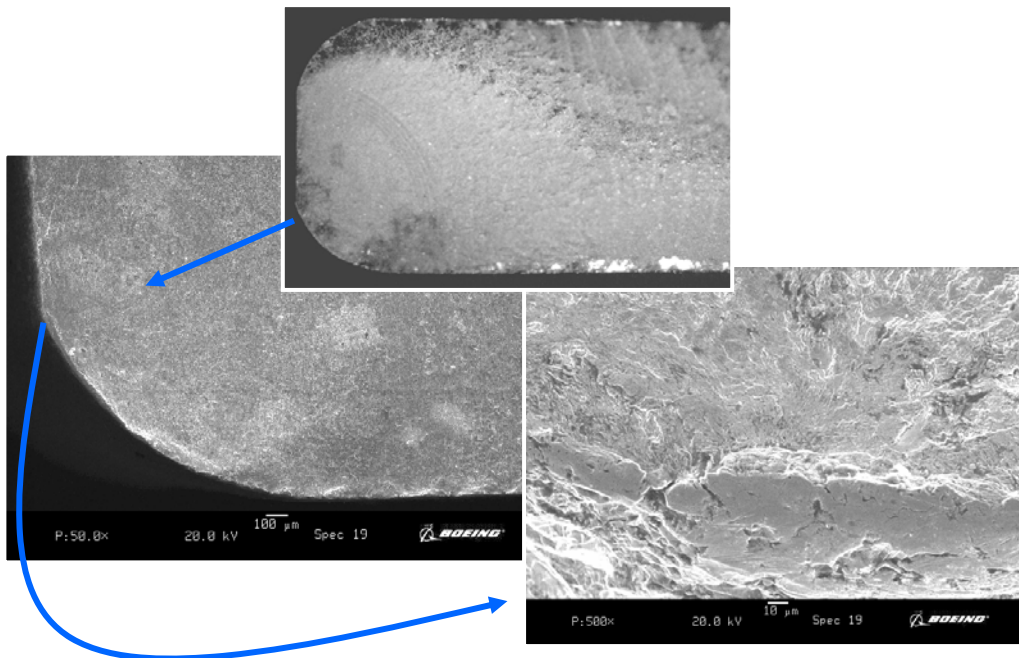


Figure 13-2 Fracture Surface of Specimen 27

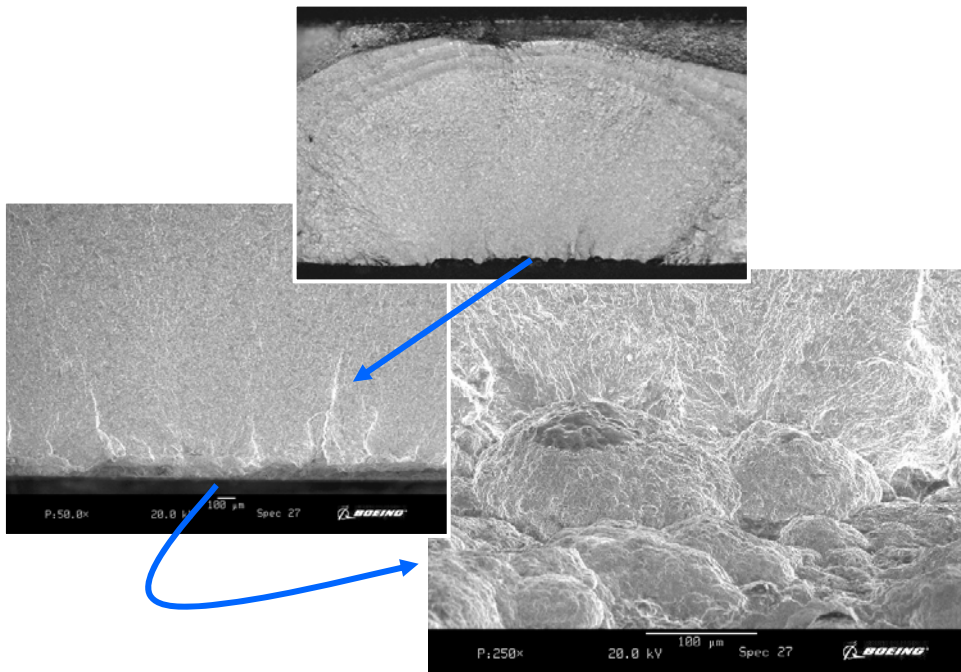


Figure 13-3 Fracture Surface of Specimen 30

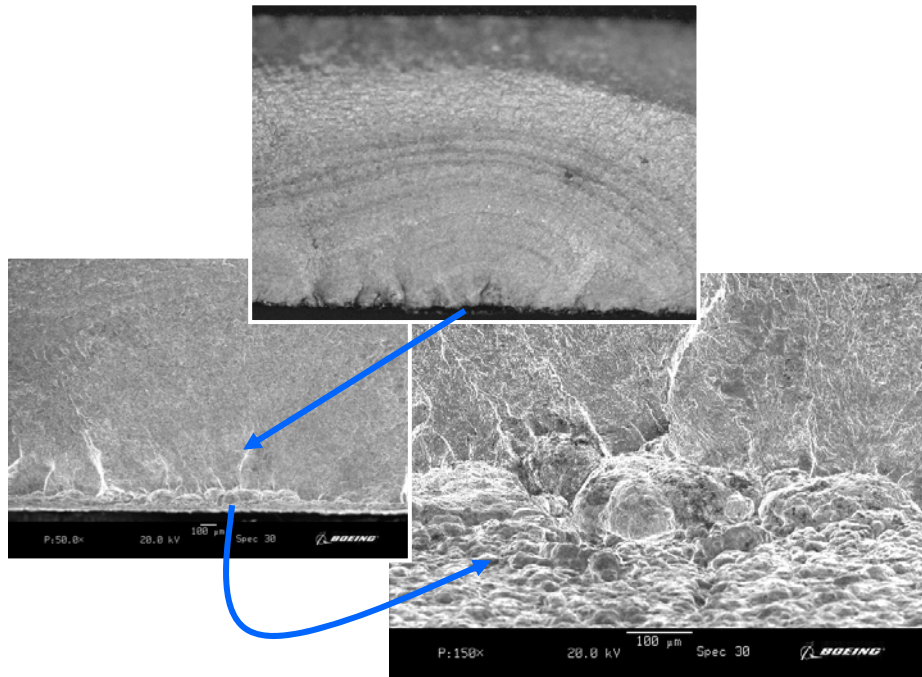


Figure 13-4 Fracture Surface of Specimen 39

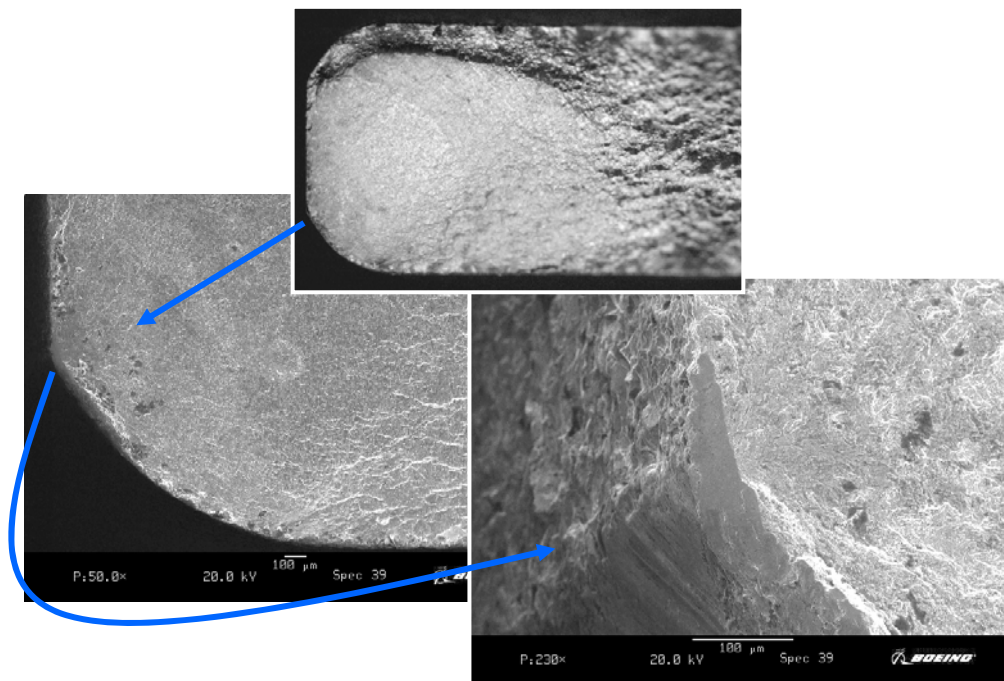


Figure 13-5 Fracture Surface of Specimen 44

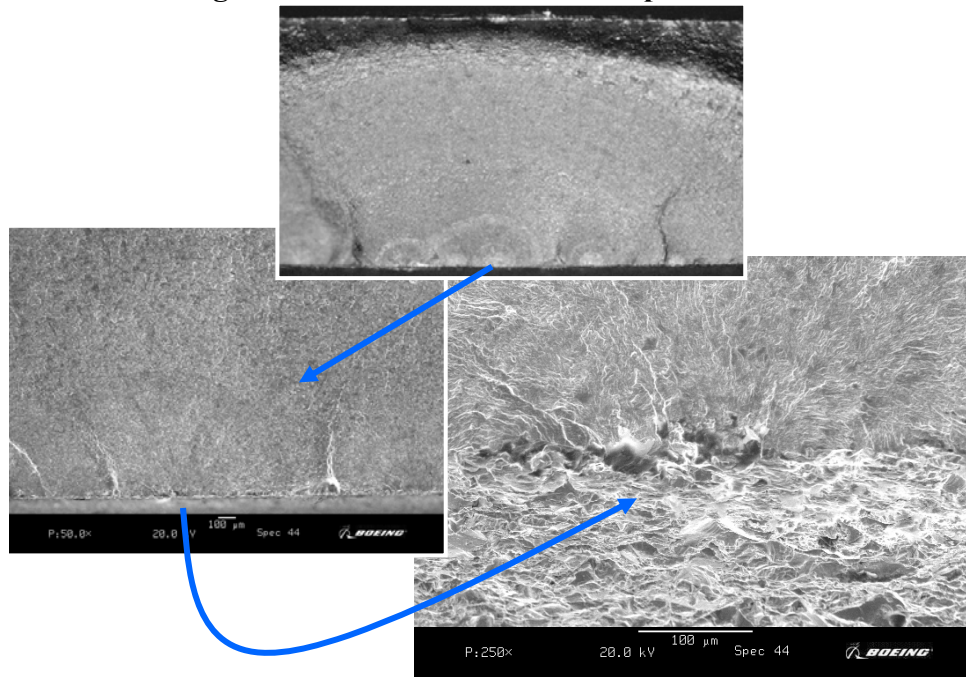


Figure 13-6 Fracture Surface of Specimen 49

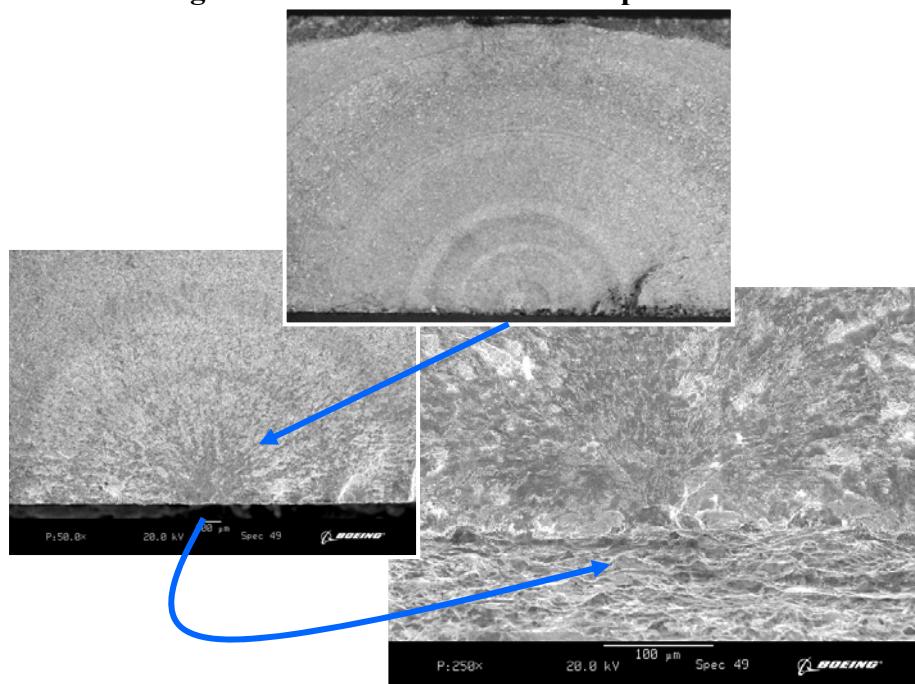


Figure 13-7 Fracture Surface of Specimen 50

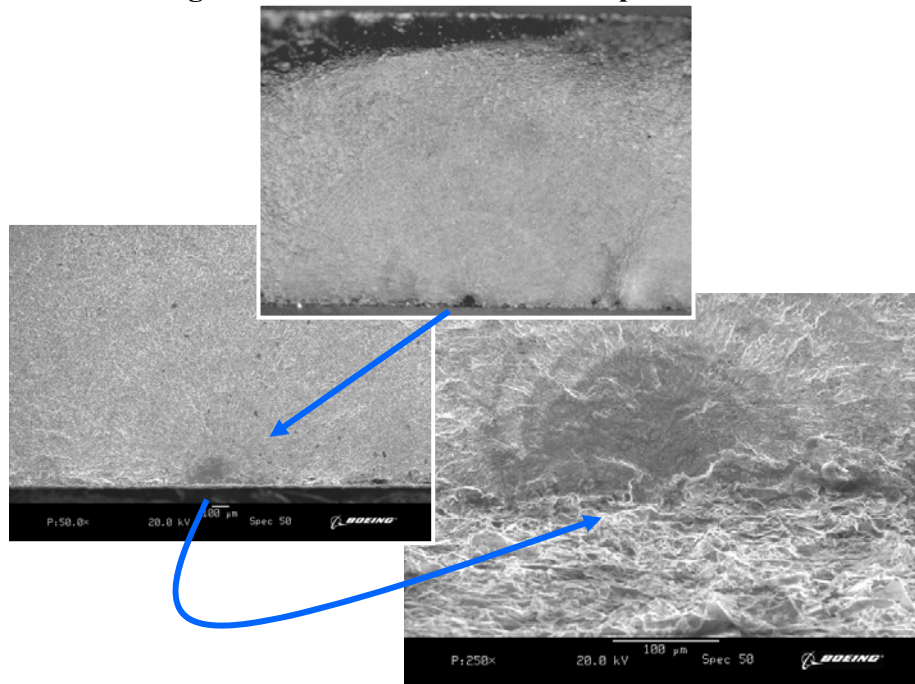


Figure 13-8 Fracture Surface of Specimen 55

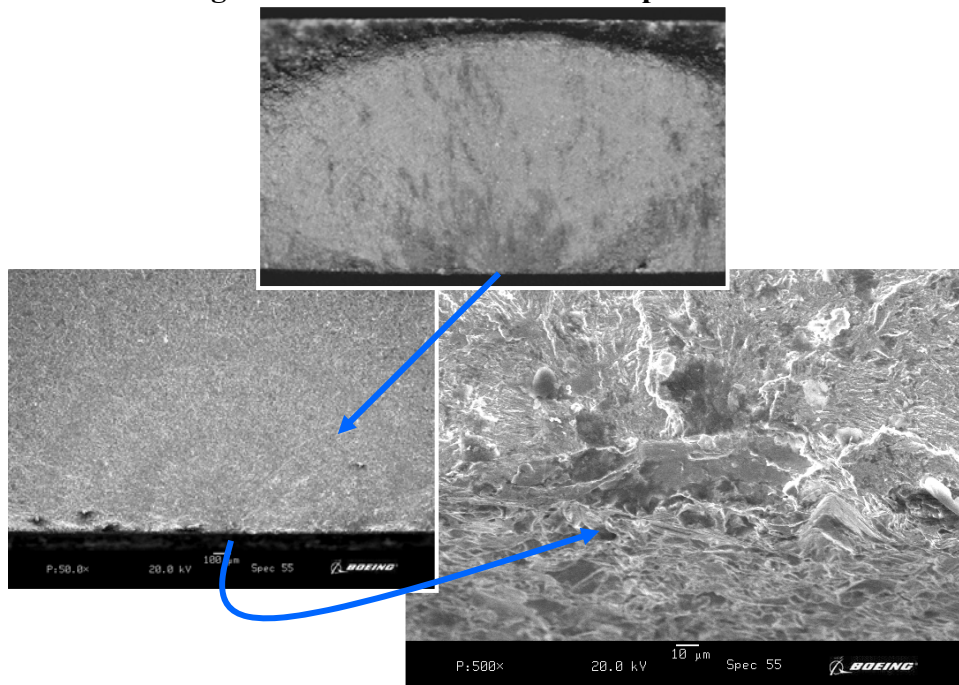
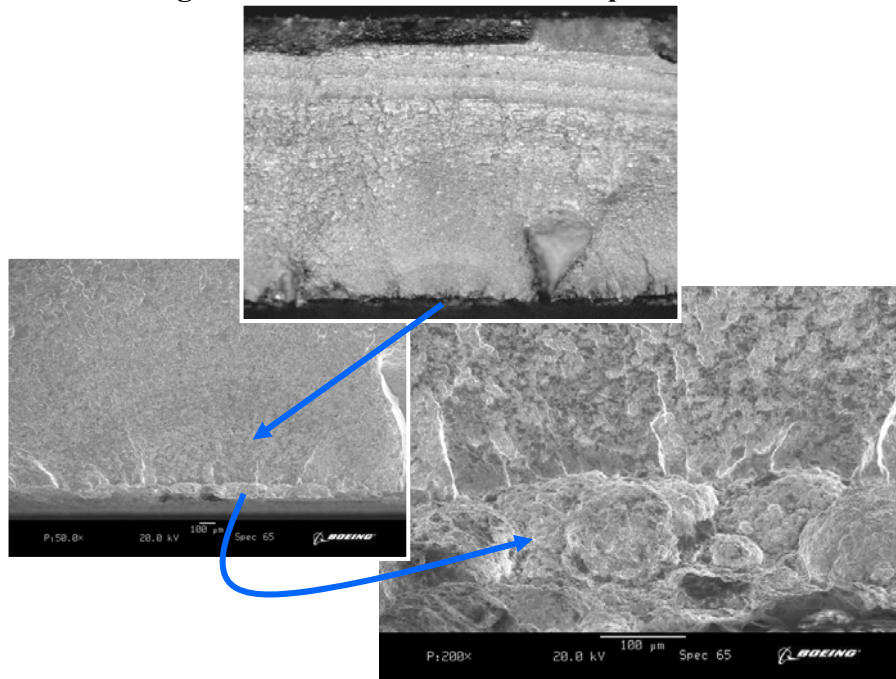


Figure 13-9 Fracture Surface of Specimen 65



References

- [1] Perez, R. Sankaran, K. K., and Smith, Jr., H. G. "Structural Life Enhancement - Corrosion Impact on Airframe Total Life Analysis", The Boeing Company, Final Report submitted to NAVAIR, October 2003.
- [2] Kondo, Y., Corrosion, Vol. 45, 1989, p7.
- [3] Akashi, M. and Nakayama, G., **A Process Model for the Initiation of Stress-Corrosion Crack Growth in BWR Plant Materials,** Effects of the Environment on the Initiation of Crack Growth", ASTM STP 1298, W. A. Van Der Sluys, R. S. Piascik, and R. Zawierucha, Eds., American Society for Testing and materials, 1997.
- [4] Akid, R. **"The Role of Stress-Assisted Localized Corrosion in the Development of Short Fatigue Cracks,"** Effects of the Environment on the Initiation of Crack Growth", ASTM STP 1298, W. A. Van Der Sluys, R. S. Piascik, and R. Zawierucha, Eds., American Society for Testing and materials, 1997.
- [5] Shi, P. and Mahadevan, S. **"Probabilistic Estimation of Pitting Corrosion Fatigue Life,"** AIAA Paper -2000-1644, April 2000
- [6] Wei, R. P., Gao, M, and Harlow, "Corrosion and Corrosion Fatigue Aspects of Aging Aircraft", Proceedings – Air Force 4th Aging Aircraft Conference, 9-11 July 1996, pp 226-250
- [7] Chen, G. S., Liao, C. M., Wan, K. C., Gao, M. and Wei, R. P., **"Pitting corrosion and Fatigue Crack Nucleation,"** Effects of the Environment on the Initiation of Crack Growth", ASTM STP 1298, W. A. Van Der Sluys, R. S. Piascik, and R. Zawierucha, Eds., American Society for Testing and materials, 1997.
- [8] Impellizzeri, L. F., and Rich, D. L., **"Spectrum Fatigue Crack Growth in Lugs,"** Fatigue Crack Growth Under Spectrum Loads, ASTM STP 595, American Society for Testing and Materials, Philadelphia, 1976, pp.320-336
- [9] Rich, D. L. And Impellizzeri, L. F., **"Fatigue Analysis of Cold-Worked and Interference Fit Fastener Holes,"** Cyclic Stress-Strain and Plastic Deformation Aspects of Fatigue Crack Growth, ASTM STP 637, American Society for Testing and Materials, Philadelphia, 1977, pp. 153-175.
- [10] Lyon, S.P., Thompson, G.E. and Johnson, J.B., "Materials Evaluation Using Wet-Dry Mixed Salt-Spray Tests," New Methods for Corrosion Testing of Aluminum Alloys, ASTM STP 1134, 1992, p. 20
- [11] Molls, T., Sharp, P.K. and Loader, C., "The Incorporation of Pitting Corrosion Damage into F-111 Fatigue Life Modeling", Report DSTO-RR-0237, Defense Science

and Technology Aeronautical and Maritime Research Laboratory, Fishermans Bend, Victoria, Australia, June 2002.

[12] “Salt Spray Corrosion testing of HP 9-4-30 F/A-18 C/D Wingfold Transmission Ring Gear Housings”, Department of Materials and Processes Engineering Report, MA #1110-01, Memo #012-01, Moog Inc. Torrance Operations, August 2001.

[13] “Accelerated Corrosion Test”, GM9540P, General Motors Engineering Standards, July 1991.

[14] Gaenzle, K. J., NADEP NORIS MEL Report FA-0011-01 dated 27 February 2001.

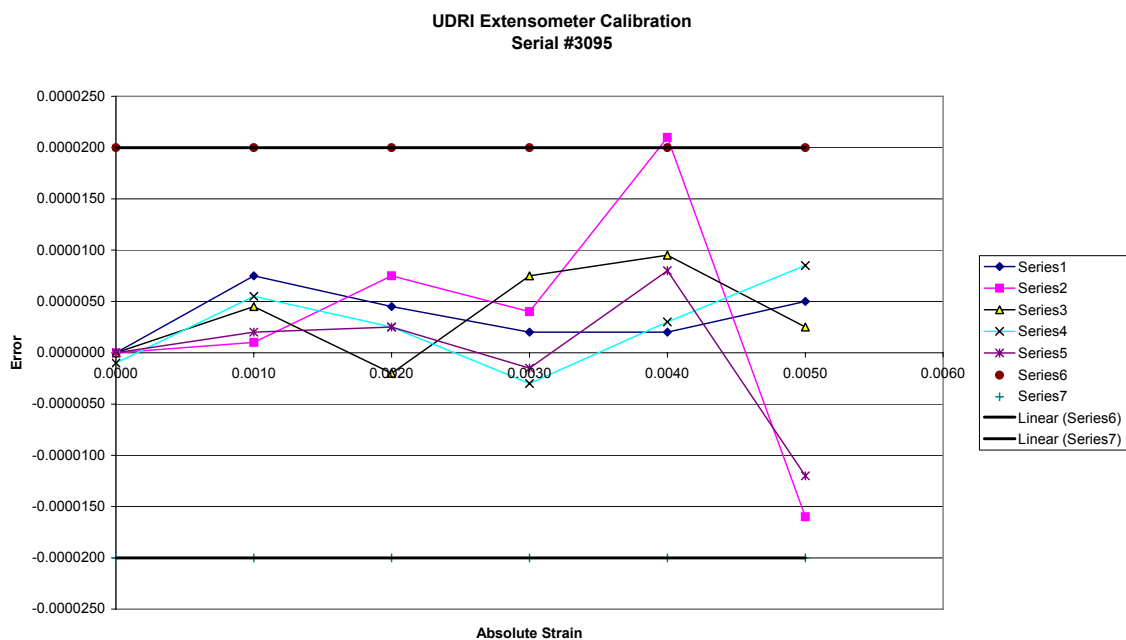
[15] Coulter, R. W., “F/A – 18 C/D Wing Fold Transmission Lugs Failure Analysis”, Boeing Tech Memo 254.02.0014.01, 12 Feb. 02.

[16] Odom, D., and Baptist, T. “Corrosion Test Report for the F/A-18A/B/C/D Wingfold Mechanical Drive Group Transmission”, Allied Signal Aerospace Report 93-67123, August 26, 1994

[17] Peterson, R. E., Stress Concentration Factors, John Wiley & Sons, New York, 1974

Appendix C

Extensometer Calibration Data Sheets



Gage Length (in)	1.000							
Range (in/V)	0.00050							
Model	MTS 440.21							
Serial #	3905							
Standard (in)	Run 1 (V)	Run 2 (V)	Run 3 (V)	Run 4(V)	Run(5)			
0.0000	0.000	0.000	0.000	-0.002	0			
0.0010	2.015	2.002	2.009	2.011	2.004			
0.0020	4.009	4.015	3.996	4.005	4.005			
0.0030	6.004	6.008	6.015	5.994	5.997			
0.0040	8.004	8.042	8.019	8.006	8.016			
0.0050	10.010	9.968	10.005	10.017	9.976			
	Run 1 (in)	Run 2 (in)	Run 3 (in)	Run 4 (in)	Run 5 (in)			
0.0000000	0.0000000	0.0000000	0.0000000	-0.0000010	0.0000000			
0.0010075	0.0010010	0.0010010	0.0010045	0.0010055	0.0010020			
0.0020045	0.0020075	0.0019980	0.0020025	0.0020025	0.0020025			
0.0030020	0.0030040	0.0030075	0.0029970	0.0029985	0.0029985			
0.0040020	0.0040210	0.0040095	0.0040030	0.0040080	0.0040080			
0.0050050	0.0049840	0.0050025	0.0050085	0.0049880	0.0049880			
	Error 1 (in/in)	Error 2 (in/in)	Error 3 (in/in)	Error 4 (in/in)	Error 5 (in/in)			
0.0000	0.0000000	0.0000000	0.0000000	-0.0000010	0.0000000			
0.0010	0.0000075	0.0000010	0.0000045	0.0000055	0.0000020			
0.0020	0.0000045	0.0000075	-0.0000020	0.0000025	0.0000025			
0.0030	0.0000020	0.0000040	0.0000075	-0.0000030	-0.0000015			
0.0040	0.0000020	0.0000210	0.0000095	0.0000030	0.0000080			
0.0050	0.0000050	-0.0000160	0.0000025	0.0000085	-0.0000120			
Class A Error Band				Volts	Inches	Fixed Error		Relative Error
Fixed Error	-0.00002	0.00002		0	0	0.00002	-0.00002	0
Relative Error%	-0.1	0.1		2	0.001	0.00002	-0.00002	0.000001
				4	0.002	0.00002	-0.00002	0.000002
				6	0.003	0.00002	-0.00002	0.000003
				8	0.004	0.00002	-0.00002	0.000004
				10	0.005	0.00002	-0.00002	0.000005

Strain gages					
D	$RG/(RG+2RL)$				
error = $2RL/RG/(1+2RL/RG)$					
RL = resistance in one lead wire					
RG = Gage resistance					
RG =	350	ohms			
RL =	0.5	ohms			
			Error on ohm Measurement	D1	D2
			0.05	0.997151	0.996867
			0.1	0.997151	0.996583
					0.03%
					0.06%

Appendix D

Residual Stress Profile Measurements Report

Report# 1882

Preliminary RESULTS SStresstech X3000 Analyzer

8/24/2004 [2(6)]

RESIDUAL STRESS RESULTS

Preliminary Results

COMPANY
SAMPLE TYPE

Radiation (hkl) :	Xka (211)	Spot Size :	X mm dia. coll.	Exposure Time :	X seconds
Tilt Settings :	-xx-0-xx X/X	Oscillation :	noneX +/- X deg	Material Removal :	noneXElectropolish
Material Constant :	X	X-ray Mod. E/(1+v) :	X MPa	Machine/ Soft Ver.	RedXBlueX3000/1.10.0

Specimen No 3

Locations L4, L5, and L6. Directions Longitudinal, 45 degrees, and Transverse.

No 3 L4 Long				No 3 L5 Long				No 3 L6 Long			
Depth inch	Stress ksi	Error +/-	FWHM °	Depth inch	Stress ksi	Error +/-	FWHM °	Depth inch	Stress ksi	Error +/-	FWHM °
0.0000	-95.6	3.1	5.13	0.0000	-97.5	2.9	5.11	0.0000	-94.6	3.6	5.19
0.0010	-70.0	5.2	3.87	0.0010	-119.2	5.5	3.81	0.0011	-103.5	6.1	3.87
0.0021	-11.8	6.6	3.81	0.0020	-26.5	6.0	3.81	0.0022	-34.6	6.1	3.84
0.0031	-4.4	6.7	3.78	0.0031	-9.7	7.4	3.72	0.0030	-6.4	6.2	3.77

No 3 L4 45 Deg				No 3 L5 45 Deg				No 3 L6 45 Deg			
Depth inch	Stress ksi	Error +/-	FWHM °	Depth inch	Stress ksi	Error +/-	FWHM °	Depth inch	Stress ksi	Error +/-	FWHM °
0.0000	-98.1	2.4	5.14	0.0000	-98.2	2.4	5.24	0.0000	-96.5	1.3	5.07
0.0010	-71.3	1.3	3.88	0.0010	-124.6	2.0	3.78	0.0011	-108.6	0.7	3.81
0.0021	-12.0	2.3	3.81	0.0020	-22.4	2.9	3.84	0.0022	-33.3	1.4	3.85
0.0031	-3.5	2.5	3.78	0.0031	-7.3	2.2	3.80	0.0030	-4.5	2.6	3.80

No 3 L4 Trans				No 3 L5 Trans				No 3 L6 Trans			
Depth inch	Stress ksi	Error +/-	FWHM °	Depth inch	Stress ksi	Error +/-	FWHM °	Depth inch	Stress ksi	Error +/-	FWHM °
0.0000	-95.7	2.7	5.21	0.0000	-93.3	1.2	5.28	0.0000	-97.3	1.8	4.90
0.0010	-73.1	3.4	3.96	0.0010	-124.4	1.7	5.75	0.0011	-112.3	1.9	3.94
0.0021	-6.4	0.8	3.90	0.0020	-23.1	0.8	3.90	0.0022	-33.7	0.8	3.87
0.0031	-1.5	1.0	3.84	0.0031	-7.7	1.4	3.75	0.0030	-1.1	0.8	3.92

0 Stress Fe Powder Performance Verification Check Measured :

0

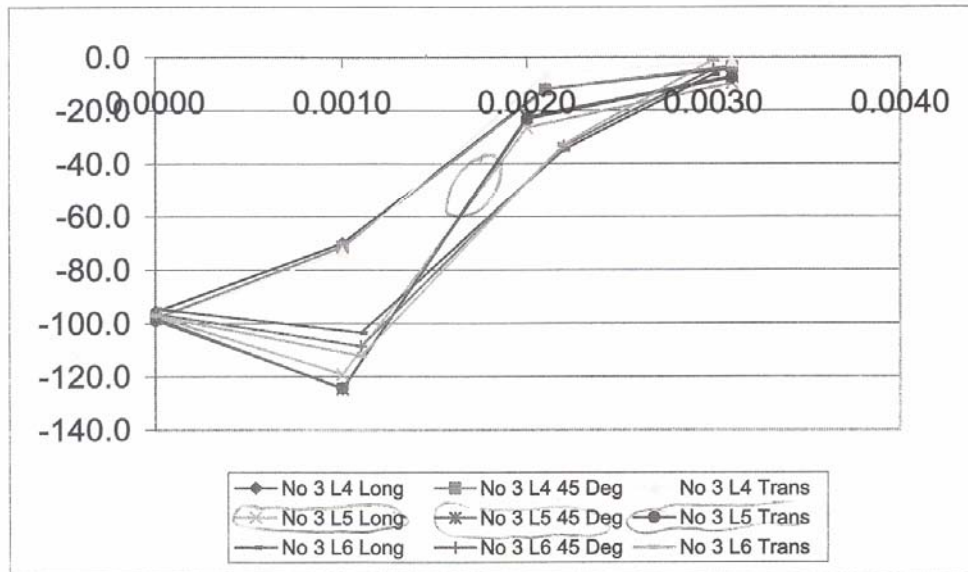
0

AST 207 Kappa Dr. Pittsburgh, PA 15230 (412)653-0675, fax (412)653-7532, e-mail: info@SStresstech.com, web: www.SStresstech.com

RESIDUAL STRESS RESULTS

0
0

0	0	0	0	0	0
0	0	0	0	0	0
0	0	0	0	0	0



FWHM - Full Width at Half Max... measure of peak width.

0 Stress Fe Powder Performance Verification Check Measured :

0

0

RESIDUAL STRESS RESULTS

AST 267 Kappa Dr, Pittsburgh, PA 15238 (412)963-0676, fax: (412)963-7552, e-mail: Info@ASTresstech.com, web: www.ASTresstech.com

COMPANY
SAMPLE TYPE

Radiation (hkl) :	Xka (211)	Spot Size :	X mm dia. coll.	Exposure Time :	X seconds
Tilt Settings :	-xx-0-xx X/X	Oscillation :	noneX +/- X deg	Material Removal :	noneXElectropolish
Material Constant :	X	X-ray Mod. E/(1+v) :	X MPa	Machine/ Soft Ver.	RedXBlueX3000/1.10.3

Specimen No 64

Locations L4, L5, and L6. Directions Longitudinal, 45 degrees, and Transverse.

No 64 L4 Long				No 64 L5 Long				No 64 L6 Long			
Depth inch	Stress ksi	Error +/-	FWHM °	Depth inch	Stress ksi	Error +/-	FWHM °	Depth inch	Stress ksi	Error +/-	FWHM °
0.0000	-97.2	2.1	5.07	0.0000	-93.8	3.2	5.24	0.0000	-93.0	3.0	5.09
0.0013	-94.7	3.7	3.81	0.0002	-114.6	2.1	4.67	0.0009	-128.6	4.6	3.78
0.0022	-43.5	4.9	3.90	0.0006	-138.9	3.5	4.03	0.0020	-33.7	5.8	3.78
0.0031	-9.8	6.5	3.74	0.0011	-131.3	5.3	3.77	0.0031	-7.7	6.5	3.72
				0.0016	-105.8	5.2	3.78				
				0.0020	-73.5	4.9	3.88				
				0.0026	-21.5	5.7	3.78				
				0.0034	-3.9	6.4	3.67				

No 64 L4 45 Deg				No 64 L5 45 Deg				No 64 L6 45 Deg			
Depth inch	Stress ksi	Error +/-	FWHM °	Depth inch	Stress ksi	Error +/-	FWHM °	Depth inch	Stress ksi	Error +/-	FWHM °
0.0000	-99.2	2.0	5.23	0.0000	-97.6	2.4	5.19	0.0000	-97.9	2.2	5.23
0.0013	-91.7	1.9	3.84	0.0002	-118.4	1.9	4.77	0.0009	-132.3	2.4	3.81
0.0022	-41.9	0.8	3.90	0.0006	-142.5	1.3	4.03	0.0020	-34.9	2.6	3.81
0.0031	-7.5	1.2	3.74	0.0011	-135.5	1.6	3.81	0.0031	-6.5	1.8	3.75
				0.0016	-110.3	2.6	3.77				
				0.0020	-76.4	1.8	3.87				
				0.0026	-20.9	1.7	3.77				
				0.0034	-2.6	1.8	3.75				

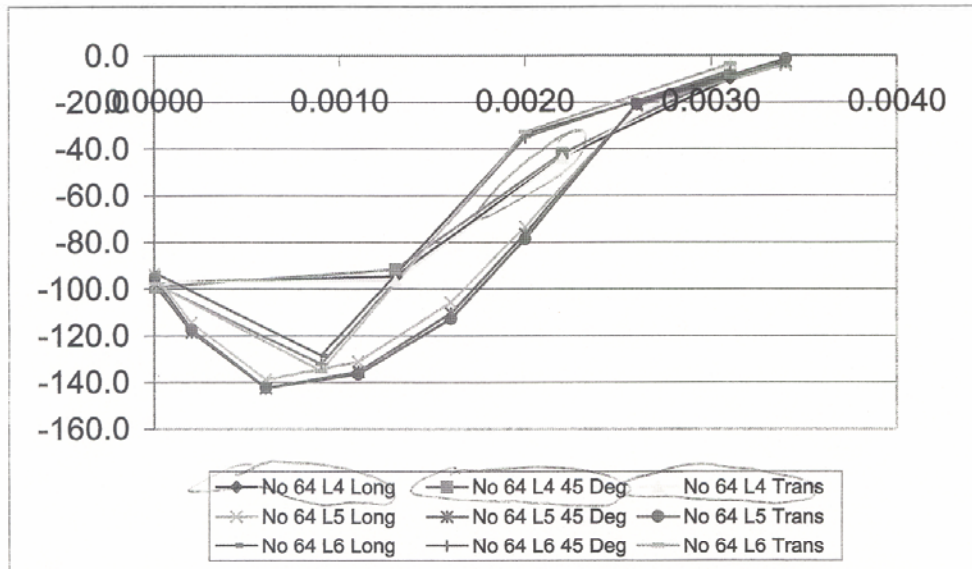
No 64 L4 Trans				No 64 L5 Trans				No 64 L6 Trans			
Depth inch	Stress ksi	Error +/-	FWHM °	Depth inch	Stress ksi	Error +/-	FWHM °	Depth inch	Stress ksi	Error +/-	FWHM °
0.0000	-97.0	1.8	5.20	0.0000	-95.3	2.0	5.29	0.0000	-97.5	2.3	5.21
0.0013	-96.5	1.1	3.78	0.0002	-117.4	0.6	4.81	0.0009	-135.3	0.9	3.78
0.0022	-43.8	0.3	3.88	0.0006	-142.4	1.0	4.04	0.0020	-32.7	1.5	3.84
0.0031	-3.7	0.5	3.75	0.0011	-136.5	1.4	3.82	0.0031	-3.5	1.3	3.74
				0.0016	-112.7	0.6	3.77				
				0.0020	-78.7	1.3	3.84				
				0.0026	-20.6	1.1	3.77				
				0.0034	-1.3	1.6	3.75				

0 Stress Fe Powder Performance Verification Check Measured : -X.x +/- X.x MPa

RESIDUAL STRESS RESULTS

COMPANY
SAMPLE TYPE

Radiation (hkl) :	Xka (211)	Spot Size :	X mm dia. coll.	Exposure Time :	X seconds
Tilt Settings :	-xx-0-xx X/X	Oscillation :	noneX +/- X deg	Material Removal :	noneXElectropolish
Material Constant :	X	X-ray Mod. E/(1+v) :	X MPa	Machine/ Soft Ver.	RedXBlueX3000/1.10.2



RESIDUAL STRESS RESULTS**Naval Air Warfare Center
Corrosion Test Plate**

Radiation (hkl) :	CrKa (211)	Spot Size :	3 mm dia. coll.	Exposure Time :	5 seconds
Tilt Settings :	-40-0-40 4/4	Oscillation :	tilt +/-5 deg	Material Removal :	Electropolish
Material Constant :	1008/1016 steel	Modul. E / Poisson v	207000 Mpa/ .285	Machine/ Soft. Ver.	RedX3000/1.12.1

Specimen No 10

Locations L1, L2, and L3. Directions Longitudinal, 45 degrees, and Transverse.

No 10 L1 Long				No 10 L2 Long				No 10 L3 Long			
Depth inch	Stress ksi	Error +/-	FWHM °	Depth inch	Stress ksi	Error +/-	FWHM °	Depth inch	Stress ksi	Error +/-	FWHM °
0.0000	-99.0	3.5	5.26	0.0000	-101.6	3.7	5.23	0.0000	-95.9	2.4	5.33
0.0003	-124.4	2.6	4.50	0.0011	-116.2	5.4	3.85	0.0010	-128.3	4.8	3.82
0.0006	-133.8	3.9	4.01	0.0021	-32.1	7.4	3.88	0.0020	-81.5	7.2	3.88
0.0007	-131.4	5.5	3.87	0.0030	-6.6	8.2	3.75	0.0030	-16.2	6.6	3.82
0.0011	-120.5	6.0	3.87								
0.0016	-101.5	6.5	3.81								
0.0020	-85.5	5.8	3.85								
0.0030	-12.5	7.5	3.77								

No 10 L1 45 Deg				No 10 L2 45 Deg				No 10 L3 45 Deg			
Depth inch	Stress ksi	Error +/-	FWHM °	Depth inch	Stress ksi	Error +/-	FWHM °	Depth inch	Stress ksi	Error +/-	FWHM °
0.0000	-101.1	1.8	5.29	0.0000	-101.8	1.5	5.17	0.0000	-95.9	1.2	5.40
0.0003	-128.0	0.7	4.45	0.0011	-118.0	1.8	3.87	0.0010	-135.5	2.4	3.85
0.0006	-138.0	0.7	4.01	0.0021	-32.8	2.2	3.84	0.0020	-84.2	0.7	3.90
0.0007	-136.9	1.0	3.90	0.0030	-5.7	2.7	3.80	0.0030	-15.7	1.7	3.87
0.0011	-130.3	1.0	3.80								
0.0016	-110.4	0.8	3.80								
0.0020	-70.3	2.2	3.85								
0.0030	-11.2	2.9	3.81								

No 10 L1 Trans				No 10 L2 Trans				No 10 L3 Trans			
Depth inch	Stress ksi	Error +/-	FWHM °	Depth inch	Stress ksi	Error +/-	FWHM °	Depth inch	Stress ksi	Error +/-	FWHM °
0.0000	-99.5	2.9	5.27	0.0000	-101.1	1.9	5.20	0.0000	-97.0	2.7	5.27
0.0003	-126.8	1.5	4.58	0.0011	-124.2	0.9	3.87	0.0010	-136.0	1.1	3.88
0.0006	-138.2	1.0	4.07	0.0021	-33.0	2.0	3.87	0.0020	-88.5	1.8	3.82
0.0007	-139.1	1.0	3.88	0.0030	-3.2	0.6	3.78	0.0030	-16.4	2.7	3.87
0.0011	-134.2	1.6	3.80								
0.0016	-115.1	0.8	3.81								
0.0020	-74.8	0.5	3.82								
0.0030	-9.8	0.9	3.87								

0 Stress Fe Powder Performance Verification Check Measured : -0.4+-0.5 ksi

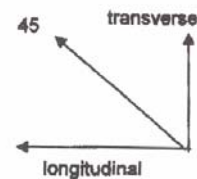
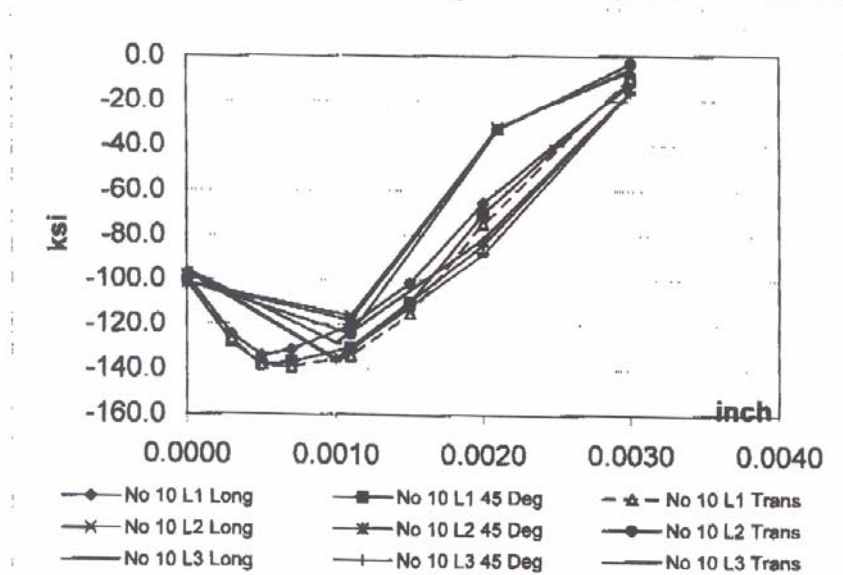
RESIDUAL STRESS RESULTS

Naval Air Warfare Center
Corrosion Test Plate

Radiation (hkl)	: CrKa (211)	Spot Size	: 3 mm dia. coll.	Exposure Time	: 5 seconds
Tilt Settings	: -40-0-40 4/4	Oscillation	: tilt +/-5 deg	Material Removal	: Electropolish
Material Constant	: 1008/1018 steel	Modul. E / Poisson v	: 207000 Mpa/285	Machine/ Soft. Ver.	: RedX3000/1.12.1

Specimen No 10

Locations L1, L2, and L3. Directions Longitudinal, 45 degrees, and Transverse.



FWHM - Full Width at Half Max... measure of peak width.

0 Stress Fe Powder Performance Verification Check Measured: -0.4+-0.5

ksi

Appendix E

Acronyms and Abbreviations

AES – auger electron spectroscopy
AFM – atomic force microscope
BEA – boundary element
CCD – charge-coupled device
CPCs – corrosion preventive compounds
DSTO – Defense Science & Technology Organization
EDS – energy dispersive spectroscopy
FEA – finite element
Htp – Defined by setting the tp1 (peak threshold bearing ratio value) and tp2 (the valley threshold bearing ratio value) to be separated by 40%
NVL (Normalized Volume Loss) – The ratio of the volume missing to the lateral area
OCP – open circuit potential
P.S. – Process Specification
PZT – piezoelectric transducer
Ra – average surface roughness
Rku (Kurtosis) – A measure of the sharpness of the profile about the mean line
RMS – mean square
Rp – maximum surface height peak
Rpk (Reduced Peak Height) – The top portion of the surface that will be worn away during the run-in period
Rq – root mean square surface roughness
Rsk (Skewness) – A measure of the symmetry of the profile about the mean line
Rt – maximum difference from the highest peak to the lowest valley
Rv – maximum surface height valley
RVE – representative volume element
Rvk (Reduced Valley Depth) – The lowest portion of the surface that will retain lubricant
Rz – average maximum height of the profile
S index (surface area index) – The ratio of the surface area of the profile to the surface area of an ideal plane
SCE – saturated calomel reference electrode
SEM – scanning electron microscope
TOF – time-of-flight
UFM – ultrasonic force microscope